

## University of Southampton Research Repository

Copyright © and Moral Rights for this thesis and, where applicable, any accompanying data are retained by the author and/or other copyright owners. A copy can be downloaded for personal non-commercial research or study, without prior permission or charge. This thesis and the accompanying data cannot be reproduced or quoted extensively from without first obtaining permission in writing from the copyright holder/s. The content of the thesis and accompanying research data (where applicable) must not be changed in any way or sold commercially in any format or medium without the formal permission of the copyright holder/s.

When referring to this thesis and any accompanying data, full bibliographic details must be given, e.g.

Thesis: Author (Year of Submission) "Full thesis title", University of Southampton, name of the University Faculty or School or Department, PhD Thesis, pagination.

Data: Author (Year) Title. URI [dataset]



**UNIVERSITY OF SOUTHAMPTON**

FACULTY OF NATURAL AND ENVIRONMENTAL SCIENCES

Ocean and Earth Science

Volume 1 of 1

# **Critical Metals in Porphyry Copper Deposits**

by

**Katie Anne McFall**

Thesis for the degree of Doctor of Philosophy

September 2016









UNIVERSITY OF SOUTHAMPTON

## **ABSTRACT**

FACULTY OF NATURAL AND ENVIRONMENTAL SCIENCES

Ocean and Earth Science

Thesis for the degree of Doctor of Philosophy

### **CRITICAL METALS IN PORPHYRY COPPER DEPOSITS**

Katie Anne McFall

Critical metals are elements essential to high-tech industry and green technology which are associated with a significant supply risk. Diversifying supplies of these elements is therefore a high priority. Porphyry copper deposits contain potentially economic enrichments of some of these elements, namely rhenium, platinum group elements (PGEs), bismuth and tellurium. This thesis investigates the source, transport mechanism and distribution of these critical elements in two post-collisional Tethyan porphyry deposits. The Muratdere Cu-Mo (Au-Re) porphyry deposit, Turkey, described here for the first time, contains two generations of molybdenite with contrasting Re concentrations. The early, Re-poor molybdenites have magmatic  $\delta^{34}\text{S}_{\text{CDT}}$  values, while the late, vein hosted Re-rich molybdenite has  $\delta^{34}\text{S}_{\text{CDT}}$  values matching those of the surrounding country rock suggesting that the additional Re has been sourced from hydrothermal fluid-country rock interaction. The Skouries Cu-Au porphyry deposit, Greece, is PGE, Te and Bi enriched. In contrast to Muratdere, Skouries is shown to be an orthomagmatic system hosted by a series of overprinting dykes, with the metal enrichment hypothesised to have been provided by periodic mafic recharge of a deeper source magma chamber. The mineralising fluids in Skouries are shown to have been highly oxidised and hypersaline with complex cation chemistry (Na, K, Fe, Mn and Ca), and with the overall fluid evolution progressing from an early  $\text{CO}_2$  rich fluid to a later brine. The PGEs in the deposit are located in the main hypogene mineralising veinsets, associated with potassic alteration, and are found to be hosted in bismuth and tellurium complexes. A variety of platinum group minerals are identified, including sopcheite ( $\text{Ag}_4\text{Pd}_3\text{Te}_4$ ) and sobolevskite ( $\text{PdBi}$ ). LA-ICP-MS of fluid inclusions, combined with microthermometry, has shown gold, bismuth and palladium to be hydrothermally transported by high temperature ( $>500^\circ\text{C}$ ), high salinity ( $>65$  wt%  $\text{NaCl}+\text{KCl}$ ) and highly oxidised fluids, and a bismuth-tellurium collector model is proposed to allow concentration of palladium from under-saturated fluids into platinum group minerals. High semi-metal (Te and Bi) contents in porphyries are therefore proposed to be an indicator of PGE enrichment.



# Table of Contents

<b>Table of Contents .....</b>	<b>i</b>
<b>List of Tables .....</b>	<b>vii</b>
<b>List of Figures .....</b>	<b>ix</b>
<b>DECLARATION OF AUTHORSHIP .....</b>	<b>xv</b>
<b>Acknowledgements .....</b>	<b>xvii</b>
<b>Definitions and Abbreviations .....</b>	<b>xix</b>
<b>Chapter 1: Introduction .....</b>	<b>1</b>
1.1 Critical metals .....	1
1.1.1 How is criticality defined?.....	2
1.1.2 How can criticality be managed?.....	4
1.1.3 Critical metals within the scope of this project .....	6
1.2 Porphyry copper deposits .....	10
1.2.1 Common features of porphyry copper deposits .....	11
1.2.2 Genetic models for porphyry copper deposits.....	13
1.3 Tethyan metallogenic belt .....	17
1.4 Project rationale .....	20
<b>Chapter 2: Methodology .....</b>	<b>23</b>
2.1 Fieldwork and sample collection .....	23
2.1.1 Core logging and sampling.....	23
2.1.2 Available datasets .....	24
2.2 Micro-analysis .....	24
2.2.1 Scanning electron microscope (SEM) .....	24
2.2.2 Electron probe micro-analysis (EPMA) .....	25
2.2.3 Laser Raman Spectroscopy .....	26
2.3 X-ray diffraction (XRD) .....	26
2.4 Fluid inclusion micro-thermometry .....	27
2.5 LA-ICP-MS.....	28

2.5.1	LA-ICP-MS of molybdenites .....	28
2.5.2	LA-ICP-MS of fluid inclusions .....	30
2.6	Ni-S fire assay .....	36
2.7	Stable isotopes .....	38
2.7.1	Sulphur .....	38
2.7.2	Oxygen and hydrogen .....	38
<b>Chapter 3: Enhanced rhenium concentrations in the Muratdere Cu-Mo (Au-Re) porphyry deposit, Turkey due to hydrothermal fluid-country rock interactions.....</b>		<b>41</b>
3.1	Introduction.....	41
3.1.1	Current models for rhenium enrichment in porphyry copper deposits .	41
3.1.2	Transport of rhenium in porphyry deposits .....	43
3.1.3	Hosting of rhenium in molybdenite .....	43
3.2	Regional geology.....	44
3.3	Deposit geology .....	47
3.3.1	Alteration & mineralisation .....	49
3.4	Analytical results.....	53
3.4.1	Whole rock assay data.....	53
3.4.2	Composition of molybdenites .....	54
3.4.3	Platinum group element (PGE) analysis .....	57
3.4.4	Stable isotopes .....	57
3.4.5	Fluid inclusions .....	59
3.5	Discussion .....	62
3.5.1	Fluid evolution of the Muratdere deposit.....	62
3.5.2	Muratdere deposit genetic model .....	66
3.5.3	Critical metal enrichment in the Muratdere deposit .....	67
3.6	Conclusions.....	72
<b>Chapter 4: A fluid history of the Skouries Cu-Au (Pd, Pt, Te) porphyry deposit, Greece.. .....</b>		<b>73</b>

4.1	Introduction .....	73
4.1.1	Alkali porphyry deposits .....	73
4.1.2	Regional geology .....	74
4.1.3	Past work .....	76
4.2	Skouries geology .....	77
4.2.1	Intrusive phases .....	79
4.2.2	Alteration and mineralogy .....	81
4.2.3	Ore mineral paragenesis and accessory minerals from SEM .....	91
4.3	Stable isotopes .....	94
4.3.1	Sulphur isotopes .....	94
4.3.2	Oxygen and hydrogen isotopes .....	95
4.4	Fluid inclusions .....	96
4.4.1	Petrography .....	96
4.4.2	SEM analysis of fluid inclusions .....	104
4.4.3	Fluid inclusion microthermometry .....	108
4.4.4	LA-ICP-MS of fluid inclusions .....	111
4.5	Discussion .....	117
4.5.1	Interpretation of fluid inclusion petrography .....	117
4.5.2	Interpretation of microthermometry .....	118
4.5.3	Fluid chemistry .....	125
4.5.4	Synthesis and fluid history .....	127
4.6	Conclusions and genetic model .....	131
<b>Chapter 5:</b>	<b>Platinum group minerals in the Skouries Cu-Au (Pd, Pt, Te) porphyry deposit.....</b>	<b>133</b>
5.1	Introduction .....	133
5.1.1	Platinum group elements in Porphyries .....	133
5.1.2	Previous work on PGEs in Skouries.....	136
5.2	Mineral chemistry and platinum group mineral classification .....	137
5.2.1	Samples analysed.....	137

5.2.2	Platinum group minerals .....	137
5.2.3	Other precious-metal bearing minerals .....	144
5.2.4	Bornite and galena chemistry .....	144
5.3	Discussion .....	147
5.4	Conclusions .....	149
<b>Chapter 6: Platinum group element transport in the Skouries Cu-Au (Pd, Pt, Te)</b>		
	<b>porphyry deposit.....</b>	<b>151</b>
6.1	Introduction.....	151
6.2	Methods.....	152
6.3	Results.....	153
6.3.1	Interferences on palladium .....	153
6.3.2	Platinum group element and semi-metal concentrations in fluid inclusions .....	156
6.4	Discussion .....	159
6.4.1	Hydrothermal transport of PGEs .....	159
6.4.2	The role of semi-metals in PGE enrichment.....	159
6.4.3	The source of PGE enrichment in Skouries .....	161
6.5	Conclusions .....	164
<b>Chapter 7: Conclusions..... 167</b>		
7.1	Comparing the Muratdere and Skouries deposits .....	167
7.2	Source and distribution of critical metals in porphyry deposits .....	168
7.2.1	Where are critical metals hosted in porphyry deposits? .....	169
7.2.2	What is the source of critical metal enrichment in porphyry copper deposits? .....	169
7.2.3	How are these metals transported and enriched within the system? .	170
7.2.4	What features can be used as an exploration aid to discover more critical metal enriched porphyries? .....	170
7.3	Further work.....	171
7.3.1	Platinum group element enrichment in porphyry deposits and the Skouries deposit .....	171



7.3.2	Rhenium enrichment in porphyries and the Muratdere deposit.....	172
<b>Appendices.....</b>		<b>173</b>
<b>Appendix A.....</b>		<b>175</b>
A.1	Methodology.....	175
A.1.1	EPMA calibration data .....	175
A.1.2	Transient signal fluid inclusion LA-ICP-MS signal and integration intervals.....	177
A.1.3	Changes in LA-ICP-MS limits of detection in fluid inclusions with change in signal integration length .....	178
A.1.4	Accuracy and precision of LA-ICP-MS of fluid inclusions.....	178
A.2	Muratdere deposit.....	180
A.2.1	LA-ICP-MS summary table .....	180
A.2.2	PGE analysis data table .....	182
A.2.3	Stable isotope summary data table.....	183
A.3	Skouries deposit.....	184
A.3.1	Stable isotope summary data table.....	184
A.3.2	Samples chosen for fluid inclusion analysis.....	184
A.3.3	Laser Raman results table.....	187
A.3.4	Summary data table of LA-ICP-MS of fluid inclusions using ‘method 1’.....	189
A.3.5	LA-ICP-MS data from ‘method 2’.....	191
A.4	Drill core log compilations .....	195
A.4.1	Compilation of Muratdere drill core logs .....	195
A.4.2	Compilation of Skouries drill core logs .....	199
<b>Appendix B.....</b>		<b>203</b>
<b>Appendix C.....</b>		<b>203</b>
<b>List of References .....</b>		<b>205</b>



## List of Tables

Table 1: Critical elements.....	4
Table 2: Accuracy and precision of EPMA standards.....	26
Table 3: Accuracy and precision of LA-ICP-MS for molybdenites. ....	29
Table 4: LA-ICP-MS methods for fluid inclusion analysis .....	31
Table 5: Affect of salinity on absolute element concentration in fluid inclusion LA-ICP-MS. ....	35
Table 6: Accuracy of Ni-S fire assay method.....	37
Table 7: Precision of Ni-S fire assay method.....	37
Table 8: Accuracy and precision of stable isotope results .....	39
Table 9: Summary of stable isotope results for the Muratdere deposit. ....	57
Table 10: Summary of fluid inclusion microthermometry results for the Muratdere deposit....	60
Table 11: Features of the main veinsets in the Skouries deposit .....	84
Table 12: Summary of the fluid inclusion types observed in the Skouries deposit .....	98
Table 13: Summary of PGE enriched porphyries globally.....	135
Table 14: List of samples from the Skouries deposit analysed for PGMs .....	137
Table 15: Semi-quantitative results from EDS and EPMA analysis of platinum group minerals in the Skouries deposit. ....	138
Table 16: Results from EPMA analysis of platinum group minerals in the Skouries deposit. ...	143
Table 17: EPMA results for sulphides in the Skouries deposit.....	146



# List of Figures

Figure 1: The two axis method for determining metal criticality .....	3
Figure 2: Global mine production and reserves for critical elements discussed in this thesis. ....	6
Figure 3: Diagram illustrating an ideal porphyry system (Sillitoe 2010). ....	12
Figure 4: Diagram illustrating the different tectonic settings and formation mechanisms of porphyry deposits (Richards 2011. ....	15
Figure 5: Map of the Tethyan Metallogenic Belt (Richards 2015). ....	19
Figure 6: Map of regional and deposit geology for the Muratdere deposit. ....	46
Figure 7: Photographs of the main lithological units, veinsets and alteration types in the Muratdere deposit. ....	48
Figure 8: Diagrams illustrating the paragenesis of the Muratdere deposit and the main features of the veinsets.. ....	50
Figure 9: SEM images of mineralisation in the Muratdere deposit. ....	52
Figure 10: Triplot showing the metal endowment of the main mineralising veinsets in the Muratdere deposit. ....	53
Figure 11: Results of LA-ICP-MS analysis of molybdenites from the Muratdere deposit. ....	54
Figure 12: EPMA element maps showing the distribution of trace elements in molybdenites from the Muratdere deposit. ....	56
Figure 13: Summary figure of sulphur and oxygen isotope results from the Muratdere deposit.... ....	58
Figure 14: Summary figure of fluid inclusions in the Muratdere deposit. ....	61
Figure 15: Diagram showing the transition between veinsets, alteration types and pH, temperature and sulphidation conditions in the Muratdere deposit .....	62
Figure 16: Diagram showing sulphur isotope data from the Muratdere deposit compared with ophiolites and Re-enriched porphyry deposits globally. ....	64

Figure 17: Muratdere deposit fluid oxygen and hydrogen isotopes plotted against each other and compared to global porphyry values..	66
Figure 18: Mantle normalised PGE plots for the Muratdere deposit and PGE enriched ore deposits globally.	68
Figure 19: Regional geological map for the Skouries deposit, Greece.	75
Figure 20: Geological map and cross-section for the Skouries deposit..	78
Figure 21: Photographs of the main logging units in the Skouries deposit.	80
Figure 22: Diagrams illustrating the paragenesis of the Skouries deposit.	83
Figure 23: Photomicrographs of mineralisation and alteration in the Skouries deposit	87
Figure 24: Photographs of the main mineralising veinsets in the Skouries deposit	90
Figure 25: SEM images of features of the mineralising veinsets in the Skouries desposit.	92
Figure 26: EDS element map of a mineralising vein in the Skouries deposit	93
Figure 27: Sulphur isotope results from the Skouries deposit.	94
Figure 28: Oxygen and hydrogen results for the Skouries deposit..	95
Figure 29. Illustration of typical fluid inclusion morphologies and assemblage geometries in the Skouries deposit..	97
Figure 30: Summary figure of the three main mineralising veinsets in the Skouries deposit, their fluid inclusion populations and microthermometry.	100
Figure 31: SEM images of daughter minerals in fluid inclusions from the Skouries deposit	105
Figure 32: Cathodoluminescence images of quartz from the three main mineralising veinsets in the Skouries deposit.	107
Figure 33: Calculated salinity of brine inclusions in the Skouries desposit.	110
Figure 34: Concentration of the major and minor elements present in the fluid inclusions in the Skouries deposit	115
Figure 35: Schematic P-T projection of the high-salinity H <sub>2</sub> O-NaCl system and an illustration of post-entrapment modification indicators	121
Figure 36: Skouries deposit microthermometric data and formation pressure estimates.	123

Figure 37: Copper and gold concentrations in fluid inclusions from the Skouries deposit. ....	126
Figure 38: Photomicrographs and SEM images showing platinum group minerals and precious metal tellurides from the Skouries deposit in situ. ....	142
Figure 39: EPMA element map of a zoned bornite crystal from the Skouries deposit.. ....	145
Figure 40: Comparison of whole rock Au, Pt and Pd results from the Skouries deposit with data from global ore deposits.....	148
Figure 41: Measured concentrations of <sup>111</sup> Cd and <sup>106</sup> Pd in fluid inclusions from the Skouries deposit. ....	154
Figure 42: Laser signals from LA-ICP-MS analysis of palladium bearing fluid inclusions from the Skouries deposit. ....	155
Figure 43: Concentrations of precious metals and semi-metals from laser ablation of fluid inclusions from the Skouries deposit using 'method 2'. ....	157
Figure 44: Concentrations of ore forming metals and semi-metals in fluid inclusions from the Skouries deposit.. ....	158
Figure 45: Mafic enclaves in drill core from the Skouries deposit.....	163





*Quickquid sub terra est*

*-MDSG motto*



## DECLARATION OF AUTHORSHIP

I, Katie Anne McFall, declare that this thesis, “Critical Metals in Porphyry Copper Deposits”, and the work presented in it are my own and has been generated by me as the result of my own original research.

I confirm that:

1. This work was done wholly or mainly while in candidature for a research degree at this University;
2. Where any part of this thesis has previously been submitted for a degree or any other qualification at this University or any other institution, this has been clearly stated;
3. Where I have consulted the published work of others, this is always clearly attributed;
4. Where I have quoted from the work of others, the source is always given. With the exception of such quotations, this thesis is entirely my own work;
5. I have acknowledged all main sources of help;
6. Where the thesis is based on work done by myself jointly with others, I have made clear exactly what was done by others and what I have contributed myself;
7. None of this work has been published before submission.

Signed: .....

Date: .....



## Acknowledgements

I would like to thank my supervisors for their support and patience throughout this project: Prof. Steve Roberts for his help, guidance and support throughout, and for his creative stretching of my RTSG; Dr. Jon Naden for his support, scientific guidance and discussion, particularly when the fluid inclusions weren't behaving; Prof. Damon Teagle for his scientific guidance and for whipping my writing style into shape; and Paul Lusty for his scientific advice.

Many thanks also go to all those who aided me in my fieldwork: Dr. Bob Foster, Stratex International, Mr Bahri Yildiz and the Turkey exploration team for help and support with the Muratdere deposit fieldwork; and Tim Baker, Eldorado Gold and the Stratoni team for their help and support with the Skouries deposit fieldwork. I would also like to thank Tim for his scientific advice. I would like to acknowledge and thank the expert staff at the SUERC isotope facility in East Kilbride, especially Dr. Adrian Boyce, for helping obtain and understand my stable isotope data; John Spratt for his help with microprobe analysis at the NHM; Gren Turner for his help with SEM analysis of fluid inclusions at the BGS and Simon Crust for his help with Laser Raman Spectroscopy at Kingston University. I would like to thank Dr. Jamie Wilkinson and Dr. Clara Wilkinson for their help and advice on performing LA-ICP-MS on fluid inclusions at the NHM; and Dr. Iain McDonald for his help with PGE analysis at Cardiff University. I would also like to acknowledge Adrian, Jamie and Iain's helpful scientific discussions on various aspects of this work. I would like to thank all those who helped me obtain data at Southampton University, particularly Dr. Richard Pearce for letting me loose on the SEM at all hours, Ross Williams for his help with the XRD analysis, Dr Andy Milton for his help with the LA-ICP-MS analysis, Bob Marsh for sample photography and Bob Jones, John Ford and Dan Doran for thin section preparation, tea and emotional support. I would also like to thank all those who have given me helpful comments, discussions and advice at conferences and other events over the years, particularly Dan Smith, Bruce Yardley, Richard Herrington, John Thompson and Jeremy Richards - it is great to work in such a collegiate area of geoscience.

Last but not least I would like to thank my parents for their unfailing support, patience, and for helping to correct my spelling; and my friends, particularly Martin Wood and Izzy Hessey, for moral support and plenty of beer.

I would especially like to thank Brendan McFall for his emotional and IT support, for sitting through a lot of rather one-sided conversations about geochemistry, for pretending to enjoy my 'interesting' mineral facts and for standing by me through everything over the last 4 years.



## Definitions and Abbreviations

BGS = British Geological Survey

Bi = Bismuth

BSE = Back scatter electron

CL = Cathodoluminescence

$\delta D_{V-SMOW}$  = Hydrogen isotope composition relative to V-SMOW standard

$\delta^{18}O_{V-SMOW}$  = Oxygen isotope composition relative to V-SMOW standard

$\delta^{34}S_{V-CDT}$  = Sulphur isotope composition relative to Canon Diablo Trilobite

EDS = Electron dispersive spectrometry

EPMA = Electron probe micro-analysis

HFSE = High field strength elements

IAESZ = Izmir-Ankara-Erzincan Suture Zone

LA-ICP-MS = Laser-ablation inductively coupled mass spectrometry

LILE = Large-ion lithophile elements

LOD = Limits of detection

MORB = Mid-ocean ridge basalt

NHM = Natural History museum, London

Pd = Palladium

PGEs = Platinum group elements

PGMs = Platinum group minerals

ppb = parts per billion

ppm = parts per million

Pt = Platinum

Re = Rhenium

RD = Relative difference

RSD = Relative standard deviation

SCLM = Sub-crustal lithospheric mantle

SD or  $\sigma$  = standard deviation

SEM = Scanning electron microscope

SMM = Serbo-Macedonian Metallogenic province

SUERC = Scottish Universities Environmental Research Centre

Te = Tellurium

T<sub>F</sub> = Formation temperature

T<sub>FM</sub> = Temperature of first melting

T<sub>HOM</sub> = Total homogenisation temperature

T<sub>HV-L</sub> = Vapour homogenisation temperature

T<sub>mHAL</sub> = Halite dissolution temperature

T<sub>mICE</sub> = Ice melting temperature

T<sub>mSYL</sub> = Sylvite dissolution temperature

TMB = Tethyan Metallogenic Belt

wt% = weight percent

$\bar{x}$  = mean of population x

XRD = X-ray diffraction



*This work is dedicated to Brendan for always believing in me,  
and for the steady supply of tea.*



# Chapter 1: Introduction

## 1.1 Critical metals

With a rising global population, the demands for raw materials grow ever greater, so ensuring secure and sustainable supplies of elements vital to industry is of critical importance. As technology advances, new elements become important – for example, green technology is reliant on several metals and semi-metals which are not used in many other applications. ‘Critical metals’ are metals that are essential in various industrial applications, are difficult to substitute and for which the main supply is restricted to just one or two countries. This project examines the source, distribution and enrichment mechanisms of those critical metals which are commonly found in porphyry copper deposits, with an aim to allow more efficient extraction and exploration for these elements, diversifying supply.

The abundance of individual metals in the earth’s crust varies greatly, with rock forming minerals such as Fe, Al and Ca having crustal abundances on the order of weight percent, while metals such as Au, Pd and Pt have crustal abundances on the order of ppb (Graedel et al. 2014). Ore deposits arise out of an unusual set of geological circumstances which concentrate one or more elements into a spatially restricted area of the earth’s crust, thus raising their relative abundance to an ‘economic’ level. It is not, however, just geological factors which make an ore deposit economic. Some deposits are located in politically unstable areas of the world, or in a country with legislation averse to mining, while others come with associated environmental hazards which are considered too high for economic extraction to take place - for example, very arsenic rich gold deposits. Some elements also require very complex or energy intensive extraction methods in order to be separated from their host minerals. Opening a mine is a huge investment, with a large mine costing anything between \$100 million to \$1 billion to open. Mines have an average lifespan of 10 – 100 years, so if metal prices fall suddenly or the local political situation changes, deposits which were once economic can quickly become uneconomic. This relationship between the global metals market and economic extraction leads to the concept of reserves and resources – a mineral ‘resource’ is a concentration of an element that is currently economic, or may become economically extractable in the future. ‘Reserves’ are the part of the mineral resource which has been fully geologically evaluated and is commercially and legally mineable (Gunn 2014a). The heterogeneity of ore deposit distribution means that some global regions have more reserves of certain minerals than others. This can lead to ‘resource nationalism’, where countries stockpile minerals, or strictly control their export in order to secure their own supply and exert control over their neighbours. The complex link between ore deposits and geo-politics is one of the key factors

in whether an element is considered 'critical' or not. For example, miners' strikes in Chile in 2010 threatened the supply of Cu and Re, causing a noted increase in Cu and Re prices (Lukac 2010; Webber & Farchy 2010), and this restricted supply line led to Re being defined as a 'critical element' by some governments (John 2015).

Our geological knowledge of commonly used industrial minerals such as iron, aluminium and copper is generally good which means that mining companies have a good idea of where to look for deposits and how best to process them, allowing for supply to generally match demand. However, as a new wave of technology has emerged new metals have become important to the global economy. In particular, concerns about climate change require specialist metals for the production and development of green technologies. For example platinum group elements (PGE) are needed for fuel cells and catalytic converters; tellurium is needed for photovoltaic electricity generation; silver for high performance mirrors and rhenium for the next generation of energy efficient jet engines (Buchert et al. 2009; Moss et al. 2011; Jaffe et al. 2011; Graedel et al. 2014; Gunn 2014b; John 2015). Our geological knowledge of where to find and how to extract these new 'technological' elements is more limited compared to the traditional industrial elements. Gaining a better understanding of the distribution, host mineralogy and enrichment mechanisms of critical metals in ore deposits is important as it will allow more efficient exploration and extraction, with the aim to eliminate supply risk for these essential elements.

### **1.1.1 How is criticality defined?**

Security of supply of raw materials is not a new issue, with ancient mining responding to, and indeed driving, the development of new technologies in much the same way the modern extraction industries do (Sykes et al. 2016; Thompson 2016). The first attempts to define 'critical metals' were undertaken by the USA and the EU during the 1970s and 1980s, using estimates of supply risk and economic importance to highlight elements that were strategically important (Buijs & Sievers 2011; Graedel et al. 2014). Many of those elements are no longer considered critical today due to the changing needs of industry and technology, the changing geopolitical landscape, and the advance of exploration and extraction technology (Buijs & Sievers 2011; Buijs et al. 2012; Graedel et al. 2014). This evolution of which elements are seen as 'critical' is important as many of the elements which are essential today may be rendered obsolete by advances in technology – for example, the development of Lithium-ion batteries and their widespread use in smartphones and laptops has meant that global demand for lithium has drastically increased, however future advances in battery technology may replace the need for lithium with another element (Scrosati & Garche 2010).

In 2008 the US national research council began to use a two-parameter model to assess metals. Metals were scored according to the impact of supply restriction and the risk of supply restriction, with metals which scored highly on both being classified as 'critical' (NRC Minerals 2008; Graedel et al. 2014). The European Commission (EC) used this two-parameter method to produce a report on critical elements in 2010, with supply risk being defined as an aggregate of the political stability of the producing countries, the potential to substitute the metal, the environmental risks associated with extraction and the extent to which they are recycled. Supply restriction was defined as the impact of supply disruption on European industry. They evaluated 41 metals and minerals, and classified 10 as 'critical' (figure 1): Sb, Be, Co, Ga, Ge, In, Mg, Nb, Ta, W, rare earth elements (REEs) and platinum group elements (PGEs) (European Commission 2010). This was followed by a report in 2014 which expanded the number of elements evaluated to 54, identifying 20 critical elements, adding borates, chromium, coking coal, magnesite, phosphate rock and silicon metal to the 2010 list (European Commission 2014).

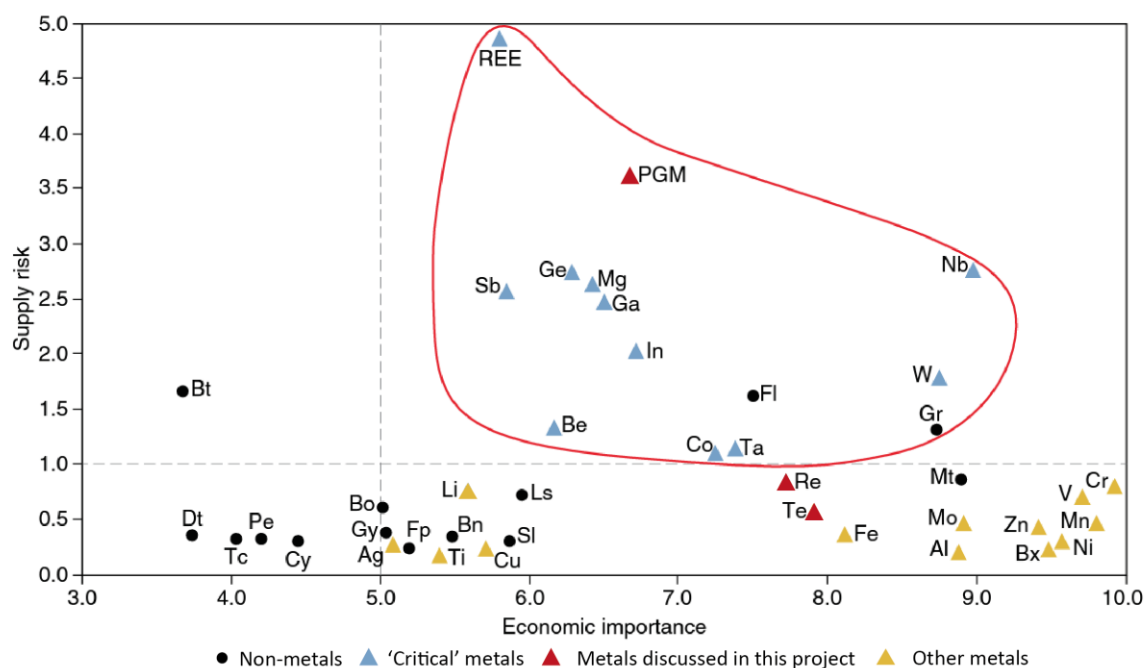


Figure 1: Metals assessed for criticality using the two axis method by the European Commission (EC) in their 2010 working report on critical metals. The metals circled in red are those the EC deemed 'critical'. The metals with red symbols are those which are common co-products of porphyry deposits and are discussed in this project (adapted from European Commission 2010; Graedel et al. 2014).

The US department of energy produced a critical minerals strategy in 2011 which assessed elements in terms of importance to clean energy and their supply risk in the short term (five years) and the long term (25 years). They identified Y, Dy, Eu, Tb, Nd, Ce, La, In and Te as critical in the short term, with Li also becoming critical in the long term (Bauer et al. 2010). Not all of these elements are the same as those highlighted by the EC, showing that whether an element is

## Chapter 1

‘critical’ or not depends on the geographical area being considered, and the intended usage as much as on the risk of supply. A table summarising which elements have been defined as critical in various countries from 1996 – 2015 can be seen below (table 1). Elements which appear on multiple lists include REEs, PGEs, Te, Re, Sb, W, Ta, Ge, Be, Cr, Ga, In, Li, Co, Nb, Ni and Mg (Bauer et al. 2010; European Commission 2010; UK House of Commons 2010; DoD 2013; Skirrow et al. 2013; European Commission 2014; Chakhmouradian et al. 2015).

*Table 1: Critical elements as defined by various countries since 1996 – the elements which are commonly found in porphyry deposits, and therefore discussed in this project, are highlighted in red (adapted from data in Chakhmouradian et al. 2015)*

Organisation	Elements defined as critical	Category	Reference
European Commission	Sb, Be, borates, Cr, Co, fluorite, Ga, Ge, graphite, In, magnesite, Mg, Nb, <b>PGE</b> , phosphate, REE, Si, W	Critical raw materials	European Commission 2014
Geoscience Australia	REE, Ga, In, W, <b>PGE</b> , Co, Nb, Mg, <b>Mo</b> , Sb, Li, V, Ni, Ta, <b>Te</b> , Cr, Mn	Critical elements	Skirrow et al. 2013
US department of Defense	Sn, Sb, Al <sub>2</sub> O <sub>3</sub> , SiC, Y, W, Ta, <b>Bi</b> , Ge, Mn metal, Dy, fluorite, Be metal, Er, Cr metal, Ga, Tb, Tm, Sc	Strategic non-proprietary materials	DoD 2013
UK government	Sb, Be, Cr, Co, Ga, Ge, <b>Au</b> , Hf, In, Li, Mg, Ni, Nb, <b>PGE</b> , <b>Re</b> , REE, Ta, Ti, W, V	Strategically important metals	UK House of Commons, 2011
European Commission	Sb, Be, Co, fluorite, Ga, Ge, graphite, In, Mg, Nb, <b>PGE</b> , REE, Ta, W	Critical raw materials	European Commission, 2010
US department of Energy	Dy, Eu, Nd, Tb, Y, Ce, In, La, <b>Te</b> , Li	Short term critical materials	Bauer et al. 2010
US department of Energy	Dy, Eu, Nd, Tb, Y, <b>Te</b> , Li	Long term critical materials	Bauer et al. 2010
Government of the Russian Federation	U, Mn, Cr, Ti, Al <sub>2</sub> O <sub>3</sub> , <b>Cu</b> , Ni, Pb, <b>Mo</b> , W, Sn, Zr, Ta, Nb, Co, Sc, Be, Sb, Li, Ge, <b>Re</b> , HREE, <b>Au</b> , <b>Ag</b> , <b>PGE</b> , diamonds, ultra-pure quartz	Strategic resources	Resolution 50-p of 16.01.1996 (taken from Chakhmouradian et al. 2015)

New methods are being developed to define criticality using further parameters and incorporating both data and expert judgement (Graedel et al. 2012; Mudd et al. 2016). However, assessing which elements are ‘critical’ is complex. What can be drawn from the attempts to define criticality so far is that it is an evolving concept and that there are degrees of criticality, meaning that some elements have greater supply risks or would have a greater impact than others which are still considered critical. Whatever their degree of criticality, diversifying sources of these elements is important, as is keeping an eye on emerging technology trends to identify potential critical elements for the future.

### 1.1.2 How can criticality be managed?

Although geological scarcity of elements is highly unlikely due to the nature of reserves and resources the main supply risks are associated with import dependence, resource nationalism and the concentration of supply of some elements in politically unstable countries (Graedel et al. 2014). These risks can be mitigated by investigating substitute elements, investigating the potential to recycle materials for these elements and creating stockpiles (Buijs & Sievers 2011; Graedel et al. 2014). These solutions all carry their own risks – for example substitute elements

may cause a drop in efficiency of the product, recycling is very energy-intensive and cannot fully cover demand, and stockpiling distorts the market for that element and can exacerbate the problem (Buijs & Sievers 2011; Hagelüken 2014; Graedel et al. 2014). More sustainable solutions include research into better recycling technologies and more efficient manufacturing processes; metallurgical research into more efficient extraction of these elements; and geological research to enable better exploration for, and exploitation of, critical metal enriched deposits. This project aims to help with the latter of these solutions, focusing on critical elements which occur as co-products in porphyry copper deposits.

Many critical elements are co-products of industrial minerals – for example rhenium is often found as a co-product of copper and molybdenum, and is rarely the primary product of any mine (Naumov 2007). This presents a challenge as the production of these elements is affected by price changes in their companion metals, so if a Cu-Mo-Re mine becomes uneconomic and has to close due to a drop in copper price this has a knock-on effect for the supply of rhenium. However, this can also be advantageous as it means, conversely, that the economic success of these projects is not dependant on the demand for the critical metal by-product. As discussed above, if new technologies or substitute elements are discovered an element which was ‘critical’ when a mine opens may not be in such high demand for the whole life-cycle of the mine. Therefore extracting this metal as a co-product means the mine is less dependent on the development of a niche market or technology (Mudd et al. 2016).

Of particular interest are deposits which are currently being mined and which may have untapped potential to produce critical metals as a by-product. This is often due to limitations in processing technology making extraction of these co-products uneconomic, or to a lack of understanding of the behaviour and distribution of the critical metal in that type of deposit meaning it goes unrecognised. This project looks at several critical metals which are potential by-products of porphyry copper deposits – rhenium (Re), platinum group elements (PGEs), tellurium (Te), and bismuth (Bi) – and by examining two case studies (Muratdere Cu-Mo (Au-Re) porphyry deposit, Turkey and Skouries Cu-Au (Pd, Pt, Te, Bi) porphyry deposit, Greece) attempts to expand our understanding of their source, distribution and mineralogy in porphyry systems.

### 1.1.3 Critical metals within the scope of this project

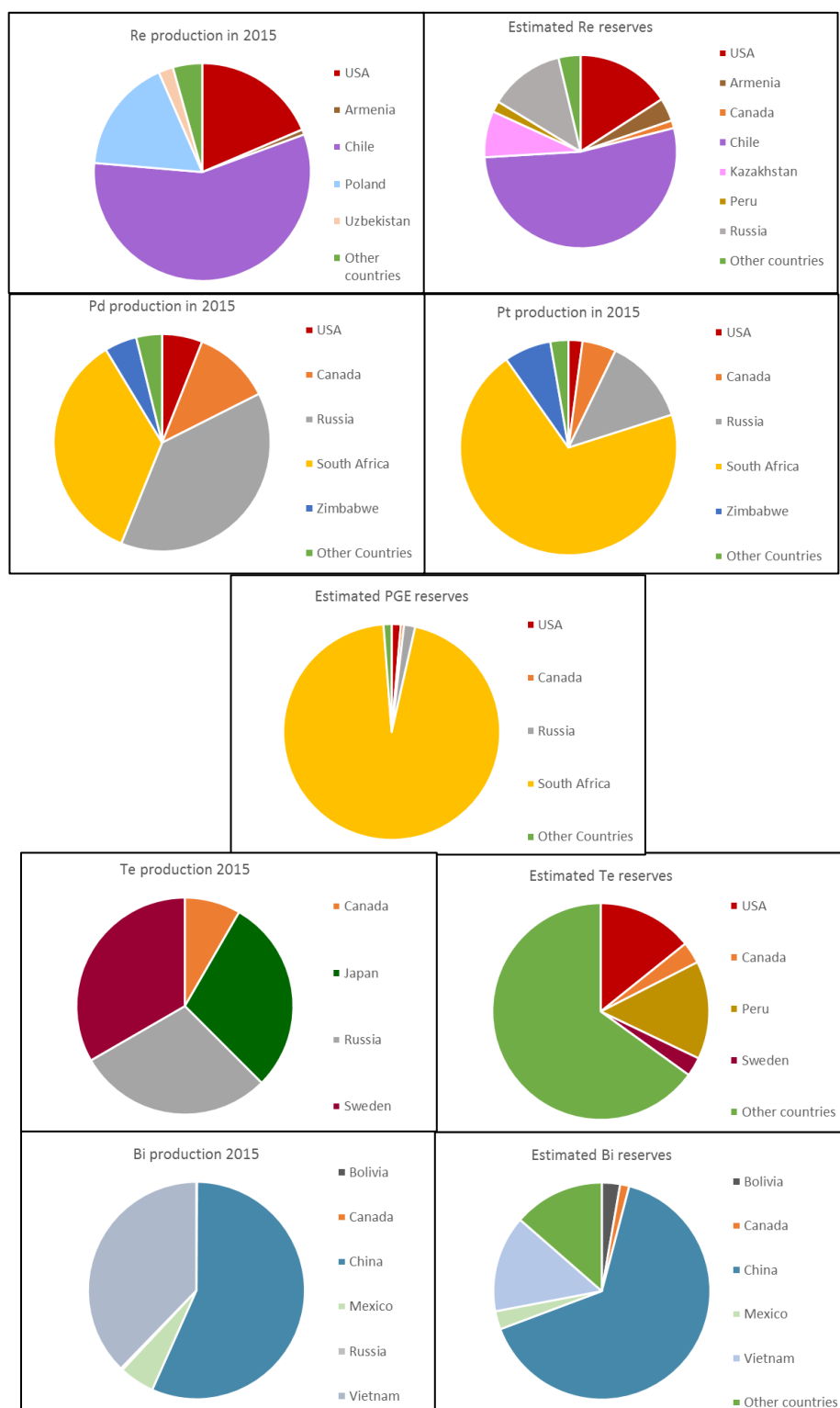


Figure 2: Pie charts showing the global mine production of critical elements found in porphyry deposits in 2015, and estimated reserves of these elements divided by country. This highlights the supply risks associated with some of these elements. Data taken from USGS commodity surveys (Polyak 2015; Anderson 2016a; Loferski 2016; Anderson 2016b).



### 1.1.3.1 Rhenium

Rhenium (Re) is a metallic element with a very high melting point (3180°C), second only to tungsten (Millensifer et al. 2014). The majority of rhenium usage is in super alloy production to make Ni-Re alloys for use in turbine blades for jet engines and industrial gas turbine engines. These alloys can withstand very high temperatures allowing prolonged engine life, increased performance and increased energy efficiency (John 2015). The other main use of Re is in Pt-Re catalysts for the processing of crude oil, which improve refinery efficiency. Secondary uses for Re include vacuum tubes, X-ray tubes, heating elements and various medical procedures (John 2015). There are currently no substitute elements which can be used in turbine blades without a degradation in performance and efficiency, and current materials research is not looking prospective, so it is unlikely that the demand for Re is going to decrease in the near future (John 2015). Rhenium is currently recycled from spent catalysts, and research is being undertaken to allow recycling of turbine blades (Millensifer et al. 2014).

Rhenium is one of the most dispersed elements in the earth's crust, with average crystal abundance estimated to be 0.2 – 2 ppb (Morris & Short 1969; Millensifer et al. 2014). Almost all primary Re production is from porphyry copper deposits, with the remainder being recovered from sediment-hosted copper deposits such as the Kupferschiefer (Millensifer et al. 2014). There is also potential to recover Re from vein type deposits, with the Merlin Mo-Re deposit in Australia providing an example of the potential of this type of deposit. Re has also been noted in uranium deposits and in Ni-Cu-PGE magmatic sulphide deposits (Millensifer et al. 2014). Rhenium is extracted from copper ore by roasting molybdenum concentrates and recovering rhenium oxide via scrubbing of the gases emitted (John 2015). Research is also being undertaken into other, solute based processing methods (e.g. Gerhardt et al. 2001; Zhan-Fang et al. 2009). In 2015 approximately 45,650 tonnes of Re was produced globally, of which 57% came from Chile, with the USA and Poland each producing around 18% (figure 2, Polyak 2016). Estimated global reserves of Re (estimated by the USGS – see Polyak 2016 for details) come to a total of approximately 2,450,000 tonnes, of which 53% are thought to be in Chile (figure 2).

### 1.1.3.2 Platinum group elements

Platinum group elements (Ru, Rh, Pd, Os, Ir and Pt) or PGEs are essential for many industrial applications. Their main use is in catalytic convertors, which decrease harmful gas emissions from car exhausts, however they are also used in a wide range of other industrial applications such as the manufacture of nitric oxide, explosives and nitric acid. Platinum (Pt) catalysts are also used in the petroleum industry to refine crude oil, and palladium (Pd) and Pt are used in electronics and jewellery (Michael et al. 2014; Loferski 2016). Although many PGEs can substitute for each other

in applications such as catalysts there are currently no substitution elements which can replace PGEs while still providing the same level of performance, although high prices have led to a drive to reduce the amount of PGEs used in technologies. For example, catalytic converters now need less PGE content to work as efficiently as they once did (Gunn 2014b). PGEs are also an important constituent of fuel cells, which have applications as power systems for space craft. Hydrogen fuel cells also form one of the two main competing technologies for electric car propulsion, alongside Lithium-ion battery power (Carrette et al. 2001; Khaligh & Li 2010). If fuel cells become the technology of choice for future electric cars, then there will be a large increase in demand for PGEs. PGE recycling is possible after some applications and in 2010 approximately 23% of global Pt use and 19% of global Pd use was from recycled sources (Gunn 2014b).

There are very limited concentrations of PGEs in the earth's crust, with average Pt and Pd contents of approximately 5 ppb; and Rh, Ru and Ir contents of approximately 1 ppb, although they are relatively enriched in ultramafic rocks with contents of 10-20 ppb (British Geological Survey 2014). Viable PGE deposits usually require an average Pt or Pd content of between 5 – 15 ppm (Michael et al. 2014), and are typically associated with primary magmatic sulphides hosted by mafic or ultramafic rocks. The two main types of magmatic deposit are those which are sulphide rich, containing Cu and Ni as co-products, and those which contain PGEs concentrated in stratiform layers in large intrusions with a low (<10%) sulphide content, of which the largest is the Bushveld Complex in South Africa (Naldrett 2010). PGEs are usually hosted in platinum group minerals (PGMs), of which more than 100 have been identified (Cabri 2002). These can be categorised as alloys, sulphides, antimonides, bismuthides and tellurides, with merenskyite ((Pd,Pt)(Te,Bi)<sub>2</sub>) being one of the most common ore minerals. PGEs are processed by smelting ore concentrate, although research is being carried out into more energy efficient extraction methods (Jenkin et al. 2016). Global Pt mine production in 2015 was approximately 178,000 tonnes, while global Pd production was approximately 207,500 tonnes (figure 2, Loferski 2016). Of this South Africa produced 70% of the global Pt and 35% of global Pd, with Russia producing 12% of global Pt and 38% of global Pd. Global PGE reserves are estimated to be 66,110,000 tonnes, 95% of which are thought to be in South Africa (figure 2) (Loferski 2016). This potentially poses a major future supply risk, hence the importance of diversifying the source of these elements.

### 1.1.3.3 Tellurium and bismuth

Tellurium and bismuth are semi-metals found as by-products in porphyry deposit ore. They are occasionally extracted at smelter, however there is currently a lack of efficient extraction processes to allow for the full exploitation of this potential source. An interesting recent development is the use of deep eutectic solvent ionic liquids to extract tellurobismuthide (Bi<sub>2</sub>Te<sub>3</sub>),

as well as native gold and tellurium from hydrothermal ores (Jenkin et al. 2016). Although in the early stages of development this method has the potential to allow for the economic and energy-efficient extraction of these elements from porphyry ores.

Tellurium compounds exhibit enhanced electrical conductivity, so the main uses of tellurium are in the production of cadmium-telluride (Cd-Te) solar cells. and in thermoelectric power generation (Goldfarb 2015; Anderson 2016b). Tellurium is also used as an alloying additive in steel, copper, lead and iron to improve machinability. Alternative uses include the processing of rubber, as a catalyst in synthetic fibre production, as well as in photoreceptor devices and pigments (Anderson 2016b). Substitute elements such as bismuth and selenium are available for most of tellurium's metallurgical and catalytic uses, although usually with losses in efficiency. Amorphous silicon and copper-indium-gallium-selenide are the two principal competitors to Te in the field of solar cells, but Cd-Te cells prove more efficient than Cu-In-Ga-Se cells and are very competitive compared to silicon cells (Gloeckler et al. 2013; Green et al. 2015). Large scale tellurium recycling has not yet been successfully achieved due to the dispersive nature of its applications and the long life span of Cd-Te solar cells (Anderson 2016b).

Tellurium has an average crustal value of 3 ppb, being hosted as telluride minerals, often with precious metals (Goldfarb 2015). It is extracted from anode slimes at copper refineries after the processing of ore from porphyry copper deposits and some VMS deposits. Tellurium minerals are found in many gold deposits - for example Cripple Creek, USA and Perama Hill, Greece (Voudouris et al. 2006; Goldfarb 2015). These are not, however, currently being mined for Te due to a lack of an efficient extraction technique (Goldfarb 2015). There are currently two mines recovering tellurium as a primary ore – the Dashiugou Au-Te vein deposit in southern China and the Kankberg Au-Te deposit in Sweden, which between them account for 15% of the world's Te production (Mao et al. 2002; Hayes et al. 2013; Goldfarb 2015). In 2015 the global mine production of Te was 120 tonnes (production from the USA withheld for proprietary reasons so this is a minimum estimate), with the majority mined in Japan, Sweden and Russia (Anderson 2016b). The global reserves of Te are estimated to be 24,600 tonnes, with the USA and Peru being the two countries with the largest proportions (figure 2, Anderson 2016b). Advances in processing technology and geological knowledge are expected to increase available reserves over the next few years.

Bismuth is primarily used in pharmaceuticals but also has applications in superconductors, pigments for cosmetics and paints, in solder, and in fusible alloys used in fire sprinkler triggering mechanisms and fuel tank safety plugs (Anderson 2014). Bismuth has some substitute elements – for example it can be replaced in pharmaceutical applications by alumina, antibiotics and

magnesia and by indium in low temperature solders. Bismuth is however an environmentally friendly substitute for lead - it has similar properties but lower toxicity, and so is increasingly used in place of lead in applications such as plumbing, hunting ammunition, lubricating grease and fishing weights (Anderson 2016a).

Bismuth has an average crustal abundance of 8 ppb (Anderson 2016a) and is mainly found as a co-product in intrusion related ore deposits, although there are currently two mines with bismuth as their primary products – the Tasna mine in Bolivia, and an unnamed deposit in China (Anderson 2016a). The main source of Bismuth is in primary Bi-bearing minerals in Sn-W polymetallic ore deposits, often in greisen skarn deposits such as the Nui Phao deposit in northern Vietnam (Ishihara 2008; Sanematsu & Ishihara 2011). Bismuth is also recovered as a by-product of smelting lead ores, as well as from the ore processing of fluor spar, tin and tungsten (Anderson 2016a). Total global production of bismuth in 2015 was 13,253 tonnes, with 57% produced in China and 38% from Vietnam, almost all from the Nui Phao deposit. Global reserves are estimated to be 368,000 tonnes, 65% of which are in China (figure 2).

## 1.2 Porphyry copper deposits

Porphyry copper deposits are large volume ( $10 - >100 \text{ km}^3$ ), low grade magmatic-hydrothermal ore deposits which are associated with felsic to intermediate magmatism, and are interpreted to have formed beneath ancient stratovolcanoes (Hattori & Keith 2001; Sinclair 2007; Sillitoe 2010). They are characterised by intense and extensive hydrothermal alteration of surrounding host rocks, with mineralisation hosted in structurally controlled vein networks known as stockworks. Porphyry deposits are often part of larger porphyry systems, which may also contain skarns, epithermal base and precious metal mineralisation and carbonate replacement deposits (Sillitoe 2010). Porphyry deposits supply 50-60% of the world's copper, a fifth of its gold, 95% of its molybdenum and the majority of its rhenium (Sinclair 2007). They can also contain economic amounts of Ag, Bi, Te, Se, Pd and Pt (Watterson et al. 1977; Tarkian & Stribrny 1999; Economou-Eliopoulos & Eliopoulos 2000; Sinclair 2007).

Porphyry copper deposits are typically found in subduction related island-arc and back-arc settings (Sillitoe 1973; Sillitoe & Bonham 1984; Sinclair 2007; Sillitoe 2010), however they are also found related to collisional lithospheric delamination and post-collisional stress relaxation (Richards 2009; Richards 2014; Wang et al. 2014; Chen et al. 2015). They are commonly located in linear, tectonically controlled orogen parallel belts (Sillitoe 2010). Porphyry deposits range in age from Archean to Recent, with the majority of preserved porphyries being of Jurassic age or younger (Singer et al. 2005; Sinclair 2007; Sillitoe 2010).

### 1.2.1 Common features of porphyry copper deposits

Porphyry copper deposits are spatially and temporally related to large multiphase batholiths at depth (figure 3). These batholiths are typically equigranular and of granitic to dioritic composition, can be associated with several deposits, and are interpreted to be a genetically related precursor to the overlying deposits (Sillitoe 2010). Commonly deposits are also related to co-magmatic subaerial volcanic rocks, erupted just prior to mineralisation (e.g. Waite et al. 1997), although these are often eroded and so no longer visible. Porphyry copper deposits are thought to be associated with effusive, rather than explosive volcanism, as large explosive events release magmatic volatiles rather than concentrating them to allow the formation of ore deposits (Cloos 2001; Cooke et al. 2005). However there is evidence that porphyry deposits may form beneath stratovolcanoes (Hattori & Keith 2001), and long term degassing can occur in explosive systems, with multiple degassing events which often interact with hydrothermal fluids (e.g. Moretti et al. 2013).

The deposits themselves are hosted in small (<1 km) intrusions which form as stocks or dykes from the underlying precursor pluton (figure 3). The stocks are I-type calc-alkaline, shoshonitic or alkaline, and belong to the magnetite-series (Ishihara 1981; Seedorff et al. 2005). Deposits typically form multiple overprinting intrusive bodies (e.g. Holliday et al. 2002; Wilson et al. 2003; Steinberger et al. 2013; Siron et al. 2016), displaying the porphyritic texture which gives these deposits their name, typically with an aplitic groundmass (Sillitoe 2010). The porphyritic texture is thought to be due to sudden crystallisation, reflecting the concentration and sudden release of a fluid phase (Cloos 2001). This volatile release results in the intense fracturing of the intrusions and host rocks, with the majority of the mineralisation occurring in vein sets which permeate the system (Sillitoe 2010).

Mineralisation and alteration form large haloes which exhibit vertical and lateral zonation (figure 3). Porphyry alteration zones consist of potassic alteration in the core of deposits, of which biotite and K-feldspar are the key alteration minerals, with a marginal propylitic alteration zone consisting of chlorite, epidote, albite and carbonate. Potassic alteration is usually associated with the majority of the mineralisation, with pyrite, chalcopyrite and bornite being the common ore minerals. Propylitic alteration is associated with pyrite, and occasionally sphalerite and galena. A sodic-calcic alteration zone is commonly present at depth, consisting of albite, actinolite and magnetite with no associated mineralisation. The upper parts of porphyry copper deposits typically show chlorite-sericite alteration, which also includes hematite, alongside phyllic alteration which consists of quartz and sericite. These alteration zones are commonly associated with pyrite-chalcopyrite, and phyllic alteration commonly contains enargite, tennantite, bornite,

chalcocite and sphalerite. If not eroded away the area above a porphyry deposit consists of a lithocap of advanced argillic alteration, which is made up of vuggy and residual quartz, alunite, pyrophyllite, dickite and kaolinite, with associated pyrite, enargite, chalcocite and covellite (Sillitoe 2010). These alteration zones form valuable exploration indicators, as does the metal zonation often seen in porphyry deposits, with low temperature assemblages of Zn-Pb-Ag defining kilometer scale haloes around a central Cu-Au rich zone (Landtwing et al. 2010; Sillitoe 2010).

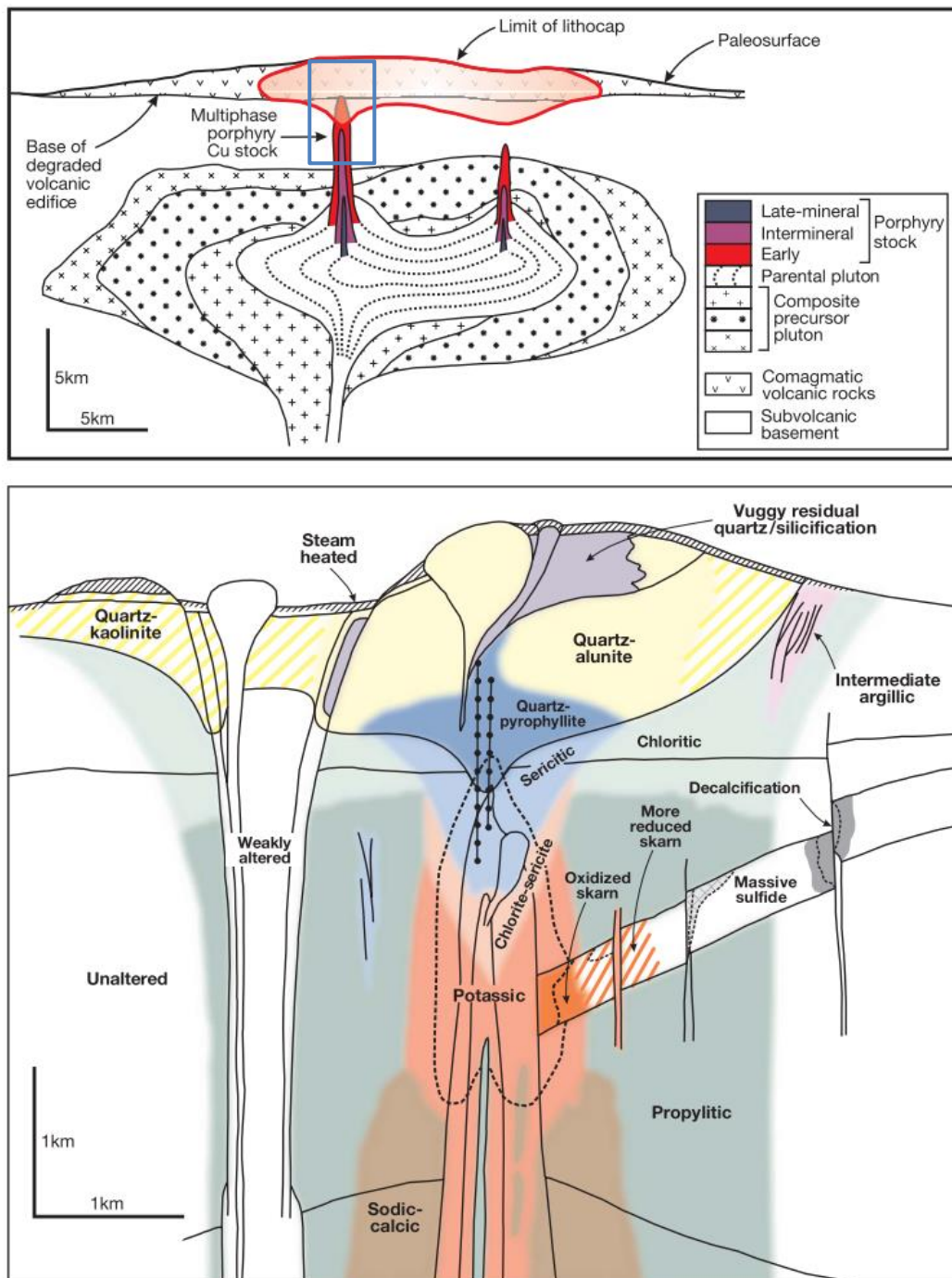


Figure 3: a.) Diagram showing an idealised magmatic system associated with porphyry copper deposits, with a precursor pluton and multiphase porphyry stocks. b.) Diagram of the area outlined in blue in a.) showing the alteration zones and peripheral mineralisation types associated with a classic porphyry copper deposit (diagrams from Sillitoe 2010).

The majority of the metal in porphyry deposits is found in veins, with the rest in disseminated sulphide grains in potassically altered host rocks. The veins in porphyry deposits are associated with the porphyry stocks and dykes, meaning that multiphase porphyry stocks will produce multiple overprinting veinsets. This makes detailed surveys of vein paragenesis in porphyry deposits very important in order to understand the fluid history of the deposit, and particularly when determining which fluid brought in a particular element. Deposits typically contain very similar vein types, described and categorised by Sillitoe (2010) as three groups:

1. An early vein type consisting of one or more of K-feldspar, magnetite (M type), biotite (EB type) and actinolite. These do not contain quartz or sulphides and are associated with potassic alteration.
2. Granular quartz veins containing sulphides with narrow or absent alteration selvages, containing magnetite (A type), or molybdenite in a central suture (B type), and associated with potassic alteration. This group hosts the majority of the metal content of deposits.
3. Late crystalline quartz veins containing sulphides with feldspar destructive alteration selvages (D type). These are associated with chlorite-sericite and phyllic alteration.

Although these vein types are useful as a first pass classification system, porphyry vein systems are commonly more complex, being further complicated by reopening of veins during subsequent hydrothermal events (Sillitoe 2010).

### **1.2.2 Genetic models for porphyry copper deposits**

Porphyries have been found to be related to “I-type” granitoids with primitive Sr ratios (0.702-0.705), which indicate an origin either from the upper mantle or recycled oceanic crust (Richards 2011). They are usually situated at convergent plate margins where the hot metal and volatile rich magma rising above the subducting plate provides a source of fluids to the upper crust (figure 4). While there are many plutons which appear to have the right features to generate a porphyry deposit, only a few of them contain any mineralisation, so before considering critical metal enrichment the mechanisms of general porphyry mineralisation must be considered.

#### **1.2.2.1 Mantle and magmatic porphyry formation processes**

Porphyry deposits situated in subduction settings are formed from volatile and metal enriched arc magmas (figure 4). These are proposed to have formed by solute-rich aqueous fluids being released from the subducting slab at depth through melting (Dreyer et al. 2010) or slab dehydration (Tatsumi 1989). These fluids metasomatise the overlying asthenospheric mantle, enriching it in volatiles, sulphur, silica and large ion lithophile elements (LILE) (Tatsumi 1989; Alt et

al. 1993; McInnes et al. 1999; De Hoog et al. 2001; Dreyer et al. 2010) - possibly oxidising the overlying mantle through the addition of H<sub>2</sub>O, CO<sub>2</sub> and ferric iron (Mungall 2002). This is hypothesised to create new mineral phases, such as amphibole and mica, and to lower the mantle solidus temperature to the point where melting begins (Tatsumi 1989; Peacock et al. 1994). These hydrous basaltic melts are then thought to intrude the overlying lithosphere and pool at the base of the crust in a 'hot zone' (Annen et al. 2006; Solano et al. 2012a). This 'hot zone' forms an underplated layer, crystallising dense mafic minerals such as olivine and pyroxenes and forming ultramafic cumulates at the base of the crust (Herzberg et al. 1983; Huppert & Sparks 1988; Fyfe 1992; Richards 2003). This hot melt is thought to assimilate crustal rocks through partial melting, leading to the evolution of more evolved, less dense magmas of intermediate composition, enriched in volatiles, sulphur and incompatible elements (Hildreth & Moorbath 1988; Hamlyn et al. 1985; Richards et al. 1991; Richards 2003; Annen et al. 2006; Solano et al. 2012b). The metal content of arc magmas is believed to come from the mantle (Pettke et al. 2010; Wilkinson 2013), although pre-existing copper rich cumulates or ore deposits from an earlier subduction cycle may enhance the magma fertility (Core et al. 2006; Lee et al. 2012) while molybdenum has been hypothesised to have a crustal origin (Farmer & Depaolo 1984). Chalcophile and siderophile elements such as Cu, Ni, Au and PGE partition strongly into sulphide phases relative to silicate melts. This means that during the formation of the under plating cumulate layer, sparse, highly siderophile elements ( $D > 10^5$ ) such as Au and PGEs will partition into the residual sulphide phase, depleting the magma (Campbell & Naldrett 1979). This has been suggested to explain the formation of Au poor porphyry deposits associated with early arc events (Richards 2013), however as arc magmas are oxidised it is also possible that sulphur could be present as SO<sub>2</sub>, meaning that Cu and Au would act as incompatible elements, remaining in the melt (Spooner 1993).

This volatile and metal rich melt ascends to upper crustal levels (~4-10 km), forming a magma chamber which ultimately becomes the precursor pluton described above (Annen et al. 2006; Sillitoe 2010; Wilkinson 2013). These chambers are long-lived, with suggested lifespans of between 100 Kyr to 30 Myr (Matzel et al. 2006; Schaltegger et al. 2009; Rezeau et al. 2016), and are periodically rejuvenated by andesitic or mafic magma from the deep crustal melt reservoir (Glazner et al. 2004; Rezeau et al. 2016). This periodic introduction of a more mafic melt has been suggested as a source of sulphur and chalcophile elements, providing the levels needed to form an economic ore deposit (Hattori & Keith 2001; Scaillet 2010; Tapster et al. 2016; Rezeau et al. 2016). Periodically porphyry stocks and dykes are intruded into the shallow (1-4 km) crust from the chamber (Wilkinson 2013), forming the deposit's host intrusions.



Arc magmas are highly oxidised, with disseminated metal contents. This means a mechanism is needed to concentrate any metals present into an exsolving fluid. One suggested mechanism is magnetite crystallisation in the oxidised magma chamber. This is thought to trigger the reduction of the melt, and may trigger the formation of an immiscible sulphide melt (Jenner et al. 2010). This would scavenge siderophile elements from the melt, including Fe, Au, Pd, Pt and to a lesser extent Cu, providing an efficient enrichment mechanism (Halter et al. 2002; Sun et al. 2004; Nadeau et al. 2010). An alternative reduction mechanism suggested is the assimilation of reduced country rocks, for example shales or limestones, which may also provide additional metal sources (Cloos 2001). The periodic injection of mafic magma into this upper-crustal staging magma chamber may trigger volatile exsolution and dissolution of sulphide into the volatile phase, transporting Cu and Au in reduced sulphur species (Harris et al. 2003; Audétat et al. 2008; Nadeau et al. 2010), rather than as halogen ligands (Candela & Holland 1986; Hedenquist & Lowenstern 1994).

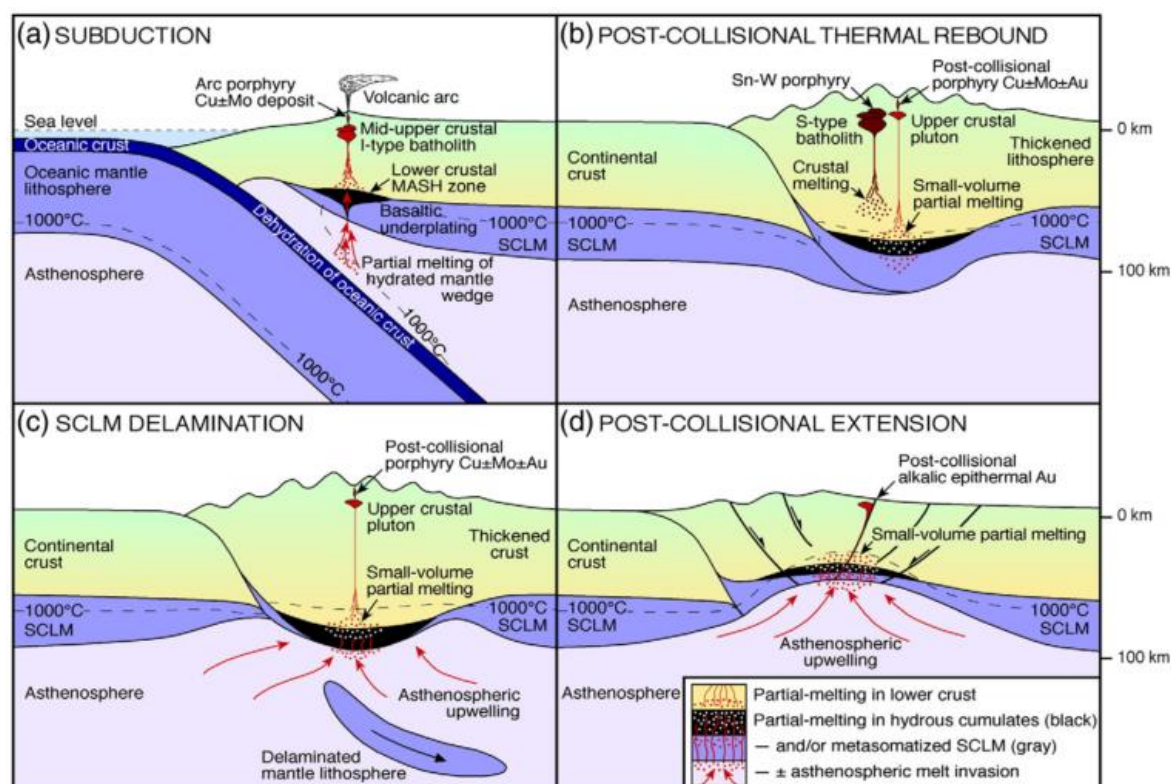


Figure 4: a.) Porphyry copper deposit formation mechanisms in a subduction arc setting. b.), c.) and d.) show porphyry deposit formation in post-collisional settings. Diagram taken from Richards 2011.

#### 1.2.2.2 Hydrothermal transport and ore mineral precipitation triggers

The metals in porphyry copper deposits are hydrothermally transported, and found precipitated in veins and potassic alteration (Sillitoe 2010). These hydrothermal fluids exsolve from the magma, either via mafic melt input into the chamber (Nadeau et al. 2010), or due to pressure reduction as the shallow porphyry intrusions ascend through the crust (Fournier 1999). Copper

and precious metals are thought to be transported in these fluids as either sulphide complexes or chlorine ligands (Hedenquist & Lowenstern 1994; Audétat et al. 2008; Tooth et al. 2008). These fluids require a precipitation trigger in order to deposit ore minerals. Suggested mechanisms include a drop in temperature, reducing the solubility of ore minerals (Crerar & Barnes 1976; Landtwing et al. 2010); expansion of magmatic vapour causing a change in pressure (Weis et al. 2012); a change in oxidation state of the fluid, possibly due to reactions with the wall rock (Sillitoe 2010; Richards 2013); salt saturation triggering the precipitation of halite disassociating Cl from metal bearing ligands (Lecumberri-Sanchez et al. 2015); or reaction between shallow brines and magmatic vapour (Blundy et al. 2015). These trigger mechanisms are discussed further in relation to the Skouries porphyry copper deposit in chapter 4.

### **1.2.2.3 Post-collisional porphyry copper deposits**

Although the majority of porphyry deposits are thought to be associated with subduction zones (Sillitoe 2010), recent discoveries and advances in geochronology and tectonic reconstruction have shown the occurrence of a significant number of porphyries both in continent-continent collisional environments such as Tibet (Chen et al. 2015), and in post-collisional environments featuring subduction reversal or migration and post-collisional rifting (figure 4, Richards 2009; Richards 2011). After the cessation of arc magmatism, brief resurgences in magmatism may be stimulated by rifting or collision, resulting in the formation of further porphyry deposits (Davies & von Blanckenburg 1995; Paquette et al. 2003). The main features of these deposits are very similar to those found in subduction zone environments (Richards 2009; Richards 2011) but trace element geochemistry suggests that their source magmas formed through different processes (Chen et al. 2015). The associated magmas in these deposits are commonly calc-alkaline, but are more likely to include intrusions of alkaline composition than subduction related porphyries (Richards 2009). As discussed above it has been hypothesised that arc magmatism forms under plated hydrous ultramafic cumulates, with chalcophile metal enriched residual sulphide phases. If these are subject to remelting either by thermal rebound after lithospheric thickening or by invasions of small volumes of hot asthenospheric magma, then these Au rich residual phases may re-dissolve, generating magmas with high Au/Cu ratios and potential PGE enrichment (Solomon 1990; Tarkian & Stribrny 1999; Richards 2009). This may explain the presence of Au rich porphyry deposits in post-collisional settings.

Post-collisional porphyry deposits are proposed to have formed from hydrous magmas derived from partial remelting of metasomatised lithospheric mantle and hydrous cumulate zones of former arc systems (figure 4, Richards 2009). These primitive magmas may ascend to upper crustal levels and mix with more felsic magmas, enriching these upper crustal magmas in volatiles

and supplying heat to the system (Delibaş et al. 2016). This magma upwelling has been proposed to occur in response to a variety of mechanisms, including lithospheric thickening, thermal rebound, stress relaxation following slab rollback, subcontinental lithospheric mantle delamination or lithospheric extension (Richards 2009; Delibaş et al. 2016).

Post-subduction arc extension can cause decompression melting in upwelling, subduction metasomatised asthenosphere leading to the generation of mafic alkaline (shoshonitic) magmas (figure 4, Richards 2009; Moritz et al. 2016). Trans-lithospheric extensional structures have been proposed as a channel for rapid ascent of these mantle-derived magmas to upper crustal levels (Richards et al. 1990; Moritz et al. 2016).

Post-subduction arc contraction has been proposed to lead to crustal thickening and delamination of the sub-continent lithospheric mantle, with arc-derived basaltic magmas cooling below the lower crust to form amphibolites (Richards 2011; Chen et al. 2015). The amphibolites store subduction-derived water (Davidson 1996; Tiepolo & Tribuzio 2008; Richards 2011), so that partial melting of these amphibolites forms a hydrous, fertile melt. This partial melting may occur due to isotherms rebounding in a period of post-collisional relaxation, or due to asthenospheric melts upwelling to the base of the crust in the wake of slab roll-back or break-off (Richards 2009; Wang et al. 2014). These hydrous melts are proposed to mix with upper crustal magmas (Delibaş et al. 2016; Rezeau et al. 2016) resulting in felsic calc-alkaline to sub-alkaline magmas with crustal radiogenic isotopic signatures (Davies & von Blanckenburg 1995), depletion in high field strength elements (HFSE), and high large-ion lithophile elements (LILE) contents (Yang et al. 2016). The assimilation of garnets and amphiboles from the lower crust are thought to be responsible for their high Sr/Y and La/Yb signature of these magmas (Hou et al. 2004). The potassic nature of the magmas produced is hypothesised to be due to either the inheritance of enriched mantle components or mixing with contemporary mantle derived ultra-potassic magmas (Chen et al. 2015).

### **1.3 Tethyan metallogenic belt**

Both of the case studies investigated in this project are hosted within the Tethyan metallogenic belt (TMB), which is co-incident with the Tethyan orogenic belt. This stretches from the Alps to Indonesia, incorporating the Carpathians, Balkans, Taurides, Zagros, Makran, Himalayas and Indochina (figure 5; Richards 2015; Richards 2016b).

The Tethyan orogenic belt was formed by the closure of the Paleotethyan ocean and the Neotethyan ocean between the mid-Paleozoic and the present (Stampfli & Borel 2004; Richards 2015). The Paleotethyan ocean was formed in the mid-Paleozoic, and was destroyed by the Late

Triassic with the formation of the Pangea supercontinent by the joining of Laurentia and Gondwana (Stampfli & Borel 2004; Richards 2015). Relatively few mineral deposits are associated with the Paleotethys, with the majority of the TMB being associated with the closure of the Neotethys (Richards 2015). This has been proposed to be due to the lack of preservation of these deposits (Richards 2016), but could also be due to widespread anoxia in the Paleotethys in the Late Permian inhibiting oxidised magma formation (Şengör & Atayman 2009; Richards 2016).

The Neotethys began opening in the Permian – Early Triassic through rifting of the Cimmerian continental fragments from the northern margin of Gondwana. The Neotethys then progressively closed throughout the Mesozoic and Cenozoic, accreting on the southern margin of Laurasia from the Late-Triassic – Early Jurassic to the Eocene and Miocene, when it was destroyed by the collision of India and Africa-Arabia with Eurasia (Richards 2015; Richards 2016a; Richards 2016b). The closure of the Neotethys was associated with numerous small back-arc basins, such as the Vadar Ocean, which opened between the Cimmerian continent and Eurasia during the late Mesozoic-Paleogene (Richards 2015; Richards 2016b). Post-collisional processes are still ongoing, with continuing subduction of the Indian lithosphere under Eurasia in the Makran subduction zone (e.g. Kopp et al. 2000; Li et al. 2008).

The Tethyan metallogenic belt is an ideal environment to study the formation and features of porphyry deposits as it contains all stages of collisional events, including back-arc rifting and is associated with a large variety of sizes and types of porphyry deposits (Richards 2016a). These include classic subduction type deposits associated with the initial closure of the Neotethys in the Mesozoic, such as the Cretaceous porphyries Elatsite, Majdanpek and Bor in the Balkans (e.g. Von Quadt et al. 2002; Zimmerman et al. 2003; Clark & Ullrich 2004). Other subduction related deposits include the mid-Miocene Reko Diq deposit in the Chagai arc, western Pakistan, formed by the Makran subduction zone (Razique et al. 2014). The majority of the porphyry deposits in the TMB were formed by the onset of terminal collision and post-collisional tectonic adjustments in the late Oligocene to mid-Miocene (Richards 2016b), with post-collisional porphyries in the TMB including the Sungun and Sar Cheshmeh deposits in Iran, and mid-Miocene porphyry deposits in the Gangdese belt of Tibet (e.g. Hezarkhani & Williams-Jones 1998; Hou et al. 2004; Hou et al. 2011; Aghazadeh et al. 2015). The Skouries Cu-Au porphyry deposit, Greece is a post-collisional Miocene porphyry (Siron et al. 2016), while the Muratdere Cu-Mo (Re-Au) porphyry deposit, Turkey is also post-collisional, but thought to be early Eocene in age.



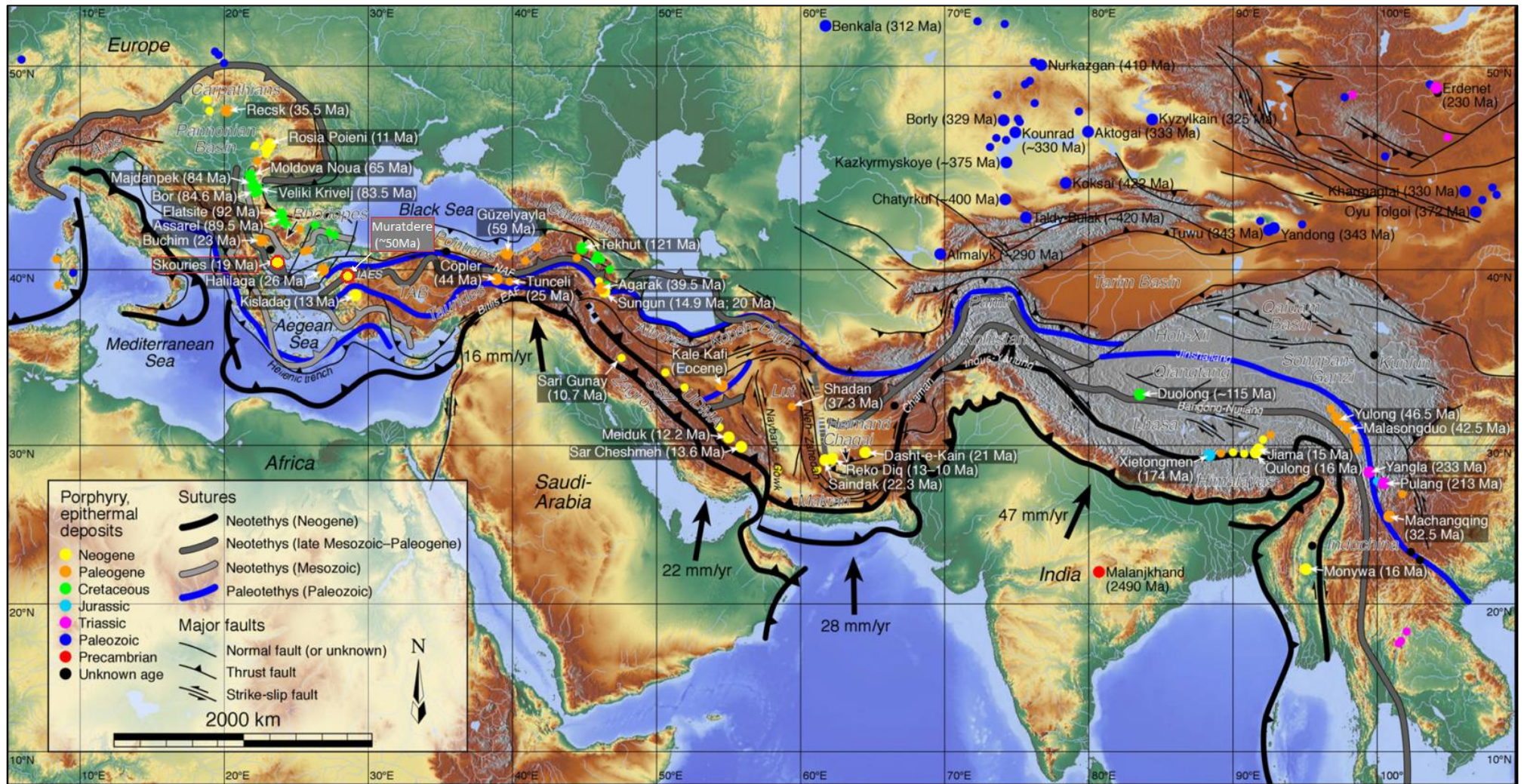


Figure 5: Map of the major structures and sutures of differing ages in the Tethyan Metallogenic Belt, with the major porphyry deposits marked. The deposits studied in this project, Skouries and Muratdere, are highlighted. Diagram taken from Richards 2015.

## 1.4 Project rationale

As discussed above critical metals are essential to high-tech industry and green technology, but have a significant attendant supply risk. This means that diversifying sources of these metals is of key importance. Porphyry copper deposits commonly also contain critical metals, but the full exploitation of these potential co-products requires a better understanding of both where these elements are hosted within porphyry deposits and their detailed mineralogy. It also requires an understanding of the source and mechanism of these enrichments to aid in exploration for critical metal enriched porphyries. Classification of common identifying features for critical metal enriched porphyries could also provide indicators to companies that their deposit may be enriched in an element not routinely included in assay, such as Pd, Pt and Te.

This thesis aims to fill some of these knowledge gaps by investigating the source, transport mechanism and distribution of Re, Pd, Pt, Te and Bi in two case study porphyry deposits. The first case study is the Muratdere Cu-Mo (Au-Re) porphyry deposit, Turkey, described here for the first time. This deposit is enriched in Re, which is present in differing concentrations in two generations of molybdenite, allowing study of potential Re enrichment mechanisms. The second case study is the Skouries Cu-Au deposit, Greece. This deposit is known to be platinum group element enriched (Eliopoulos & Economou-Eliopoulos 1991), however this project describes the location of the PGEs in the deposit and their mineralogy for the first time. Skouries is also enriched in bismuth and tellurium. Both of these deposits are in the Tethyan metallogenic belt - as discussed above this provides an excellent study area as the tectonic regimes and relative ages are fairly well defined, providing a chance to compare these case studies to other porphyries throughout the belt.

The research questions this project aims to answer are:

- Where are critical metals hosted in porphyry copper deposits?
- What is the source of critical metal enrichment in porphyry deposits?
- How are these metals transported and enriched within the system?
- What features can be used as exploration aids to discover more critical metal enriched porphyries?

The subsequent chapters are outlined as follows:

## **Chapter 2: Methodology**

This chapter details the methodologies used to acquire the data presented in this thesis, including discussions of precision and accuracy.

## **Chapter 3: Enhanced Re concentrations in the Muratdere Cu-Mo (Au-Re) porphyry deposit, Turkey due to hydrothermal fluid-country rock interactions**

Although many porphyries are rhenium-enriched the source of this enrichment is still not fully understood. This chapter provides the first account of the main geological and mineralogical features of porphyry Cu-Mo (Au-Re) mineralisation at Muratdere, coupling petrology with XRD, stable isotope, fluid inclusion micro-thermometric and platinum group element analyses to provide insights into the source and mechanisms of Re enrichment in porphyry systems. The Muratdere porphyry deposit has two generations of molybdenite with contrasting Re contents, determined from LA-ICP-MS analysis, which provides further constraints on the controls on Re distribution as well as an opportunity to better understand the likely source and mechanisms of Re enrichment in porphyry systems. This chapter is adapted from a paper drafted for submission to *Mineralium Deposita*.

## **Chapter 4: A fluid history of the Skouries Cu-Au (Pd, Pt, Te) porphyry deposit, Greece**

The Skouries deposit is well known, however there has not yet been a thorough stable isotope and fluid inclusion survey performed to ascertain the vein paragenesis and fluid characteristics of the deposit. This chapter presents the results of detailed vein logging, SEM imaging of mineralising veins and vein-specific stable isotope analyses. Detailed fluid inclusion petrology and micro-thermometry was performed using optical microscopy, SEM and Laser Raman Spectroscopy, as was LA-ICP-MS of fluid inclusions in the mineralising veinsets. This was used to develop a genetic model for the deposit, and to understand the chemical and physical conditions of the fluids transporting the metals. This chapter is adapted from a paper drafted for *Economic Geology*.

## **Chapter 5: Platinum group minerals in the Skouries Cu-Au (Pd, Pt, Te) porphyry deposit**

Although the Skouries deposit is famously enriched in PGEs to date their mineralogy and location within the deposit and the paragenesis have not been identified. This chapter presents the results of a survey of the mineralised veinsets using optical microscopy, SEM-EDS and EPMA to locate PGMs, identify their mineralogy and to quantify their chemistry. SEM-EDS and EPMA were also

## Chapter 1

used to analyse semi-metal distribution within Skouries, including Bi and Te. This chapter is adapted from a paper drafted for Economic Geology.

## **Chapter 6: Platinum group element transport in the Skouries Cu-Au (Pd, Pt, Te) porphyry deposit**

Although porphyries are a potential economic source of PGEs, Te and Bi, the transport mechanisms and source of these critical metals in porphyry deposits are still uncertain. This chapter presents preliminary data from LA-ICP-MS of fluid inclusions for precious and semi-metals, including the potential detection of Pd for the first time in natural fluid inclusions, and discusses implications of the fluid chemistry and PGM mineralogy in Skouries for critical metal transport and ore formation mechanisms in PGE porphyries.

## **Chapter 7: Conclusions and further work**

This chapter draws together the results from the previous chapters, comparing and contrasting the Muratdere and Skouries deposits and their enrichment mechanisms. Implications for other critical metal enriched porphyry deposits, and applications as exploration indicators are also discussed, along with potential future work to further understand these systems.



## **Chapter 2: Methodology**

### **2.1 Fieldwork and sample collection**

This thesis presents results of investigations of two case study porphyry deposits. The first is the Muratdere Cu-Mo (Au-Re) porphyry deposit, Bozüyük, Bilecik Province, Turkey. This project is a joint venture between Stratex International and Lodos Madencilik, and was visited in August 2012. The second is the Skouries Cu-Au (Pd, Pt, Te) porphyry deposit, Stratoní, Chalkidiki Peninsula, Greece. This project is owned and operated by Hellas Gold, a subsidiary of Eldorado Gold Corp, and was visited during the summer of 2013.

#### **2.1.1 Core logging and sampling**

At both deposits a regional overview was gained by spending 2-3 days in the field examining the regional geology, however as both deposits are unexposed core logging was performed in order to gain an understanding of the 3D structure of the deposits and their mineralogical and paragenetic features.

At the Muratdere deposit 6 diamond drill cores were logged at a 5 - 10 m scale, with a total of 1160 m of core logged over 10 days. The drill cores chosen are located within the core of the deposit, and the main features, alteration types, lithologies and veinsets were noted. Sections of interest were sampled for petrographic and geochemical study, ensuring all lithologies, alteration types and veinsets were sampled. Samples of altered material for XRD analysis were also taken at regular intervals down the core. A total of 99 samples were taken, and the locations and a brief description of samples analysed for this study are given in electronic appendix B. 32 key samples were selected for optical petrological analysis using petrological microscopes at the University of Southampton, and were made into polished thin sections. Polished blocks were made of 8 samples to further study the sulphide mineralogy and for laser sulphur isotope analysis (described below).

At the Skouries deposit 5 drill holes were logged at a 2m scale in order to correlate features with assay intervals, with a total of 3464 m of core logged over 6 weeks. The drill holes chosen for study are situated in the intrusive core of the deposit and chosen to ensure all the principal lithologies and veinsets were intercepted. While logging lithology, alteration and mineralisation were recorded. In addition a thorough vein survey was carried out with vein stages present, their size and cross-cutting relationships and density recorded for each 2 m interval. Representative samples were taken from all stages of the deposit paragenesis for petrological and geochemical

analysis. A total of 118 samples were taken, and the locations and a list of analyses carried out are given in electronic appendix C. 36 key samples were chosen for optical petrological analysis using petrological microscopes at the University of Southampton, and were made into polished thin sections. Polished blocks were made of 10 samples to further study the sulphide mineralogy and for laser sulphur isotope analysis.

### **2.1.2 Available datasets**

Lodos Madencilik and Eldorado Gold provided trace and major element datasets for the Muratdere deposit, and the Skouries deposit respectively. These were obtained by taking a groove out of a 2m length of core, powdering it and sending the powders away to a commercial lab for analysis. This means that the exact method of preparation and analysis is unknown, and so no precision or accuracy information is available for this data. This data was only used to determine geochemical patterns and for comparison purposes with data obtained over the course of this study, and is labelled in the text as 'whole rock assay data'.

## **2.2 Micro-analysis**

### **2.2.1 Scanning electron microscope (SEM)**

Polished thin sections were analysed on a LEO1450VP (variable pressure) electron microscope, located at the National Oceanography Centre, Southampton, equipped with a Princeton Tech, light element, energy dispersive X-ray spectrometer and Four Quadrant Backscattered Electron Detector, Type 222. Backscattered electron (BSE) images were used to constrain paragenetic relationships, while non-standardised energy dispersive spectroscopy (EDS) was used for first pass mineral identification and semi-quantitative analysis using spectrum indexes from the AzTec software package. The beam current used was 700 pA, with an accelerating voltage of 20 kV, and a working distance of 19 mm.

#### **2.2.1.1 Scanning electron microscope analysis of fluid inclusions**

Doubly polished fluid inclusion chips ~150  $\mu\text{m}$  thick were analysed on a LEO 535VP variable pressure SEM, located at the British Geological Survey (BGS), equipped with secondary electron imaging, backscattered electron imaging, a fully calibrated Oxford Instruments INCA 450 EDXA X-ray microanalysis system and a GATAN MonoCL3 spectral CL spectrometer and imaging system. The beam current used was 80  $\mu\text{A}$ , with an accelerating voltage of 20 kV and a working distance of 15 mm. Fluid inclusion chips were glued to the edge of a piece of plastic, snapped and then carbon coated before being analysed in order to generate high quality secondary electron and

backscatter electron images of daughter minerals, and to use EDXA to identify the daughter minerals present in type III inclusions. INCA software was used to process the EDXA data, and to produce semi-quantitative mineral identifications. Polished thin sections were also imaged using CL in order to distinguish the different quartz generations in hydrothermal veins.

### 2.2.2 Electron probe micro-analysis (EPMA)

A Cameca SX100 WDX electron microprobe, located at the Natural History Museum (NHM) was used to gain trace element data for ore minerals, including PGMs. The minerals were located using co-ordinates relative to a reference point acquired on the SEM. A beam current of 20 nA and an accelerating voltage of 20 keV were used to analyse for S ( $K\alpha$ ), Pt ( $L\alpha$ ), Mn ( $K\alpha$ ), Fe ( $K\alpha$ ), Co ( $K\alpha$ ), Ni ( $K\alpha$ ), Cu ( $K\alpha$ ), Zn ( $K\alpha$ ), As ( $L\alpha$ ), Se ( $L\alpha$ ), Pd ( $L\alpha$ ), Ag ( $L\alpha$ ), Sb ( $L\alpha$ ), Te ( $L\alpha$ ), Pb ( $M\alpha$ ), Bi ( $M\beta$ ), Cr ( $K\alpha$ ), Ru ( $L\alpha$ ), Rh ( $L\alpha$ ), Os ( $M\alpha$ ), Ir ( $L\alpha$ ), Au ( $L\alpha$ ) and Si ( $K\alpha$ ). Internal empirical corrections were performed to compensate for peak overlap. EPMA was also used to map elements in sulphides.

To determine the quality of this EPMA data 7 standards (NHM in house standards) for the elements of interest: Pt, Cu, Se, Pd, Ag, Te, Bi, Au and Pb were measured at the beginning and end of the session in order to check the calibration and to calculate accuracy and precision (table 2). Precision (%RSD) was calculated using the following formula:

$$\%RSD = 100 \times \sigma_x / \bar{x}$$

$\sigma_x$  = standard deviation of element from mean over all runs;  $\bar{x}$  = mean value of element over all runs. Degree of precision is defined as: 0-3 %RSD: excellent precision; 3-7 %RSD: very good precision; 7-10 %RSD: good precision; >10 %RSD: poor precision (Piercey 2014).

Accuracy (%RD) was calculated using the following formula:

$$\%RD = 100 \times (\bar{x} - STD) / STD$$

$\bar{x}$  = mean value of element over all runs; STD = compiled or published known value of element in standard material. Degree of accuracy is defined as: +/- 0-3 %RD: excellent accuracy; +/- 3-7 %RD: very good accuracy; +/- 7-10 %RD: good accuracy; > +/- 10 %RD: poor accuracy (Piercey 2014).

All of the elements analysed show excellent precision and accuracy (table 2).

Table 2: Accuracy and precision for the EPMA method at NHM. These are calculated from NHM in-house pure element standards.

Element	STD (wt%)	$\bar{x}$ (wt%)	$\sigma_x$	%RSD	%RD
Pt	100	99.41	0.11	0.11	0.59
Pd	100	99.76	0.00	0.00	0.24
Au	100	99.58	0.19	0.19	0.42
Ag	100	99.77	0.20	0.20	0.23
Bi	53	47.75	0.11	0.09	0.35
Te	47	52.82	0.04	0.24	1.60
Se	27	27.72	0.02	0.02	0.35
Pb	73	72.75	0.02	0.05	2.65
Cu	100	100.86	0.01	0.00	0.85

### 2.2.3 Laser Raman Spectroscopy

Fluid inclusions were analysed on a confocal Renishaw inVia Raman microscope, using a 514nm Edge Laser, at Kingston University in order to identify the liquid and vapour phases of the inclusions. Fluid inclusion wafers were placed on a Raman-neutral slide and placed in the microscope. Once the microscope was focussed on the appropriate phase the inclusions were analysed using the laser at 100% power for 30 seconds in order to gain a high resolution spectrum. The peaks of this spectrum were then compared with values given in Burke, 2001 in order to gain a qualitative interpretation of the phases present (Pasteris et al. 1988; Burke 2001).

## 2.3 X-ray diffraction (XRD)

Fine grained clay phases were often too small to identify individually using the SEM, and so whole rock samples were analysed for both bulk mineral composition and clay composition. XRD analysis was performed at the University of Southampton, using a Philips X'Pert pro XRD machine with a Cu X-ray tube. Each sample was crushed to 500  $\mu\text{m}$  and 1.5 g of sample and 0.5 g of corundum were added with isopropanol to a pot containing corundum beads for micronising. Weights were measured to an accuracy of  $\pm 0.001$  g and the beads were placed in the pot using a stencil to ensure that they were in the correct position. The pot was then laced in a micronizing mill for 8 minutes to ensure that the powder was a consistent size. The contents of the pot were dried 66  $^{\circ}\text{C}$ , powdered using a pestle and mortar and poured into a mount to prevent orientation of the crystal phases. Radiation was obtained from Cu tubing at 1.54  $\text{\AA}$  wavelength. A scan speed of 1.2  $^{\circ}/\text{min}$  was used with data recorded every 0.02  $^{\circ}\theta$ . Mineral identification was undertaken using the JC powder diffraction studies database. XRD analysis was also performed on two bulk molybdenite samples – the samples were prepared by scraping the molybdenite with a dental pick to create a powder before continuing the preparation and analysis as above.

## 2.4 Fluid inclusion micro-thermometry

Doubly polished wafers of vein quartz of  $\sim 250\ \mu\text{m}$  thickness were prepared for fluid inclusion microthermometry. Microthermometric data were obtained using a Linkham THM600 heating-freezing stage at the University of Southampton. The stage was calibrated at low temperatures using a set of synthetic fluid inclusion standards from Syn Fliinc. Repeated measurements of the  $\text{CO}_2$  melting point at a rate of  $0.1^\circ/\text{minute}$  gave a reproducibility of  $\pm 0.5^\circ\text{C}$  ( $2\sigma$ ). At high temperatures the melting point of sodium nitrate ( $+306.8^\circ\text{C}$ ) was used for calibration, giving a reproducibility of  $\pm 5^\circ\text{C}$  ( $2\sigma$ ).

As microthermometry can be destructive the fluid inclusion wafers were broken into multiple chips 1-4 mm in size in order to prevent the destruction of the fluid inclusion population in the whole sample. Fluid inclusion populations were then identified in the chips using optical microscopy. Samples were initially heated to  $110^\circ\text{C}$ , and held there for 5 minutes in order to drive off water vapour from the chamber. Test runs were made at cooling/heating rates of  $10^\circ\text{C}/\text{minute}$  in order to determine the general temperature ranges of the phase changes.

Fluid inclusions were cooled to  $-150^\circ\text{C}$  at a rate of  $50^\circ\text{C}/\text{minute}$ , and held there for 5 minutes to allow them to freeze. If the inclusion did not freeze then the sample was taken down to  $-180^\circ\text{C}$  then cycled up to  $-90^\circ\text{C}$  and back down again 10-15 times in order to promote freezing (Patrick 1986; Shepherd et al. 1985). They were then heated at a rate of  $10^\circ\text{C}/\text{minute}$  and heated until  $-57^\circ\text{C}$ , where the rate was slowed to  $0.1^\circ\text{C}/\text{minute}$  over the  $\text{CO}_2$  melting point, until  $-56^\circ\text{C}$ , where the rate was taken back up to  $10^\circ\text{C}/\text{minute}$  until near where  $T_{\text{FM}}$  was expected, where the rate was reduced to  $0.5^\circ\text{C}/\text{minute}$  until  $T_{\text{FM}}$ ,  $T_{\text{ICE}}$  and  $T_{\text{CLATH}}$  (where present) were recorded. The rate was then increased to  $10^\circ\text{C}/\text{minute}$  again until close to  $30^\circ\text{C}$ , where it was slowed to  $1^\circ\text{C}/\text{minute}$  to measure  $\text{CO}_2$  homogenisation (where present). This heating and cooling ramp was repeated for all fluid inclusions, with modifications according to the expected  $T_{\text{M}}$  for the different inclusions.

Heating runs were undertaken at  $20^\circ\text{C}/\text{minute}$ , until vapour bubbles became agitated, or daughter minerals began to show signs of dissolving, at which point heating proceeded at  $5^\circ\text{C}/\text{minute}$  until all the phase changes were recorded.

## 2.5 LA-ICP-MS

### 2.5.1 LA-ICP-MS of molybdenites

Polished thin sections containing molybdenum from the Muratdere deposit were analysed using an UP-193 Laser Ablation System with a wavelength of 193 nm. Ablated material was collected in an argon gas flow and fed into the plasma feed of a Thermo Scientific X-Series 2 Inductively Coupled Plasma Mass Spectrometer, housed at Southampton University. The laser was operated at 85Hz pulse rate with a dwell time of 60 seconds. The ablation diameter was 50µm, except on some smaller grains where a diameter of 25µm was used. In each case where the spot size was changed the standards were reanalysed to monitor the effect of spot size on count rate. Trace element abundance was measured using the following isotopes:  $^{82}\text{Se}$ ,  $^{97}\text{Mo}$ ,  $^{107}\text{Ag}$ ,  $^{125}\text{Te}$ ,  $^{182}\text{W}$ ,  $^{185}\text{Re}$ ,  $^{187}\text{Re}$ ,  $^{193}\text{Ir}$ ,  $^{195}\text{Pt}$  and  $^{197}\text{Au}$ . Collected data was calibrated against U.S. National Institute of Standards and Technology (NIST) SRM 614, 612 and 610 reference glasses using the compositional values for these glasses given by Jochum et al. (2011) before and after each analytical run. Re concentrations in NIST standards are not published in Jochum et al. (2011) so values published in Sylvester & Eggins (1997) were used for Re calibration. The data was processed using the PlasmaLab software package, and all LA-ICP-MS data were internally standardized to the stoichiometric concentrations of molybdenum in molybdenite ( $\text{MoS}_2$ ). Total Re concentration was calculated by combining  $^{185}\text{Re}$  and  $^{187}\text{Re}$  in the proportions of their natural isotope abundance. As Re is heterogeneously distributed in molybdenite (Newberry 1979a) several spots were analysed on each grain and then averaged to give an approximation of the total Re content, and the standard deviation is also presented to give an indication of the spread present (electronic appendix B).

#### 2.5.1.1 Accuracy, precision and uncertainties

Accuracy and precision were calculated for each element using the NIST standards, as discussed above (table 3). The NIST 610 standard shows excellent accuracy for all elements and very good to excellent precision, except for  $^{195}\text{Pt}$ , which has poor precision. NIST 612 shows excellent to very good accuracy on all elements, but poor precision. NIST 614 shows excellent accuracy for  $^{195}\text{Pt}$ , and good accuracy for  $^{182}\text{W}$ , but poor accuracy for all other elements, and poor precision for all elements. This shows that this method is accurate for measurement of elements in the abundance of 100s of ppb, but shows poor accuracy and precision for elements with abundances on the order of 10s of ppb. As the main aim of this method is to establish the Re concentration of individual molybdenite grains, where the Re concentration is predicted to be >100 ppm these precision and accuracy levels are acceptable.

NIST glasses are not an ideal standard for analysing sulphides, as they are not matrix matched, and this can introduce significant errors (Danyushevsky et al. 2011). However unfortunately at the time of analysis no sulphide standards were available. Using Mo as the internal standard is also not ideal as if Re substitutes for Mo in molybdenite then it is not an independent variable (Newberry 1979b; Voudouris et al. 2009). However, sulphur was not analysed for and so could not be used as an internal standard, and evidence at Muratdere suggests that Re hosting in molybdenite in the Muratdere deposit is not necessarily by substitution (see discussion in chapter 3).

*Table 3: Accuracy and precision for LA-ICP-MS of molybdenites at Southampton University. These are calculated from NIST 610, 612 and 614 glass standards. Standard concentrations are from Jochum et al. and Sylvester & Eggins (Jochum et al. 2011; Sylvester & Eggins 1997).*

Standard	Element	STD (ppm)	$\bar{x}$ (ppm)	$\sigma_x$	%RSD	%RD
NIST 614 (n=71)	97Mo	0.79	1.21	0.91	74.89	53.40
NIST 614	107Ag	0.41	0.21	0.08	37.75	48.53
NIST 614	182W	0.78	0.73	0.19	26.28	6.44
NIST 614	185Re	0.17	0.30	0.14	46.88	76.11
NIST 614	187Re	0.19	0.29	0.15	49.59	54.38
NIST 614	195Pt	2.40	2.40	0.34	14.02	0.14
NIST 614	197Au	0.50	0.55	0.20	36.26	10.06
NIST 612 (n=75)	97Mo	37.4	36.63	8.54	23.33	2.07
NIST 612	107Ag	22	23.05	4.36	18.91	4.78
NIST 612	182W	38	37.49	7.43	19.82	1.34
NIST 612	185Re	6.6	6.75	1.31	19.40	2.32
NIST 612	187Re	6.6	6.87	1.32	19.21	4.03
NIST 612	195Pt	2.5	2.60	0.40	15.28	3.91
NIST 612	197Au	4.8	4.62	0.91	19.75	3.80
NIST 610 (n=75)	97Mo	417	424.33	17.16	4.05	1.76
NIST 610	107Ag	251	255.75	8.17	3.19	1.89
NIST 610	182W	444	450.17	10.80	2.40	1.39
NIST 610	185Re	49.9	50.55	1.46	2.90	1.30
NIST 610	187Re	49.9	50.52	1.19	2.35	1.24
NIST 610	195Pt	3.1	3.11	0.40	12.87	0.23
NIST 610	197Au	23.6	23.98	0.99	4.12	1.60

## 2.5.2 LA-ICP-MS of fluid inclusions

LA-ICP-MS was performed on fluid inclusions in quartz from the mineralising veins in the Skouries porphyry deposit, Greece. The results of this analysis are discussed in chapters 4 and 5.

### 2.5.2.1 Method

Laser ablation analyses were carried out at the Natural History Museum, London, using an ESI New-Wave NWR213, 213-nm aperture-imaged laser ablation system (Jeffries et al. 1998) equipped with beam homogenization optics. Ablated particulate material was analysed by an Agilent 7500cs inductively coupled plasma mass spectrometer. The carrier gas used was helium (Pettke et al. 2012). 200  $\mu\text{m}$  thick double polished vein quartz chip samples were glued to a slide using a low-contaminant adhesive, and loaded into the sample chamber which was then purged of gas.

Analysis was performed in batches of around 20 inclusions, with duplicate analyses of NIST 612 and NIST 610 glass made at each end of the sample run. The glass samples were analysed with a fixed spot size of 50  $\mu\text{m}$ , a frequency of 10 Hz, and at a fluence of 3.5  $\text{Jcm}^{-2}$ . For fluid inclusion analysis a frequency of 10 Hz was used and spot sizes of 15  $\mu\text{m}$  to 50  $\mu\text{m}$  were used, selecting the smallest spot size possible to completely ablate the inclusion in order to eliminate the risk of any surrounding inclusions being breached. Ablation commenced at low energy density (fluence of  $<2 \text{ Jcm}^{-2}$ ), in order to eliminate the risk of quartz sharding, which has been shown to result in element fractionation (Stoffell et al. 2004). The fluence was increased in small increments over a time period of approximately 10s until an energy density of 3  $\text{Jcm}^{-2}$  was achieved, at which point the laser power was kept constant. The spot size was also kept constant, and this produced clean, smooth sided ablation pits in most samples. The inclusions sampled were isolated, regular shaped, 10 – 30  $\mu\text{m}$  inclusions 20  $\mu\text{m}$  to 90  $\mu\text{m}$  deep in the chip. In order to reach the deeper inclusions ( $>50 \mu\text{m}$  deep) stepwise widening of the spot-size was used in order to ensure continued ablation to the depth of the inclusion.

Two ‘methods’ were used with different dwell times (table 4): ‘method 1’ analyses for a range of elements commonly found in fluids, while the ‘method 2’ focuses on metals and semi-metals, with a longer dwell time on each in order to lower limits of detection and increase sensitivity for these ore forming elements. Although Te, Se and Pd are not commonly analysed for in fluid inclusions (Pettke et al. 2012)  $^{206}\text{Pd}$ ,  $^{78}\text{Se}$ ,  $^{130}\text{Te}$  and  $^{209}\text{Bi}$  were added to the element lists in order to attempt to identify their carrier fluids, as Skouries is known to be enriched in these elements.  $^{106}\text{Pd}$  was chosen, rather than  $^{105}\text{Pd}$ , as  $^{40}\text{Ar}^{65}\text{Cu}^+$  interferes on  $^{105}\text{Pd}$ . The potential interferences on  $^{106}\text{Pd}$  are  $^{106}\text{Cd}$ ,  $^{90}\text{Zr}^{16}\text{O}$ , and  $^{40}\text{Ar}^{66}\text{Zn}$  (Sylvester & Eggins 1997; Thomas 2002; Motelica-Heino et



al. 2001).  $^{106}\text{Cd}$  is a potential isobaric interference for  $^{106}\text{Pd}$ , however  $^{106}\text{Cd}$  only makes up 1.25% of the natural abundance of Cd isotopes, while  $^{106}\text{Pd}$  makes up 27.33% of Pd isotopes. Similarly  $^{110}\text{Cd}$  is a potential isobaric interference for  $^{110}\text{Pd}$ , with  $^{110}\text{Cd}$  making up 12.49% of the natural abundance of isotopes, and  $^{110}\text{Pd}$  making up 11.72% (Thomas 2002), so  $^{106}\text{Pd}$  was used as the primary Pd indicator in this study.  $^{66}\text{Zn}$  and  $^{90}\text{Zr}$  were analysed in order to check for interference – if they correlate or co-vary with  $^{106}\text{Pd}$  then  $^{106}\text{Pd}$  values may be the result of interference, however, if they do not co-vary then it is likely to be a true reading. A correction was performed using  $^{111}\text{Cd}$  to remove the  $^{106}\text{Cd}$  signal from the  $^{106}\text{Pd}$  signal (see chapter 6 for more information).

*Table 4: Summary of the two methods used to analyse fluid inclusions by LA-ICP-MS, dwell time in milliseconds for each element shown in brackets*

	Method 1	Method 2
Total acquisition time	120 seconds	120 seconds
Isotopes analysed (dwell time in milli-seconds)	$^7\text{Li}$ (10), $^{23}\text{Na}$ (10), $^{24}\text{Mg}$ (10), $^{27}\text{Al}$ (5), $^{29}\text{Si}$ (5), $^{39}\text{K}$ (10), $^{43}\text{Ca}$ (10), $^{49}\text{Ti}$ (5), $^{51}\text{V}$ (10), $^{53}\text{Cr}$ (10), $^{55}\text{Mn}$ (10), $^{57}\text{Fe}$ (10), $^{59}\text{Co}$ (10), $^{60}\text{Ni}$ (10), $^{65}\text{Cu}$ (10), $^{66}\text{Zn}$ (10), $^{75}\text{As}$ (10), $^{78}\text{Se}$ (20), $^{85}\text{Rb}$ (10), $^{88}\text{Sr}$ (10), $^{89}\text{Y}$ (10), $^{90}\text{Zr}$ (10), $^{95}\text{Mo}$ (10), $^{106}\text{Pd}$ (20), $^{107}\text{Ag}$ (20), $^{111}\text{Cd}$ (10), $^{118}\text{Sn}$ (10), $^{121}\text{Sb}$ (10), $^{130}\text{Te}$ (20), $^{133}\text{Cs}$ (10), $^{137}\text{Ba}$ (10), $^{139}\text{La}$ (10), $^{182}\text{W}$ (10), $^{197}\text{Au}$ (20), $^{208}\text{Pb}$ (10), $^{209}\text{Bi}$ (20), $^{232}\text{Th}$ (10), $^{238}\text{U}$ (10).	$^{23}\text{Na}$ (10), $^{29}\text{Si}$ (5), $^{57}\text{Fe}$ (10), $^{65}\text{Cu}$ (10), $^{75}\text{As}$ (10), $^{78}\text{Se}$ (30), $^{95}\text{Mo}$ (10), $^{106}\text{Pd}$ (30), $^{107}\text{Ag}$ (30), $^{110}\text{Pd}$ (30), $^{111}\text{Cd}$ (10), $^{121}\text{Sb}$ (20), $^{130}\text{Te}$ (30), $^{197}\text{Au}$ (30), $^{208}\text{Pb}$ (10), $^{209}\text{Bi}$ (20).

### 2.5.2.2 Processing methods

Following laser ablation analysis absolute quantification of the fluid inclusion concentrations was achieved by first integrating the signal interval and subtracting the background contribution using the ExLAM 2000 package (Zacharias & Wilkinson 2007). Sensitivity for each element was computed using the external standard, NIST 612 glass, enabling calculation of element intensity ratios (Jochum et al. 2011). Although glass standards are not matrix-matched to fluid inclusions, external calibration has been shown to be relatively matrix-insensitive, and non-matrix matched standards are not a significant source of error in this method when compared to ablation quality and internal standard issues (Heinrich et al. 2003). An internal standard was then used to convert these element intensity ratios into absolute concentrations. Weight percent sodium was used as it is present in all the fluids analysed, is possible to calculate from microthermometry, and has been shown to return more accurate data than Cl-based quantification (Pettke et al. 2012).

Unfortunately, due to the high temperature of the system it was not possible to perform microthermometry on the same inclusions which LA-ICP-MS was performed on, as a large proportion of the inclusions burst prior to homogenisation. Instead great care was taken to ensure all the inclusions analysed underwent thorough petrological classification in order to classify them according to their daughter mineralogy and vapour phase proportions (see chapter 4 for further information). These were then matched with petrologically identical inclusion assemblages from other fragments of the same sample chip, ensuring they represented the same quartz phase, vein stage, and as far as possible fluid generation. Microthermometry was then performed on these proxy assemblages in order to give salinity values, and therefore an approximate Na wt% for the inclusions analysed by LA-ICP-MS (electronic appendix C).

### **2.5.2.3 Accuracy, precision, limits of detection and interferences**

Limits of detection (LOD) were calculated using the standard deviation of the instrument background signals for each element in every inclusion. LODs in this study were calculated using  $3\sigma_{BG}$ , meaning that any count intensities below 3 times the standard deviation of the background counts were 'below the limits of detection', and LODs are given for each inclusion in appendix C. During processing it is possible to change the limits of detection by integrating different signal interval lengths from the inclusion signal. Absolute concentrations were calculated by integrating both 'long' and 'short' signal intervals for each inclusions. 'Long' intervals incorporate the whole of the signal from the fluid inclusion, defined as the period between where the Na and K signals become elevated to where they return to background values. 'Short' intervals are the shortest ablation interval (>10 time slices) which includes all of the signals from the daughter minerals (appendix A1.2, appendix C). When comparing the LODs produced by the two intervals using 'short' intervals results in limits of detection being on average 7% lower for all elements (appendix A1.3). Therefore, short intervals were used for all processing in this project.

Full calculation of the uncertainties in a fluid inclusion analysis is difficult due to the large number of experimental variables and the critical influence of signal shape (Heinrich et al. 2003). The largest source of error in fluid inclusion LA-ICP-MS the independent estimate of the concentration of the internal standard (Pettke et al. 2012). Two types of inclusion were analysed in this study, with different microthermometric properties (see chapter 4). Type III inclusions are multisolid inclusions containing NaCl-KCl-FeCl<sub>2</sub>-(CO<sub>2</sub>)-H<sub>2</sub>O, which homogenise by halite dissolution, and the NaCl content of these inclusions was calculated using the H<sub>2</sub>O-NaCl-KCl fluid system in the AqSo WHS software package developed by Bakker (Bakker 2012). Type IV inclusions are vapour rich and salinities were calculated using the FLUIDS software package (Bakker 2003). The calculations used and uncertainties associated with these salinity values are discussed further in chapter 4, however

the NaCl concentrations calculated for the type III inclusions are only close approximations as there is not yet sufficient experimental data for the NaCl-KCl-FeCl<sub>2</sub>-(CO<sub>2</sub>)-H<sub>2</sub>O system to take into account all of the cations present. Similarly, the type IV inclusions were difficult to gain microthermometric data for (see chapter 4), and so the NaCl concentrations produced are only from a small subset (n=5) of these inclusions and therefore contain large uncertainties. The fact that the microthermometry was not performed on the same inclusions as the LA-ICP-MS adds additional uncertainty. Although every effort was made to ensure that the proxy inclusions analysed were from the same generation of fluid as the inclusions which underwent laser ablation the range of NaCl contents calculated for inclusions even within the same assemblage at Skouries was quite large (discussed further in chapter 4). In order to quantify this uncertainty absolute element concentrations were calculated for each inclusion using different internal standard values: the average salinity from the proxy assemblage; the minimum measured salinity of the proxy assemblage; the maximum measured salinity from the proxy assemblage; and 1 standard deviation (SD) away from the average of the proxy assemblage (values in table 5, appendix C). These results were then used to calculate the maximum percentage error in absolute element concentration that would result from the salinity of the inclusion being ablated being an end member of that population's salinity range, as well as the more likely error from the standard deviation. The maximum error caused by uncertainty over the internal standard value is approximately +/- 55%, and the likely error is approximately +/-23%. This error is systematic, meaning that the concentrations are all changed by the same percentage, so the ratios between element concentrations are not affected by internal standard uncertainty. This means that for Type IV inclusions, which are associated with the most uncertainty, it is best to use ratios when making interpretations.

Instrumental precision and accuracy were determined by analysing NIST 610 standards at the beginning and end of each run. Instrumental precision is represented by two standard deviations from the mean (2 $\sigma$ ), with most elements having 2 $\sigma$  below 10% (appendix A1.4). <sup>57</sup>Fe and <sup>78</sup>Se both showed poor precision, with <sup>57</sup>Fe having a 2 $\sigma$  of 40%, and <sup>78</sup>Se having a 2 $\sigma$  of 368%. The rest of the elements have very good to excellent precision, when calculated as %RSD (appendix C). Accuracy was determined by calculating %RD (appendix C), with <sup>57</sup>Fe, <sup>78</sup>Se and <sup>106</sup>Pd showing poor accuracy, and the rest of the elements showing very good to excellent accuracy. The poor accuracy shown in the Pd readings is likely to be due to the lack of proper constraint of standard values and heterogeneity in standards (Jochum et al. 2011), especially given the excellent precision shown for that element. Tellurium was not detected in any of the standards or samples, and the selenium results have also been discounted due to the poor precision and accuracy seen for that element.

## Chapter 2

Fe is a major component of fluid inclusion systems and so cannot be discounted; however, it will be treated with care.

Instrumental precision can also be calculated from  $2\sigma$  from measured fluid inclusion assemblages which obey Roedder's rules, and this has been suggested as the best way of assessing precision in LA-ICP-MS of fluid inclusions (Roedder & Ribbe 1984; Heinrich et al. 2003; Pettke et al. 2005). Doing this for the inclusions from Skouries yielded very high  $2\sigma$  values, and this is probably due to the fact that the majority of the inclusions have undergone post-entrapment modification and/or heterogenous trapping (see chapter 4). It is also difficult to get consistent results from multi-solid inclusions as partial ablation of daughter minerals may result in large concentration ranges for a single assemblage (Heinrich et al. 2003).

*Table 5: Summary of the measured salinities used as internal standards in the calibration of the fluid inclusion LA-ICP-MS signals, and the uncertainties associated with the range of salinities measured. This table shows the percentage difference in absolute element concentrations resulting from: using a Na% value 1 SD away from the average for that assemblage; using the maximum measured Na% value for the assemblage rather than the average; and using the minimum measured Na% value for that assemblage rather than the average.*

Veinset	Fluid inclusion type	Minimum NaCl wt%	Average NaCl wt%	Maximum NaCl wt%	1SD (NaCl wt%)	Minimum Na wt%	Average Na wt%	Maximum Na wt%	1SD (Na wt%)	1 SD difference in calibration Na wt%	Difference between Max and Av Na% calibration	Difference between Min and Av Na% calibration
M-3	Type IIIA	34	38	58	6.42	13.3	14.8	22.6	2.5	17%	52%	13%
M-3	Type IIIB	32	39	53	6.34	12.5	15.2	20.7	2.5	16%	40%	13%
M-3	Type IV	6	10	13	2.32	2.3	3.9	5.1	0.9	23%	37%	35%
M-4	Type IIIA	34	44	59	9.75	13.3	17.2	23	3.8	22%	35%	20%
M-4	Type IIIB	26	39	60	9.64	10.1	15.2	23.4	3.8	25%	53%	33%
M-4	Type IV	6	10	13	2.32	2.3	3.9	5.1	0.9	23%	25%	50%
M-5	Type IIIA	27	36	51	10.68	10.5	14	19.9	4.2	30%	43%	21%
M-5	Type IIIB	18	37	59	10.9	7	14.4	23	4.3	30%	55%	53%
M-5	Type IV	6	10	13	2.32	2.3	3.9	5.1	0.9	23%	25%	50%

## 2.6 Ni-S fire assay

Nickel sulfide fire assay was performed at Cardiff University. 16 whole rock samples were crushed in a tungsten-carbide mill and the level of background contamination was determined by crushing sand between each sample and analysing the sand for the levels of PGEs. 15  $\pm$  0.1 g of sample was then mixed with 12  $\pm$  0.1 g NaCO<sub>3</sub>, 24  $\pm$  0.2 g borax, 0.9  $\pm$  0.1 g S, 1.08  $\pm$  0.1g Ni, and 5  $\pm$  0.05g silica, poured into a crucible and placed in a furnace at 1100°C for 90 minutes. After removal and cooling the Ni-S bead was removed with a hammer and its mass recorded. These were crushed and dissolved in 150 ml of warm HCl. 150 ml of cold de-ionised water was used to cool the sample before adding 1 ml of Tellurium chloride and 3 ml of tin chloride. The samples were then heated to 150°C and left for 60 minutes. Once cooled the sample was filtered under vacuum through a 0.45 micron pore size membrane filter on a Sartorius filtration system. The sample was then washed with 100-200 ml of 10% HCl and 200-300 ml of deionised water. Once filter was clean it was removed and deposited in a Teflon vial with a crystal of NaCl, 4 ml of concentrated Primar grade HCl followed by 3 ml of concentrated HNO<sub>3</sub> and warmed gently for 2 hours to digest. The sample was then transferred to a 50 ml nalgene volumetric flask, spiked with 1 ml of thallium spike and made up to volume with deionised water. This solution was then analysed by an inductively coupled plasma mass spectrometer (McDonald 1998).

The sand samples showed background contamination of 0.47 ppb Pt, 0.12 ppb Pd, 0.32 ppb Au and 2.25 ppb Re. This was then subtracted from the samples to account for contamination from the tungsten mill, as were the background count levels of the 3 blanks analysed. The accuracy of the PGE determination was assessed via replicate analysis of the certified reference material WITS1 and WMG1 (table 6), showing excellent accuracy for all elements except Re, for which there is no standard data. The precision on the unknown PGE concentrations was assessed by duplicate analysis of 3 samples (table 7), showing excellent precision for Pd, Os and Ir on all samples, and good precision for Ru, Pt, Au and Re on some of the samples, with others showing poor precision. This range in precision values could be due to nugget effect within the samples analysed.

Table 6: Accuracy of Ni-S fire assay method calculated from the analysis of two standards

Standard	Element	STD (ppb)	Measured value	%RD
WITS1	189Os	1.40	1.11	0.21
WITS1	193Ir	1.40	1.48	0.06
WITS1	99Ru	3.90	4.08	0.05
WITS1	103Rh	1.10	1.12	0.02
WITS1	195Pt	5.70	6.24	0.10
WITS1	106Pd	5.00	5.42	0.08
WITS1	197Au	4.90	6.55	0.34
WITS1	185Re	No data	0.02	na
WMG1	189Os	24	22.56	0.06
WMG1	193Ir	46	48.01	0.04
WMG1	99Ru	35	31.47	0.10
WMG1	103Rh	26	26.77	0.03
WMG1	195Pt	731	727.20	0.01
WMG1	106Pd	382	393.16	0.03
WMG1	197Au	110	108.81	0.01
WMG1	185Re	No data	0.31	na

Table 7: Precision of Ni-S fire assay method calculated from repeat analysis of the same samples

Sample	Element	$\bar{x}$ (wt%)	$\sigma_x$	%RSD
MDD 03 245.3	189Os	<dt	na	na
MDD 03 245.3	193Ir	<dt	na	na
MDD 03 245.3	99Ru	0.54	0.05	9.48
MDD 03 245.3	103Rh	0.20	0.02	10.49
MDD 03 245.3	195Pt	1.54	0.33	21.30
MDD 03 245.3	106Pd	1.73	0.04	2.43
MDD 03 245.3	197Au	299.41	16.82	5.62
MDD 03 245.3	185Re	90.16	4.52	5.01
MDD 03 265.0	189Os	<dt	na	na
MDD 03 265.0	193Ir	<dt	na	na
MDD 03 265.0	99Ru	<dt	na	na
MDD 03 265.0	103Rh	0.09	0.01	8.45
MDD 03 265.0	195Pt	0.90	0.12	13.40
MDD 03 265.0	106Pd	0.11	0.01	7.76
MDD 03 265.0	197Au	39.48	1.01	2.56
MDD 03 265.0	185Re	65.24	4.46	6.84
MDD 33 55.5	189Os	0.03	0.00	0.62
MDD 33 55.5	193Ir	0.04	0.00	0.27
MDD 33 55.5	99Ru	0.14	0.01	9.25
MDD 33 55.5	103Rh	<dt	na	na
MDD 33 55.5	195Pt	1.18	0.08	6.53
MDD 33 55.5	106Pd	0.30	0.01	2.24
MDD 33 55.5	197Au	107.62	102.96	95.67
MDD 33 55.5	185Re	17.59	17.24	97.99

## **2.7 Stable isotopes**

Stable isotope analyses were completed at the Scottish Universities Environmental Research Centre (SUERC) in East Kilbride.

### **2.7.1 Sulphur**

Samples were crushed and then sulphides and sulphates were separated by careful hand picking, and were checked for purity under an optical microscope.

#### **2.7.1.1 Sulphides**

Sulphur isotope analyses used two different methods – ‘Conventional’ analysis of hand-picked sulfides (after Robinson & Kusakabe 1975) and ‘Laser’ analysis via in situ via laser extraction (after Fallick et al. 1992) on sulfides too small or in too small a quantity to pick, or showing complex textural relationships. The instrumental error for the conventional method is  $\pm 0.014\text{‰}$ , and for the laser method is  $\pm 0.043\text{‰}$ . Initial  $\delta^{66}\text{SO}_2$  data were converted to  $\delta^{34}\text{S}$  values by calibration with international standards NBS-123 ( $+17.1\text{‰}$ ) and IAEA-S-3 ( $-31\text{‰}$ ), as well as Scottish Universities Environmental Research Centre’s (SUERC) internal lab standard CP-1 ( $-4.6\text{‰}$ ). All sulphur isotope compositions were calculated relative to Canon Diablo Trilobite (V-CDT) and are reported in standard notation. The accuracy of the conventional method is excellent, as is the precision (table 8).

#### **2.7.1.2 Sulphates**

Sulphur dioxide gas was extracted from the sulphates following the method of Coleman and Moore (1978). The resultant gases were then processed in a similar way to that used for sulfides (see above) and calibrated with NBS-127 international standard with a  $2\sigma$  reproducibility of  $\pm 2.8\text{‰}$ . The accuracy of this method is very good, and the precision is excellent (table 8).

### **2.7.2 Oxygen and hydrogen**

10 quartz samples were separated by careful hand picking and were checked for purity by optical microscopy. The samples were conventionally analysed for oxygen isotopic composition by a technique modified after Clayton and Mayeda (1963). Sample decomposition was carried out with bromine pentafluoride; the resultant oxygen reacted with graphite rods to produce carbon dioxide, the isotopic composition of which was determined using a VG SIRA 10 mass spectrometer. The accuracy of the technique was confirmed by the periodic analysis of the TOR1, JJB8 and SCXO standards, with a  $2\sigma$  reproducibility of  $\pm 0.09\text{‰}$ . All oxygen isotope compositions



were calculated relative to the V-SMOW standard and are reported in standard notation. The accuracy of this method is excellent, as is the precision (table 8).

Hydrogen isotope analyses were obtained from 5 coarsely crushed samples of cleaned vein-quartz. Splits of the samples (up to around 1 g) were washed in warm aqua regia and handpicked before analysis. The water of the fluid inclusions in quartz was released by heating the samples to above 500 °C by means of an induction furnace, and then reacted with zinc powder at 410 °C to generate hydrogen (Friedman 1953) for isotope analysis. The results were reported in per mil relative to V-SMOW standards, with a  $2\sigma$  reproducibility of  $\pm 3.4\%$ .

*Table 8: Accuracy and precision of stable isotope results*

Element	Standard	Mineral	STD	$\bar{x}$	$\sigma_x$	$2\sigma$	%RSD	%RD
Oxygen	JJB8	Quartz	30.3	30.3	0.0	0.1	0.2	0.0
Oxygen	SCXO	Quartz	5.2	5.2	0.2	0.4	4.0	0.3
Oxygen	TOR1	Quartz	9.6	9.6	0.2	0.5	2.5	0.1
Sulphur	CP1	Chalcopyrite	-4.6	-4.6	0.3	0.7	7.2	0.9
Sulphur	IAEA S3	Ag <sub>2</sub> S	-31.0	-31.6	na	na	na	1.94
Sulphur	NBS 123	Sphalerite	17.1	16.8	0.3	0.6	1.7	1.8
Sulphur	NBS127	Barite	20.3	19.6	1.4	2.8	7.2	3.5



## **Chapter 3: Enhanced rhenium concentrations in the Muratdere Cu-Mo (Au-Re) porphyry deposit, Turkey due to hydrothermal fluid-country rock interactions**

### **3.1 Introduction**

Porphyry copper deposits provide 90% of the world's rhenium production, with the large copper mines in Chile providing the largest proportion (John 2015). Re in porphyries is mainly hosted in molybdenite ( $\text{MoS}_2$ ) (Fleischer 1959) which typically has Re contents between 8 ppm and 1 wt% in porphyry deposits (Mao et al. 2003; Berzina et al. 2005; Voudouris et al. 2009). The Muratdere Cu-Mo (Au-Re) porphyry deposit, located in the Tethyan Metallogenic Belt, Turkey, has a JORC-compliant Inferred Resource of 51 million tonnes comprising 186,000 tonnes Cu, 204,296 oz. Au, 3.9 million oz. Ag, 6,390 tonnes Mo and 17,594 kg Re (Stratex International 2016), with whole-rock Re concentrations of up to 2.37 ppm. Muratdere is considerably enriched in Re when compared with average Re concentrations of andesites of 0.2 – 0.6 ppm, and granodiorites of 0.02 – 0.09 ppm (Imai et al. 1995) and an average crustal Re concentration of 0.7 ppb (Naumov 2007). Despite our understanding that the Re in porphyry systems is located within molybdenite (Fleischer 1959) the mechanisms of Re enrichment in porphyry copper deposits remain poorly understood. These uncertainties include the source of Re in porphyry deposits and the mechanisms of its incorporation into molybdenite.

This chapter provides the first account of the main geological and mineralogical features of porphyry Cu-Mo (Re-Au) mineralisation at Muratdere and couples this with XRD, stable isotope, fluid inclusion microthermometric and platinum group element analyses to provide insights into the source and mechanisms of Re enrichment in porphyry systems. Furthermore, the Muratdere porphyry deposit has two generations of molybdenite with contrasting Re contents, determined from LA-ICP-MS analysis, which provides further constraints on the controls on Re distribution.

#### **3.1.1 Current models for rhenium enrichment in porphyry copper deposits**

Re is a moderately chalcophile metal, which mimics the behaviour of Cu and the platinum group elements in melts, preferentially partitioning into sulphide droplets in hot mafic melts (Patten et al. 2013). However, it has been shown that Re has a strong dependency on  $f\text{O}_2$ , behaving as a

chalcophile element in relatively reduced magmas and preferentially partitioning into silicates in more oxidised arc magmas (Fonseca et al. 2007).

One suggested mechanism for Re enrichment in porphyry deposits is that ultramafic melts rise through the crust and are injected into colder felsic porphyry-related magma, enriching it in sulphur, Au and Re, along with other volatiles (Hattori & Keith 2001; Sinclair & Jonasson 2014). This assertion is supported by the positive correlation between Re and Au contents of porphyries globally (Sinclair & Jonasson 2014), REE patterns consistent with amphibole and residual garnet fractionation in igneous rocks associated with porphyry deposits (Richards 2011), and the common association of Re and Au enriched porphyry deposits with mafic magmatic and volcanic phases. Deposits which involve mantle underplating or metasomatism, or the melting of mafic or ultramafic rocks as part of their genesis also tend to have higher Re in molybdenite than those hosted by intermediate crustal rocks (Stein et al. 2001; Berzina et al. 2005). An additional potential source of Re is the subduction of anoxic sediments which show high Re concentrations (Sun et al. 2003) and there are many reports of high Re-bearing molybdenites at convergent margin volcanoes, with concentrations of up to 11.5 wt% Re in molybdenite (Bernard et al. 1990).

By comparing the Re content of more than 75 porphyries, Berzina et al (2005) concluded that bulk Re concentrations are closely linked to the parent magmas, with Re deposition controlled by the solubility of Re hosting phases under hydrothermal conditions. They note that high Re deposits in Siberia have low initial  $^{87}\text{Sr}/^{86}\text{Sr}$  values (0.70406 – 0.70496), with Re depleted deposits having higher  $^{87}\text{Sr}/^{86}\text{Sr}$  values, possibly reflecting crustal contamination, and that most Re bearing parent magmas had  $\delta^{34}\text{S}_{\text{CDT}}$  values around zero per mil, as expected for a magmatic sulphur source. In addition, they also note that deposits formed under oxidising conditions contain more Re, as do deposits with evidence of elevated chloride activity in the hydrothermal fluids (Berzina et al. 2005).

Paradoxically, although Re is most commonly hosted by molybdenite in porphyry deposits, Mo-dominated Mo-Cu porphyry deposits typically contain less Re than Cu-dominated Cu-Mo or Cu-Au-Mo deposits, with the Re content of global porphyry deposits increasing with increasing Cu/Mo ratio (Berzina et al. 2005). This has been attributed to the fact that the Re budget available in the source melt is preferentially sequestered by molybdenite, so assuming all available Re is taken up by the molybdenite present, the limited presence of molybdenite in low molybdenum deposits results in high Re concentrations, whereas in high molybdenum deposits the Re content is diluted across many more molybdenite crystals (Stein et al. 2001).

### 3.1.2 Transport of rhenium in porphyry deposits

Re is transported as a chloride complex in supercritical hydrothermal fluids (Xiong et al. 2006; Xiong & Wood 2002). These chloride complexes are volatile, for example  $\text{ReCl}_6$  has a melting point of  $20^\circ\text{C}$  (Sun et al. 2003), and both native Re and Rheniite ( $\text{ReS}_2$ ) have been observed sublimating from volcanic gases at the Kudryavy volcano in Russia (Korzinsky et al. 1994). Experimental work has shown that Re can also be transported as a bisulphide complex,  $\text{ReS}_2$ , in sulphur bearing, reducing environments (Xiong & Wood 2002).  $\text{ReS}_2$  has slight prograde solubility in high temperature ( $400\text{--}500^\circ\text{C}$ ) environments, which suggests that molybdenites deposited at low temperatures may contain more Re. However, various studies have shown that temperature of deposition and Re concentrations do not always correlate in porphyry deposits (Popov 1988; Popov et al. 2003; Berzina et al. 2005), and Re is preferentially transported as a chloride complex in high salinity, oxidising fluids. The addition of reduced sulphur to these Re bearing fluids has been suggested as a depositional mechanism for Re (Xiong & Wood 2002).

### 3.1.3 Hosting of rhenium in molybdenite

Molybdenite is made up of stacks of planar S-Mo-S layers, and has 2 polytypes – the most common is the hexagonal 2H polytype, whereas the rhombohedral 3R polytype is more rare (Newberry 1979a). It is still unknown how polytype affects Re concentrations in molybdenite. Theoretically the crystal structure of the 3R polytype should allow space for more impurities, and a relationship between the amount of Re and the amount of 3R molybdenite in porphyry deposits has been proposed (Newberry 1979b). Both the 2H to 3R polytype ratio of molybdenites and the abundance of Re in molybdenites have been suggested to increase over time during the potassic alteration phase, with the highest abundances shown in B veins (Newberry 1979b). However, it has since been shown that high concentrations of Re can be present in the 2H polytype, suggesting that Re content of molybdenites is independent of polytype (Voudouris et al. 2009; Grabezhev & Voudouris 2014). It is thought that Re is incorporated into molybdenite by isomorphous substitution of Mo, rather than by the formation of nanophases of Re within the lattice (Voudouris et al. 2009; da Silva et al. 2013).

Re is distributed heterogeneously within molybdenite grains, with variations of up to an order of magnitude found across a single grain (Voudouris et al. 2009; Ciobanu et al. 2013; Grabezhev & Voudouris 2014). These variations in Re concentration are often picked out by oscillatory zoning. These zones could represent changes in the Re content, oxidation state, pH, pressure or temperature of the surrounding hydrothermal fluids (Ciobanu et al. 2013), or the zoning could be due to the intrinsic mechanisms of crystal formation. As the ionic radius of  $\text{Re}^{4+}$  ( $0.63 \text{ \AA}$ ) is slightly

smaller than that of  $\text{Mo}^{4+}$  (0.65 Å) isovalent substitution of Re for Mo would cause the unit cell volume to decrease (Shannon 1981; Schönfeld et al. 1983; Voudouris et al. 2009). This leads to lattice stretching which may cause the creation of microzones through lattice defects (Grabazhev & Voudouris 2014). Alternatively this zonation could be caused by differing crystal growth rates, or by the expansion of the molybdenite lattice due to polytypism (Fron del & Wickman 1970; Ortoleva et al. 1987; Newberry 1979a; Newberry 1979b).

### 3.2 Regional geology

The Muratdere Cu-Mo porphyry deposit is part of the Tethyan metallogenic belt (Yigit, 2006). In Turkey, the porphyry deposits in the Tethyan Belt are related to Late Cretaceous to Miocene granitoids formed in association with the closure of the Neotethys and the Paleotethys (Yigit 2006; Yigit 2009) and are associated with a number of island arcs and continental fragments (Richards 2015). Following the closure of the Paleotethys ocean in the early Jurassic, northward subduction of the Neotethys caused calc-alkaline magmatism and ophiolite accretion through to the Late Cretaceous (Boztug & Arehart 2007; Kaygusuz et al. 2008; Dokuz et al. 2010). However, the majority of the volcanic and magmatic products from that period have since been eroded away. The Muratdere deposit is situated 250 km west of Ankara, in the North Anatolian Belt, a Jurassic-Cretaceous ophiolitic melange, which stretches across the centre of Turkey (Tekeli 1981, figure 6). The deposit is just to the south of the Izmir-Ankara-Erzincan suture zone (IAESZ), a feature which was formed in the late Cretaceous to Palaeocene as the Kirşehir micro-continental block collided with the Central Pontide margin (Kaymakci et al. 2009; Robertson et al. 2009; Sarıfakioğlu et al. 2010; Lefebvre et al. 2013; Espurt et al. 2014). As subduction of the Neotethys continued through the late Paleocene to early Eocene, the Tauride-Anatolian block collided with the IAESZ (Kaymakci et al. 2009; Arslan et al. 2013). This collision led to calc-alkaline magmatism in response to slab roll back and breakoff (Boztuğ et al. 2006; Boztug & Arehart 2007; Boztuğ & Harlavan 2008; Kaygusuz et al. 2008), and this post-collisional magmatism is associated with many porphyry deposits across the north of Turkey, including the Muratdere deposit. It is thought that this magmatism was particularly fertile due to upwelling of asthenospheric mantle, which caused partial melting of lithosphere previously modified by subduction (Altunkaynak & Dilek 2006; Altunkaynak 2007; Sarıfakioğlu et al. 2013). Post-collisional extension and collapse meant that subsequent magmatism was more localised and alkaline (Akay 2009; Kuscu 2016).

The Muratdere deposit lies within the Tavşanlı Zone, south of the IAESZ; a blueschist sequence overlain by a late Cretaceous accretionary complex (Okay 2008, figure 6). Ophiolite nappes are present along the IAESZ, preserving mafic-ultramafic rocks, which are remnants of oceanic lithosphere; and ophiolitic melange, which comprises oceanic and continental fragments (Uysal et

al. 2009). These ophiolites have suprasubduction zone-type characteristics (Pearce et al. 1984; Robertson 2002) and formed before island-arc formation during the Late Cretaceous (Robertson 2002). Muratdere is hosted by granodioritic bodies intruded into an extension of the Dağküplü ophiolite, within the Eskişehir ophiolite group (Uysal et al. 2009; Sarıfakıoğlu et al. 2010). The Eskişehir ophiolite group is a 1500 to 4500 m thick sequence of dismembered peridotite tectonite and mafic cumulates, comprising an incomplete and inverted ophiolite sequence (Uysal et al. 2009). The Dağküplü section includes mantle peridotites, gabbroic cumulates, diabase dykes and amphibolite facies metamorphic sole rocks (Okay 2008; Sarıfakıoğlu et al. 2010).

These ophiolitic units are intruded by an E–W trending series of Eocene granitoids 400 km long and 60 km wide, with ages of 54–48 Ma (Harris et al. 1986; Ataman 1972; Bingöl et al. 1982; Delaloye & Bingöl 2000; Altunkaynak 2007; Okay 2008). These range in composition from diorite and granodiorite to syenite. The volcanic equivalents are not preserved in the area. The plutons are commonly associated with granodiorite porphyry sheets with compositional zoning from core to edge (Altunkaynak 2007; Okay 2008). The early Eocene magmatism in this region is interpreted to be a result of extension, following the exhumation of thickened crust after final suturing of the Eurasian and Afro-Arabian plates in ~52 Ma (Kuscu 2016).

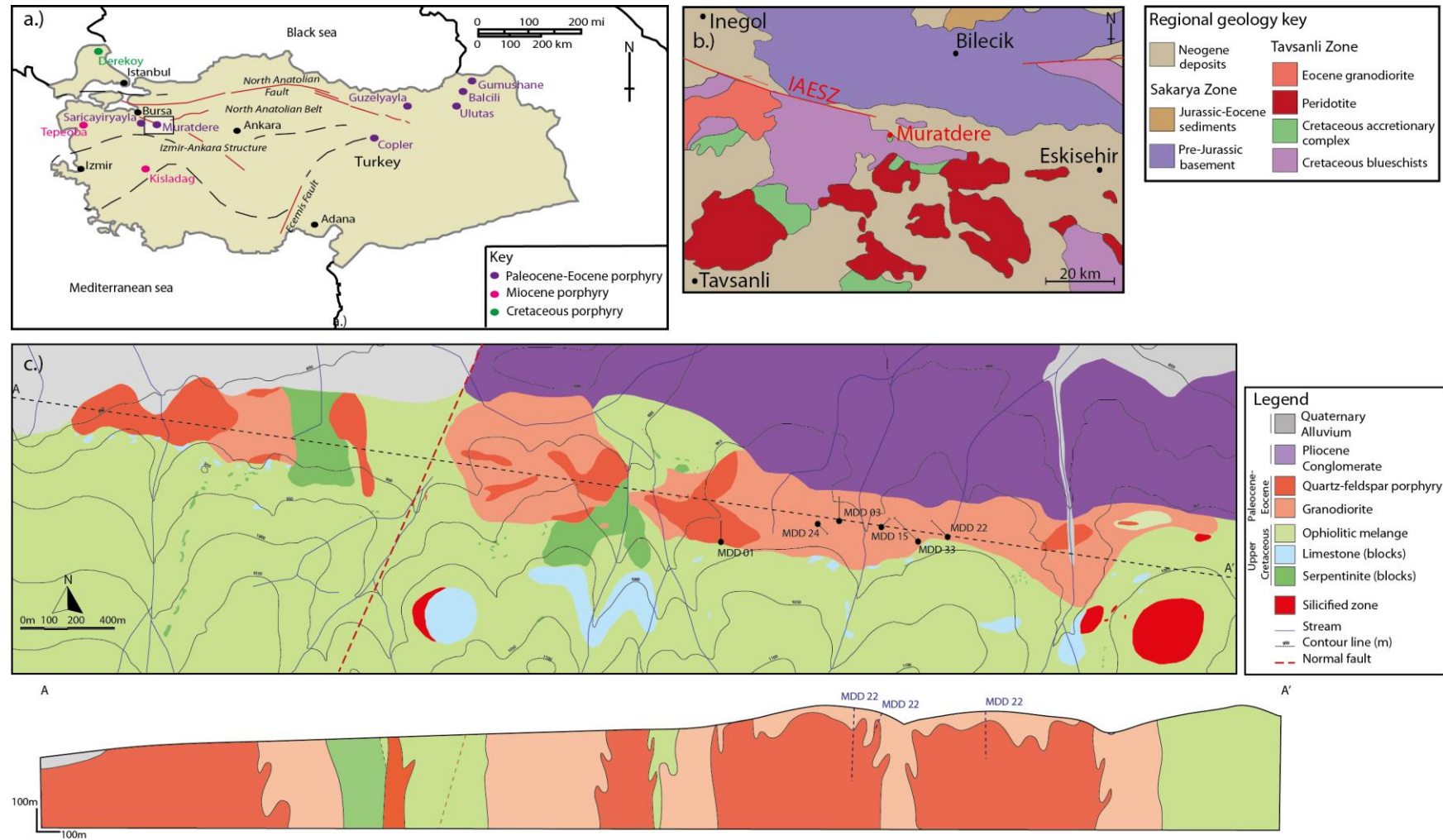


Figure 6: a.) Generalised map of Turkey, highlighting local deposits and regional structural features. b.) Map showing regional geology of the area around Muratdere (after Okay & Tüysüz 1999), outlined on figure a.) by the black rectangle. c.) Geological map and cross section of deposit showing drill hole locations. Interpretive cross section drawn from logging performed during this project and company data.



### 3.3 Deposit geology

The Muratdere Cu-Mo deposit is hosted by a suite of E–W striking granitic intrusions, with a strike length of 4 km and an average width of 400 m (figure 6). The exact age of the plutons is not known. However, they are inferred to be Eocene in age due to their petrological similarity and spatial correlation with other E–W trending granitoids in the region (Altunkaynak 2007; Yigit 2009). The intrusions are hosted within an ophiolitic melange which comprises peridotite lenses, gabbro dykes, gabbro cumulates and limestone blocks, all of which have been metamorphosed to greenschist facies. Highly serpentinised peridotite is observed at the bottom of drill hole MDD 03 (from ~300m), which is situated at the periphery of one of the intrusions.

A WNW trending post-Pliocene active normal fault zone, the Eskisehir Fault Zone, which post-dates the mineralisation runs ~20 km to the south-east of Muratdere (Ocakoglu, 2007). The deposit is situated within the Thrace-Eskisehir fault zone, a NW-SE trending active dextral strike-slip fault (Sakinç et al. 1999) and is cross-cut by a series of E-W trending faults. In drill core, these occur as breccia zones up to 3 m thick and at the surface they are seen as small scale faults with a typical orientation of WSW, dipping approximately 60° to the east and throw of 0.7-1.5 m. A large scale N-S trending normal fault bisects the deposit, down throwing it to the west.

The earliest intrusive phase at Muratdere is a granodiorite exposed as several discrete bodies at the surface, with diameters ranging from 200 m to 2.3 km, and with a minimum vertical extent of 300 m. The granodiorite is cross-cut by a quartz-feldspar porphyry unit, which consists of phenocrystic quartz, plagioclase feldspar and minor biotite embedded in a quartzofeldspathic groundmass. The quartz feldspar porphyry intrudes the granodiorite as branching vertical pipe-like bodies, with diameters ranging from 50 m to 400 m and a minimum depth of 300 m (figures 6 and 7, appendix A4.1). The drill holes chosen for analysis in this paper are situated within the two main quartz feldspar porphyry pipes to the east of the normal fault (figure 6).

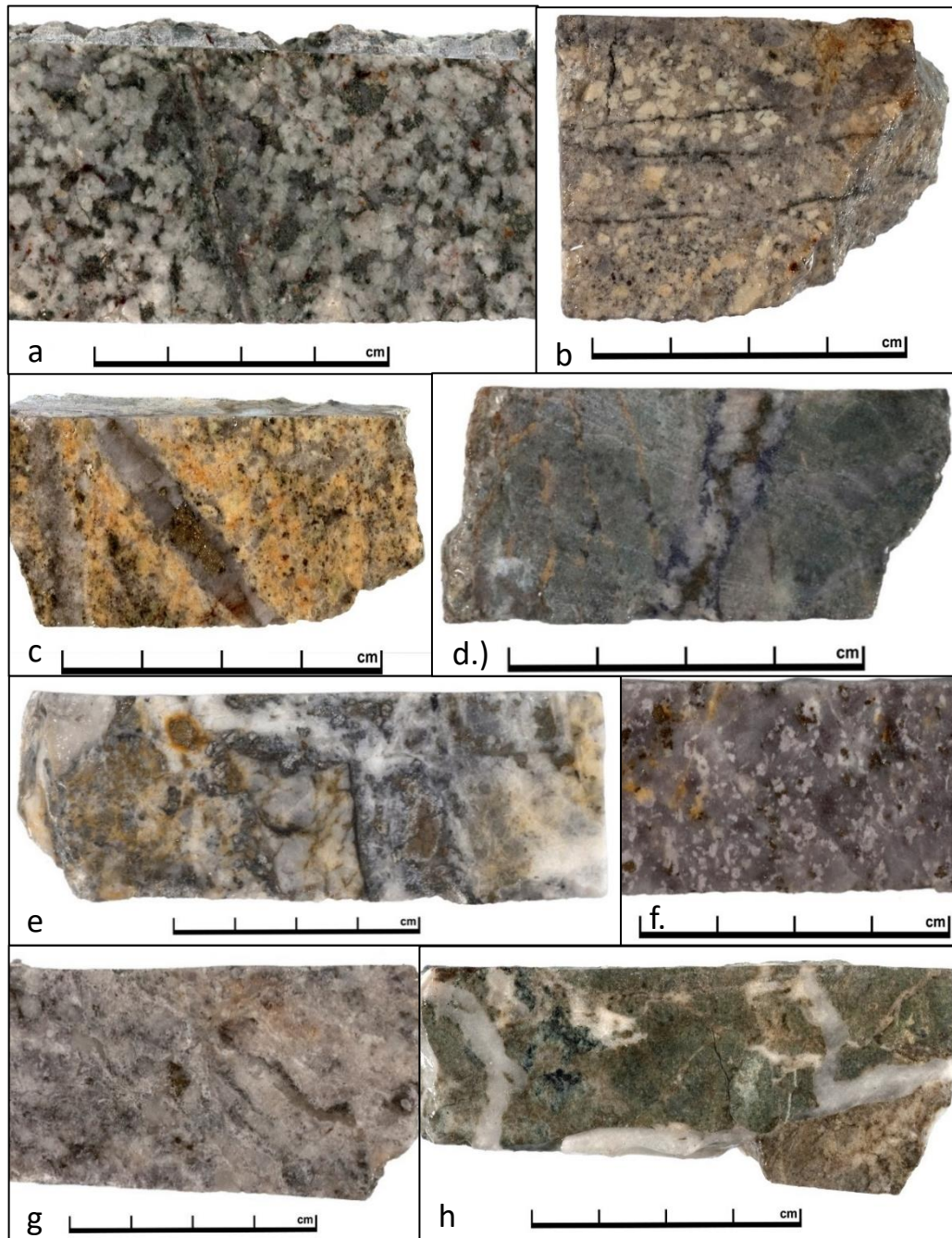


Figure 7: Sections of drill core showing the main lithologies, veinsets and alteration phases. a.) Granodiorite unit, crosscut by V4 vein with associated propylitic alteration, including hematite. b.) Quartz-feldspar porphyry unit showing potassic alteration, containing 'micro-fracture hosted' disseminated molybdenite and chalcopyrite (very small) and crosscut by biotite-magnetite veinlets. c.) V2 vein with pyrite-chalcopyrite centre. Associated with intense potassic alteration, and minor propylitic overprint seen here as epidote alteration of feldspar. d.) V3 vein with chalcopyrite in centre and molybdenite concentrated at vein margins. Host rock shows strong propylitic alteration with chlorite and orange anhydrite veinlets. e.) V5 showing altered sphalerite crystals, pyrite, chalcopyrite and galena in a quartz-barite groundmass. f.) Silicified quartz-feldspar porphyry with disseminated chalcopyrite and molybdenite. g.) V6 and V7 anhydrite veining associated with advanced argillic alteration – groundmass replaced by kaolinite-pyrophyllite. h.) V6 anhydrite veining associates with intense propylitic overprint of previously potassically altered quartz-feldspar porphyry.

### 3.3.1 Alteration & mineralisation

32 samples were made into polished thin sections and analysed using both reflective and transmitted light microscopy in order to identify the main mineralising phases. SEM was used to determine detailed sulphide paragenesis and to identify unknown phases. XRD analysis was performed on 38 bulk rock samples to determine the alteration mineralogy, and detailed XRD clay mineral analysis was performed on 8 samples (electronic appendix B).

Within the core of the Muratdere deposit, which is exposed on the eastern side of the normal fault, both intrusive phases have been subjected to extensive potassic alteration, as well as silicification. Detailed logs of the distribution of alteration minerals, from XRD analyses, with respect to intrusive phase and sulphide mineralogy are given in appendix A4.1. Potassic alteration is characterised by secondary potassium feldspar replacement of both phenocrystic and groundmass feldspars, often causing complete replacement of the core (figure 7). Magnetite is also present within the potassic alteration, both disseminated in the groundmass and along thin veinlets. Secondary hydrothermal biotite replacement also occurs in the granodiorite phase, with fine grained biotite overgrowing primary biotite. Propylitic alteration occurs towards the base of the drill holes, with a minimum depth of 95 m, and a maximum depth of 290 m, characterised by chlorite, epidote, dolomite and pyrite. Drill core intervals which contain propylitic alteration have lower Au assay results than those with potassic alteration. Chlorite overprints some of the potassically altered zones in the centre of the deposit, replacing biotite phenocrysts. The potassic core of the deposit is surrounded and partially overprinted by areas of intense chlorite-sericite alteration, characterised by the presence of smectite, illite and sericite, and commonly associated with gypsum and hematite. These alteration minerals replace feldspar phenocrysts. Secondary quartz alteration is also present as areas of silicification up to 12 m thick, where the entire drill core is replaced by quartz, commonly associated with gypsum or barite. An advanced argillic overprint is observed around fractures and faults, with kaolinite, diaspore, pyrophyllite and bohmite detected in the groundmass of fault breccias by XRD. The altered peridotite at the base of drill hole MDD 03 contains dolomite, talc, lizardite and sepiolite.

The initial mineralisation within the quartz-feldspar porphyry is micro-fracture hosted pyrite, chalcopyrite, and molybdenite, which occurs within the zones of potassic alteration. These sulphides are anhedral with rounded morphologies. The pyrite and chalcopyrite are intergrown, rarely with microscopic galena grains located on boundaries, whereas the molybdenites are spherical, and are commonly associated with chalcopyrite. Interstitial pyrite-chalcopyrite assemblages are also present, commonly with small inclusions of the host-rock minerals, including rutile and zircon.

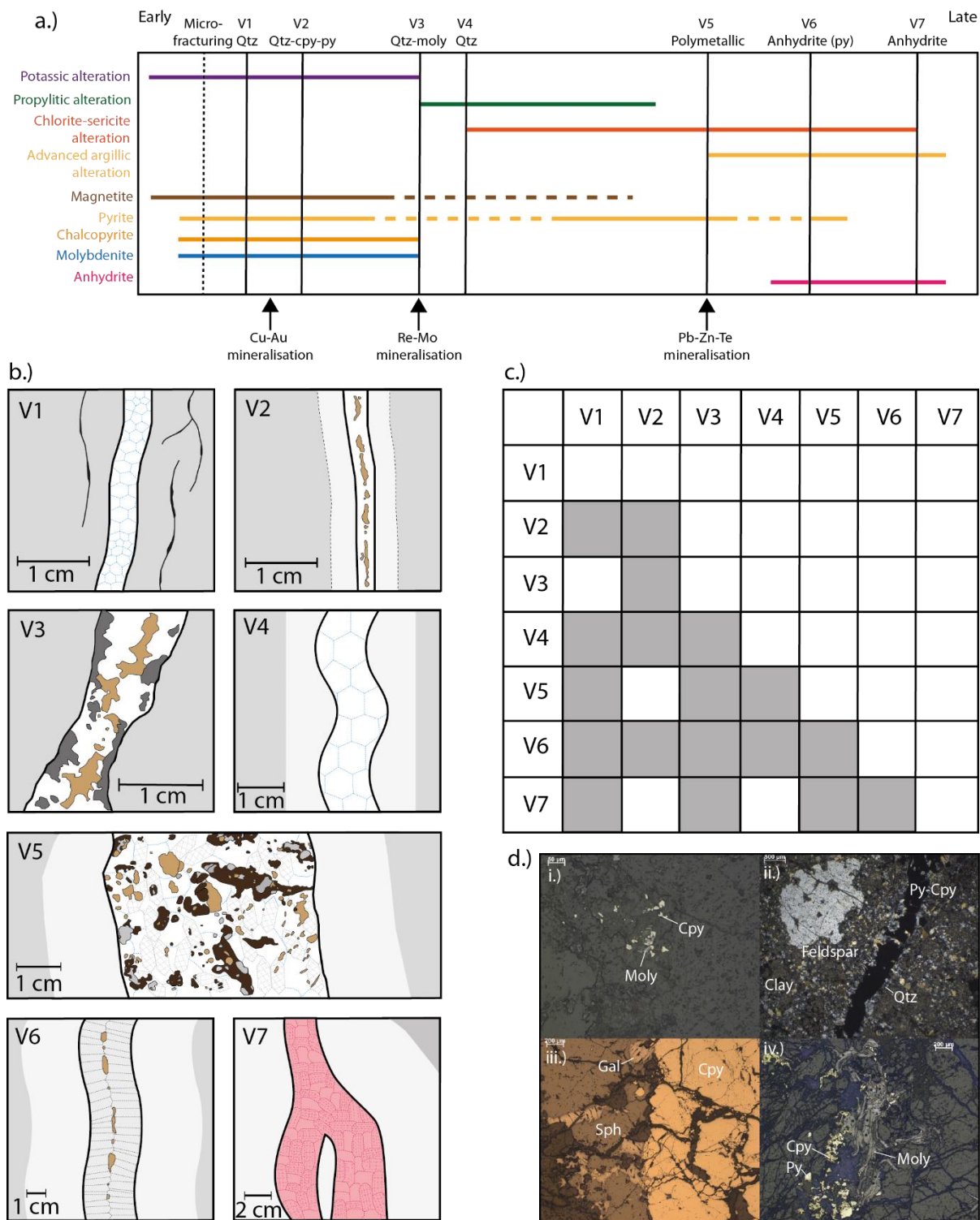


Figure 8: Paragenetic diagram showing: a.) The relative order of mineralizing and alteration events in the Muratdere deposit, with the main mineralisation events highlighted. b.) A schematic drawing showing the main features of each veinset. Blue dotted lines represent quartz crystal morphology, grey and pink dotted lines represent grey and pink anhydrite crystals respectively. Gold represents chalcopyrite, yellow – pyrite, dark grey - molybdenite, light grey – galena and brown – sphalerite. Black veinlets next to V1 represent biotite veinlets, while light grey halos around veins represents an alteration selvage. c.) Paragenetic diagram showing the crosscutting relationships of veinsets. d.) Photomicrographs of the main phases of mineralisation. i.) Reflective light microscopy of micro-fracture hosted sulphides, the earliest mineralizing event. ii.) Transmitted light microscopy of V2 event showing associated alteration. iii.) Reflective light microscopy of V3 showing bladed molybdenite and chalcopyrite. iv.) Reflective light microscopy of V5 event showing sulphide assemblage. Abbreviations: cpy = chalcopyrite, py = pyrite, gal = galena, sph = sphalerite, moly = molybdenite & Qtz = quartz.

The remainder of the mineralisation at Muratdere is associated with a series of crosscutting vein sets. The relative timings of these veinsets have been established by the crosscutting relationships shown in figure 8.

Veinset, V1, comprises microcrystalline silica with an interlocking texture. The veins are 2-10 mm wide, with an average width of 8 mm, and are only found in regions of potassic alteration. These are crosscut by a pyrite and chalcopyrite bearing veinset, V2. These veins are straight to wavy, 5-30 mm in width, average 15 mm, with the sulphides hosted in a central suture and may be considered as A veins (Sillitoe 2010). They commonly have a secondary potassium feldspar selvage, and are found in areas of the core showing potassic alteration.

The third veinset (V3) is also sulphide-bearing, crosscuts V2 and is distinct in that it contains molybdenite as well as pyrite and chalcopyrite. These veins are irregular with a width range of 5 – 30 mm, and an average width of 15 mm, with equigranular quartz crystals. These veins have not developed a vein selvage and occur in potassically altered areas of the core and areas with a mild propylitic and chlorite-sericite overprint. The sulphides are typically situated towards the centre of the vein although in some instances the molybdenite is concentrated along the vein margins. Pyrite and chalcopyrite, when present, commonly enclose molybdenite, indicating they are a later phase in the vein formation. The molybdenite within the V3 veins has a very distinctive bladed morphology in comparison to the micro fracture-hosted molybdenite, that is more rounded (figures 8 and 9). Locally, microscopic crystals of sphalerite are present between the blades of molybdenite (figure 9).

Veinset (V4) consists of equigranular quartz veins, that cross cut all previous veinsets. The V4 veins have sinuous margins and are 5-15 mm wide, with an average of 10 mm. They are found across the deposit and have a clay (illite-smectite) selvage, showing them to be associated with chlorite-sericite alteration (Sillitoe 2010).

Veinset V5 is a polymetallic vein set which crosscuts V1, V3 and V4. These veins are irregular, typically 4-12 cm wide, with an average width of 5 cm. The veins comprise large interlocking quartz and barite crystals, with intergrown sphalerite-galena-pyrite-chalcopyrite assemblages, along with rare molybdenite and pyrargite, distributed throughout the vein. The V5 veins have a clay selvage and are associated with propylitic and chlorite sericite alteration as well as extensive silicification. Veinset V6 comprises grey gypsum-pyrite, which cross cut V1-V5, as well as locally developed fault breccias. These veins are sinuous, ranging from 1 to 26 cm wide with an average of 8 cm, and have a kaolinite-pyrophyllite selvage. The veins comprise subhedral syntaxial gypsum crystals perpendicular to the vein margins, with pyrite in a central suture. They are commonly



observed in areas of intense advanced argillic alteration, as well as being associated with propylitic alteration.

The final vein set (V7) consists of pink gypsum veins, which cross cut veinsets V1, V3, V5, V6 and fault breccias. This veinset is irregular, commonly branching, and ranges from 5 cm to 45 cm in width. These veins consist of anhedral gypsum crystals and have a kaolinite-pyrophyllite selvage. Both V6 and V7 are commonly associated with dolomite.

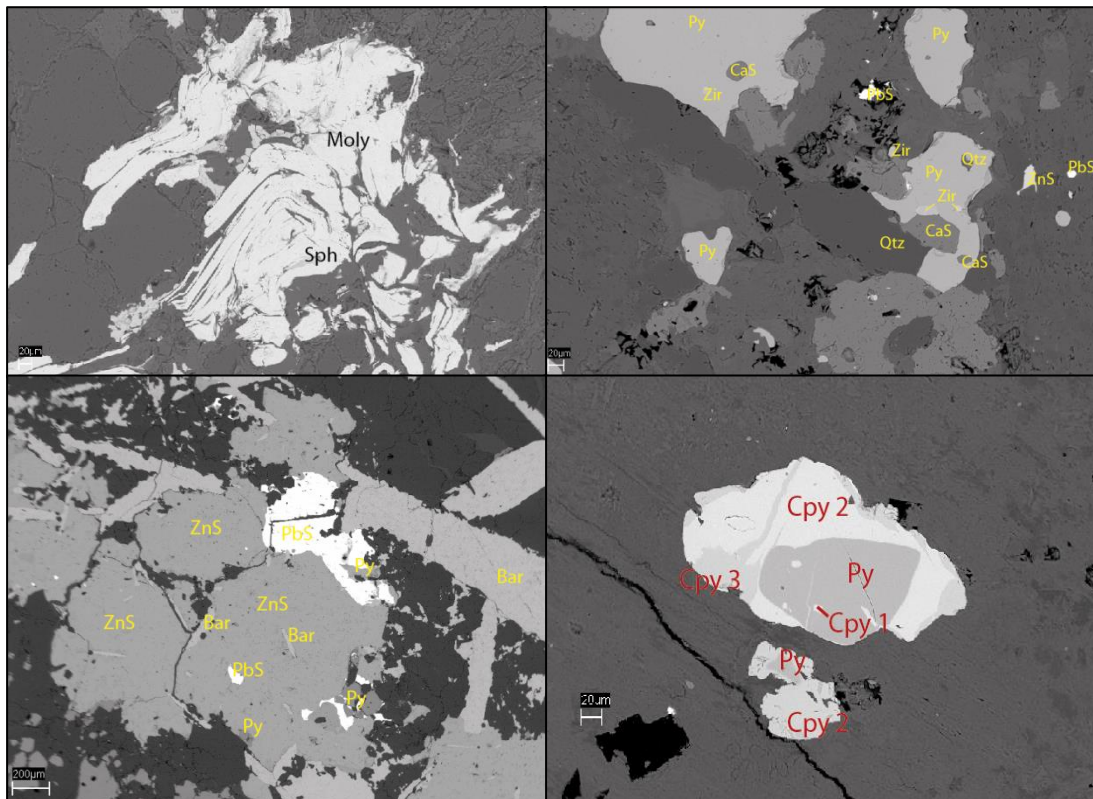


Figure 9: a) SEM image of bladed molybdenite in V3. b) SEM image of disseminated pyrite showing the phases included within the pyrites, including zircons. c) SEM image of V5 sulphide assemblage showing the relationship between the main sulphides and the barite. d) SEM image of sulphide assemblage in V2 illustrating the three generations of chalcopyrite present. Abbreviations: Moly = molybdenite, Sph = sphalerite, Zir = zircon, Py = pyrite, ZnS = sphalerite, Qtz = quartz, PbS = galena, Cpy = chalcopyrite.

### 3.4 Analytical results

#### 3.4.1 Whole rock assay data

Whole rock assay data for the Muratdere deposit (provided by Lodos Madencilik) shows maximum Re values of up to 2.37 ppm, Au values of up to 1.35 ppm, Mo concentrations of up to 1120 ppm and Cu contents of up to 11700 ppm in the mineralised host rocks; the deposit has a whole rock assay Cu/Mo of 0.05 and Re/Mo of 0.003. Whole rock assay data from sections of drill core containing only one type of vein (where available) were compared with sections with no visible mineralisation in order to estimate the effect of the different veinsets on metal content. When plotted on a Cu-Au-Re triplot (figure 10) the assay data from V2 plots between the quartz feldspar porphyry data and that for V3, while V3 plots towards the data from the altered peridotite country rock. V5 plots in a different area of the triplot, showing a very different proportion of metals, with much higher Au. As well as being enriched in Re Muratdere also has an average Te concentration of 0.5 ppm, which is a significant enrichment. This appears to be associated with the V5 veinset, as sections of core containing V5 veins have whole rock assay Te concentrations of up to 3.45 ppm.

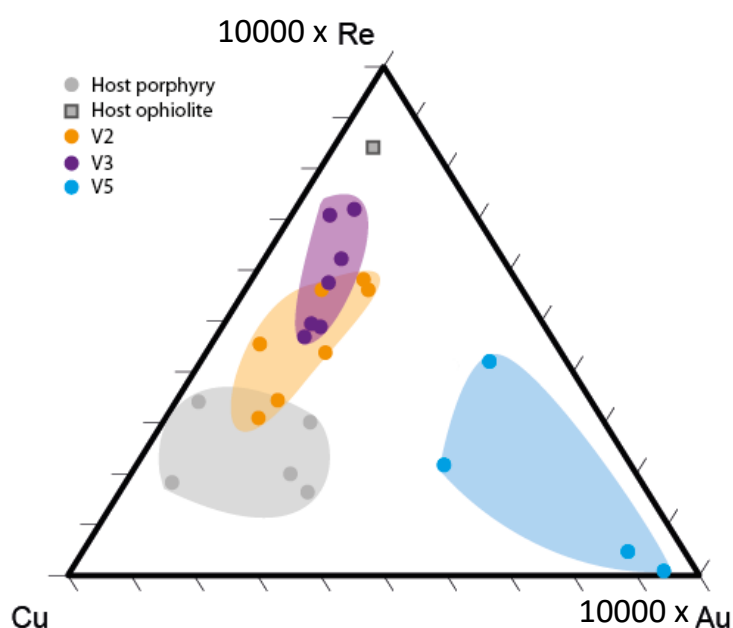


Figure 10: Triplot of Re, Cu and Au values from assay data, along with assay values of host porphyry and ophiolitic country rock without mineralisation. Re and Au values have been multiplied by 10000 in order to normalise them.

## 3.4.2 Composition of molybdenites

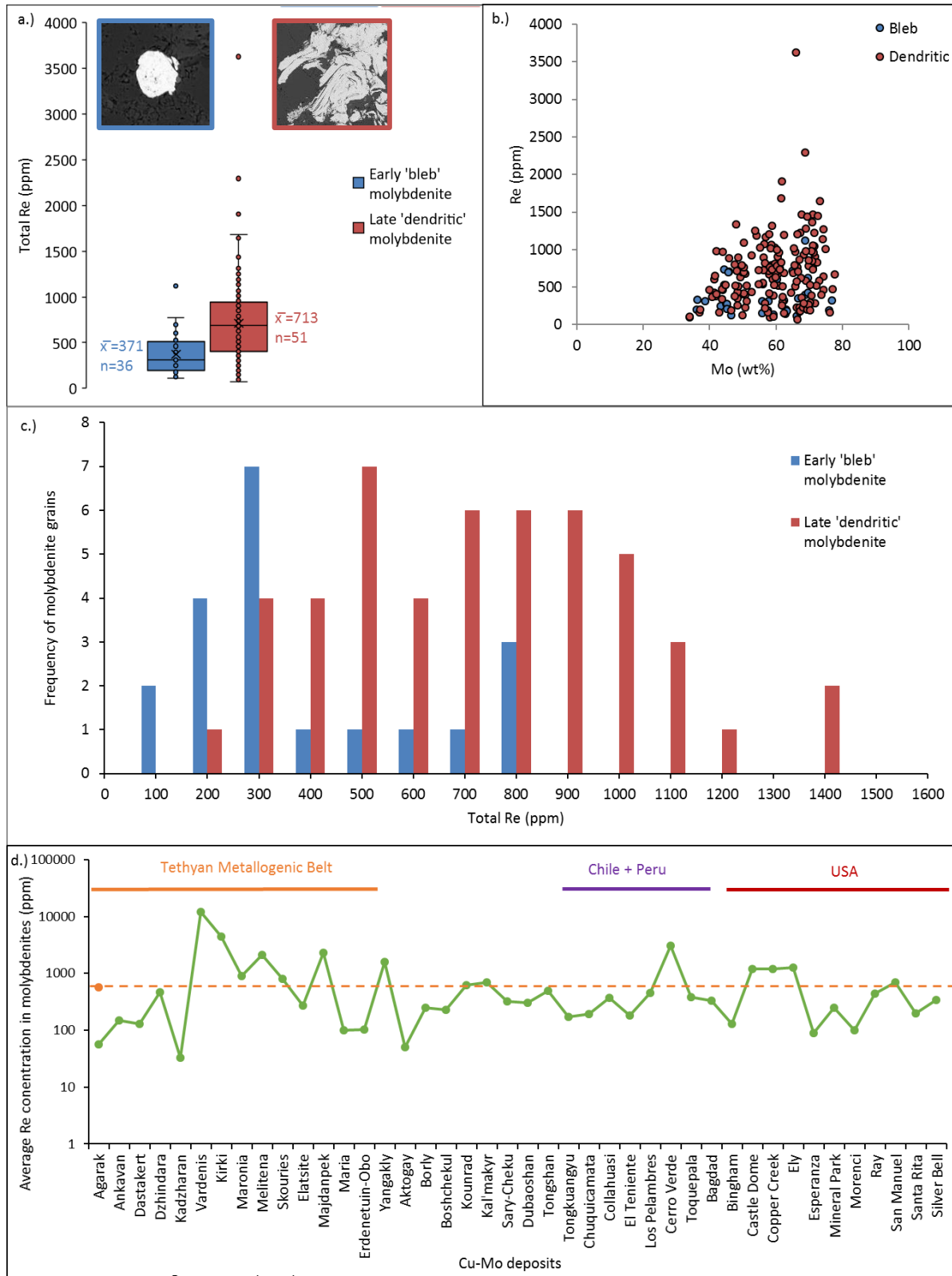


Figure 11: a.) Box plot showing the results of individual LA-ICP-MS analyses for Re in the two molybdenite generations representing the mean, quartiles and outliers. The two morphologies of molybdenite are shown in the inset. b.) Molybdenum and rhenium concentrations from all molybdenite analyses plotted against each other. c.) Histogram showing the results of average Re concentration in molybdenite grains. d.) Plot showing the average concentration of Re in molybdenite of Cu-Mo porphyries globally, compared to the average concentration of Re in molybdenite in Muratdere (dashed orange line). The different metallogenic provinces are highlighted (data from Berzina et al. 2005; Singer et al. 2005; Grabezhev 2007; Voudouris et al. 2009; Grabezhev & Voudouris 2014).



Two distinct settings of molybdenite in Muratdere (see figures 8, 9 and 11), the early micro fracture hosted, spherical molybdenite and the later V3 vein hosted bladed molybdenite, were analysed for their trace element contents using LA-ICP-MS (see chapter 2 for method). This method was chosen as the two generations are often found within the same sample, and the micro fracture hosted molybdenite is very small and often intergrown with and included in other sulphides, making separation of pure molybdenite of a single generation very difficult. Four samples, hosting both molybdenite generations, were chosen for analysis. 67 molybdenite crystals were analysed – 12 micro-fracture hosted molybdenites and 57 vein hosted molybdenites, with a total of 200 spot analyses performed using the methods detailed in chapter 2.

The molybdenites contain an average Mo content of 57.55 wt%, and average trace element concentrations of 676 ppm Re, 7.98 ppm Ag, 5.13 ppm W, 0.86 ppm Pt and 0.51 ppm Au (appendix A2.1). Re and Mo are heterogenous across the crystals measured, with total Mo measurements having a standard deviation of 8.57 wt%, and total Re measurements having a standard deviation of 283 ppm. Individual crystals had multiple 50µm spot analyses taken from them (n=1 to 27), with the aim being to ablate as much of the visible surface area of the crystal as possible in order to allow average Re concentrations to be calculated, and in order to quantify this heterogeneity. Average Re concentrations calculated for individual molybdenites have standard deviations ranging between 7 and 393 ppm (A 2.1).

The early spherical, micro fracture hosted molybdenites within the quartz porphyry have a mean Re content of 371 +/- 10 ppm, with a minimum of 114 ppm and a maximum of 1118 ppm (n=37). In contrast the later, bladed, vein hosted molybdenites in V3 have a mean Re content of 713 +/-20 ppm, with a minimum of 72 ppm and a maximum of 3627 ppm (n=165, figure 11). An unpaired t-test shows that the two populations of Re concentrations – those from V3 hosted molybdenite and those from micro-fracture hosted molybdenite – have significantly different mean rhenium contents at a confidence level >99% ( $p = 3.8 \times 10^{-7}$ ).

EPMA was used to determine the distribution of Re in three of the dendritic, V3 hosted molybdenite crystals analysed with LA-ICP-MS (figure 12). They show that Re is distributed heterogeneously throughout the crystals, with alternating Re-rich and Re-poor zones. This produces oscillatory zoning, similar to that observed in other porphyry deposits (Ciobanu et al. 2013; Voudouris et al. 2009; Grabezhev & Voudouris 2014). The zoning is best developed parallel to the cleavage, and is well preserved, not showing any evidence of re-mobilisation. The high Re zones are 10 to 20 µm thick, and comprise <5 to 10% of the crystal surface area. One sample also contains 'growth ring' zoning at the edge of the crystal (discussed further below), containing

zones with higher Re concentration than the oscillatory zoning (figure 12). The Re enriched layers do not correspond to a depletion in molybdenum, which is fairly homogenous across the crystals. This is also seen in the LA-ICP-MS data, where Re and Mo concentrations from the same ablation spots do not show any correlation, with an  $R^2$  value of 0.1.

A bulk sample of both generations of molybdenite were analysed using XRD in order to determine their polytype. Both the early, Re-poor, micro-fracture hosted molybdenite and the later, Re-rich, vein hosted molybdenite are the 2H polytype.

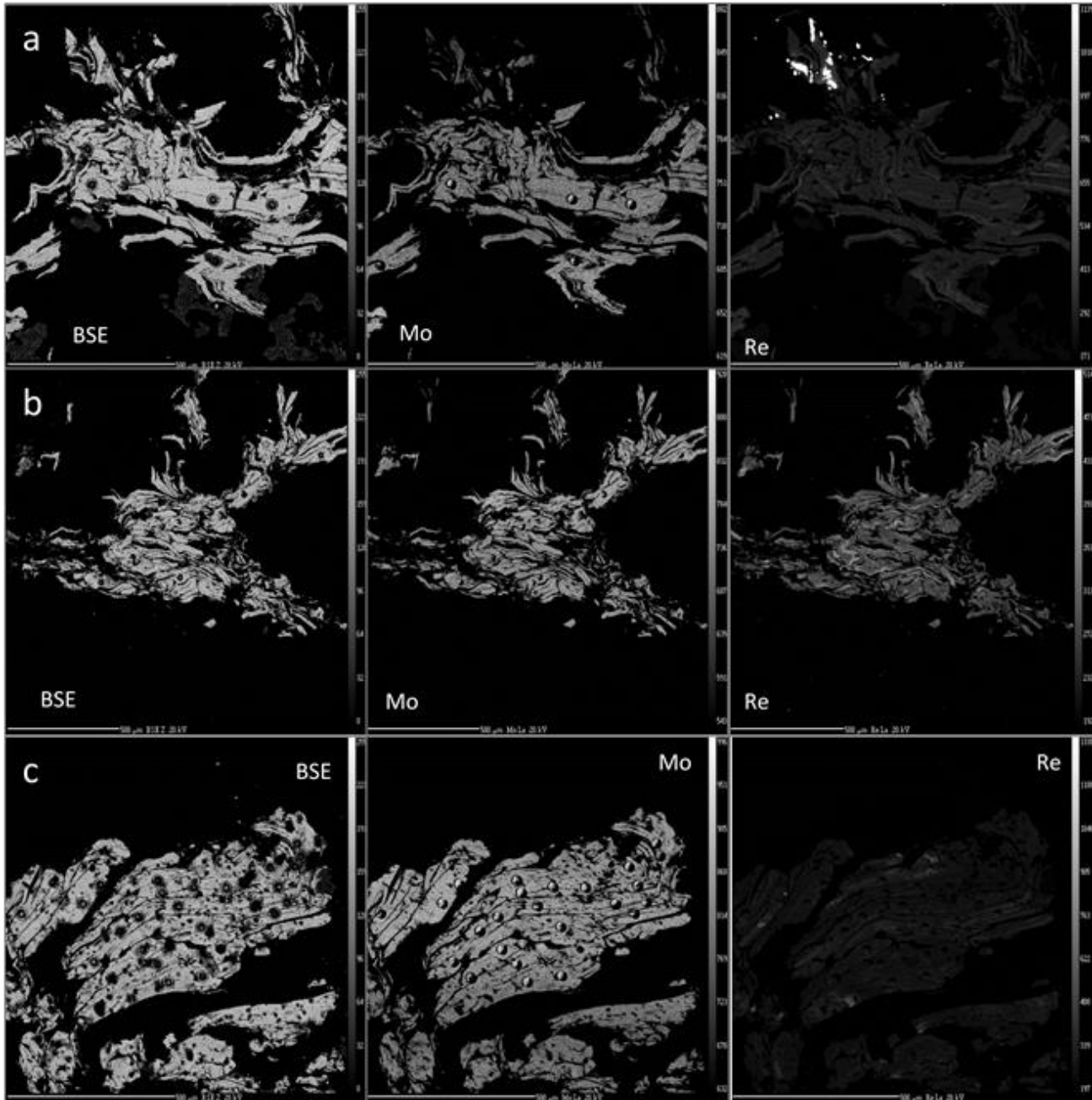


Figure 12: EPMA element maps of molybdenite crystals from Muratdere showing (from left to right) the BSE image, a Mo map and a Re map for a.) Sample MDD 22 84.7a; b.) Sample MDD 24 84.7b; c.) Sample MDD 33 155.0. The brightness in the Mo and Re images corresponds to the concentration of the element, with bright patches showing high concentration. The very bright spots in the Re image from sample a.) are sphalerite crystals, as Zn can interfere with Re in EPMA. The dark circles seen on the samples were made by LA-ICP-MS analysis, showing the origin of the heterogenous Re concentration values produced.

### 3.4.3 Platinum group element (PGE) analysis

Whole rock data shows that Muratdere is relatively enriched in moderately chalcophile elements Cu and Re, as well as chalcophile elements Au and Te. These are often found associated with platinum group elements (PGE) in ore deposits, and so 16 whole rock samples representing the different lithologies and vein types were analysed for PGE by nickel sulphide fire assay at the University of Cardiff, using the methods outlined in chapter 2. The sample suite also included an altered peridotite from the bottom of drill hole MDD 03 which represents the surrounding ophiolitic country rock in order to compare PGE profiles between the deposit and the ophiolite. The average PGE contents for the samples from within the deposit are: 0.03 ppb Os, 0.04 Ir, 0.15 ppb Ir, 0.15 ppb Ru, 0.14 ppb Rh, 1.91 ppb Pt, 0.68 ppb Pd, 183.93 ppb Au and 222.89 ppb Re. These contrast with the altered peridotite sample, which has values of: 1.15 ppb Os, 1.78 ppb Ir, 2.72 ppb Ru, 0.58 ppb Rh, 3.35 ppb Pt, 1.07 ppb Pd, 3.33 ppb Au and 0.25 ppb Re (appendix A2.2). The samples within the deposit show values below mantle compositions, except for Pt and Pd which are at approximately mantle values, and Au which has up to 1000 times mantle levels. Samples containing the V3 veinset contain more Pt than the other samples, and the country rock sample (serpentinised peridotite) has PGE values just below mantle values, with slightly increased Au and slightly decreased Pt and Pd.

### 3.4.4 Stable isotopes

Table 9: Summary of stable isotope results – averages of the results for each veinset.

Veinset	$\delta^{18}\text{O}_{\text{SMOW}}$ Quartz	Approximate temperature	$\delta^{18}\text{O}_{\text{SMOW}}$ Fluid	$\delta\text{D}$	$\delta^{34}\text{S}_{\text{CDT}}$ sulphide	$\delta^{34}\text{S}_{\text{CDT}}$ sulphate
Micro-fracture	8.2	350	2.6		2.4	
V1	9.6	320	3.3	-73		
V2	8.5	320	2.3		4.4	
V3	8.1	320	1.9	-73	7.4	
V4	9.6	315	3.1	-74	0.3	
V5	11.4	250	2.4			17.7
V6						18.2
V7						16.1

#### 3.4.4.1 Sulphur isotopes

35 picked sulphide samples were analysed at SUERC, using the methods outlined in chapter 2, representing the different mineralising stages in Muratdere, and 12 sulphate samples were analysed, comprising barite from V5 and gypsum from V6 and V7. The Muratdere deposit  $\delta^{34}\text{S}_{\text{CDT}}$  values in sulphides range between -5.5 ‰ and +8.9 ‰, with an average of +2 ‰. The  $\delta^{34}\text{S}_{\text{CDT}}$

values for sulphates range between +12.6‰ and +20.3‰ with an average of +17.5‰ (figure 13, table 9, appendix A2.3).

Discriminating sulphide  $\delta^{34}\text{S}$  values using the mineral and vein paragenesis established for the deposit shows that the micro fracture hosted sulphides (cpy-py-moly) have a  $\delta^{34}\text{S}_{\text{CDT}}$  range of -2.2 ‰ to +4.6 ‰, with a mean of +2.6 ‰, whereas the earliest mineralised vein set, (V2) has a  $\delta^{34}\text{S}_{\text{CDT}}$  of sulphides (py-cpy) of +1.9 ‰ to +6.3 ‰, with a mean of +4.4 ‰. Sulphides (cpy-py-mo) in the V3 veins have a  $\delta^{34}\text{S}$  range of +5.6 ‰ to +8.9 ‰ with a mean of +7.5 ‰. These data suggest a systematic increase in  $\delta^{34}\text{S}$  values with progressively younger generations of veins. However, this trend is reversed for the polymetallic veinset, V5, which has sulphide (py-cpy-gal-sph)  $\delta^{34}\text{S}$  values between -5.5 ‰ and +3.11 ‰, with a mean of -0.4 ‰, showing a relative decrease. Discriminating the sulphate results by veinset shows that the barite in V5 has  $\delta^{34}\text{S}$  values of +16.6 ‰ to +19.2 ‰ with a mean of +17.6 ‰. V6, the first gypsum veinset has gypsum  $\delta^{34}\text{S}$  values of +12.6 ‰ to +18.4 ‰ with a mean of +15.5 ‰ and V7, the final gypsum veinset has  $\delta^{34}\text{S}$  values of +18.7 ‰ to +20.3 ‰ with a mean of +19.4 ‰ (figure 13, table 9).

#### 3.4.4.2 Oxygen and hydrogen Isotopes

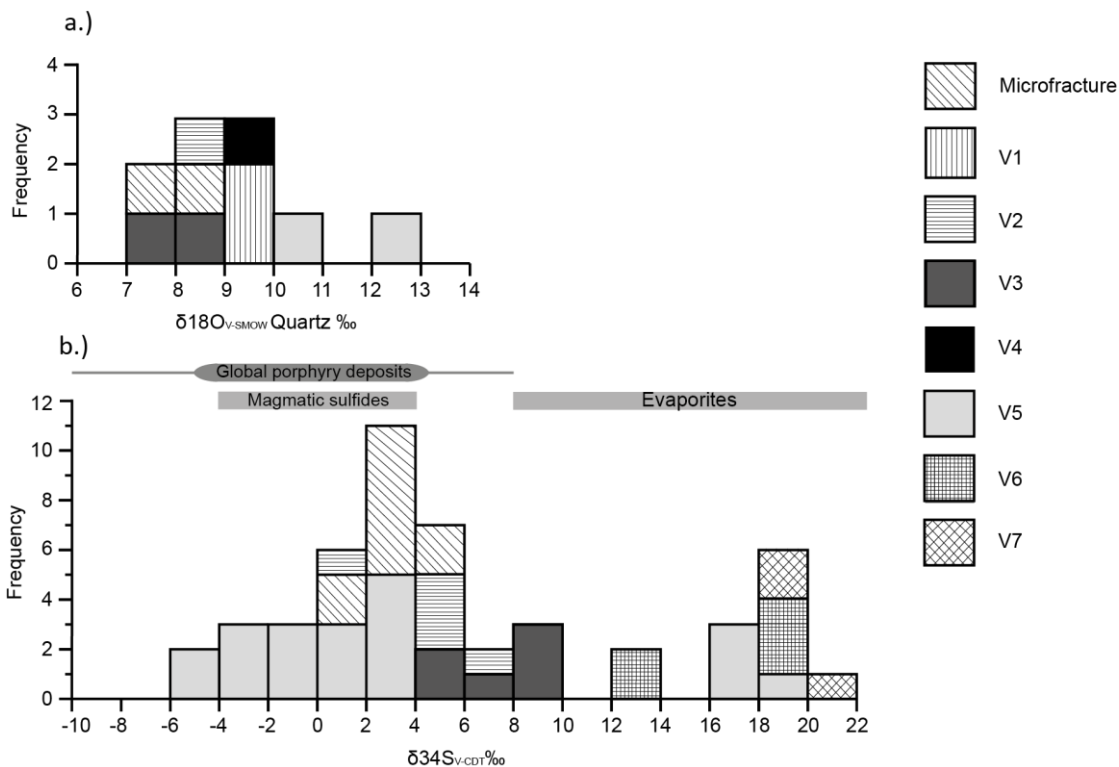


Figure 13: a.) Histogram of  $\delta^{18}\text{O}_{\text{SMOW}}$  quartz results, discriminated by veinset. b.) Histogram of  $\delta^{34}\text{S}_{\text{CDT}}$  results for sulphides (micro-fracture, V2, V3, V5) and sulphates (V5 > 12‰, V6, V7). Global porphyry sulphide values (Hattori & Keith 2001), magmatic sulphide values and evaporite sulphate values (Ohmoto 1972) are included for comparison purposes.

The oxygen isotope values for Muratdere range from +7.5 ‰ to +12.3 ‰, with a mean of +9.2 ‰. V1-4 show a limited range of  $\delta^{18}\text{O}$  values from +7.5 ‰ to +9.6 ‰, with a mean of +8.7 ‰. V5

however has  $\delta^{18}\text{O}$  values ranging from +10.4 ‰ to +12.3 ‰, with a mean of +11.4 ‰ (table 9, figure 13). Hydrogen isotope values from Muratdere show a narrow range from -70 ‰ to -75 ‰ with a mean of -73 ‰ (table 9).

### 3.4.5 Fluid inclusions

A set of 6 vein samples representing all the main vein phases were prepared as doubly polished thin sections (~100  $\mu\text{m}$  thick). Only samples from V1-V4 were analysed, as the quartz V5 was too cloudy and opaque to view fluid inclusions. 200 inclusions were analysed using the methods outlined in chapter 2, of which 174 yielded useable data.

The fluid inclusion assemblages of veins V1, to V4 share common characteristics, with the same inclusion populations observed in each veinset (figure 14, table 10). There are three main types of inclusion present, which have been classified according to the classifications of Nash (1976) (figure 14). The first type are rare polyphase inclusions, containing 10 – 45% vapour, along with one or more halite crystals. These are classified as type III inclusions (Nash 1976), and do not show any microthermometric evidence of  $\text{CO}_2$ . The type III inclusions are observed as 6-12  $\mu\text{m}$ , average 8  $\mu\text{m}$ , isolated inclusions in the centre of quartz crystals, are commonly decrepitated and are not present in V4 samples. The second type consists of aqueous two phase inclusions 4-12  $\mu\text{m}$  in size, average of 7  $\mu\text{m}$ , with high vapour percentages ranging from 70-95%. As no evidence for  $\text{CO}_2$  was observed these are classified as type II inclusions (Nash 1976). They are found as isolated inclusions in the centre of quartz crystals, and as pseudo-secondary trails which appear to truncate at crystal boundaries, although as the quartz is commonly annealed it can be difficult to distinguish secondary from pseudo-secondary inclusions. Type II inclusions often show evidence of necking and decrepitation. The third type are aqueous two phase inclusions with a vapour percentage ranging from 10% to 40%, and sizes ranging from 4-14  $\mu\text{m}$ , average 7  $\mu\text{m}$ , and these have been classified as type I inclusions (Nash 1976). They are secondary, being observed in trails crossing crystal boundaries, and do not show evidence for the presence of  $\text{CO}_2$ .

A summary of the microthermometric results is shown in table 10, and a full data set is available in the electronic appendix B - 90 type I inclusions were analysed, 76 type II inclusions and 14 type III inclusions (figure 14, table 10, appendix B). Unfortunately, due to their rarity and frequent decrepitation it was difficult to analyse type III inclusions, hence the small population size. Due to the small size of the fluid inclusions first melting temperatures ( $T_{\text{FM}}^{\circ}\text{C}$ ) were difficult to determine, as were the final ice melting temperatures ( $T_{\text{mICE}}^{\circ}\text{C}$ ), although great care was taken to try and ensure accuracy. The equation of Sterner et al (1988) was used to calculate salinities of liquid-rich fluid inclusions from measuring ice-melting temperatures. No pressure corrections were made to

estimate formation temperatures ( $T_F$ ) from homogenisation temperatures ( $T_{HOM}$ ) as formation pressures were unknown. However, as pressures were probably 300 bars or less (Kelly & Rye 1979) pressure corrections are unlikely to yield corrections greater than 20°C.

The secondary type I inclusions are low temperature and low salinity. Type II inclusions are higher temperature, however the salinity is still low and 37 of the 76 inclusions analysed show homogenisation temperatures above the critical point for their salinity (Fuentevilla et al. 2012). This suggests that they have undergone necking, or have been heterogeneously trapped (Bodnar 2003a). Given that a large proportion of type II inclusions show evidence of necking and decrepitation when examined optically it is likely that they have undergone post-trapping modification and so care must be taken when interpreting data from this population. Type III inclusions are the highest temperature and salinity, however the salinities calculated are low for a porphyry environment (Wilkinson 2001), and all of the type III inclusions measured homogenise above the critical point for NaCl, showing post-entrapment modification to have occurred. This is supported by the fact that type III inclusions are commonly decrepitated.

*Table 10: Summary of fluid inclusion microthermometry results for the three types of fluid inclusion present in Muratdere.*

Inclusion type	n	$T_{FM}$ (°C)			$T_{m_{ICE}}$ (°C)			$T_{HOM}$ (°C)			Average salinity (wt% NaCl)
		Mode	Min	Max	Mode	Min	Max	Mean	Min	Max	
Type I	90	-13	-28	-8	-0.8	-7	-0.2	280	152	420	7.1
Type II	76	-15	-30	-12	-2.3	-8.3	-0.8	441	327	595	6.4
Type III	14	-15	-15	-13	-12.6	-16.2	-10.1	569	523	589	14.8

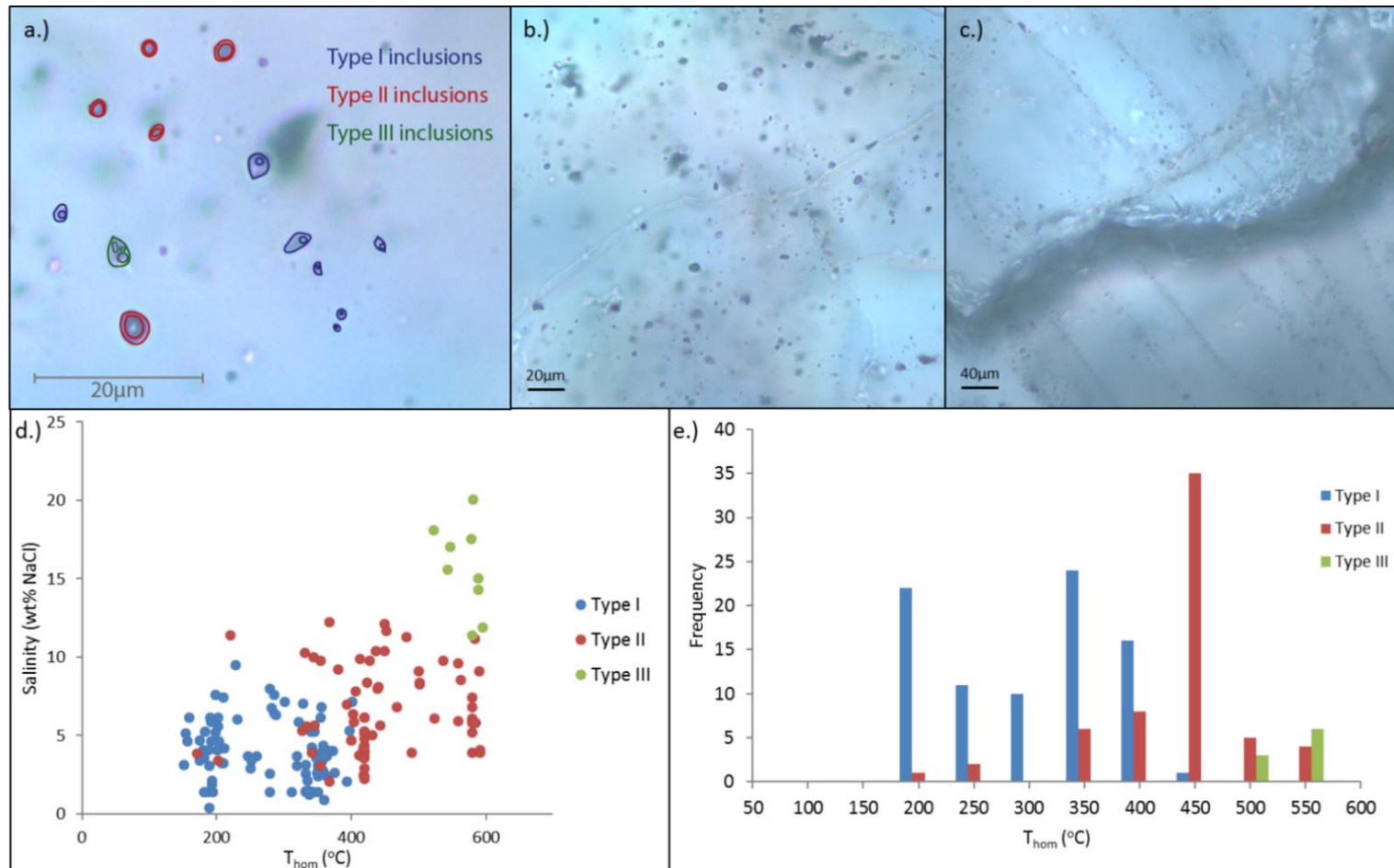


Figure 14: a.) Sketch of the three types of fluid inclusion present in Muratdere. b.) Photomicrograph of a typical fluid inclusion assemblage in Muratdere, illustrating the small size and large proportion of types I and II inclusions. c.) Secondary trails of type II inclusions cross a crystal boundary. d.) Graph showing salinity against homogenisation temperature for the three populations. Note the relatively low salinities for a porphyry deposit. e.) Histogram showing the homogenisation temperatures of the three inclusion type.

### 3.5 Discussion

The results outlined above allow a genetic model to be generated for the Muratdere deposit. This allows the comparison of Muratdere's genesis and features with those of other Re enriched Cu-Mo porphyries globally in order to examine the potential sources of Re enrichment. Given that Muratdere has two phases of molybdenite with different Re concentrations the features of these two molybdenite generations, and potential explanations for the difference in Re concentration seen are also discussed below.

#### 3.5.1 Fluid evolution of the Muratdere deposit

The Muratdere deposit was formed by several stages of mineralising fluid, as seen by the crosscutting veinsets and overprinting alteration zones. The early veinsets, V1, V2 and V3 are associated with the majority of the mineralisation, while V5 contains a very different metal budget (figure 10), including relatively high concentrations of Pb, Zn and Te, which are not seen in high concentrations in the rest of the deposit. V2 and V3 are associated with potassic alteration and magnetite, whereas V4 and V5 are associated with chlorite-sericite alteration and hematite. The transition between magnetite and hematite in the alteration assemblages associated with the veinsets shows an increase in the oxygen fugacity of the system. This is also shown by the presence of barite in V5 and gypsum in V6 and V7, showing a transition between an H<sub>2</sub>S dominated precipitation environment in V3 to an SO<sub>4</sub> dominated system in V5, V6 and V7. V6 and V7 veins are also associated with a late advanced argillic overprint, and represent a transition towards more acidic, high sulphidation conditions (figure 15).

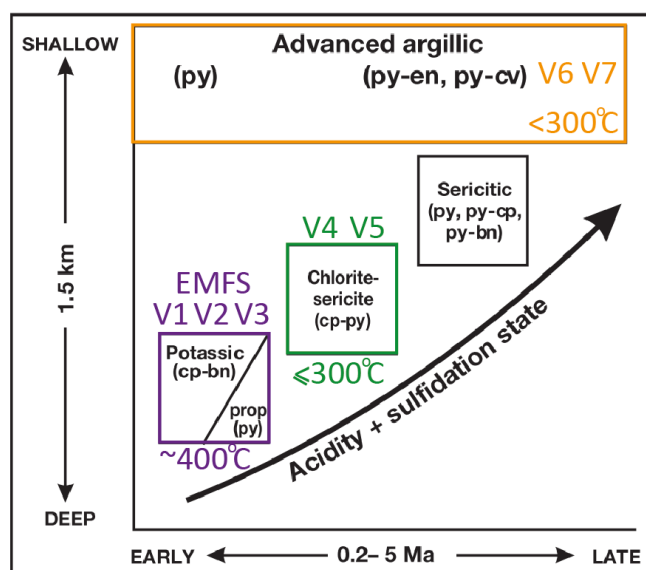


Figure 15: Diagram showing the transition between alteration types and pH, temperature and sulphidation conditions during the paragenesis of the Muratdere deposit. EMFS = early micro-fracture sulphides, V1 to V7 = vein stages. Figure adapted from Sillitoe, 2010.



The fluid inclusion populations in V1, V2, V3 and V4 are the same, save for the fact that V4 does not contain any type III inclusions. The secondary type I inclusions have much lower temperatures of homogenisation and salinities than would be expected for a porphyry deposit (Wilkinson 2001), and are proposed to represent a secondary fluid overprint. Their low temperatures (average 280°C) suggest they may be part of the fluid generation responsible for the chlorite-sericite or the advanced argillic overprint observed in the deposit. The type II inclusions are higher temperature, but with very low salinities, and as discussed above are likely to have undergone post-trapping modification. This makes them difficult to interpret, especially as their paragenesis is unclear so they may also represent a secondary overprint. Alternatively, they may represent a co-existing vapour phase within the primary mineralising fluids. The rare type III inclusions in the early veinsets resemble more 'typical' porphyry inclusions with high homogenisation temperatures and halite daughter minerals (Wilkinson 2001), and are interpreted to represent the original mineralising fluid. However, their salinities are low for a porphyry deposit, and they all homogenise above the critical point for NaCl (Fuentevilla et al. 2012), showing they have undergone major post-entrapment modification. This is likely due to overprinting by a later fluid (figure 14), and means that the temperature and salinity conditions of the type III inclusions no longer reflect those of the original fluid.

#### 3.5.1.1 Sulphur isotopes

Sulphides from the Muratdere deposit have fairly wide ranging  $\delta^{34}\text{S}_{\text{CDT}}$  values when compared to the sulphur isotope values of sulphides in porphyries globally (figure 13, table 9, Hattori & Keith 2001). The majority of porphyry Cu deposits do not exceed  $\delta^{34}\text{S}_{\text{CDT}}$  values of  $\sim +4$  ‰, whereas the highest  $\delta^{34}\text{S}_{\text{CDT}}$  recorded from Muratdere is  $+8.9$  ‰ (Hattori & Keith 2001). The range of  $\delta^{34}\text{S}$  values at Muratdere are most similar to those seen at Cerro Verde-Santa Rosa in Peru (Eastoe 1983). Muratdere's  $\delta^{34}\text{S}_{\text{CDT}}$  average of  $+2$  ‰ is similar to many deposits and is within the upper end of the range for magmatic sulphur (Ohmoto 1972). Whole rock sulphur extracts from other post-collisional granitoids in central Anatolia also show high  $\delta^{34}\text{S}_{\text{CDT}}$  values, averaging between  $+3.3$  ‰ and  $+13.2$  ‰ (Boztug & Arehart 2007), and this is thought to be due to crustal contamination during magma-crust interaction.

The sulphur isotope values of sulphides from the Muratdere deposit change with each stage of the deposit's paragenesis, and indicates changing sulphur sources within the deposit. The micro fracture hosted sulphides and sulphides from V2 have broadly magmatic  $\delta^{34}\text{S}_{\text{CDT}}$  values, corresponding to an enriched melt source. The sulphides in the Re-rich, molybdenite bearing V3 have higher  $\delta^{34}\text{S}_{\text{CDT}}$  values than the earlier mineralizing events, and V3 molybdenites have the highest  $\delta^{34}\text{S}_{\text{CDT}}$  values of the sulphides ( $8.2$  to  $8.8$  ‰). These values are significantly higher than

the  $\delta^{34}\text{S}_{\text{CDT}}$  values of the micro-fracture hosted chalcopyrites ( $-2.2\text{‰}$  to  $+4.6\text{‰}$ ), which are intergrown with the disseminated molybdenites and so are assumed to have the same sulphur source. This is in contrast to results from porphyry systems in Russia and Mongolia (Berzina et al. 2005), where the  $\delta^{34}\text{S}_{\text{CDT}}$  values of molybdenite in Re enriched deposits (Aksug and Erdenetuin-Obo) varies from  $-0.9$  to  $+3.2\text{‰}$ , while the  $\delta^{34}\text{S}_{\text{CDT}}$  data for molybdenites from Re-poor deposits (Zhireken, Shatkhtama and Sora) are higher, ranging from  $+3.7$  to  $+10.2\text{‰}$  (figure 16).

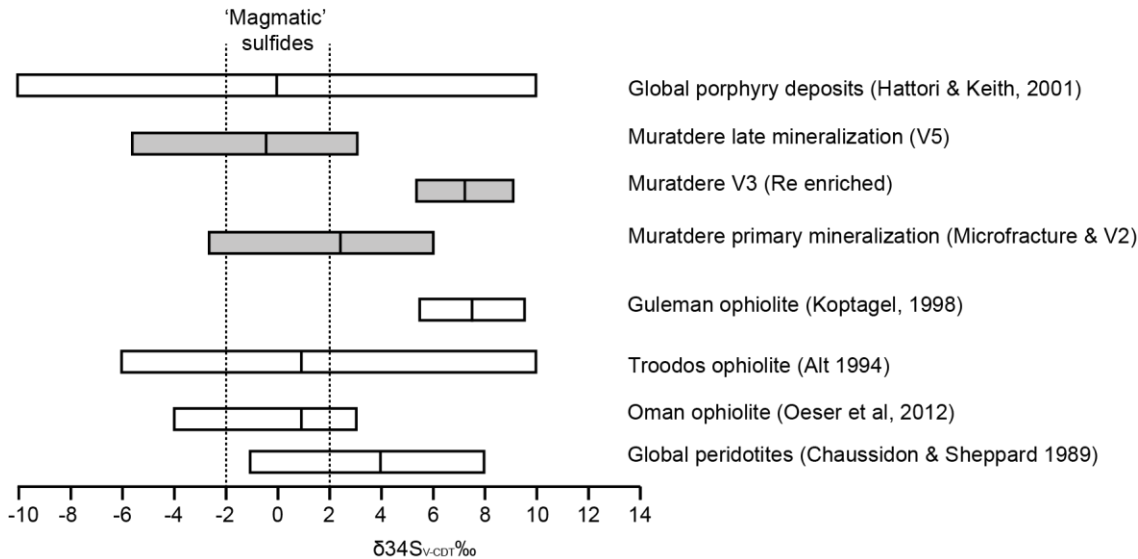


Figure 16: Diagram showing the range and mean  $\delta^{34}\text{S}_{\text{CDT}}$  values for a range of ophiolites and porphyry deposits, with the mean represented by a line in the centre of the box (Ohmoto 1972; Chaussidon et al. 1989; Alt 1994; Osman Koptagel et al. 1998; Berzina et al. 2005; Oeser et al 2012). The grey shaded boxes represent the  $\delta^{34}\text{S}_{\text{CDT}}$  values from this study, the 'Re-enriched porphyry deposits' are Aksug and Erdenetuin-Obo deposits in Russia and Mongolia, and the 'Re-poor' porphyry deposits are Zhireken, Shatkhtama and Sora from Russia and Mongolia (Berzina et al. 2005).

The higher  $\delta^{34}\text{S}_{\text{CDT}}$  values seen in V3, as opposed to those in V2, suggests that either a new sulphur source became available at this point in the paragenesis, or these increasing values are part of an overall fractionation trend towards higher  $\delta^{34}\text{S}_{\text{CDT}}$  values. These higher  $\delta^{34}\text{S}_{\text{CDT}}$  values could also be the result of contamination by sulphates, however there are no sulphates present in the country rocks surrounding the deposit, and the first oxidised sulphur observed within the deposit is the barite present in V5. Another possibility is that new sulphur with higher  $\delta^{34}\text{S}_{\text{CDT}}$  values was scavenged from the surrounding ophiolite country rock –  $\delta^{34}\text{S}_{\text{CDT}}$  data from the Guleman group in south-eastern Anatolia, a similar Late Cretaceous ophiolite to the Dağküplü ophiolite, shows ophiolite  $\delta^{34}\text{S}_{\text{CDT}}$  values of  $+5.8\text{‰}$  to  $+8.8\text{‰}$  (Koptagel et al. 1998) which match the values seen in V3 ( $+5.6\text{‰}$  to  $+8.9\text{‰}$ ). These values are higher than the  $\delta^{34}\text{S}_{\text{CDT}}$  values recorded in the Oman ophiolite (Oeser et al. 2012), but are within the values recorded for peridotites globally (Chaussidon et al. 1989) and in the Troodos ophiolite (figure 16, Alt 1994). This means the surrounding Dağküplü ophiolite could be the source of the new sulphur seen. If this is the case it is likely that this would have occurred through hydrothermal fluids scavenging sulphur and metals

from the surrounding country rock, as the temperatures of felsic magmas are lower than those needed to assimilate the peridotite country rock (Ito & Kennedy 1967).

The next mineralising veinset in Muratdere, V5 has lower sulphide  $\delta^{34}\text{S}_{\text{CDT}}$  values with a mean  $\delta^{34}\text{S}_{\text{CDT}}$  of -0.4‰, giving a strongly magmatic signature and showing the deposit has reverted to a magmatic sulphur source. This also shows that the raised sulphur isotope values in V3 are not part of a general progression towards higher  $\delta^{34}\text{S}_{\text{CDT}}$  values in the deposit.

The  $\delta^{34}\text{S}_{\text{CDT}}$  values from the sulphates in Muratdere are broadly within the expected range for Eocene seawater sulphate, which is +16‰ to +23‰ (Thode & Monster 1965; Claypool et al. 1980), with an evolution towards heavier values in the later veinsets.

### 3.5.1.2 Oxygen and hydrogen isotopes

The oxygen and hydrogen isotope results recorded at Muratdere are very similar to the values seen for porphyries globally, for example quartz from veins in the Bingham deposit, Utah, show  $\delta^{18}\text{O}$  values of +8.6 ‰ to +9 ‰, and  $\delta\text{D}$  values of -69 ‰ to -83 ‰ (Sheppard et al. 1971; Sheppard & Gustafson 1976; Ford & Green 1977; Bowman et al. 1987; Zaluski et al. 1994). The  $\delta^{18}\text{O}_{\text{H}_2\text{O}}$  values of ore-forming fluids from quartz were calculated using the equation  $1000\ln\alpha_{\text{quartz-H}_2\text{O}} = 3.38 \times 10^6 \text{ T}^{-2} - 3.40$  (Clayton et al. 1972). The temperatures used were from fluid inclusion microthermometry – the samples from the early veinsets (V1 – V3) were assumed to have the same temperature as the type III inclusions, V4 and V5 were assumed to be a product of the overprinting fluid and so the temperature from type II inclusions was used. However, this means that the fluid  $\delta^{18}\text{O}_{\text{V-SMOW}}$  values are only approximate as there are no definite temperatures for each veinset. Also as the secondary fluid is present in all veinsets measured, the oxygen and hydrogen results may be reflecting this secondary fluid, rather than the primary ore forming fluid, or a mixture of the two.

The fluid oxygen and hydrogen isotope results, when plotted against each other, are similar to those seen in porphyries globally (figure 17, Sheppard et al. 1971; Sheppard & Gustafson 1976; Ford & Green 1977; Bowman et al. 1987; Zaluski et al. 1994). The early veinsets (V1 to V3) show a strongly magmatic signature, and are most similar to the global porphyries, whereas V4 and V5 plot slightly outside the magmatic fluid field, potentially indicating some external fluid input (figure 17).

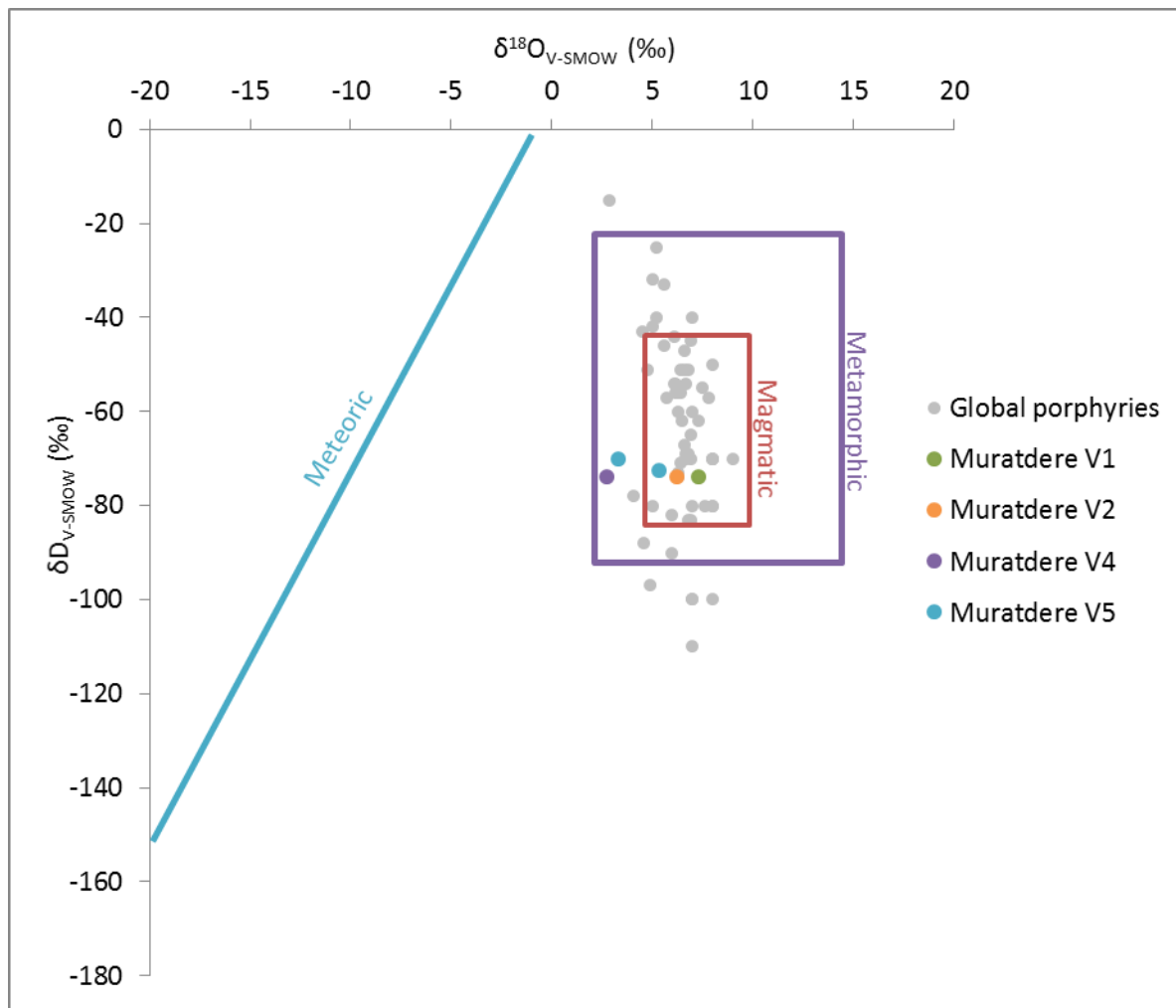


Figure 17: Fluid oxygen isotope values vs hydrogen isotope values for Muratdere compared with global porphyries. Fluid  $\delta^{18}\text{O}$  calculated according to equation from Matsuhisa et al (1979). Magmatic, metamorphic and meteoric water values from Taylor & Sheppard (1986), global porphyry fluid data from Sheppard et al. 1971; Sheppard & Gustafson 1976; Ford & Green 1977; Bowman et al. 1987; and Zaluski et al. 1994.

### 3.5.2 Muratdere deposit genetic model

The Muratdere deposit is hosted by a granodioritic stock intruded into ophiolitic country rocks, including peridotites. The main mineralisation is situated in hydrothermal veinsets which are interpreted to be genetically related to later quartz-feldspar porphyry stocks. These have probably intruded from a deeper source pluton, as suggested in the models for porphyry formation in Sillitoe, 2010. As these stocks ascended through the crust they exsolved volatiles, creating the hydrothermal veining observed (Cloos 2001).

The initial mineralising fluids, represented by the type III inclusions, were high temperature, magmatic, oxidised and of moderate salinity. These formed veinsets V1 to V3, transporting Au, Cu, Mo and Re as chloride ligands (Xiong & Wood 2002; Richards 2011). Possible precipitation triggers for these early veinsets include the introduction of reduced sulphur, possibly from

magmatic vapour (Blundy et al. 2015; Hedenquist & Lowenstern 1994; Henley & McNabb 1978; Henley & Berger 2013), which may be represented by the type II inclusions. V3 veins may have formed at slightly lower temperatures than V1 and V2, as they are often associated with propylitic alteration.

The next veinsets, V4 and V5, were formed by lower temperature fluids, which likely also formed the chlorite-sericite alteration. These fluids were highly oxidised, more acidic and at a lower temperature and higher sulphidation state than the early mineralising fluids, with drop in temperature a potential precipitation trigger (Wilkinson 2013). The fluids which generated V4 and V5 may also have had some external input via mixing with ground water, as shown by their slightly lower  $\delta^{18}\text{O}_{\text{V-SMOW}}$  values (figure 17). The final veinsets, V6 and V7 were formed by a late stage fluid which also formed the advanced argillic alteration. This fluid was low temperature, with high oxygen fugacity, acidity and sulphidation state, and may represent the transition to epithermal conditions (Einaudi et al. 2003; Sillitoe 2010).

### **3.5.3 Critical metal enrichment in the Muratdere deposit**

#### **3.5.3.1 Platinum group elements and tellurium**

Muratdere's PGE concentrations are low when compared to PGE enriched porphyry deposits globally, with all samples analysed falling below mantle values (figure 18, Eliopoulos & Economou-Eliopoulos 1991; Maier 1999; Thompson et al. 2001; Augé et al. 2002; Auge et al. 2005; Eliopoulos et al. 2014), showing that Muratdere is not a PGE enriched deposit. However, as the other deposits which have been analysed for PGE content all contain visible platinum group minerals (PGMs), and are known to be PGE enriched it is likely that the levels seen in Muratdere are more typical for a Cu-Mo porphyry deposit. The Pd-Pt ratio in Muratdere is consistent with other porphyries globally, but Muratdere's Au-(Pd+Pt) ratio is different, meaning that Au is decoupled from Pt and Pd in Muratdere. A comparison of mantle normalised PGE plots shows that Muratdere has a 'flatter' profile than other deposits, with no significant Pt peak (figure 18). Its profile is most similar to those of the British Columbia deposits (Thompson et al. 2001), but without the Pt enrichment. All porphyries show a relative enrichment in heavy PGEs (Rh, Pt, Pd) when compared to light PGEs (Os, Ir, Ru), and Muratdere is no exception.

In common with other peridotites from an ophiolitic setting the serpentinised peridotite country rock sample analysed has mantle values of the high refractory iridium group platinum group elements (IPGEs) – Os, Ir and Ru, with slightly lower contents of the more volatile palladium group PGEs (PPGEs – Rh, Pt and Pd) (figure 18, Cabri 2002). The PGEs present in the samples from within the deposit are probably sourced in the melt, with the samples comprising micro-fracture hosted

sulphides, V2 and V5 containing less PGEs than the country rock. However, samples containing veinset V3 have the same amount of Pt and Pd as the country rock (figure 18). As both Pt and Pd are the most hydrothermally mobile PGEs (Xiong & Wood 2000) this suggests that there was some hydrothermal interaction between V3 and the surrounding peridotites (Mountain & Wood 1988). This lends weight to the theory that veinset V3 has undergone hydrothermal interaction with the surrounding peridotitic country rock, scavenging metals and higher  $\delta^{34}\text{S}_{\text{CDT}}$  sulphur.

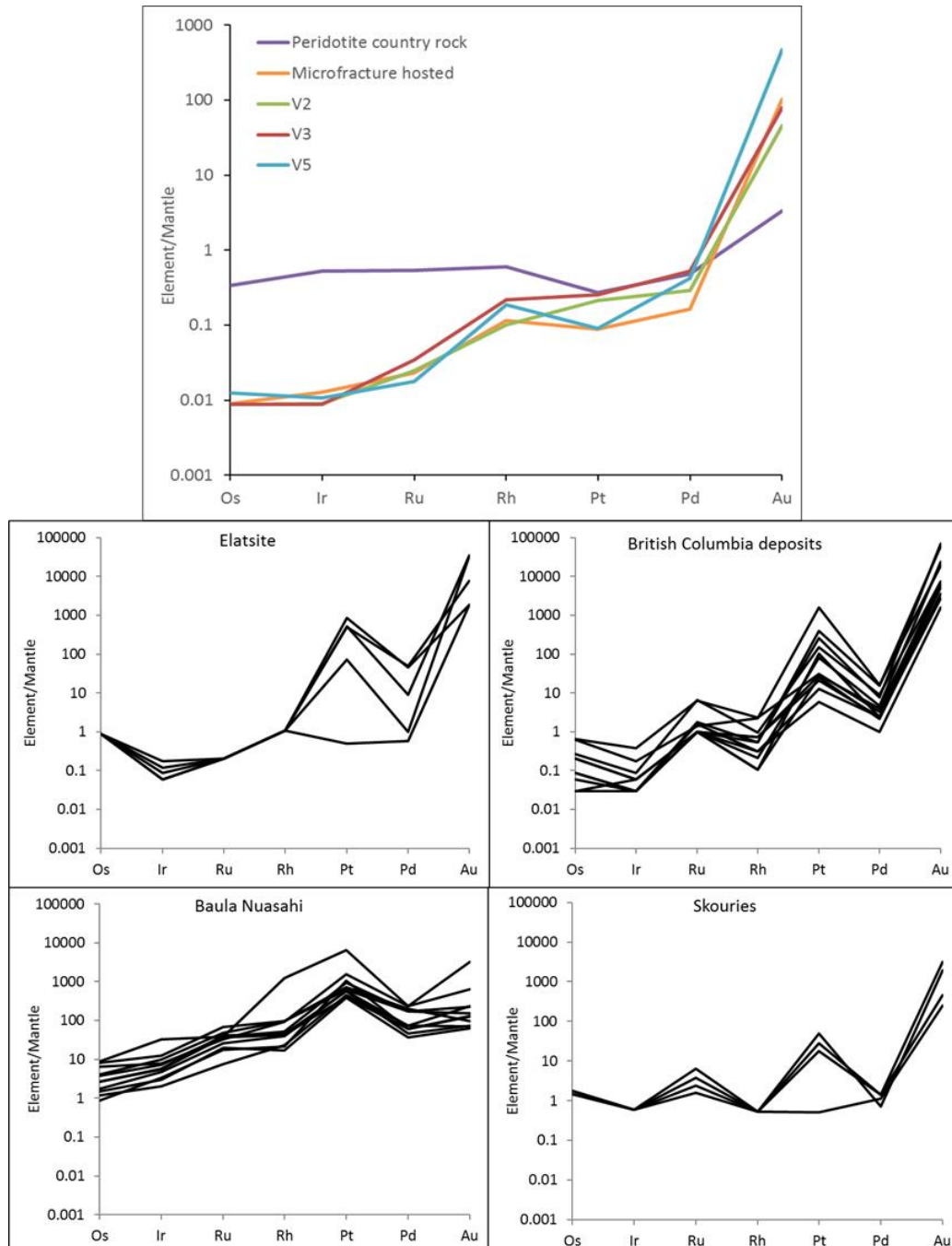


Figure 18: Mantle normalised PGE values for Muratdere and other PGE enriched deposits – Skouries, Elatsite and the British Columbia deposits are other porphyry copper deposits while Baula Nuasahi is a layered ultramafic intrusion with associated hydrothermal mineralisation (data from: Eliopoulos & Economou-Eliopoulos 1991; Thompson et al. 2001; Augé et al. 2002; Augé et al. 2005; Eliopoulos et al. 2014; normalisation values from Maier 1999).

Muratdere is enriched in tellurium, which is found in the latest mineralising veinset, V5. Tellurium-rich hydrothermal deposits are thought to be associated with the porphyry-epithermal transition (Voudouris 2006), and the famously Re enriched Pagoni Rachi deposit in Thrace, Greece contains very similar polymetallic intermediate sulphidation veins, associated with chlorite-sericite alteration, with high Te concentrations (Voudouris 2006; Voudouris et al. 2013).

### **3.5.3.2 Rhenium hosting in molybdenites**

The average Re content of molybdenite in Muratdere is comparable to that of other Cu-Mo porphyries such as Ray, San Manuel, Maronia, Kounrad and Kal'makyr (figure 11, Berzina et al. 2005) and is around the global average (681 ppm; figure 11). Muratdere contains two Re bearing phases - early, micro-fracture hosted molybdenite and later V3 vein hosted molybdenite. The later vein hosted molybdenites in V3 contain significantly more Re than the early micro-fracture hosted molybdenite. Despite recognising different generations of molybdenite in porphyry systems previous studies have not reported systematic differences in Re content between different molybdenite generations (Berzina et al. 2005; Voudouris et al. 2009; Tessalina et al. 2008; Grabezhev & Voudouris 2014), although some differences are seen between veinsets in El Teniente (Spencer et al. 2015), and oscillatory zoning of Re within individual molybdenites has been suggested to indicate that successive hydrothermal events with different Re contents may occur in porphyry deposits (Ciobanu et al. 2013).

Oscillatory zoning is observed in molybdenites in many porphyry deposits, including the highly Re enriched Pagoni Rachi deposit, Greece, and the Re-enriched Vosnesensk deposit, Russia (Voudouris et al. 2009; Grabezhev & Voudouris 2014). This oscillatory zoning is also observed in the bladed molybdenites of Muratdere, and is interpreted to represent the original growth pattern of the crystals (Grabezhev & Voudouris 2014). The Re-rich molybdenites in Muratdere are of the 2H polytype, as are those at Pagoni Rachi and Vosnesensk (Voudouris et al. 2009; Grabezhev & Voudouris 2014). This disagrees with the conclusions of Newberry (Newberry 1979a; Newberry 1979b) which state that the 3R polytype should be associated with Re enrichment. Unlike other deposits Muratdere does not appear to show any evidence for isomorphous substitution of Re for Mo in molybdenites – although there is an overall positive correlation between Re and Mo in the assay data, individual LA-ICP-MS spot analyses of the molybdenites show no correlation between Mo and Re content. This is in contrast to molybdenite data from Pagoni Rachi, a highly Re enriched deposit in Greece with well-defined molybdenite chemistry and structure, where Re and Mo in molybdenite show a strong negative correlation (Voudouris et al. 2009). EPMA mapping of Muratdere molybdenites also does not show corresponding Mo

depleted areas in Re enriched zones within the molybdenites, which might be expected if Re was replacing Mo stoichiometrically (Voudouris et al. 2009; da Silva et al. 2013).

### 3.5.3.3 Potential sources of rhenium in Muratdere

The source of Re in porphyry deposits has generally been agreed to be from a Re-enriched source melt, either as a primary melt or secondary ultramafic input. This has been suggested to be derived from degassing of a down going slab (Sun et al. 2003), incorporation of Re enriched anoxic sediments into the accretionary wedge (Svetlana G. Tessalina et al. 2008) or partial melting of previously metasomatised mantle lithosphere triggered by a local ascent of asthenospheric mantle (Voudouris 2006; Voudouris et al. 2009). Eocene magmatism in the north of Turkey is thought to be post-collisional, with metal enrichment resulting from upwelling asthenospheric mantle melting previously metasomatised crust (Stein et al. 2001; Berzina et al. 2005; Kuscu 2016). This could provide a Re (and indeed Cu and Au) enrichment mechanism for Muratdere, however this does not explain the difference in Re content between the two generations, as if the whole Re budget for a given system is sequestered into molybdenite (Stein et al. 2001) the earlier molybdenites would be expected to have higher Re contents. This suggests that a new source of Re became available between the micro-fracturing event and the precipitation of the V3 molybdenites.

Potential new sources of Re are a fresh influx of enriched melt, a change in fluid conditions which promotes the transport and deposition of Re, remobilisation of Re from earlier molybdenites, or scavenging of Re from the country rock. It is interesting that V3 not only has the higher Re content, but also evidence of a new, heavier sulphur source and it is likely that these are linked.

A potential source for the new sulphur and the Re enrichment in V3 is an influx of mafic or ultramafic magma into the felsic pluton. Re is highly chalcophile and so partitions into the immiscible sulphide phase often seen in these magmas, and this has been suggested as a possible source of Re in porphyries (Sinclair & Jonasson 2014). If this were the case a new intrusive phase, or evidence of a change in the host porphyry composition might be expected between veinsets V2 and V3, and this is not seen. There may still have been a fresh input into the source magma chamber at depth, however that would not explain the high  $\delta^{34}\text{S}_{\text{CDT}}$  signature of the sulphur seen in V3, as if it had come from a new influx of melt it should have a magmatic signature (around 0 ‰). A fresh influx of melt would also be expected to result in V3 being enriched in Au and Cu relative to the other veinsets, and potentially also in PGEs (Sinclair & Jonasson 2014), however this is not seen in the assay data or the PGE analysis.



Another possible cause of the Re enrichment seen in V3 is a change in the fluid conditions to those which better favour Re deposition (Xiong & Wood 2002). Oxygen and hydrogen isotope analysis has shown that there was no change in fluid source between V1, V2 and V3 and they also contain the same fluid inclusion populations with the same range of salinities and homogenisation temperatures, although the pervasive late low temperature overprint makes interpreting formation temperatures from fluid inclusions difficult. V3 may have been formed by lower temperature fluids than the micro-fracture hosted mineralisation due to its infrequent association with propylitic alteration, and this has been suggested to promote the precipitation of Re enriched molybdenite due to the prograde solubility of  $\text{ReS}_2$  (Xiong & Wood 2002). However, a lower temperature also does not explain the higher  $\delta^{34}\text{S}_{\text{CDT}}$  signature seen in V3. The presence of type III inclusions in V3 suggest it was still a higher salinity fluid, and the associated magnetite alteration shows oxygen fugacity to be very similar to that of the early mineralising fluids. The additional Re seen in the molybdenites in V3 could also be the result of remobilisation of rhenium from the earlier molybdenites by the V3 forming fluid (Golden et al. 2013; Ciobanu et al. 2013). This may be the case, however the preservation of cleavage-parallel oscillatory zoning in the molybdenites suggests that Re leaching and re-mobilisation has not occurred, and the earlier molybdenites are the 2H polytype, which has been shown to be less sensitive to leaching (Stein et al. 2003).

Another potential source for the new Re and sulphur seen in V3 is the surrounding ophiolitic country rock. As discussed above  $\delta^{34}\text{S}_{\text{CDT}}$  values like those seen in V3 are found in peridotites from similar ophiolites to the one hosting Muratdere, so interaction with the country rock is a potential source of the heavy  $\delta^{34}\text{S}_{\text{CDT}}$ . V3 samples have low IPGE values and yet have the same Pt and Pd values as the country rock. As these are the hydrothermally mobile PGEs this suggests that there may have been particular hydrothermal interaction between the fluids creating V3 and the surrounding peridotites. Ophiolites contain between 0.17 ppb and 1.95 ppb Re (Ravizza et al. 2001; Peucker-Ehrenbrink et al. 2012; Becker & Dale 2016), and the highly serpentinised peridotite seen at the bottom of drill hole MDD 03 has a Re content of 0.25 ppb. This host rock Re concentration would require hydrothermal fluid interaction with less than 1 km<sup>3</sup> of peridotite in order to produce the level of enrichment seen in V3. Muratdere has an alteration footprint of approximately 1.6 km<sup>3</sup> which would allow enough fluid-rock interaction to scavenge the amount of Re observed in V3 molybdenites. It is likely that this interaction combined with specific fluid conditions allowed the efficient scavenging and precipitation of Re. An oxidised, highly saline fluid would be needed to transport large quantities of Re, followed by the addition of reduced sulphur, or a drop in temperature or salinity in order to precipitate the hydrothermally transported Re (Xiong & Wood 2002).

### 3.6 Conclusions

Muratdere is a post-collisional Cu-Mo (Au-Re) porphyry deposit hosted by granodiorite and quartz-feldspar porphyry stocks. The deposit contains three main vein stages – an early mineralising stage which is associated with potassic alteration and hosts the Cu, Mo and Re mineralisation; a porphyry-epithermal transition stage consisting of intermediate sulphidation polymetallic veins associated with chlorite-sericite alteration which host Zn, Pb, Au and Te mineralisation; and a late advanced argillic overprint, associated with gypsum veinsets. These show the evolving fluid conditions in the deposit from high temperature, oxidised and saline magmatic fluids (~550°C, 14 wt% NaCl) to low temperature and salinity (~280°C, 6 wt% NaCl), high sulphidation, more acidic oxidised fluids which show evidence of mixing with ground water. The alteration types and veinsets present are similar to those seen at the highly Re-enriched Pagoni Rachi deposit, Greece.

The Muratdere deposit contains two generations of molybdenite. The earlier micro-fracture hosted molybdenite contains Re contents similar to those expected in a deposit with the Cu/Mo of Muratdere and magmatic  $\delta^{34}\text{S}$  values show that this Re is likely from an enriched melt source. This is proposed to be the result of upwelling asthenospheric mantle melting previously metasomatised crust. The later, vein hosted molybdenites in V3 contain significantly more Re than the earlier micro fracture hosted molybdenites. V3 has very similar  $\delta^{18}\text{O}_{\text{SMOW}}$ ,  $\delta\text{D}_{\text{SMOW}}$ , fluid inclusion population, temperatures and salinities to the earlier mineralizing events, however it has higher  $\delta^{34}\text{S}_{\text{CDT}}$  values, near the upper end of  $\delta^{34}\text{S}_{\text{CDT}}$  values recorded in porphyries globally (Hattori & Keith 2001). This strongly suggests that the increase in Re content seen in V3 is linked to a new source of sulphur in the system. The  $\delta^{34}\text{S}_{\text{CDT}}$  values in V3 are very similar to those recorded for Anatolian peridotites, which also host elevated levels of Re relative to the average crustal value (0.25 ppb as opposed to 0.07 ppb). The hydrothermally mobile PPGE (Ru, Pt, Pd) content in V3 matches the PPGE content of the surrounding ophiolite, while the refractory IPGE (Os, Ir, Rh) contents of V3 are less than those recorded in the ophiolite. This suggests that there has been hydrothermal interaction between the fluids which formed V3 and the surrounding ophiolite. These fluids could have scavenged sulphur and additional Re from the country rock, potentially explaining the difference in Re content.

## **Chapter 4: A fluid history of the Skouries Cu-Au (Pd, Pt, Te) porphyry deposit, Greece**

### **4.1 Introduction**

Skouries is an alkali Cu-Au porphyry deposit, situated in the Chalkidiki peninsula, Greece. It is famous for having a significant enrichment in PGEs (Eliopoulos & Economou-Eliopoulos 1991; Tarkian & Stribrny 1999; Economou-Eliopoulos & Eliopoulos 2000), however there is still a lot that is not understood about this system. Skouries is made up of overprinting pipe-like intrusions, each of which is associated with separate veinsets and alteration, giving it a complex paragenesis. Previous work on the deposit has defined the petrology and geochemistry of the igneous phases (Kroll et al. 2002), ascertained the amount of PGEs present in the deposit (Eliopoulos & Economou-Eliopoulos 1991) and defined the source of fluids using Pb and Sr isotopes (Frei 1995). However there has not yet been a thorough stable isotope and fluid inclusion survey performed to ascertain the vein paragenesis and fluid characteristics. Gaining a clear understanding of the hydrothermal system at Skouries is important not only to enhance our knowledge of alkali porphyry systems, but also to allow contextual study of the location, source and transport mechanism of the PGEs in this deposit (discussed further in chapters 5 and 6). This chapter presents the results of detailed vein logging, SEM imaging of mineralising veins and vein-specific stable isotope analyses. Detailed fluid inclusion petrology and micro-thermometry was performed using optical microscopy, SEM and Laser Raman Spectroscopy, as was LA-ICP-MS of fluid inclusions in the mineralising veinsets. This was used to develop a genetic model for the deposit, and to understand the chemical and physical conditions of the fluids transporting the metals.

#### **4.1.1 Alkali porphyry deposits**

Gold rich porphyry deposits are commonly associated with alkalic and shoshonitic intrusions (Sillitoe 1979), and these are an important sub-class of magmatic hydrothermal ore deposits. Although calc-alkaline porphyry models are relatively well understood (Sillitoe 2010), alkalic porphyry models are less well developed due to their relative scarcity, geological heterogeneity and small alteration footprint (Bissig & Cooke 2014). Well known shoshonitic porphyry copper-gold districts include the Cadia district, New South Wales, Australia (Holliday et al. 2002; Wilson et al. 2003); the Goonumbla volcanic complex, New South Wales, Australia (Heithersay & Walshe 1995); the Northparkes district, Australia (Lickfold et al. 2007) and central Quesnellia, British Columbia, including the Mt Milligan and Chochi deposits (Barrie 1993). Well known deposits

include Bajo de la Alumbrera deposit, Argentina (Müller & Forrestal 1998; Ulrich & Heinrich 2002); the Dinkidi Cu-Au porphyry, Philippines; the Emperor deposit, Fiji (Harris et al. 2013); Grasberg; Batu Hijau and Oyu Tolgoi (Perelló et al. 2001; Wilson et al. 2003). These deposits tend to be hosted by pericratonic and intraoceanic arc assemblages (Bissig & Cooke 2014), and are commonly associated with post-collisional magmatism (Müller & Groves 1993). Like many calc-alkaline deposits, alkalic porphyry deposits are usually associated with multiple, overprinting intrusive events with associated hydrothermal alteration and mineralisation (e.g. Holliday et al. 2002; Wilson et al. 2003; Lickfold et al. 2007; Harris et al. 2013; Rezeau et al. 2016), and these intrusions commonly show evolution from mafic to intermediate silica-under-saturated potassic magmas, with a later resurgence in mafic magmatism resulting in swarms of mafic dykes (Micko et al. 2014; Bissig & Cooke 2014). This is thought to be due to short-lived contractional or transpressional regimes favouring intrusive magmatism, followed by arc rifting (Harris et al. 2013; Bissig & Cooke 2014). Other common features of alkali porphyry deposits include megacrystic potassium feldspar rocks and abundant primary and hydrothermal magnetite, both of which are seen in Skouries (Pass et al. 2014). Elevated CO<sub>2</sub> contents have also been documented in some alkalic porphyry ore fluids (Ronacher et al. 2004), and this is consistent with high CO<sub>2</sub> solubility in mantle-derived alkalic magmas (Wyllie & Huang 1976).

Alkalic porphyry deposits commonly have calcic alteration envelopes, and rarely exhibit extensive phyllic or argillic alteration zones (Bissig & Cooke 2014). Secondary orthoclase with hematite dusting, abundant magnetite and secondary biotite are features of potassic alteration in these systems (e.g. Holliday et al. 2002; Wilson et al. 2003), and sulphides are typically zoned from a bornite rich core to a chalcopyrite-pyrite outer zone and then a barren pyrite envelope (Wilson et al. 2003). Skouries is hosted by shoshonitic monzonites and syenites (Kroll et al. 2002), and shows many of the typical features described above. Other regions with shoshonitic porphyry deposits in the Tethyan belt include the Eastern Pontides in Turkey (Eyuboglu et al. 2011; Yigit 2012), and the Kerman Cenozoic magmatic arc, Iran (Shafiei 2010; Hou et al. 2011).

### **4.1.2 Regional geology**

The Skouries Cu-Au porphyry copper deposit is located on the Chalkidiki Peninsula in north-eastern Greece, 90 km south-east of Thessaloniki (figure 19). It is part of the Kassandra mining district (Kroll et al. 2002), which is in the Serbomacedonian Massif (SMM) of Northern Greece. The SMM extends from Serbia into the Chalkidiki peninsula, where it is bordered by the Rhodope Massif (RM). These are interpreted to be the oldest fragments of the Balkan peninsula basement (Frei 1992), and the SMM hosts the Serbomacedonian metallogenic province (SMP). The SMP is associated with Late Cretaceous to Tertiary magmatism (Jankovic 1977), and is a subdivision of

the Tethyan Metallogenic Belt (TMB) which incorporates all deposits associated with the closure of the Tethyan Ocean (Jankovic 1997; Richards 2015), including the PGE enriched Elatsite porphyry deposit in Bulgaria (Tarkian et al. 2003).

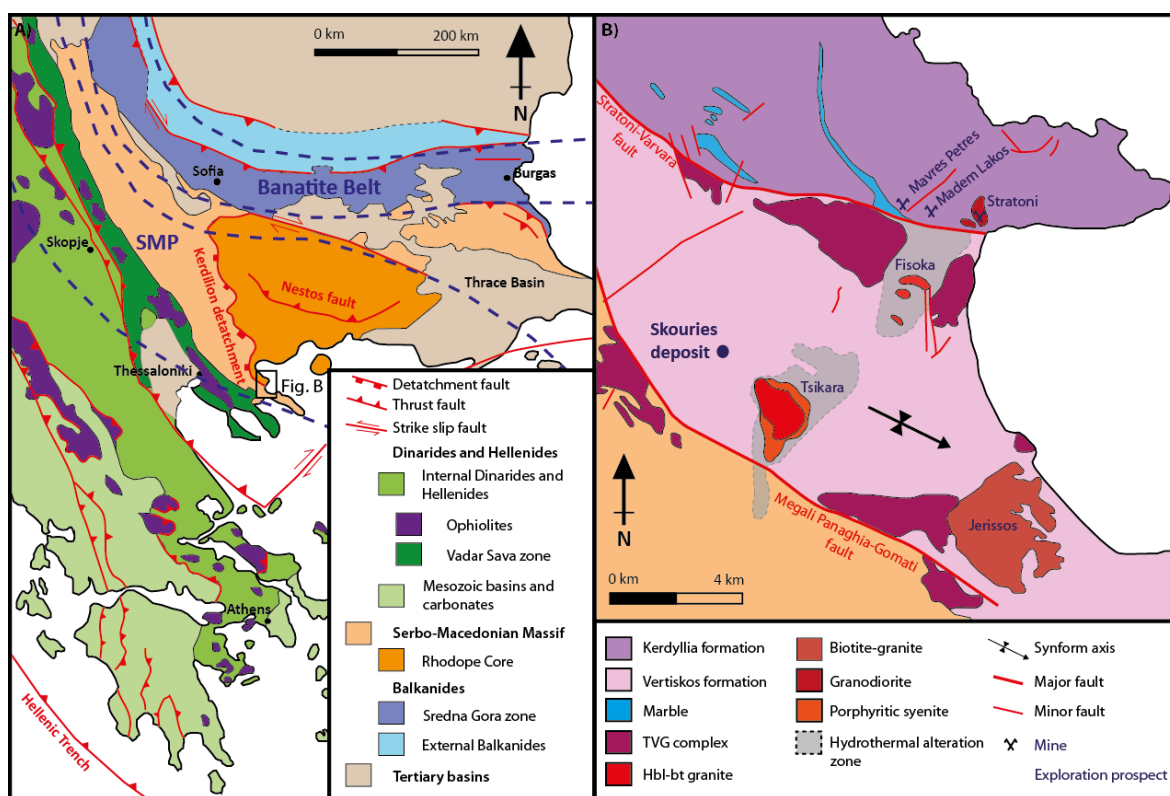


Figure 19: A) Regional geology map showing the major tectono-stratigraphic units, metallogenic belts and major structural features (after Hahn 2015; incorporating data from Frei 1995). B) Local geology map of the region around Skouries (inset in A) showing the geological units, major structures and regional mines and exploration prospects (after Kroll et al. 2002; Frei 1995; Eliopoulos & Economou-Eliopoulos 1991; Eldorado Gold Corp 2015).

The Skouries deposit is situated within the Vertiskos Formation, the upper unit in the SMM, which is separated from the lower Kerdyllia formation by the NW striking Stratoni-Varvara fault (figure 19, Kroll et al. 2002). The Vertiskos formation consists of muscovite-biotite-garnet-staurolite-tourmaline schists, amphibolite lenses and two-mica schists and augen gneisses, all containing abundant quartz veins, and has undergone retrograde metamorphism to greenschist facies (Frei 1995; Kroll et al. 2002; Hahn 2015). The Kerdyllia formation is of a higher metamorphic grade, containing gneisses, amphibolite and marble lenses (Frei 1995; Kroll et al. 2002). The SMM also contains lamprophyres and mafic dykes, with a mafic and ultra-mafic intrusive complex in the Vertiskos formation (the Therma-Volvi-Gomati Complex) being thought to represent a dismembered ophiolite sequence (Dixon & Dimitriadis 1984; Frei 1995). These mafic intrusions have been postulated as a possible metal source for Skouries (Eliopoulos et al. 2014). Skouries is situated near the Vertiskos-Kerdillion fault, which connects the SMM to the Rhodope core, a synmetamorphic Eocene-Miocene metamorphic core complex (Hahn 2015). The exhumation of

this core produced heterogeneous strains on the crust (Brun & Sokoutis 2007; Brun & Sokoutis 2010) which may have promoted post-collisional magmatism in the region (Hahn 2015).

The Skouries deposit is hosted by one of a series of calc-alkaline, shoshonitic, north-east striking igneous intrusions which intrude the Vertiskos formation (figure 19). They are in the centre of a trans-tensional area between two normal faults with strike-slip movement, but are undeformed (Kroll et al. 2002; Hahn 2015). Some of these intrusions show evidence of mineralisation, including phyllic alteration halos (Kroll et al. 2002). Neogene calc-alkalic volcanism in the region is not thought to be directly related to subduction, but instead was generated during post-collisional extension by partial melting of subduction-modified lithospheric mantle and crust, with this metasomatism occurring during Neotethyan subduction (Rosu et al. 2005; Harangi et al. 2007; Harris et al. 2013; Richards 2015). Skouries was formed during the Miocene, with an intrusion age of  $20.56 \pm 0.48$  Ma, and a mineralisation age of  $19.9 \pm 0.9$  Ma (Hahn et al. 2012). Other intrusion-related deposits in the region include the Olympias and Stratoni Pb-Zn (Ag-Au) carbonate-replacement deposits, and the Tsikara, Fisoka and Piavitsa prospects (Eldorado Gold Corp 2015).

### 4.1.3 Past work

There is evidence for ancient mining in the Stratoni area during the time of Alexander the Great, with 1 MT of ore being extracted from Madem Lakos and Olympias between 350 and 300 BC (Forward et al. 2011). There is little evidence of ancient mining at Skouries itself however, and the first reported discovery was in Neubauer (1957), where Skouries is described as a trachytic lens with oxidised copper ore (Papadakis & Michailidis 1976). Drilling was undertaken by TVX Hellas, leading to the identification of porphyry style stockwork veinlets, mineralisation and alteration (Zachos 1963). Later work identified Skouries' cylindrical morphology (Gundlach et al. 1971), classifying it as a syenitic porphyry containing primary magnetite, and identifying pervasive potassic alteration with irregular propylitic alteration zones (Papadakis & Michailidis 1976). A more recent study identified Skouries as being made up of several cross-cutting intrusive monzonite phases, and described some of the mineralising veins, as well as performing whole rock and trace element analysis (Kroll et al. 2002).

A Pb isotope survey of Skouries and the surrounding intrusions was carried out in 1995 in order to determine whether the Pb in the system derives from the country rocks or the mantle (Frei 1995). It was concluded that the Pb isotopes in Skouries illustrate crustal affinity, and correspond to the isotopic characteristics of other intrusions in the area including Fissoka, a local exploration prospect. It was concluded that the similarity of Pb isotopes to surrounding country rock of the Vertiskos Formation suggests assimilation of the country rocks at depth, which may indicate the

presence of a magma plume which existed for some time at crustal levels before giving rise to individual shallow level porphyritic intrusions. Sr isotopes showed the fluids to have ascended from the magma with minimal interaction with the country rock, suggesting this was a self-sustaining isolated system (Frei 1995). Frei also performed limited stable isotope ( $\delta^{18}\text{O}$  and  $\delta^{34}\text{S}$ ) analyses of vein quartz and sulphur, and quotes fluid inclusion results from an unpublished thesis, however detailed vein descriptions and paragenesis are not presented. Kroll et al. (2002) performed whole rock and trace element analysis, concluding that the Skouries deposit is shoshonitic, with high  $f\text{O}_2$  of parent melts, and that high F concentrations in micas and high whole rock LILE concentrations reflects a mainly fluid derived component during magma genesis in the upper mantle, stemming from dehydration of the subducting slab (Kroll et al. 2002). A recent study by Siron et al (2016) performed regional U-Pb dating and whole rock geochemistry on deposits and intrusions in the Kassandra mining district. This study highlights the high Sr/Y and La/Yb values found at Skouries, which are interpreted to indicate the fractionation of amphibole, and the enriched LREE patterns and high LILE concentrations, which are proposed to indicate interaction with subduction enriched continental lithosphere. PGE analyses has also been performed on Skouries (Eliopoulos & Economou-Eliopoulos 1991; Tarkian & Stribrny 1999; Eliopoulos et al. 2014), and are discussed further in chapter 5. Although Kroll et al. (2002) and Siron et al (2016) performed petrological analysis and defined lithological units this study uses lithological units and veinsets defined as the result of a logging campaign performed in the summer of 2013.

Skouries is currently operated by Eldorado Gold, with a resource estimate of 3.791 million in situ ounces of Au and 152.736 million tonnes of 0.51% Cu (Eldorado Gold Corp 2015).

## 4.2 Skouries geology

5 drill holes were logged for this study, situated in the intrusive core of the deposit and chosen to ensure all the principle lithologies and veinsets were intercepted (locations shown in figure 20, full logs in appendix A4.2). In total 3464 m of drill core was logged at a 2m scale in order to correlate features with assay intervals. Additional logging, mapping and assay information from Eldorado Gold Corp supplemented this work. Representative samples were taken from all stages of the deposit paragenesis, and polished thin sections were made of 37 key samples (electronic appendix C). These were examined using optical microscopy in order to gain an understanding of the petrology and paragenesis of the deposit. SEM analysis was carried out using BSE and EDS to clarify the paragenesis of the sulphides, to identify unknown minerals and to create element maps of vein areas (method discussed in detail in chapter 2).

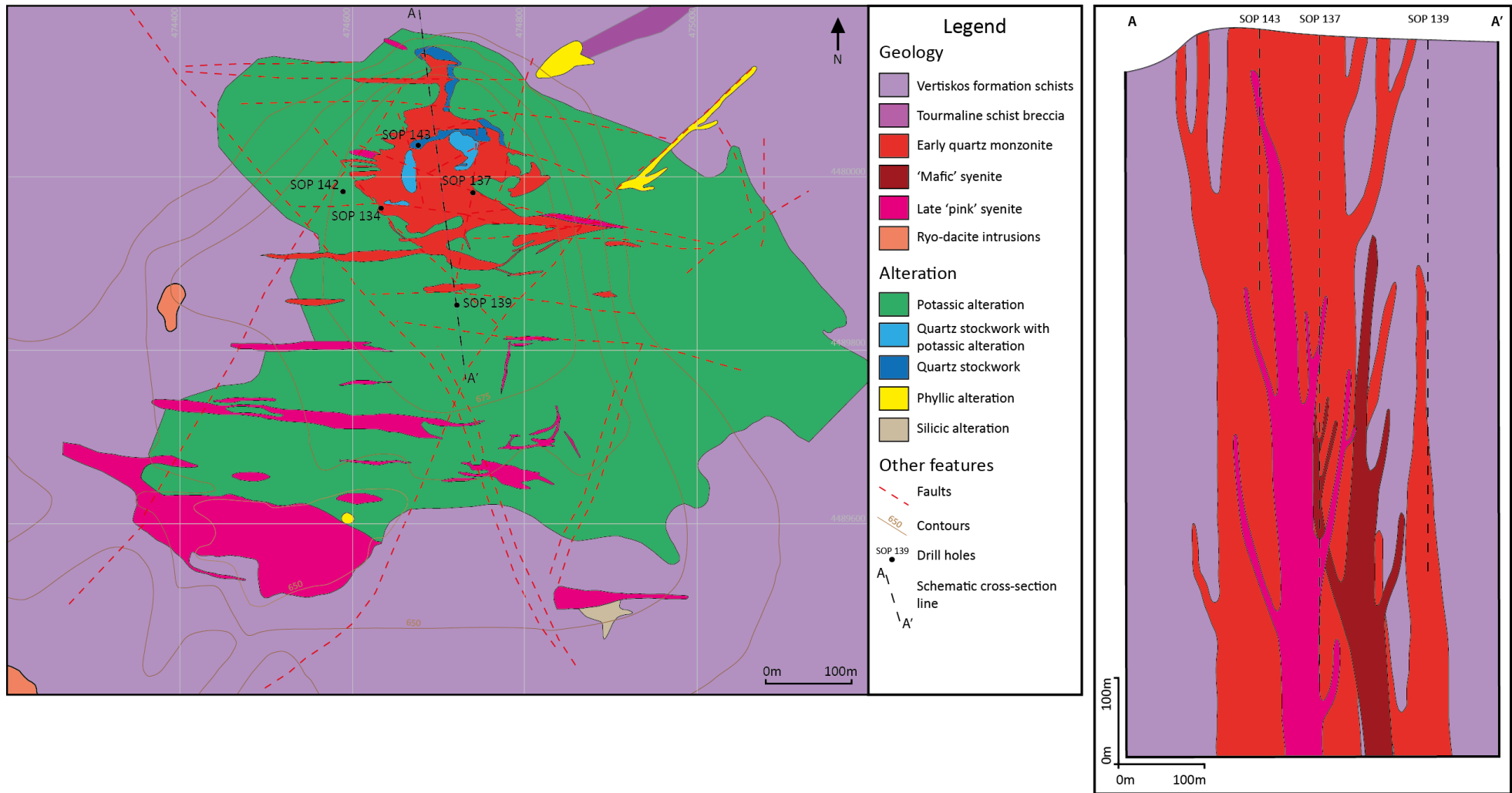


Figure 20: Geological map and schematic cross section of Skouries. Geological map after mapping by TVX Hellas, schematic cross section adapted from Kroll et al (2002) using logging performed in this study. Drill holes shown are ones logged in this study.



#### 4.2.1 Intrusive phases

The Skouries deposit is hosted in a pipe shaped system consisting of several generations of porphyritic intrusions of a monzonitic to syenitic composition (figure 20). These intrusions are similar petrologically, close temporally, and are strongly potassically altered, often obscuring the original petrology. Six logging units were identified by their differing composition, phenocryst size and density, and their cross-cutting relationships (figure 21).

The first intrusive phase in the paragenesis is the 'BPO' unit - a porphyritic quartz monzonite consisting of 70-80% phenocrysts in an aphanitic potassium feldspar matrix: 65-80% subhedral potassium feldspar phenocrysts 3 - 8 mm in diameter, often zoned; 10-25% primary anhedral biotite phenocrysts 1-2 mm in diameter; and 5-10% anhedral quartz phenocrysts 2 - 5 mm in diameter. The zoned potassium feldspars often show remnant plagioclase feldspar centres under transmitted light microscopy, leading to the classification of this unit as a monzonite.

This unit is crosscut by the second intrusive phase, the 'CPO' unit. This is petrologically very similar to the 'BPO' unit, but with a higher proportion of phenocrysts, and larger phenocryst sizes. The 'CPO' has 80-90% phenocrysts consisting of 10-30%, 4-8 mm fairly equigranular anhedral potassium feldspar phenocrysts (average 4mm), often zoned and showing remnant plagioclase feldspar; 20-60% 1-2 mm subhedral potassium feldspar phenocrysts; 5-10% subhedral 1-4 mm biotite phenocrysts (average diameter 3 mm), often altered to magnetite and 5% anhedral quartz phenocrysts <4mm (average 3mm) in an aphanitic potassium feldspar groundmass. It is likely that the BPO and CPO units represent different stages of the same igneous phase as they are petrologically very similar.

The third igneous intrusive phase is a dark grey 'mafic' porphyritic syenite 'GPO', which crosscuts the other units, often brecciating them and infilling fractures. This intrusive phase consists of 5-20% subhedral to euhedral potassium feldspar phenocrysts 2-3mm; 5-10% biotite 1 mm subhedral phenocrysts, 3% 1 mm euhedral amphibole phenocrysts and 1% primary disseminated magnetite in an aphanitic dark grey groundmass. The 'GPO' unit is crosscut by another unit, 'MPO', which contains the same phenocrysts in the same proportions, but with larger crystal sizes - 2 - 8 mm diameter potassium feldspar phenocrysts, and 2 - 4 mm biotite and amphibole phenocrysts. It is likely that these are the same unit at different stages of its evolution, or with different cooling histories.

The final units are the syenite 'PPO' and 'FPO' units. The PPO unit consists of 60% matrix supported phenocrysts: 10 - 35% 3 - 10 mm anhedral-subhedral potassium feldspar; 20-40% 1 - 2 mm anhedral potassium feldspar; 5 - 10% <1 mm anhedral biotite; 2% subhedral 1 - 2 mm

amphibole. These are hosted in a pervasively altered potassium feldspar-rich aphanitic groundmass containing disseminated magnetite. The feldspars are often zoned and the unit contains rare unaltered plagioclase feldspar phenocrysts, along with potassium feldspar megacrysts 1 - 4 cm in diameter. The FPO unit consists of 20% <1 mm potassium feldspar phenocrysts and 5% <1 mm biotite phenocrysts in an aphanitic grey-pink groundmass. The FPO unit crosscuts the PPO unit at shallow levels but below 500 m in the deposit mixing textures are seen between the two units, suggesting that they represent the same igneous phase. In places thin (20 cm to 50 cm) dykes of 'MPO' crosscut 'PPO', suggesting that there is a later dark grey porphyritic syenite intrusive phase. This later phase is usually unaltered and so may represent a late barren phase. v

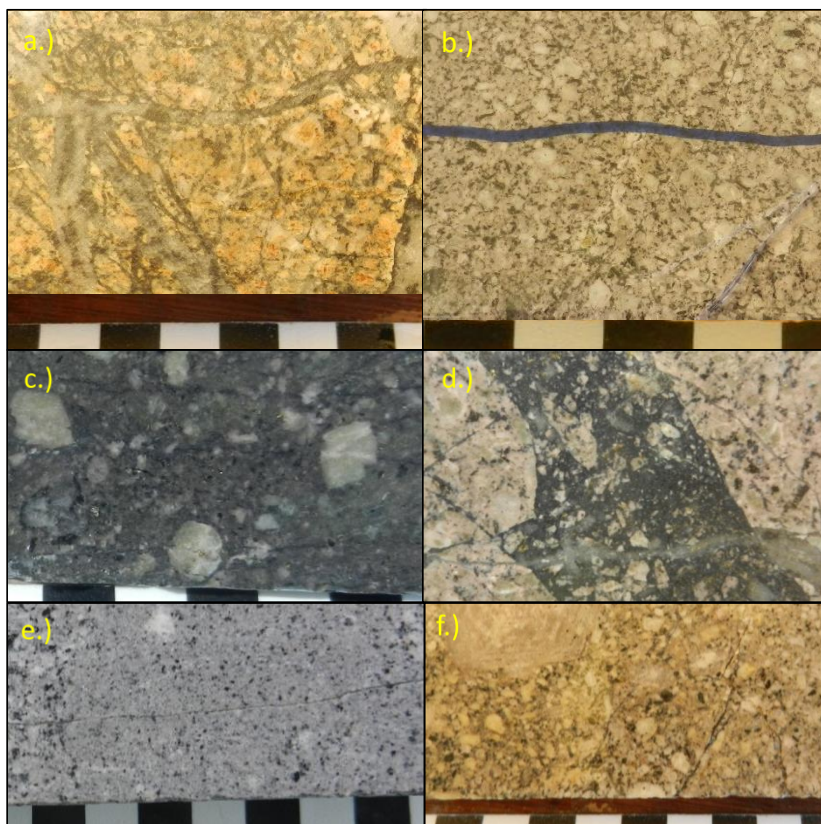


*Figure 21: Photos of the main logging units in drill core: a.) BPO igneous unit – porphyritic quartz monzonite. b.) CPO igneous unit – porphyritic quartz monzonite. c.) MPO igneous unit – porphyritic syenite. d.) GPO igneous unit (porphyritic syenite) brecciating CPO. e.) FPO igneous unit – syenite. f.) PPO igneous unit – porphyritic syenite.*

Although these lithological units were useful distinguishers for logging they show a lot of similarities, with the only distinguishing features commonly being texture and modal percentage of biotite, and so may not be truly separate lithologies. The CPO and BPO units in particular are often mixed and do not show a sharp contact anywhere within the core, instead displaying a gradational boundary. The MPO is seen crosscutting both CPO and BPO, although it is only present for short intervals in the core (20 cm - 2 m). The PPO unit clearly crosscuts the other units,

and so is interpreted to be the latest stage. The FPO unit is found predominately at the base of hole 137, below 700m, and is associated with the PPO unit showing mixing textures. This means FPO may not be a distinct lithology, but instead may represent rapid crystal size change due to fluid release towards the top of the underlying magma chamber. The petrological similarity between the units, along with their cross-cutting, pipe-like morphology suggests that they are dykes intruding from the top of a larger magma chamber at depth, with their changing compositions echoing the development of the magma chamber below, and this agrees with the conclusions reached by previous studies (Kroll et al. 2002). This means that the igneous paragenesis can be simplified to instead indicate phases of magmatic activity - an early quartz monzonite porphyritic phase; an intermineral, more mafic, porphyritic syenite; and a later pink porphyritic syenite phase, potentially followed by a post-mineralisation 'mafic' porphyritic syenite. This means that the intermineral porphyritic syenite may represent a recharge of the magma chamber with more mafic magma, and the later pink porphyritic syenite a return to more felsic magmatism.

#### **4.2.2 Alteration and mineralogy**

The Skouries deposit is a small (less than 400m in diameter) vertical, pipe-like body of quartz-sulphide vein stockwork mineralisation centred on the host porphyry stock. Potassic alteration and copper mineralisation, including veining, extend into the surrounding country rock with approximately two thirds of the measured and indicated tonnes hosted outside the porphyry (Eldorado Gold Corp 2015). Based on crosscutting and overprinting relationships 14 stages of veining and associated alteration have been identified (table 11). These vein and alteration stages have been classified into four groups: early (E) stage, associated with the early quartz monzonite porphyritic phase (BPO and CPO); main (M) stage, associated with the intermineral 'mafic' porphyritic syenites and the later 'pink' porphyritic syenite; and the late (L) stage which crosscuts all of the above and is associated with low temperature alteration assemblages (figure 22).

The Cu-Au mineralisation is associated with the main stage veins, particularly M-3, M-4 and M-5, and in disseminated chalcopyrite and bornite observed in the potassic alteration associated with these veinsets. The Cu in the deposit is primarily hosted in chalcopyrite and bornite, although there is an oxidation horizon down to 30 m containing malachite and azurite; and covellite and chalcocite are found down to approximately 60 m. The precious metals (Au, Ag) are mainly hosted in electrum, which is found as an accessory mineral in potassic alteration, M-3, M-4 and M-5 veins. Rare native gold has also been observed in M-4 veins, and the deposit also contains PGMs and precious metal tellurides and selenides, which are discussed further in chapter 4.

Vein densities range from 74% of the core in the most altered areas to 3.5% in the least altered areas. Vein densities were estimated by eye while logging and recorded as a % of the visible surface area in bisected core for each 2m logging interval. These estimates were then checked using imageJ to analyse photos of core sections in order to calculate the error of the visual estimations in the field. Visual estimates were shown to be accurate to within 10% in high vein density areas, with a tendency to over-estimate vein density, and to within 3% in low vein density areas. The vein type with the highest density are the E-3 veins (see below for full description of vein types), which commonly show vein densities of >45% of the surface area, while the mineralising veinsets, M-3, M-4 and M-5 show vein densities of 3.5% - 11%, with a mean vein density of ~5%. Of these M-5 veins are the most sparse, rarely occurring in densities greater than 4%, while M-4 veins form stockworks of up to 11% of total core area and M-3 veins account for up to 10% of the core area in the sections where they occur, although this is mainly due to their variable thickness (up to 4 cm), rather than increased numbers of veins in one section. Vein density is greatest in the core of the deposit, with drill holes logged within the country rock (SOP 142 and SOP 102A) showing significantly lower vein densities of less than 5%. M-3 veins are only present within the core of the deposit, whereas M-4 and M-5 veins are both present within the surrounding country rock.

The deposit has pervasive, strong, potassic alteration which commonly destroys original textures and mineralogy (figure 23). The large propylitic and phyllic alteration zones seen in other porphyries are not present in Skouries. Propylitic alteration is seen as an irregular and patchy overprint in a narrow halo around the intrusions, while the later phyllic alteration is associated with faults and fractures in the deposit. The different alteration phases of the deposit are described in more detail with relation to their associated vein stages below.

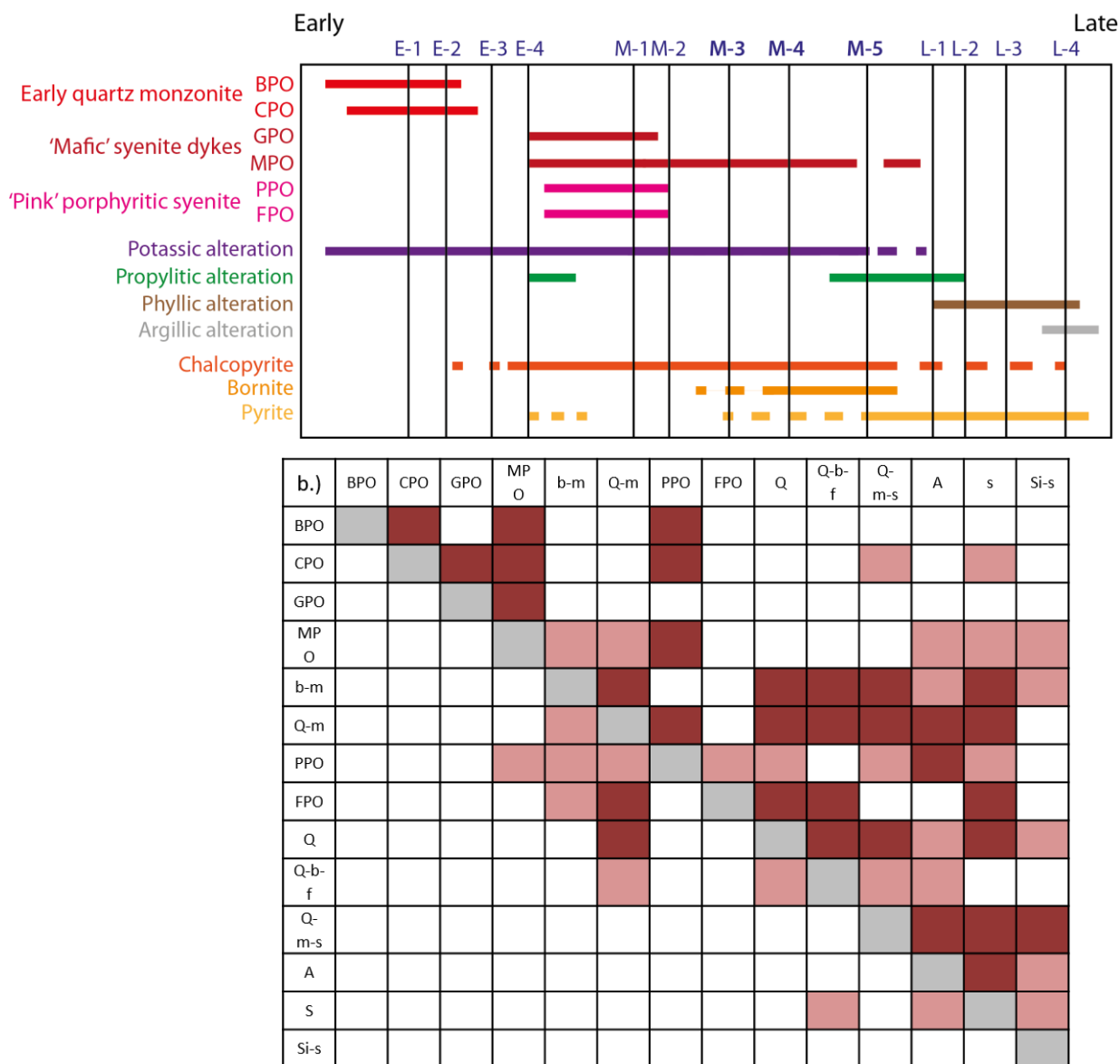


Figure 22: a.) Diagram illustrating the paragenesis of the deposit. This illustrates the crosscutting relationships of the veins and igneous units, and the alteration and ore minerals associated with those phases. Vein stage is represented by the vertical lines, with the mineralising veins (M-3, M-4, M-5) highlighted in bold. b.) Plot showing cross-correlation of the igneous phases and common veinsets (defined by description, not paragenetic vein stage, see table 11). Boxes shaded red illustrate that the phase in the column crosscuts that in the row. Dark red indicates that it is clearly seen crosscutting in several different cores, light red indicates it was seen crosscutting in one core only and only one clear observation was made of this relationship.

Table 11: Description of the main vein stages of the Skouries deposit. Logging descriptors are in brackets.

Vein stage	Vein Type	Associated Igneous Phases	Description	Associated Alteration	Associated mineralisation
E-1A	Biotite-magnetite (b-m)	BPO, CPO	Wavy biotite-magnetite veinlets, 1-2 mm thick, aligned	Orthoclase, biotite, magnetite	
E-2	Quartz (Q)	BPO, CPO	Wavy quartz veinlets 2 – 10 mm thick, regular anhedral quartz crystals.	Orthoclase, biotite, magnetite	
E-3	Quartz-magnetite+/-chalcopyrite (Q-m)	BPO, CPO	Wavy, structurally aligned stockwork of 8 – 20 mm thick quartz veins with magnetite along the margins and disseminated in the centre, sometimes with minor chalcopyrite.	Magnetite	Minor chalcopyrite
E-4	Sulphide - chalcopyrite/pyrite (s)	BPO, CPO	Wavy sulphide veinlet 1-3 mm thick	Magnetite, biotite	Chalcopyrite-pyrite
M-1A	Biotite-magnetite (b-m)	PPO, FPO, MPO, GPO	Wavy biotite-magnetite veinlets, 2-5 mm thick	Orthoclase, biotite, magnetite	
M-1B	Hydrothermal orthoclase	PPO, FPO	Irregular hydrothermal orthoclase veinlets 5 mm to 10 cm thick		
M-2	Quartz (Q)	GPO, MPO, PPO, FPO	Wavy quartz veinlets 2 – 4 mm thick, regular anhedral quartz crystals.	Orthoclase, often altered to sericite	
M-3	Quartz-biotite-orthoclase-chalcopyrite+/-magnetite (Q-b-f-s)	PPO, FPO	Curvilinear quartz veins 8 – 40 mm wide with euhedral potassium feldspar and secondary biotite selvage. Often with massive sulphides in the centre of the vein, intergrown with quartz crystals. Large euhedral quartz crystals.	Secondary biotite, potassium feldspar	Chalcopyrite (bornite)

Vein stage	Vein Type	Associated Igneous Phases	Description	Associated Alteration	Associated mineralisation
M-4	Quartz-magnetite-bornite-chalcopyrite (Q-m-s)	PPO, FPO	Straight veins 1 – 5 cm wide with small anhedral quartz crystals containing trails of sulphides and magnetite parallel to vein edges.	Potassium feldspar, magnetite, secondary biotite, sericite	Bornite, chalcopyrite
M-5	Quartz-chalcopyrite-bornite veins (A veins)	PPO, FPO	Straight quartz veins 1 – 3 cm wide, containing sulphides in a central suture, with small, regular, subhedral crystals.	Potassium feldspar in selvage, chlorite	Chalcopyrite, bornite
L-1	Gypsum	BPO, CPO, GPO, MPO, PPO, FPO	Wavy gypsum veinlets 4 - 8 mm thick	Phyllic alteration, disseminated hematite	
L-2	Sulphide (s)	BPO, CPO, GPO, MPO, PPO, FPO	Wavy pyrite veinlet 2-10 mm thick	Sericite, pyrophyllite	Chalcopyrite-pyrite
L-3	Quartz-calcite	BPO, CPO, GPO, MPO, PPO, FPO	Straight quartz veins 8 – 15 mm with calcite-sericite in a central suture, cloudy white quartz	Sericite, clay	
L-4	Quartz-barite-sulphide (Si-s)	BPO, CPO, GPO, MPO, PPO, FPO	Large quartz-barite veins (5 – 15 cm) with large euhedral 'comb' morphology quartz crystals interlocking with barite. Contain large irregular masses of sulphides. Occasionally contains apatite.	Calcite, dolomite, sericite, clay	Pyrite, sphalerite, galena

#### **4.2.2.1 Early stage veins**

Early stage veins are characterised by abundant magnetite and have indistinct, wavy edges suggesting they formed at very high temperatures towards the temperatures of ductile deformation (estimated temperatures >600°C). They are associated with pervasive potassic alteration assemblages of orthoclase-biotite-magnetite. These alteration minerals are seen replacing primary feldspar, amphibole and biotite phenocrysts, and as disseminated aggregates of biotite-magnetite 1-2 mm thick. The groundmass of the host quartz monzonite is also altered to orthoclase in areas with a high proportion of early veining (figure 24).

The E-1 vein stage contains orthoclase-biotite-magnetite, and consists of wavy to sinuous magnetite-biotite veinlets 1-2 mm thick. E-2 veins consist of wavy to sinuous quartz veinlets 2-10 mm thick, containing regular anhedral quartz crystals. These veins commonly branch and cross-cut each other, and are observed with large secondary orthoclase and biotite phenocrysts overgrowing them.

E-3 veins contain quartz-magnetite+/-chalcopyrite. They consist of a wavy, structurally aligned stockwork of 8 - 20 mm thick quartz veins with magnetite along the margins and disseminated in the centre. Occasionally they also contain minor chalcopyrite disseminated within the vein quartz. They truncate E-1 and E-2 veins and often show over-pressure textures and are interpreted to have formed in a semi-ductile regime. The E-3 veins do not have an alteration envelope meaning that they are interpreted to be in equilibrium with the surrounding potassically altered host rock. The final early stage veins, E-4 veins, contain chalcopyrite-pyrite, and consist of wavy to sinuous sulphide veinlets 1-3 mm thick. These crosscut E-1 to E-3 and are often accompanied by a fine-grained magnetite-biotite alteration selvage.

These early veinsets are only seen in the early quartz monzonite intrusion, not in the later igneous phases. They are also seen in the surrounding Vertiskos gneisses and schists, with the E-3 veinset in particular being commonly seen with a secondary biotite and magnetite alteration selvage.



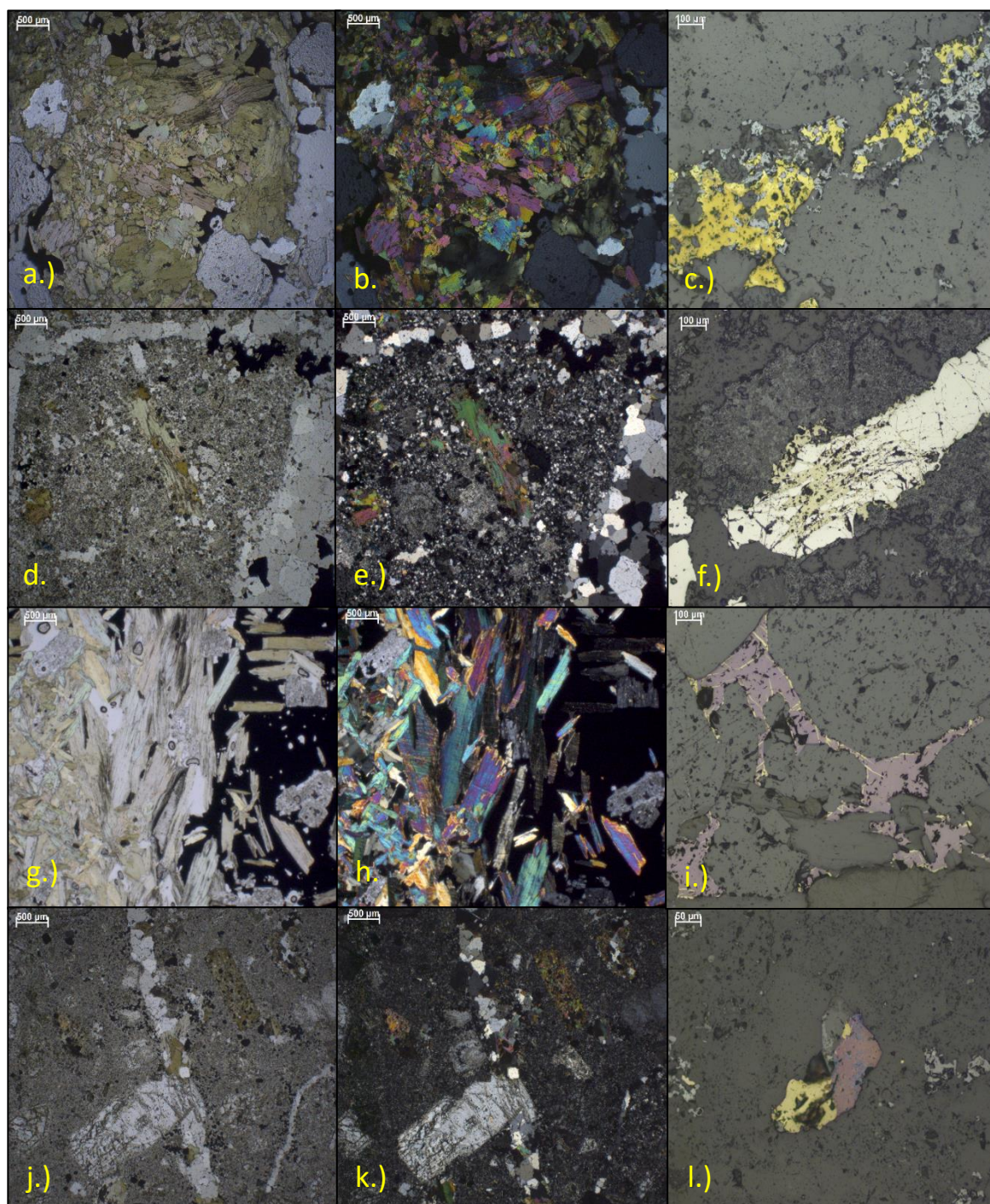


Figure 23: Photomicrographs of the main alteration and mineralisation stages of Skouries: a.) PPL and b.) XPL photomicrograph of biotite alteration on the edge of an M-4 vein, with a chlorite overprint. c.) Chalcopyrite and magnetite in M-4 vein. d.) PPL and e.) XPL photomicrograph of secondary biotite altering primary biotite phenocryst, and potassium feldspar replacing primary plagioclase phenocrysts in an altered feldspar groundmass; E-3 vein crosscuts E-2 vein. f.) Chalcopyrite filling cracks in pyrite in M-5 vein. g.) PPL and h.) XPL photomicrograph of euhedral hydrothermal biotite crystals and potassium feldspar phenocrysts at edge of massive chalcopyrite in an M-3 vein. i.) Chalcopyrite infilling cracks in bornite in M-4 vein. j.) PPL and k.) XPL photomicrograph of altered biotite and feldspar phenocrysts in an altered groundmass, crosscut by an E-2 quartz vein. The vein is overgrown by secondary hydrothermal potassium feldspar and biotite crystals. l.) Chalcopyrite, bornite and magnetite in an M-4 vein.

#### 4.2.2.2 Main stage veins

The main stage veinsets are characterised by a potassic alteration assemblage consisting of orthoclase, biotite and magnetite; as well as the presence of bornite and chalcopryrite. They are associated with the intermineral 'mafic' porphyritic syenites and the later 'pink' porphyritic syenite, both of which cross-cut the early veins. Pervasive orthoclase alteration of the groundmass of the 'pink' porphyritic syenite occurs wherever main stage veining is observed, along with secondary biotite and magnetite alteration of the mafic phenocrysts in both this unit and the intermineral 'mafic' porphyritic syenite. Main stage veining is also associated with disseminated secondary magnetite alteration envelopes, commonly with chalcopryrite and bornite also disseminated with the magnetite (figure 24). Where the potassic alteration associated with main stage veining overprints that associated with the early stage veining it results in any remnant primary textures or mineralogies being completely destroyed. In places barren 'mafic' porphyritic syenite dykes crosscut the main stage lithologies, and the first 4 vein stages (M-1 to M-4). Although M-5 veins are observed cross-cutting these dykes in places, they are not spatially associated with them, and are instead associated with the 'pink' porphyritic syenite, and so are considered to be part of the main stage veinsets.

The M-1 veinset contains hydrothermal biotite-magnetite-orthoclase. Two generations of M-1 structures occur: M-1A consists of sinuous biotite-magnetite veinlets 2 - 5mm thick, while M-1B consists of irregular hydrothermal orthoclase veinlets 5 mm - 10 cm thick which commonly show over-pressure textures or broaden to flood an area, creating large irregular patches of hydrothermal orthoclase. M-1A veins are known to be distinct from E-1 veins as they are observed truncating E-2 veins, and crosscutting E-1 and E-3 veins, however they are truncated by M-1B veins. M-2 veins consist of wavy, irregular quartz veinlets 2-4 mm. These commonly truncate in the middle of the core, and are seen crosscutting the early veinsets. They have a fine grained orthoclase alteration envelope 1-2 mm wide, which is sometimes altered to sericite, although this is interpreted to be a later event.

The M-3 veinset contains biotite, orthoclase, quartz and chalcopryrite +/- magnetite, with minor bornite. These are wavy, discontinuous and curvilinear quartz veins 8 - 40 mm wide, with a 5 - 20 mm wide interlocking potassium feldspar and secondary biotite selvage. The crystals of quartz, orthoclase and biotite are all euhedral and >6 mm, and both embayments and large crystals of biotite and orthoclase are commonly seen within the vein. M-3 veins have massive chalcopryrite in the centre. This chalcopryrite is 3 - 30mm thick, and commonly encloses euhedral quartz crystals towards the edges of the sulphide, sometimes along with biotite and orthoclase crystal inclusions. The smaller M-3 veins can contain trails of sulphide crystals, including bornite, though bornite is

rare in this veinset. These veins are interpreted to have formed under semi-ductile conditions within the 'pink' syenitic porphyry intrusion. This means that they are likely to have formed deep in the system, probably below 2 km depth.

Veinset M-4 contains magnetite, biotite, orthoclase, quartz, bornite and chalcopryrite. M-4 consists of sinuous to straight veins 1 - 5 cm wide with small anhedral quartz crystals, containing trails of chalcopryrite-bornite and magnetite parallel to vein edges. These commonly have an orthoclase selvage 5-10 mm wide, and are accompanied by a disseminated magnetite alteration envelope. M-4 veins have more bornite than chalcopryrite, with chalcopryrite commonly forming a secondary phase in fractures within bornite.

The M-5 stage veins consist of straight, planar quartz veins 1 - 3 cm wide, containing sulphides in a linear central suture, with small, regular, subhedral crystals. The sulphides present are pyrite-chalcopryrite-bornite, with pyrite appearing to be the earliest phase and, unlike M-4, they contain more chalcopryrite than bornite, with the chalcopryrite and bornite appearing to be co-precipitated. They are associated with biotite-orthoclase-chlorite alteration and often have an orthoclase selvage 5 mm wide. Secondary biotite alteration around M-5 veins often shows regression to chlorite, and the M-5 veins are often associated with minor specularite, barite, anhydrite and sericite, and very rare epidote.

The main stage veins are seen mainly in the 'pink' porphyritic syenite, with M-1B only being found in this lithology. M-3 is only very rarely observed in other lithologies, while M-1A and M-2 are commonly observed in other lithologies, and M-4 and M-5 veins are observed in almost all lithologies, and in the surrounding Vertiskos formation where they have a magnetite-biotite alteration selvage 20 - 40 mm wide.

#### **4.2.2.3 Late stage veins**

The late stage veins in the Skouries deposit are associated with phyllic alteration assemblages of sericite, quartz, calcite and dolomite, and with minor advanced argillic assemblages of kaolinite and pyrophyllite. Argillic alteration minerals are also found around small faults which are present throughout the core of the deposit (figure 2, figure 4).

L-1 stage veins consist of wavy gypsum veinlets 4 - 8 mm thick. These are found in areas with phyllic alteration and are associated with disseminated hematite. L-2 stage veins are wavy to sinuous pyrite veinlets 2-10 mm thick with a sericite-pyrophyllite alteration selvage. These are found in structurally controlled fractures, and crosscut most of the rest of the lithologies and veinsets. L-3 veins consist of straight quartz veins 8 - 15 mm with calcite-sericite in a central suture and a sericite-clay alteration selvage. They are fairly rare and are found in fractures. L-4



veins are irregular quartz-barite veins 5 - 15 cm thick with large euhedral 'comb' morphology quartz crystals on the outer edges of veins, while the centre consists of white fine grained quartz interlocked with barite crystals. The veins contain irregular masses of pyrite-sphalerite-galena, usually only in the fine grained central section, and occasionally contain apatite. They are surrounded by a calcite-dolomite-sericite-clay alteration envelope, and are found in vicinities with intense fracturing, usually structurally aligned with the fractures.

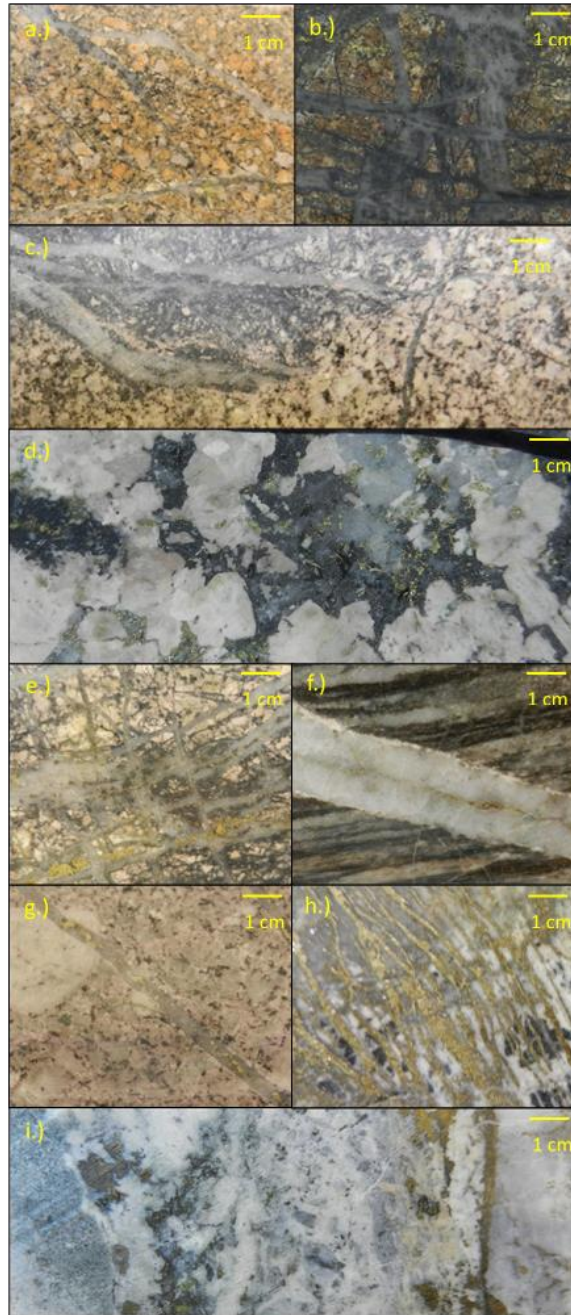


*Figure 24: Photos of the main mineralising veinsets: a.) E-1 biotite-magnetite veins crosscut by E-2 quartz veins and an E-3 quartz magnetite vein in CPO. b.) E-3 stockwork in BPO. c.) PPO dyke crosscutting BPO with E-3 veins. d.) M-3 vein in PPO – euhedral orthoclase and biotite alteration selvage. e.) M-4 veins in PPO. f.) M-5 in biotite schist country rock. g.) Small M-3 vein in PPO. h.) Sulphide veinlets (L-2) crosscutting silica alteration. i.) L-4 vein with barite, calcite and pyrite.*

Late stage veining, and the associated phyllic and argillic alteration are found in fault zones and associated with late fractures which crosscut the early and main stages. They are not found in the surrounding country rock and their distribution is patchy and rare.

#### 4.2.3 Ore mineral paragenesis and accessory minerals from SEM

8 polished thin sections from the main stage of the mineralisation were examined on the SEM in order to investigate the sulphide paragenesis, to identify any minor accessory minerals or unknowns and to create element maps of samples (see chapter 2 for methods).

Several microscopic accessory minerals were identified (figure 25) - chromites are commonly present in the potassically altered early quartz monzonite, with chromite, nichromite  $((\text{Ni}, \text{Co}, \text{Fe}^{2+})(\text{Cr}, \text{Fe}^{3+}, \text{Al})_2\text{O}_4)$ , and manganochromite  $((\text{Mn}, \text{Fe}^{2+})(\text{Cr}, \text{V})_2\text{O}_4)$  all being identified using EDS. Thorite crystals 5 - 10  $\mu\text{m}$  were observed in all samples analysed, and this ties in with the unusually high Th contents reported for Skouries (Kroll et al. 2002). The thorites are found within potassic alteration, as inclusions in hydrothermal biotites, and associated with disseminated hydrothermal magnetite and orthoclase. This suggests that the thorite is hydrothermal, rather than primary. Rare coffinite  $\text{U}(\text{SiO}_4)_{1-x}(\text{OH})_{4x}$  is also present in potassic alteration, and Ce and Th rich monazites and zircons were also identified as accessory minerals. The monazites were found in M-3 type veins as inclusions in quartz and in chalcopyrite, as were thorite crystals, suggesting they are hydrothermal. Rare crystals of pure Sn were also found as inclusions in hydrothermal biotite in the potassic alteration surrounding the main stage veins.

Veinset M-3 contains hematite as well as magnetite, with hematite replacing both chalcopyrite and magnetite (figure 25). There are minor amounts of molybdenite in M-3, along with early chalcopyrite and galena, and late pyrite. The bornites in M-3 are very Bi rich, and show dissolution textures with wittichenite (see chapter 5 for a more in depth discussion of semi-metals in Skouries). Rare blebs of native gold  $<5 \mu\text{m}$  were observed between quartz crystals in the M-3 veins.

Veinset M-4 contains, in order of paragenesis, chalcopyrite, bornite, galena and magnetite. The bornites in M-4 contain Bi, and antimony accessory minerals are present (figure 26). Veinset M-5 contains pyrite, chalcopyrite, galena, bornite and minor magnetite. Pyrite was observed as inclusion within chalcopyrite, showing that pyrite is the first mineralising phase. Galena is present as both inclusions within chalcopyrite and on the edges of chalcopyrite, completely rimming crystals in some cases, suggesting there were either several generations of galena or it was co-precipitated with chalcopyrite. The bornite appears to predate the chalcopyrite, and is observed

being replaced by magnetite. In places clay alteration, magnetite and secondary silica are observed replacing chalcopyrite, perhaps showing a later fluid phase.

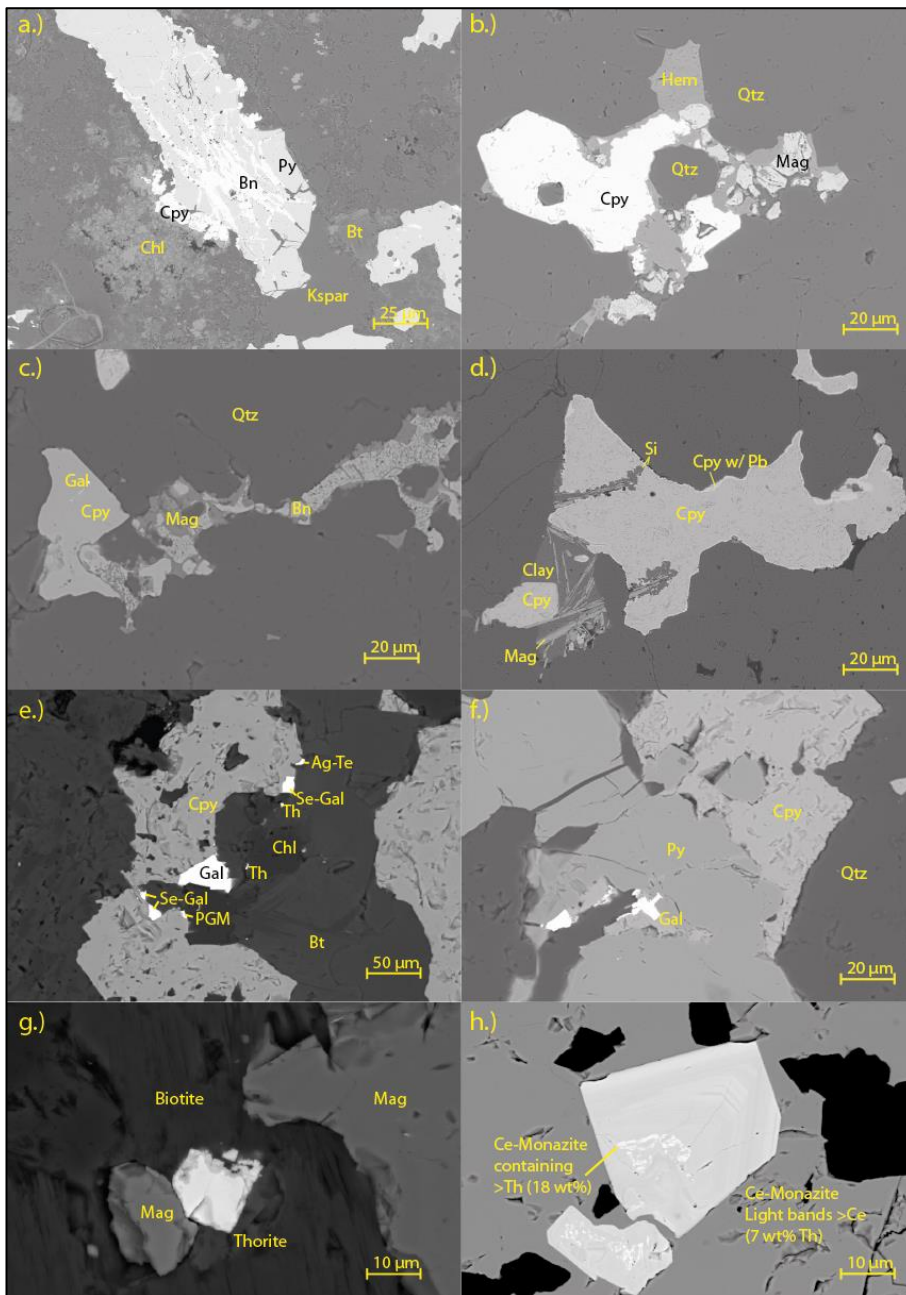


Figure 25: BSE images of mineralised veins in Skouries: a.) Bornite and chalcopyrite filling crack in pyrite crystal in potassic alteration selvage retrograding to propylitic around an M-3 vein b.) Chalcopyrite, hematite and magnetite in centre of M-3 vein – hematite altering chalcopyrite c.) Magnetite altering bornite in centre of M-5 vein d.) Silica alteration of chalcopyrite in M-5 vein, thin film of galena coating chalcopyrite e.) Se rich galena on edge of chalcopyrite in alteration selvage of M-3 vein f.) Chalcopyrite precipitating around early pyrite phase with late galena infilling cracks in M-5 g.) Thorite and magnetite in biotite alteration selvage of M-3 vein h.) Hydrothermal Ce and Th rich monazite in quartz in the centre of an M-3 vein. (Bn = bornite, Bt = biotite, Chl = chlorite, Cpy = chalcopyrite, Gal = galena, Hem = hematite, Mag = magnetite, PGM = platinum group mineral, Py = pyrite, Qtz = quartz, Th = thorite).



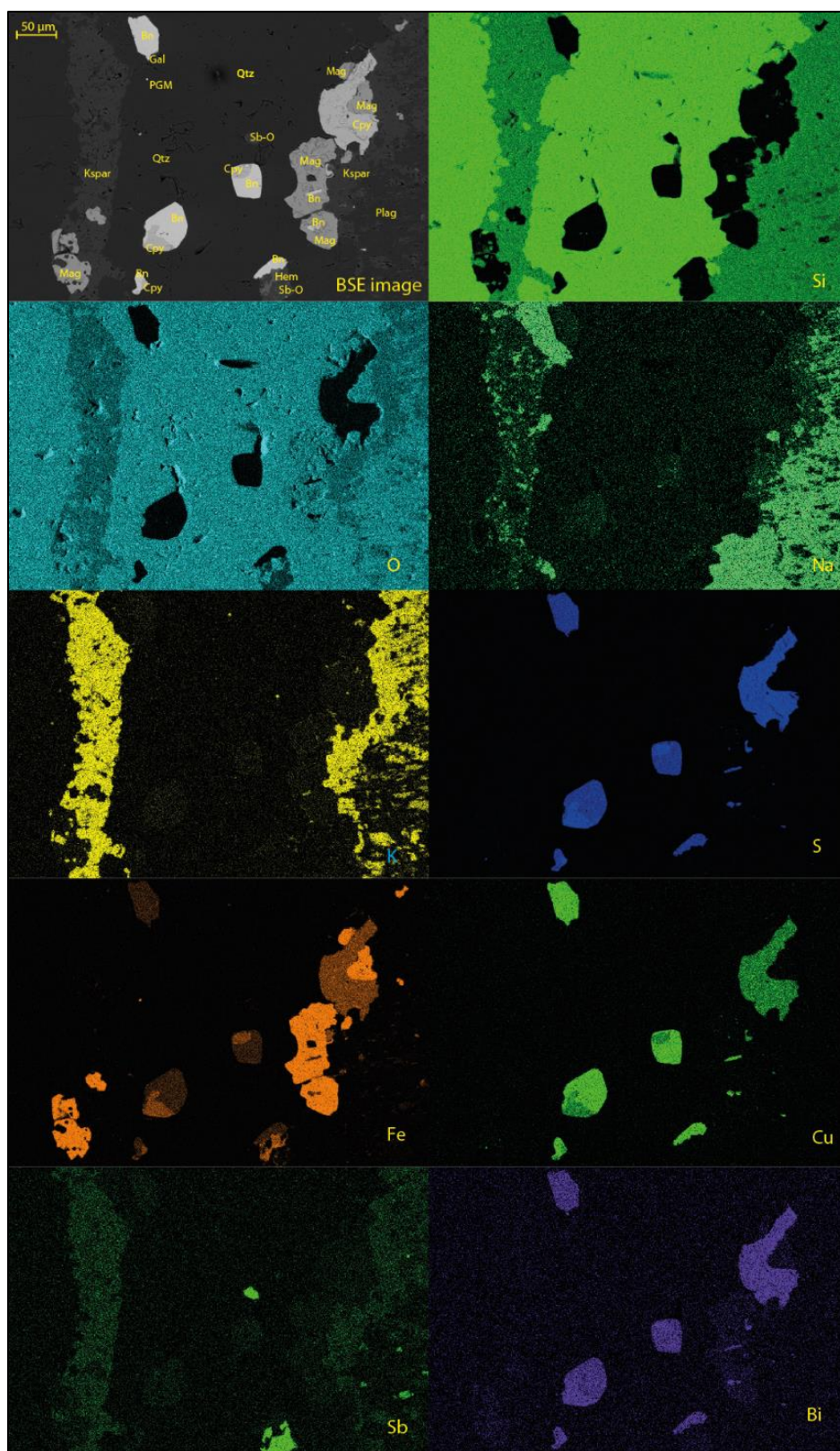


Figure 26: EDS element map of an M-4 vein showing element distribution within the vein – Si, O, Na, K, S, Fe, Cu, Sb and Bi shown here. The potassic alteration envelope can be seen, Bi is hosted in bornites (this has been confirmed with EPMA – see chapter 5), an unidentified antimony oxide mineral is present.

### 4.3 Stable isotopes

Stable isotope analyses were completed at the Scottish Universities Environmental Research Centre (SUERC) in East Kilbride.

#### 4.3.1 Sulphur isotopes

Sulphur isotope analyses were performed on 24 samples representing the different paragenetic stages and spatial areas of the deposit. ‘Conventional’ analysis of hand-picked sulphides (after Robinson & Kusakabe 1975; discussed in more detail in chapter 2) was performed on bornite, chalcopyrite and pyrite. These were extracted by crushing and picking, or in areas with very small amounts of sulphide by drilling out with a dental drill.

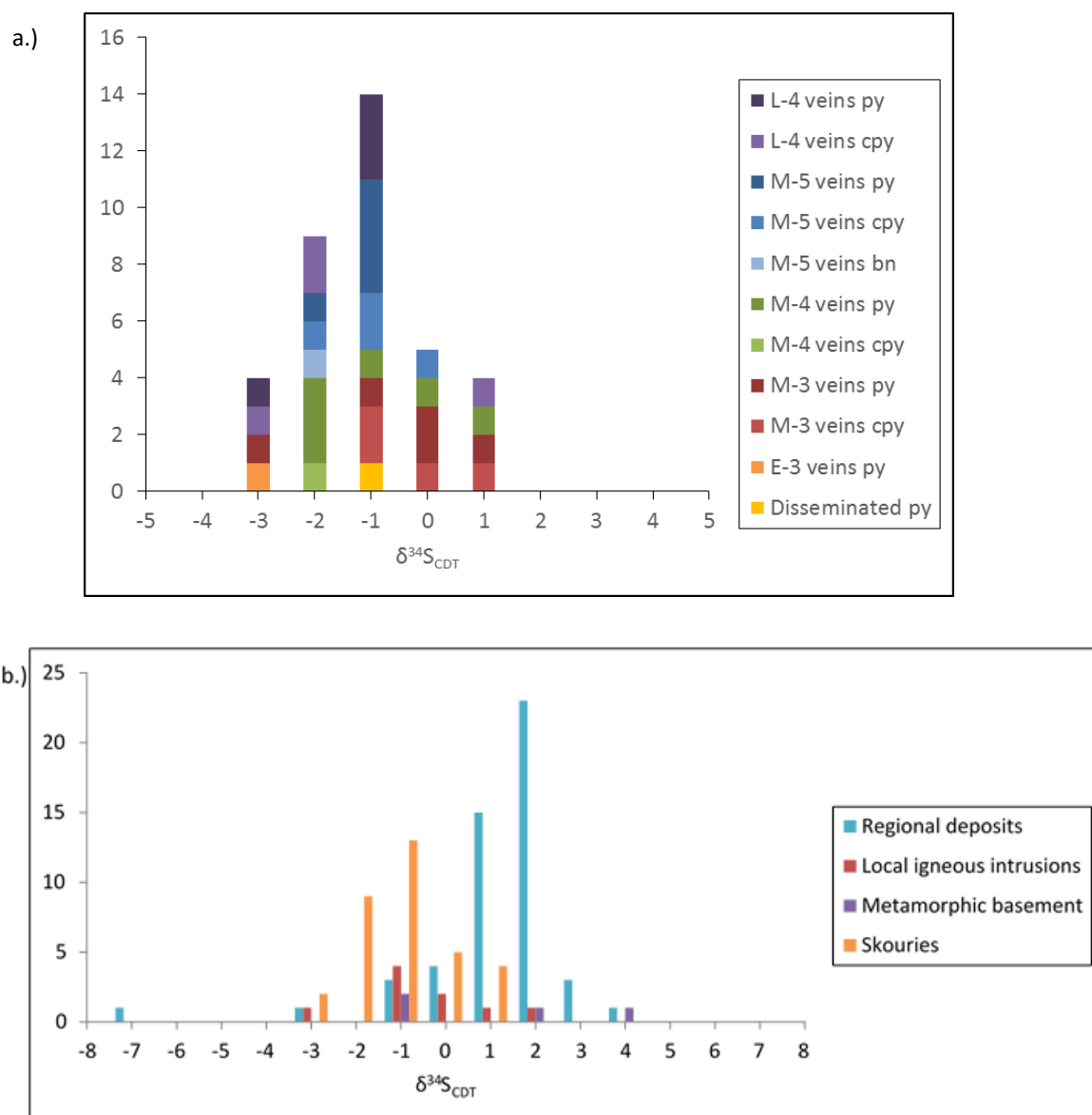


Figure 27: a.)  $\delta^{34}\text{S}_{\text{CDT}}$  results from this study discriminated by veinset and sulphide type. b.)  $\delta^{34}\text{S}_{\text{CDT}}$  values for local igneous intrusions, metamorphic basement and regional deposits Olympias, Stratoni and Piavitsa (Hahn, 2015) plotted against data for Skouries from this study.



The sulphur isotope ( $\delta^{34}\text{S}_{\text{CDT}}$ ) values for Skouries range from -3.8‰ to +1‰, with an average of -1.4‰ (n=36; appendix A3.1). This relatively narrow range of values shows limited grouping when discriminated by veinset (figure 27). The earliest mineralising veinset, veinset M-3, has  $\delta^{34}\text{S}_{\text{CDT}}$  values of -3.8‰ to +1‰, with an average of -1‰. Veinset M-4 has  $\delta^{34}\text{S}_{\text{CDT}}$  values of -3.2‰ to +0.8‰, with an average of -1.7‰. The latest mineralising veinset of the main deposit phase, M-5, has  $\delta^{34}\text{S}_{\text{CDT}}$  values of -2.3‰ to -0.4‰, with an average of -1.4‰. The pyrite bearing L-3 veinset has  $\delta^{34}\text{S}_{\text{CDT}}$  values of -3‰ to +0.8‰, with an average of -1.75‰.

These are similar to the values reported in Frei (Frei 1995), who reported  $\delta^{34}\text{S}_{\text{CDT}}$  values of -2.14‰ to 0.3‰, with an average of -0.55‰. The  $\delta^{34}\text{S}_{\text{CDT}}$  results from Skouries were compared with data from regional igneous intrusions (figure 27), metamorphic basement and local carbonate replacement deposits thought to be spatially and temporally linked to Skouries (Olympias, Stratoni, and Piavitsa) (Hahn 2015). Skouries has  $\delta^{34}\text{S}_{\text{CDT}}$  values 1-2‰ lower than the regional deposits, which have a mean  $\delta^{34}\text{S}_{\text{CDT}}$  of +1.5‰. Skouries  $\delta^{34}\text{S}_{\text{CDT}}$  values however are similar to the values measured for primary sulphides from the surrounding igneous intrusions (Hahn 2015).

#### 4.3.2 Oxygen and hydrogen isotopes

Oxygen analysis was performed on 9 crushed and picked samples of vein quartz representing the main mineralising and early vein stages of the deposit. The  $\delta^{18}\text{O}_{\text{H}_2\text{O}}$  values of ore-forming fluids from quartz were calculated using the equation  $1000\ln\alpha_{\text{quartz-H}_2\text{O}} = 3.38 \times 10^6 T^{-2} - 3.40$  (Clayton et al. 1972). Hydrogen isotope analyses were obtained from 6 coarsely crushed samples of cleaned vein-quartz from the same samples analysed for oxygen isotopes.

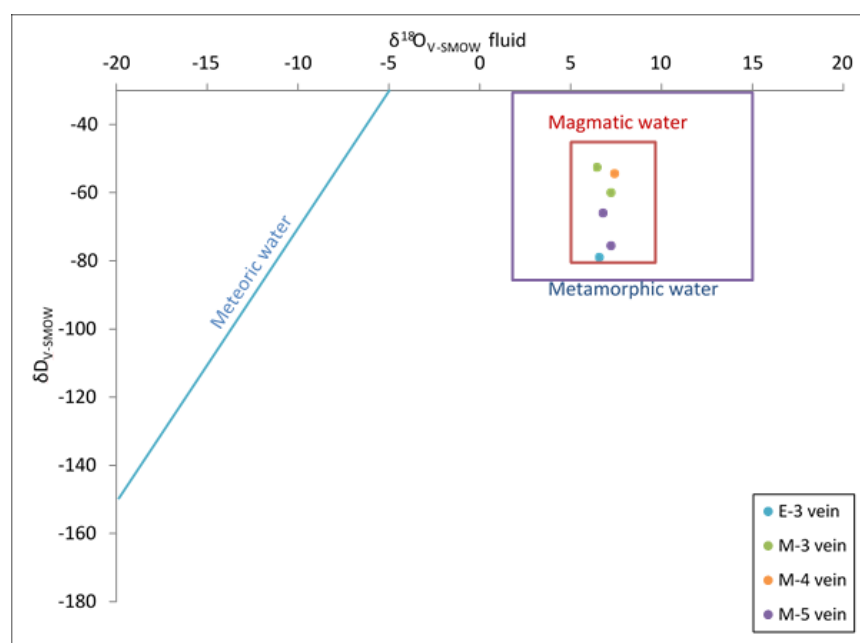


Figure 28:  $\delta^{18}\text{O}_{\text{V-SMOW}}$  fluid ( $T = 450^\circ\text{C}$ ) plotted against  $\delta\text{D}_{\text{V-SMOW}}$  data discriminated by vein stage. Fluid  $\delta^{18}\text{O}$  calculated according to equation from Matsuhisa et al (1979). Magmatic, metamorphic and meteoric water values from Taylor & Sheppard (1986).

The oxygen isotopes in Skouries have quartz  $\delta^{18}\text{O}_{\text{V-SMOW}}$  values of 9.5‰ to 10.5‰, with an average of 10‰ (n=9, appendix A3.1). When corrected for fluid temperatures of approximately 450°C this gives fluid  $\delta^{18}\text{O}_{\text{V-SMOW}}$  values of 6.42‰ to 7.42‰, with an average of 6.94‰. These values are similar to that reported by Frei (1995), who reported a vein quartz  $\delta^{18}\text{O}_{\text{V-SMOW}}$  value of 9.29‰. The hydrogen isotopes show slightly more spread, with  $\delta\text{D}_{\text{V-SMOW}}$  values of -79‰ to -52.6‰, with an average of -64.6‰ (n=6, appendix A3.1). These do not show any correlation when discriminated by vein type. When plotted against each other (figure 28) they plot within the magmatic fluid field.

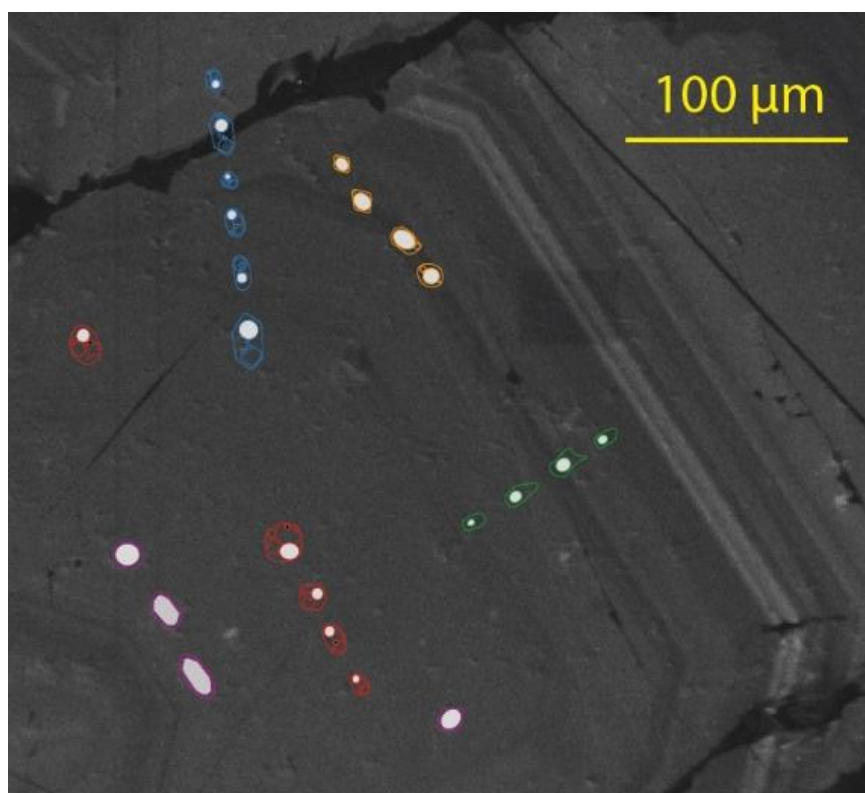
## 4.4 Fluid inclusions

### 4.4.1 Petrography

Doubly polished 150 µm thick fluid inclusion wafers were examined from 7 vein samples (appendix A3.2) representing the early and main stage veinsets. These were examined petrographically in order to determine the types and population distribution of fluid inclusions, and to identify samples suitable for micro thermometric analysis. Fluid inclusions were classified according to their phase relationships at 20°C, using the classification scheme from Nash (Nash 1976) to divide them into broad categories and the criteria from Roedder (Roedder & Ribbe 1984) to further identify assemblages and estimate their origin. Types I, III, IV and possibly II of Nash (1976) were found in Skouries (table 12). Laser raman analysis was performed on the fluid inclusions present in 3 of the samples, representing the three different main stage mineralising vein types, in order to confirm their petrology and to identify if CO<sub>2</sub> or CH<sub>4</sub> is present (appendix A3.3).






The type I inclusions are irregular in shape, often with cracks surrounding them and some leaking visible and with phase ratios which are not consistent across assemblages. Rare type I inclusions are observed with a regular oblong morphology, and have consistent phase ratios across an assemblage with 5 - 20% of their 2D surface area taken up by the vapour bubble and these are interpreted to be intact. Raman analysis has shown the presence of CO<sub>2</sub> in the vapour bubble - this is likely to be an immiscible film around the edge of the bubble; however, this was not observed optically. Some of the bubbles seem to 'dance' at room temperature, confirming the presence of CO<sub>2</sub>. These inclusions are 5 - 20 µm in diameter (or along the longest axis), and are observed in the centre of crystals, or in trails crossing growth zones but not crystal boundaries (figure 29).

The type II inclusions are oblong or diamond shaped and contain 80-95% vapour (estimated from 2D surface area). They can contain either an opaque daughter mineral, or a translucent one which can be identified as halite in some inclusions, and abuts the edge of the inclusion. However the phase ratios vary amongst this population, with many not containing a daughter mineral, or showing different daughter mineral types. A significant proportion of the diamond shaped inclusions are observed to have leaked. The inclusions are 15 - 30  $\mu\text{m}$  along the longest axis and are found both trapped along crystal boundaries and as trails across crystals, truncating at crystal boundaries (figure 29).



*Figure 29. Sketch of the fluid inclusion types overlaying a CL image of a quartz crystal from an M-4 vein to illustrate typical inclusion shapes and assemblage structures (vapour phase shaded grey). Type I inclusions (green) crosscut growth zones, type II inclusions (orange) both follow and crosscut growth zones, type IIIA inclusions (red) are isolated inclusions and follow growth zones, type IIIB inclusions crosscut growth zones and crystal boundaries while type IV inclusions (purple) follow growth zones and are found as isolated inclusions.*

Table 12: Summary of the main features of the fluid inclusion types observed in the main mineralising veinsets (\*=confirmed by Raman spectroscopy)

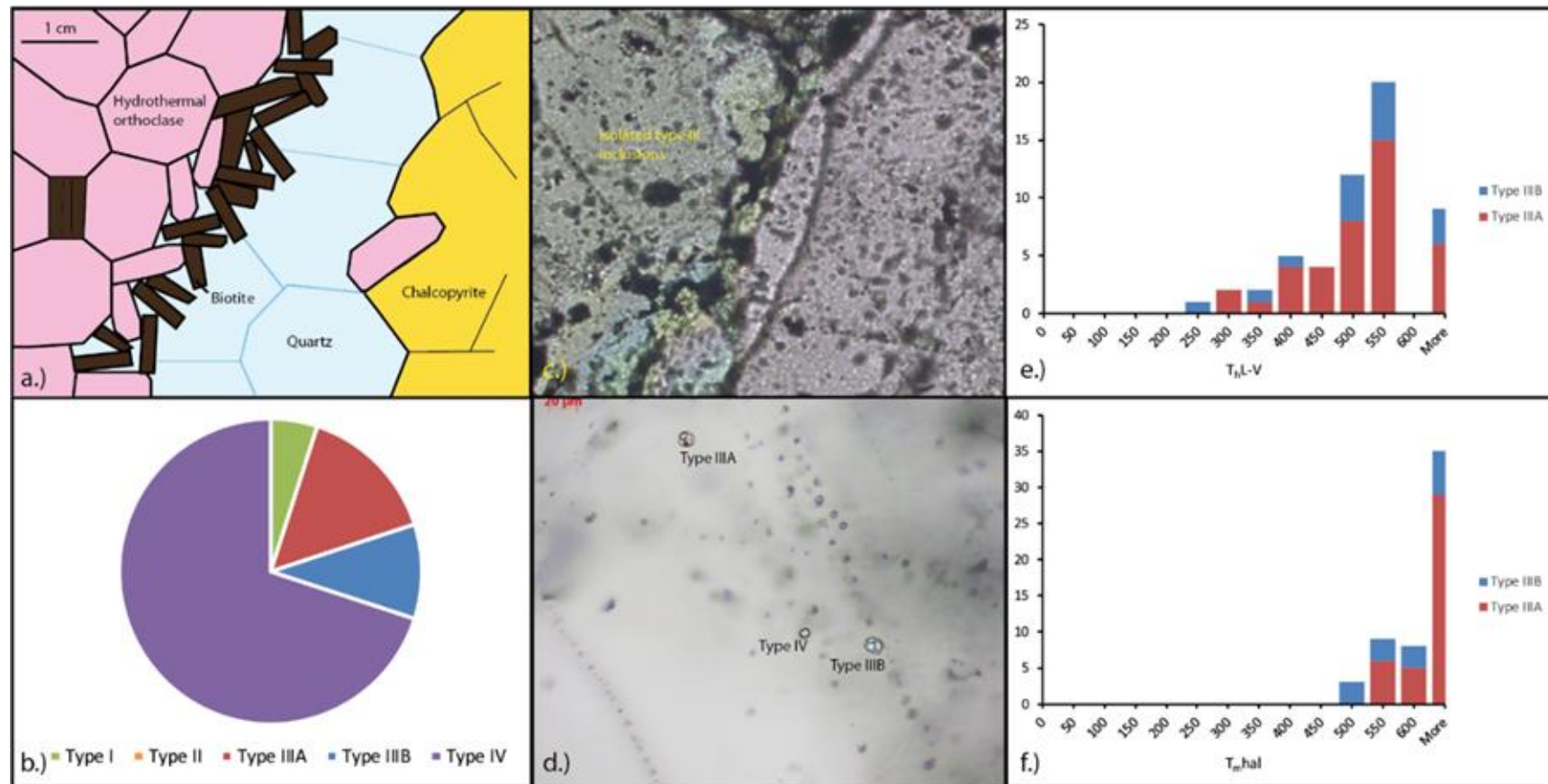
Inclusion Type	Major phases	Minor phases	Vapour %	Inclusion shape and occurrence	Inclusion size (μm)	Vein stage	Homogenization characteristics	Photo
I	Liquid (H <sub>2</sub> O*), vapour (CO <sub>2</sub> *)	None	10-20	Elongate, usually decrepitated; primary and pseudo-secondary	5-20	M-3, M-4, M-5	To liquid	
II	Liquid (H <sub>2</sub> O*), vapour (CO <sub>2</sub> *)	Opaque and translucent daughter minerals	80-95	Oblong or diamond shape, sometimes developing negative crystal morphology; pseudo-secondary	15-30	M-4, M-5	To liquid	
IIIA	Liquid (H <sub>2</sub> O*), vapour (H <sub>2</sub> O/CO <sub>2</sub> *), halite, sylvite, hematite	Hematite +/- anhydrite*, barite*, opaque and translucent daughter minerals including FeCl	15-30	Round to negative crystal morphology; primary and pseudo-secondary	5-50	E-2, E-3, M-3, M-4, M-5	Halite dissolution	
IIIB	Liquid (H <sub>2</sub> O*), vapour (H <sub>2</sub> O*), halite, sylvite	Anhydrite*, barite*, opaque and translucent daughter minerals including FeCl	15-30	Round to negative crystal morphology; pseudo-secondary and secondary	5-50	E-2, E-3, M-3, M-4, M-5	Halite dissolution	
IV	Vapour (CO <sub>2</sub> *), minor liquid (CO <sub>2</sub> *)	None	90-100	Round, teardrop shaped or negative crystal morphology; primary and pseudo-secondary	5-20	E-2, E-3, M-3, M-4, M-5	To vapour	

Type III inclusions all contain halite and sylvite daughter minerals, with a vapour bubble which covers 15 - 30% of the 2D surface area of the crystal. These crystals are observed with a round or negative crystal morphology 5 - 50  $\mu\text{m}$  along the longest axis. There are several different daughter mineral assemblages present in these inclusions, often all within the same sample and sometimes even the same field of view. While approximately 10% of type III inclusions contain a single free halite and sylvite crystal, the rest of the type III inclusions are >50% daughter minerals by 2D area, with the daughter minerals compressed both against each other and the edges of the vein. 65% of the type III inclusions contain a large hematite crystal several halite and sylvite crystals and other translucent daughter minerals, and these have been defined as type IIIA. The remaining 35% do not contain hematite, with raman identifying anhydrite in many of the non-hematite bearing inclusions, and are defined as type IIIB. FeCl, chalcopyrite, pyrite and other opaques have also been identified under the microscope in both type IIIA and type IIIB inclusions, and raman spectroscopy identified  $\text{CO}_2$  in the vapour bubble of type IIIA inclusions, but only  $\text{H}_2\text{O}$  in the vapour bubble of type IIIB inclusions, showing them to have formed from chemically distinct fluids. Phase proportions are not always constant across these inclusion populations, although some assemblages are present with identical phase proportions. Type IIIA inclusions are present as both solitary inclusions and trails trapped in, and occasionally cross-cutting, growth zones but truncating at crystal edges (figure 29), while type IIIB inclusions are commonly observed in trails cross-cutting both growth zones and crystal boundaries. The daughter minerals present in these type III inclusions were further examined using SEM (see below).

The type IV inclusions are pure  $\text{CO}_2$  (shown by raman), and are 90-100% vapour. These inclusions are 5 - 20  $\mu\text{m}$  with round, teardrop or negative crystal morphologies, and occur as both solitary isolated inclusions, trails of inclusions trapped within growth zones or as trails which cross-cut growth zones but truncate at crystal boundaries.

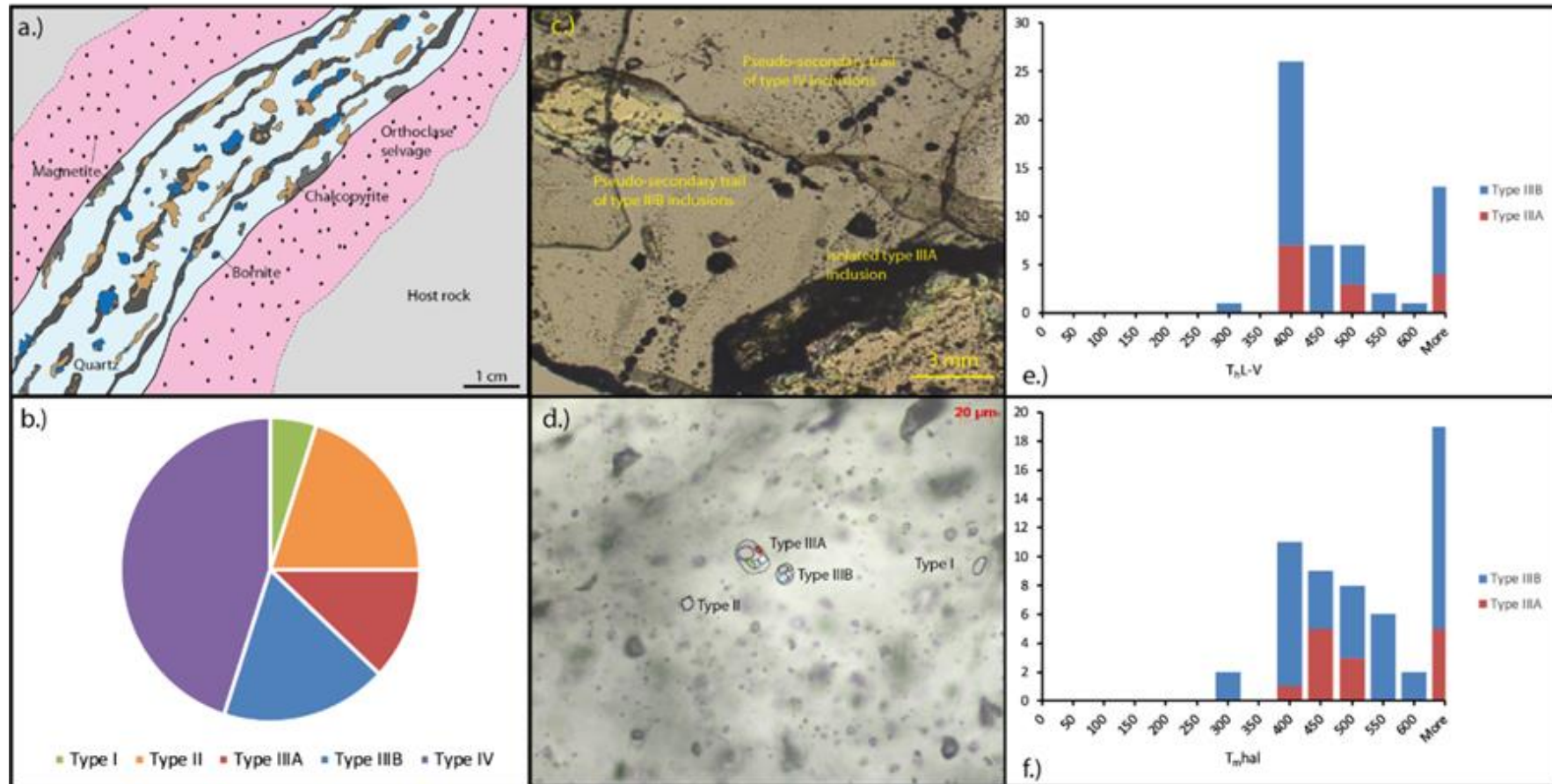
Figure 30: Summary figure of three main mineralising veinsets – M-3, M-4 and M-5. Figures a.) are a schematic representation of the mineralised veins showing the mineralisation and alteration textures and the quartz crystal morphologies. b.) Pie charts showing the proportions of the different inclusions types (Nash, 1979). c.) Photo of quartz crystals showing the gross inclusions patterns. d.) Photomicrograph of typical fluid inclusion assemblages from the veinsets with sketches of the dominant types in each veinset showing the daughter minerals. e.) Histogram of vapour homogenisation temperatures for the type III inclusions in each veinset. f.) Histogram of halite dissolution temperatures for the type III inclusions in each veinset. Figure shows the evolution of the fluids from CO<sub>2</sub> rich to brine rich during from the earliest mineralising veinset M-3 to the latest, M-5, and from lower to higher temperatures.

### Veinset M-3

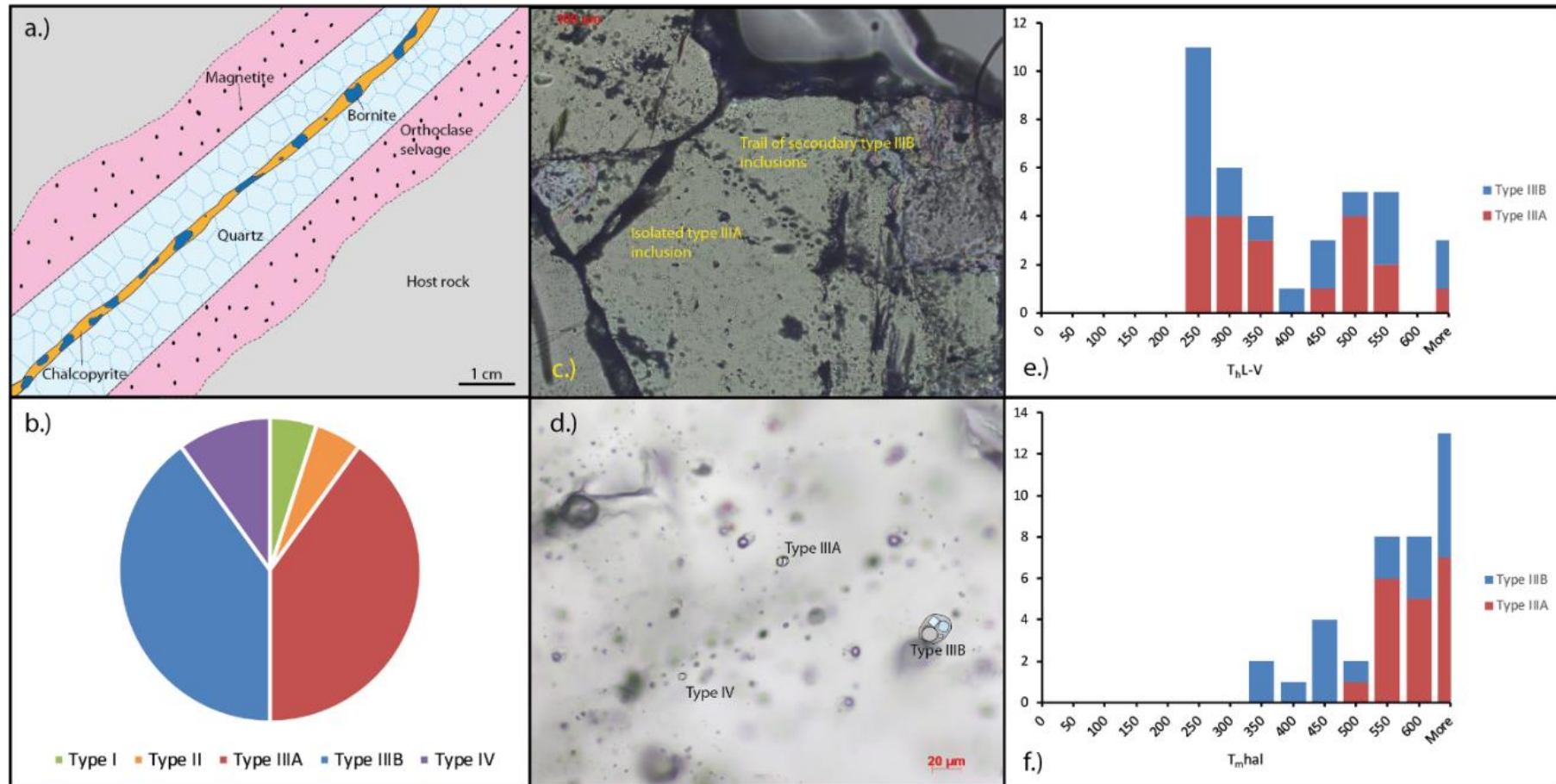




## Veinset M-4



## Veinset M-5





#### 4.4.1.1 Inclusions by veinset

Although the fluid inclusion populations are very similar in the majority of the mineralising veinsets the temperatures of vapour homogenisation vary between veinset, as do the proportions of the different fluid inclusions, indicating an overall evolution of the fluid in this deposit (figure 30).

The earliest quartz bearing veinset, E-2, contains very few fluid inclusions, with an average fluid inclusion modal % of the visible quartz of less than 1%. Those it does have are almost entirely type IV rounded pure CO<sub>2</sub> inclusions 5 - 10 µm in diameter, either solitary or in very small trails along crystal boundaries and growth zones. This veinset also contains rare type IIIA inclusions, with an average long axis length of 20 µm, which are all decrepitated. These inclusion populations and features are also found in the very similar M-2 veinset, however the E-2 veinset also includes silicate melt inclusions.

The quartz-magnetite veinset, E-3, also has very sparse fluid inclusions, with inclusions making up <1% of the chip. The inclusions present are rounded type IV CO<sub>2</sub> inclusions 5-10 µm, a very minor amount of type IIIA inclusions 20 µm, and type IV micro-inclusions <1 µm which are trapped on growth zones of the quartz crystals.

The first mineralising veinset, M-3, contains a total fluid inclusion density of 3 - 5%. This includes 5% type I inclusions 5 µm, which are decrepitated. It contains 25% type III inclusions 10 - 20 µm, most of which are round but some of which are beginning to develop negative crystal morphologies. These are found randomly distributed in the centre of crystals, and as small pseudo-secondary trails which stop at crystal boundaries, and some of the larger inclusions show irregular morphologies in association with cracks, which suggest that they may have leaked. Of these type III inclusions 60% are type IIIA which are found in the centre of crystals, while 40% are type IIIB, which are found as trails. The vein also contains type IV inclusions 5 to 20 µm. These are usually round in morphology, with some developing negative crystal shape. Type IV inclusions make up the remaining 70% of the inclusion population and are found both distributed randomly within the crystal or, more commonly, as inclusion trails which truncate at crystal boundaries.

The quartz-magnetite sulphide bearing M-4 veinset has a fluid inclusion density of 5 - 10% (meaning 5-10% of the surface area of the quartz is fluid inclusion), with a large proportion of type IV inclusions (35% of inclusion population), these are found in trails of inclusions 5 to 10 µm in size which cross crystals but terminate at the crystal boundary. Type IV inclusions in this veinset are commonly teardrop shaped, although some have negative crystal morphology. They are often associated with type II inclusions with a single small daughter mineral - usually an opaque. These

type II inclusions make up 30% of the fluid inclusion population, and are found as 15-30  $\mu\text{m}$  oblong inclusions, often developing a negative crystal shape. The type II inclusions are found either as an assemblage of irregularly distributed inclusions within a quartz crystal or trapped along crystal boundaries. The type III inclusions in the M-4 veins make up 30% of the inclusion population. They are round inclusions 5 - 30  $\mu\text{m}$  in size and are found as both solitary inclusions in the centre of quartz veins or as secondary trails crossing crystal boundaries within the vein. 40% of the type III inclusions in the M-4 veins are type IIIA, and these tend to be the solitary inclusions, while type IIIB form the trails. The final 5% of the inclusion population of the M-4 veins is made up of type I inclusions, which are 10 - 20  $\mu\text{m}$ , found as solitary inclusions or as trails and all show irregular morphologies indicative of leakage.

The final mineralising veinset, M-5, has a fluid inclusion density of 2%, containing 5% type I inclusions - 10-20  $\mu\text{m}$  in diameter oblongs which are usually irregular in morphology. They also contain 10% type IV inclusions 5 - 15  $\mu\text{m}$  with negative crystal morphologies, present as trails which stop at crystal boundaries, and associated with diamond shaped type II inclusions with opaque daughter minerals which make up 5% of the inclusion population, range from 5 - 25  $\mu\text{m}$  and are present as trails across crystals. The type III inclusions make up the remaining 80% of the inclusions in the M-5 veins, with negative crystal morphologies ranging from 5 - 50  $\mu\text{m}$ . 50% of these inclusions are type IIIA, some of which also contain opaque daughter minerals which have been identified as sulphides in optical microscopy, and a rare few type III inclusions contain both opaque daughter minerals and anhydrite. The smaller, type IIIB, inclusions form trails which cross crystal boundaries, while the larger type IIIA inclusions are present as solitary inclusions within the centre of the crystals.

### **4.4.2 SEM analysis of fluid inclusions**

Fluid inclusion chips from each of the seven samples chosen for fluid inclusion analysis (appendix A3.2) were glued to the edge of a piece of plastic, snapped and then carbon coated before being analysed on a LEO 535VP scanning electron microscope in order to generate high quality secondary electron and backscatter electron images of daughter minerals and to use EDS to identify the daughter minerals present in type III inclusions. This was done by systematically scanning the broken edge of each fluid inclusion chip and analysing the daughter minerals of all the inclusions observed (figure 31). Sample 4 was lost during analysis, and the majority of the inclusions larger than 10  $\mu\text{m}$  had evacuated their daughter minerals, with crystals observed surrounding cavities. This suggests a high internal pressure of the inclusions and means that these analyses are not exhaustive, however they do allow for the identification of some of the previously unknown translucent and opaque daughter minerals observed in optical microscopy. In

the future cryo-SEM could be used to freeze inclusions prior to opening in order to preserve the daughter minerals and fluids for EDS analysis, however one was not available at the time this work was undertaken.

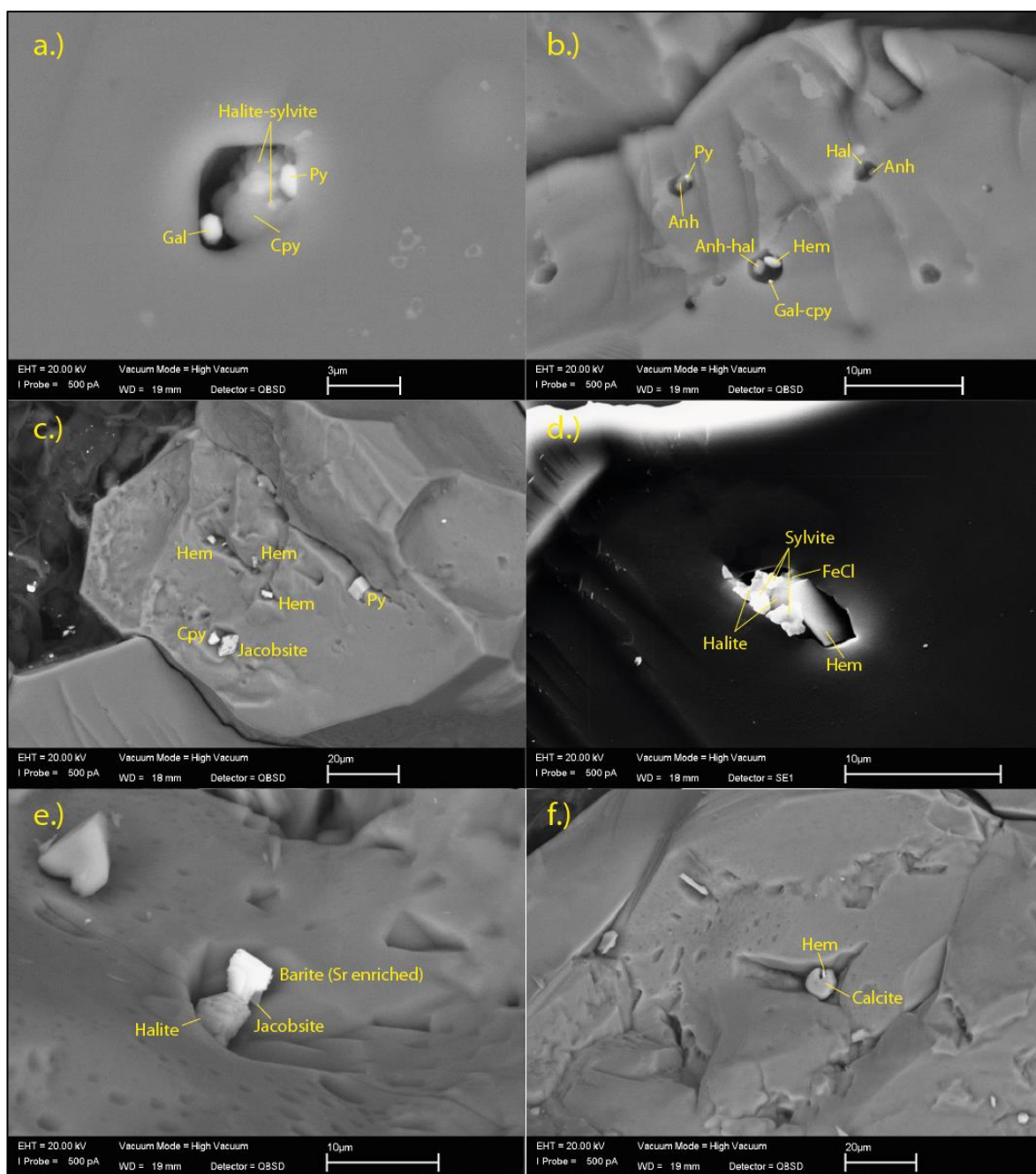


Figure 31: BSE and SE1 images of daughter minerals in type III fluid inclusions in mineralised vein quartz, mineral identification from EDS. a.) Type III inclusion with Cu and Pb sulphides in M-3 vein. b.) Type IIIA inclusions in M-4 vein. Sulphides and anhydrite present in the same inclusion. c.) Type IIIA inclusions in M-4 with sulphides and jacobsite daughter minerals. d.) Type IIIA fluid inclusion in vein M-5 with  $\text{FeCl}_2$  and hematite daughter minerals, as well as salt crystals. Inclusion full of crystals, salt saturation. e.) Type III inclusion in M-5 vein with barite daughter mineral. f.) Type III inclusion in M-5 vein with hematite and calcite daughter minerals.

## Chapter 4

Type III inclusions from sample 6, a quartz vein sample from the E-3 veinset, contain hematite, chalcopryrite, jacobsite, halite, sylvite and  $\text{FeCl}_2$  crystals. The next veinset analysed, the mineralised M-3 veinset, is represented by sample 2 where the type III inclusions contain halite, sylvite,  $\text{FeCl}_2$ , galena, chalcopryrite, pyrite, Sr-rich barite and jacobsite crystals. Sample 3, another M-3 vein, has type III inclusions with pyrite, galena, chalcopryrite, halite, hematite, anhydrite and a zircon crystal. The sulphides, hematite and anhydrite occur in the same inclusions. Type III inclusions analysed from sample 1, an M-4 vein quartz sample, have hematite and calcite daughter minerals. Type III inclusions analysed in sample 7, another M-4 vein quartz sample, contain apatite, bornite, chalcopryrite, hematite and trapped biotite and potassium feldspar crystals. The M-5 sample, sample 5, contains halite, sylvite,  $\text{FeCl}_2$ , jacobsite, hematite and tennantite crystals in type III inclusions (figure 31).

These results are not comprehensive due to the small number of inclusions analysed and the lack of preserved daughter minerals in the majority of the inclusions present, however they do show that the mineralogy of the daughter minerals in type III inclusions is very diverse, and the confirmed presence of  $\text{FeCl}_2$  in a large proportion of the inclusions analysed has implications for salinity calculations from micro-thermometry.

The veins the inclusion chips were taken from were also examined using CL (figure 32) to determine the quartz generations. Although multiple stages of silica were found in all veinsets, the majority of the inclusions are present in euhedral secondary quartz crystals which make up the majority of the veins (see figure caption for more details).

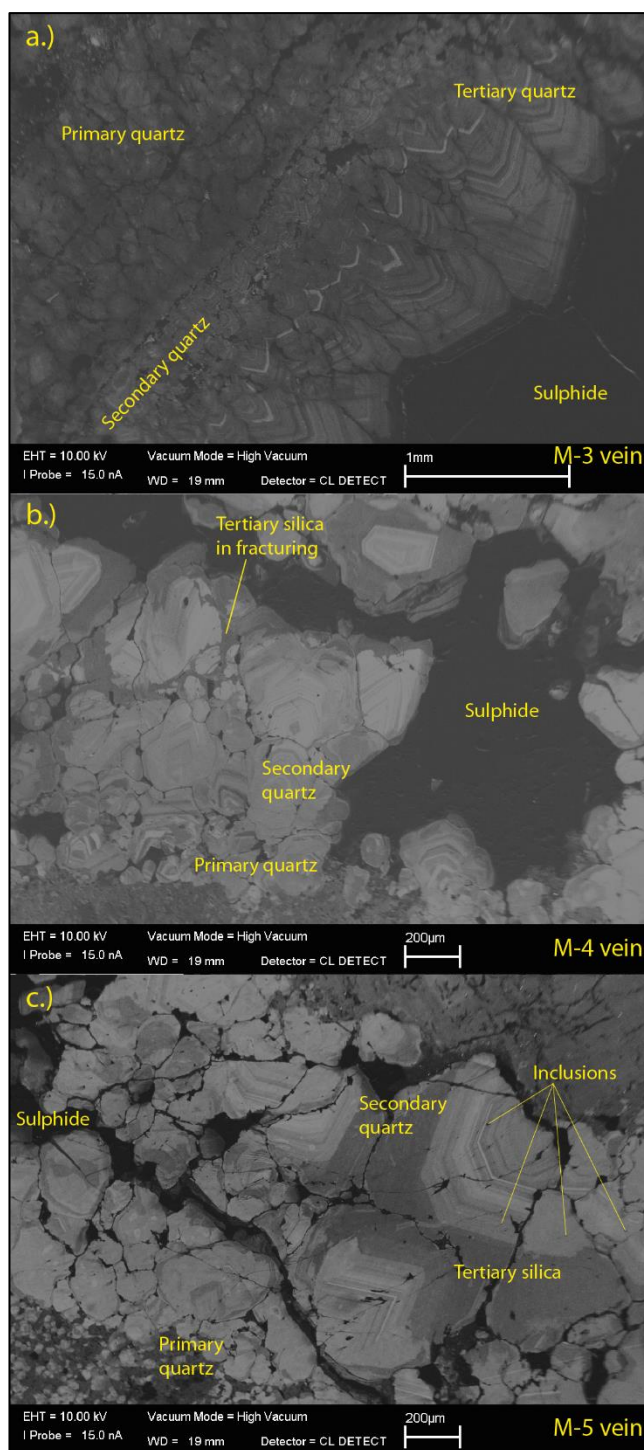


Figure 32: Cathodoluminescence images of vein quartz in the mineralising veins. a.) Quartz in vein M-3 shows layering – fine grained primary quartz with very fine grained secondary quartz growing on it and then finally large, euhedral tertiary quartz showing clear growth zones. Quarternary silica infills cracks in the tertiary quartz. b.) Quartz in M-4 vein also has multiple generations of fine grained primary quartz crystals, and large euhedral secondary quartz crystals with growth zones. The secondary quartz is brecciated by a tertiary silica bearing fluid. c.) M-5 vein has multiple silica generations. Primary quartz is fine grained, while secondary quartz forms large euhedral crystals with growth zones, which appear to host the majority of the fluid inclusions. A tertiary, silica bearing fluid brecciates the secondary quartz.

#### **4.4.3 Fluid inclusion microthermometry**

##### **4.4.3.1 Methods and limitations**

Fluid inclusion micro-thermometry was performed on the 3 main mineralising veinsets from the main stage of porphyry mineralisation (table 11) - the quartz-magnetite-sulphide-orthoclase-biotite M-3 veinset (sample 3), the quartz-magnetite-sulphide M-4 veinset (sample 7) and the quartz-sulphide M-5 veinset (sample 5). The inclusions in the early quartz bearing veinsets - E-2 and E-3 veinsets are decrepitated and too scarce to perform a thorough micro-thermometry survey. The analysis was carried out on a Linkham THMS600 heating freezing stage, using the analysis routine described in chapter 2. A detailed petrological survey was carried out on the inclusions prior to analysis in order to ensure the correct identification of the halite and sylvite daughter minerals in type III inclusions.

The main focus of micro-thermometry was the type III inclusions as they are the dominant fluid inclusion type in the mineralising veins. Although an attempt was made to ensure representative analysis was performed on each inclusion type various factors prevented this. 95% of the type I inclusions observed were observed to have leaked, making gaining representative data for this inclusion population difficult. The type II inclusions were also very sparse within the samples analysed, and although a few successful analyses were performed the majority of type II inclusions burst before homogenisation, generally at temperatures around 500°C. The highly variable phase ratios in type II inclusions make it likely that this population has undergone substantial post-entrapment modification (discussed further below), and so data from these populations should be treated with care. The type IV inclusions presented similar issues, as the majority of them burst at 400°C before homogenising at around 400°C, and although they were identified as being pure CO<sub>2</sub> with raman, no evidence of this was seen in the micro-thermometry - instead they showed no change on freezing, and no change on heating prior to bursting (discussed further below). The type III inclusions also presented analytical challenges as 40% of them burst at temperatures of >550°C, and 90% of them still had not homogenised at the stage limit of 600°C. In future it would be good to analyse these samples on a melt inclusion stage in order to gain true homogenisation temperatures, however one was not available at the time of this study. They also did not freeze - the temperature was taken down to -180°C then cycled up to -90°C and back down again as suggested in Shepherd et al (1981; Patrick 1986), however the inclusions showed no change. This is not unusual for highly saline inclusions and has been seen in several other porphyry deposits (Sheppard 1981). Over 200 inclusions were analysed, of which recoverable data was collected for 8 type I inclusions, 7 type II, 182 type III and 2 type IV inclusions (full data table in electronic appendix C).

#### 4.4.3.2 Results

Type I inclusions homogenise to liquid at temperatures ( $T_{H-V-L}$ ) between 250°C and 360°C, with an average  $T_{H-V-L}$  of 340°C. They have ice melting temperatures ( $T_{M-ICE}$ ) of -4°C to -1.9°C, with an average of -3.2°C, and calculated salinities of 3.26 wt% NaCl to 6.54 wt% NaCl, with an average of 5.23 wt% NaCl (Bakker 2003). Type II inclusions homogenise to liquid at temperatures ( $T_{H-V-L}$ ) between 380°C and above 590°C, with an average of 462°C. The type II inclusions have ice melting temperatures ( $T_{M-ICE}$ ) of between -3.9°C and -9.2°C, with an average of -6.5°C, and calculated salinities of 6.39 wt% NaCl to 13.29 wt% NaCl, with an average of 9.95 wt% NaCl. However these salinities are calculated from  $T_{M-ICE}$ , rather than from halite dissolution temperatures as the type of daughter mineral is very variable between inclusions in this population, and so it is unlikely that these are representative. The type IV inclusions which homogenised before bursting homogenised to vapour ( $T_{H-V-L}$ ) at 537°C, however most showed no change up to 600°C, or burst above 500°C.

The type III inclusions homogenise to liquid by halite dissolution, with a large proportion of them not homogenising below the stage limit of 600°C - those have therefore been treated as having a minimum homogenisation temperature of 600°C. Given that, the  $T_{H-V-L}$  for type IIIA inclusions ranges from 202°C to >590°C with an average of 413°C, while the  $T_{H-V-L}$  for type IIIB inclusions ranges from 204°C to >590°C, with an average of 396°C. Type IIIA inclusions have sylvite dissolution temperatures ( $T_{M-SYL}$ ) of between 300°C and 582°C, with an average of 484°C; while type IIIB inclusions have sylvite dissolution temperatures of between 241°C and 585°C, with an average of 435°C. The halite dissolution temperatures ( $T_{M-HAL}$ ) of type IIIA inclusions range from 405°C to >590°C, with an average of 557°C, and those of type IIIB range from 300°C to >595°C, with an average of 509°C. It is worth noting that the hematite in the majority of type IIIA inclusions did not homogenise before the stage limit.

Using the AqSo WHS software package developed by Bakker (2012), salinities were estimated for the type III inclusions using the H<sub>2</sub>O-NaCl-KCl fluid system. This is only of limited value as the type III inclusions also include FeCl<sub>2</sub> and small amounts of CO<sub>2</sub>, making this an H<sub>2</sub>O-NaCl-KCl-FeCl<sub>2</sub>-CO<sub>2</sub> system, however, although estimations of the composition of the quaternary NaCl-KCl-FeCl<sub>2</sub>-H<sub>2</sub>O system can now be made from low-temperature data (Steele-MacInnis et al. 2016), there are currently no phase equations available for this system during the heating phase. Therefore, the H<sub>2</sub>O-NaCl-KCl system was chosen as the best approximation as all type III inclusions contain significant volumes of solid sylvite and halite. The H<sub>2</sub>O-CO<sub>2</sub>-NaCl system was not used because CO<sub>2</sub> was not observed during micro thermometry of these samples the inclusions must contain less than 0.85 molal CO<sub>2</sub> (Hedenquist & Henley 1985), meaning that CO<sub>2</sub> is a minor phase in this system. However, as CO<sub>2</sub> depresses homogenisation temperatures these salinity results should be

considered minimum estimates only. Type IIIA inclusions have calculated NaCl contents of between 27.4 wt% and 59.2 wt%, with an average of 39.3 wt% NaCl; between 23.9 wt% and 59.4 wt% KCl, with an average of 49.6 wt% KCl. This gives a total salinity (NaCl+KCl) of between 73.3 wt% and 94.8 wt%, with an average salt content of 88.9 wt%. Type IIIB inclusions have calculated salt contents of between 11.2 wt% and 60.4 wt% NaCl, with an average of 38.1 wt% NaCl; between 21.6 wt% and 76.6 wt% KCl, with an average of 44.9 wt% KCl. This gives a total salinity (NaCl+KCl) of between 58.9 wt% and 94.9 wt%, with an average salt content of 83 wt%. When NaCl is plotted against KCl the inclusions plot parallel to the saturation curve, suggesting the inclusions are nearing salt saturation (figure 33).

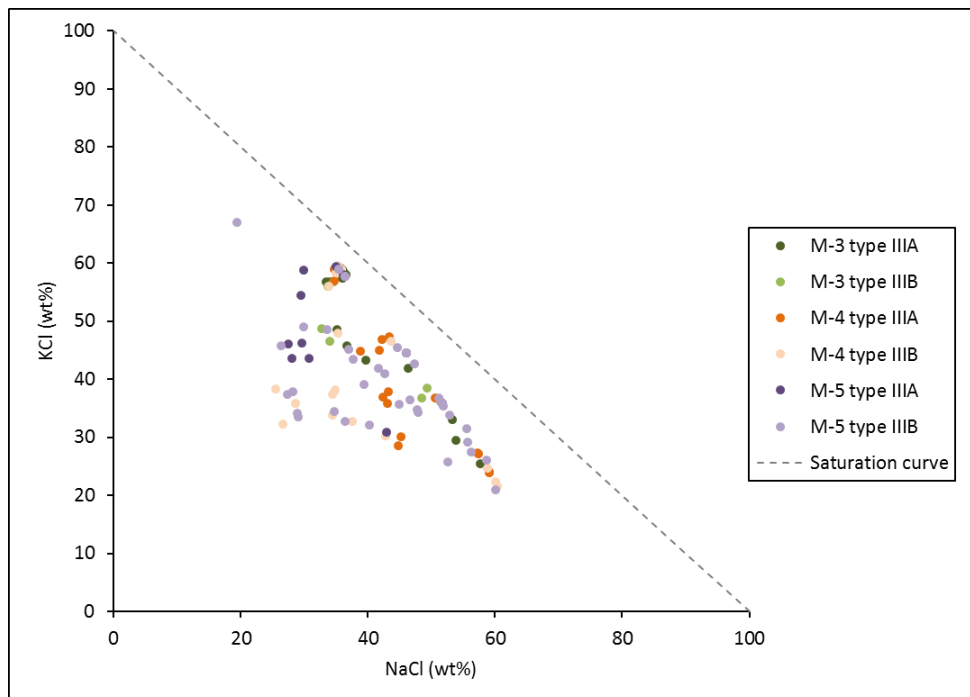


*Figure 33: Graph showing the calculated salinity of all type III inclusions, discriminated by vein type and population. Although these salinities are approximate due to the presence of multiple cations in the fluids they show the fluids to be nearing salt saturation, with inclusions plotting parallel to the 100% saturation curve.*

The type III inclusions have a large range of  $Th_{V-L}$ ,  $Th_{SYL}$ ,  $Th_{HAL}$  and therefore salinities. These do not show a correlation when plotted by population, however they do show differences between veinsets (figure 30). The earliest mineralising veinset, M-3, has  $Th_{V-L}$  between 250°C and 541°C, with an average of 462°C and  $Th_{HAL}$  between 460°C and >590°C and an average of 570°C, and a total salinity of 69.7 wt% to 94.8 wt%, with an average of 90.9 wt%. The next mineralising veinset, M-4, has  $Th_{V-L}$  between 202°C and 540°C, with an average of 341°C and  $Th_{HAL}$  between 337°C and >590°C and an average of 532°C, and a total salinity of 58.9 wt% to 94.9 wt%, with an average of 83 wt%. The last mineralising veinset in the main stage of the deposit, M-5 vein, has  $Th_{V-L}$  between 300°C and >581°C, with an average of 429°C and  $Th_{HAL}$  between 300°C and >585°C and an average



of 493°C, and a total salinity of 62.5 wt% to 94.4 wt%, with an average of 82.5 wt%. This shows an overall decrease in temperature and salinity over time.

#### **4.4.4 LA-ICP-MS of fluid inclusions**

Laser ablation was performed on fluid inclusions from the mineralising vein stages of the deposit in order to understand the fluid chemistry and metal transport in the fluids. Care was taken to ensure that the inclusions analysed were from the same assemblages that had been petrologically classified, and in choosing proxy assemblages to perform microthermometry on (see chapter 2 for a further discussion of methods, limitations and uncertainties). 120 inclusions were ablated using method 1 (see chapter 2), of which 74 returned results, and 50 returned results which are judged to be a result of the fluid, rather than sulphide ablation.

A detailed list of LA-ICP-MS results is presented in the electronic appendix C, and the results are summarised in appendix 3.4 which is subdivided according to fluid inclusion types identified from fluid inclusion petrography and microthermometric data.

##### **4.4.4.1 Major and minor elements**

Type III brine inclusions from Skouries have detectable levels of K, Ca, Mn, Fe, Li, Mg, Rb, Sr, Y, Cs, Ba, La, Th and U. K, Ca, Mn and Fe are present on the order of weight percent; Mg and Rb on the order of thousands of ppm; Li, Sr, Ba and Cs on the order of hundreds of ppm and Y, La, Th and U on the order of 10s of ppm (appendix A3.4, figure 34). The individual inclusions measured show a wide range of element concentrations, with assemblages showing standard deviations of between 10% and 70% of the mean (appendix C), and although this is not unusual for brine inclusions in porphyry deposits (Heinrich et al. 2003), it does mean that drawing inferences from changes in concentration of less than an order of magnitude must be treated with care.

K, Fe and Mn co-vary, suggesting that these (along with Na) are the main cations in the fluid (Heinrich et al. 2003; Pettke et al. 2012). Type IIIA inclusions in the first mineralising veinset, M-3, have higher concentrations of the major elements (K, Mn and Fe) than the pseudo-secondary type IIIB inclusions (appendix A3.4). In the M-4 veinset the type IIIA inclusions appear to have lower concentrations of the major elements than the type IIIB inclusions, however they are within standard deviation of each other and therefore are not statistically significant. The last of the main mineralising veinsets, M-5, has the highest concentrations of major elements of any veinset in the type IIIA inclusions, with lower concentrations in the secondary type IIIB inclusions. This corresponds with a drop in salinity and temperature in veinset M-5 (figure 34). Ca and Mg are both fairly constant across all type III inclusions and veinsets.

The minor elements also do not show much variation between veinsets and between type IIIA and IIIB, although they do show a large range within those categories. The high LILE content that Skouries displays in whole rock analysis (Kroll et al. 2002) is also seen in the fluids, with average Rb concentrations of 771 ppm to 1935 ppm, U values of 3 - 14 ppm (in brines) and average Th values of 0.1 to 1242 ppm. Rb and Sr show a strong positive correlation, with an average Rb/Sr of 7.17, and Rb also shows a strong positive correlation with Cs.

The majority of the vapour inclusions (type IV) analysed show the same suite of major and minor elements as the brines, in the same order of magnitudes (appendix A3.4, figure 34). The vapour inclusions show a very large range of concentrations, particularly of the minor elements such as U, where order of magnitude variations are observed (figure 34). K, Fe and Mn co-vary and show no difference across the first two veinsets. The last mineralising veinset analysed, M-5, has significantly higher concentrations of K, Mn and Fe than the vapour inclusions from the first two veinsets. Sr and Rb and Cs and Rb are decoupled in the vapour inclusions, showing no correlation. However, the concentrations of these elements are still relatively high in the vapour inclusions, with average Rb concentrations of between 410 and 3131 ppm. The semi-metals (As, Sb and Bi) show constant concentrations in the brine inclusions, with more scatter in the vapour inclusions, and these are discussed further in chapter 6.

Skouries brine inclusions have an order of magnitude more Ca and Mn than those analysed at Bingham and Butte (Rusk et al. 2004; Landtwing et al. 2005), and similar major element concentrations to brine inclusions analysed at Bajo de la Alumbrera, Argentina, and Elatsite (Ulrich et al. 2002; Kehayov et al. 2003). K, Mn, Fe and Ca concentrations of the vapour inclusions in Skouries are an order of magnitude higher than those measured in high density vapour inclusions in Butte and at Elatsite (Kehayov et al. 2003; Rusk et al. 2004).

#### **4.4.4.2 Ore metals**

Concentrations of Cu in the type III brine inclusions range from an average of 0.09 wt% in the type IIIA inclusions in veinset M-3 to an average of 2.06 wt% in type IIIB inclusions in M-4, with an average magmatic brine copper concentration of 0.34 wt% (appendix A3.4). The amount of copper analysed in the brine inclusions increases over time until veinset M-5, where the concentrations of copper drop to the level of those seen in M-3, meaning M-4 is the most Cu rich fluid (figure 34). Cu was also detected in the vapour inclusions - M-3 veinset vapour inclusions have an average of 1.23 wt%, M-4 have an average of 0.83 wt% and M-5 inclusions have an average of 0.93 wt%, giving a total vapour Cu average of 0.89 wt%. The vapour inclusions have higher Cu concentrations than the brine inclusions in the same veinset in M-3, and in M-4 and M-5 they are within one standard deviation of each other. These are similar to Cu concentrations

measured in both brines and vapours in other porphyry inclusions, including in Butte, Bingham and Bajo de la Alumbrera (Ulrich & Heinrich 2002; Rusk et al. 2004; Pettke et al. 2012).

Au was detected in at least one inclusion from every veinset and inclusion type, except for the vapour inclusions in M-3, and type IIIB inclusions in M-4. Limited data for the Au concentrations in the brine inclusions indicate an average Au content of the magmatic brine of 0.71 ppm (range 0.1 ppm to 5.45 ppm, appendix A3.4 and C, figure 34). Limited data for the Au concentrations of vapour inclusions (n=4) indicate a mean vapour Au concentration of 1.39 ppm (range 0.28 ppm to 4.06 ppm, appendix A3.4, figure 34) These Au concentrations are greater than those measured from inclusions in Bingham (Pettke 2008), and similar to those of inclusions analysed from Bajo de la Alumbrera (Rusk et al. 2004).

The brine inclusions in Skouries also contain high levels of Pb and Zn, on the order of percent, as well as Mo, W, Sn, and Ni on the order of 10s - 100s of ppm and Ag and Co on the order of 10s of ppm (figure 34). Pb and Zn co-vary and show consistent levels, except in veinset M-5, inclusion type IIIB where their concentrations drop. Pb and Zn are found at similar high concentrations in vapour inclusions, with their concentrations increasing between M-3 and M-5. The brine inclusions have average Ag values of between 12 and 42 ppm, with concentrations decreasing with decreasing fluid temperature. Average vapour Ag concentrations in M-3 and M-4 are 17 ppm, whereas M-5 vapour inclusions have an average Ag concentration of 7 ppm. Skouries fluids have higher Pb and Zn levels in both brine and vapour than Butte, Bingham, Bajo de la Alumbrera and Elatsite (Pettke et al. 2012; Ulrich et al. 2002; Rusk et al. 2004; Kehayov et al. 2003). Elatsite has similar high Ag levels in brine inclusions, as do Butte and Bingham (Kehayov et al. 2003; Rusk et al. 2004; Pettke et al. 2012).





Figure 34: Plots showing the major and minor elements analysed in the Skouries fluid inclusion assemblages using ‘method 1’, divided into brine inclusions on the right and vapour inclusions on the left. Each data point represents the average value of a fluid inclusion assemblage, with the numbers along the x axis representing the number of inclusions in that assemblage, and the y axis representing concentration in ppm. The homogenisation temperatures of the assemblages are represented by the graph at the top, and the assemblages are divided by veinset and type in order to give an idea of the development of the fluid over time, with the earliest on the left and the latest on the right.



## 4.5 Discussion

### 4.5.1 Interpretation of fluid inclusion petrography

A large number of the fluid inclusions analysed have inconsistent phase ratios, which suggests that post-entrapment modification has occurred. The type I inclusions show irregular shapes, lack of consistency of phase ratios and often show evidence that leakage has occurred (fluid observed in cracks surrounding fluid inclusions). This is interpreted to mean that this inclusion population was decrepitated, and therefore no longer representative of the original fluid. Their deportment in trails crossing growth zones (figure 29) means that they are pseudo-secondary, however as they are not observed crossing crystal boundaries they cannot be defined as secondary.

Type II inclusions are interpreted to have undergone post-entrapment modification due to their negative crystal morphology, inconsistent phase ratios and leakage observed. This means this inclusion population may not be representative of the original fluid, and indeed may represent type III inclusions which have undergone post-entrapment modification, drastically changing the phase ratios. The rarity of type II inclusions, along with their similar micro-thermometric values to type III inclusions support this hypothesis, as does the unusual occurrence of vapour-rich inclusions homogenising to liquid rather than vapour, and the inconsistent presence of a wide variety of daughter minerals.

Type IIIA inclusions are present as both solitary inclusions and trails trapped in, and occasionally cross-cutting, growth zones but truncating at crystal edges (figure 29), and so are interpreted to be primary/pseudo-secondary. Type IIIB inclusions are commonly observed in trails cross-cutting growth zones and crossing crystal boundaries (figure 29) meaning they are interpreted to be secondary. Although a first pass attempt has been made to divide the type III inclusions into populations based on their daughter mineralogy (table 12) micro thermometry results do not support the hypothesis that these define assemblages as defined by Roedder (Roedder & Ribbe 1984). The variable phase ratios present in type III inclusions suggest that at least some of this population have undergone post-entrapment modification, and this is discussed further below.

Type IV inclusions are interpreted to be primary, or pseudo-secondary, as they are not observed cross-cutting crystal boundaries. The consistent phase ratios and regular morphologies observed in this population suggests they may not have undergone as much post-trapping modification as the other inclusion populations, although as they are also interpreted to be the earliest inclusion phase it is unlikely that they would have escaped the modification processes which affected the later brine inclusions.

The increase in proportion of type III brine inclusions over type IV vapour inclusions over time suggests an early, gas dominated system evolving into a brine dominated system. The primary inclusions in the mineralising veinsets, M-3, M-4 and M-5, are type IIIA inclusions and rare type IV inclusions, and so these are interpreted to represent the main ore metal bearing fluid (discussed further below).

### 4.5.2 Interpretation of microthermometry

Type I inclusions in Skouries are only found in the main stage veinsets, and are commonly decrepitated, showing that they have been modified by a later event, either the intrusion of the late barren porphyritic syenite, or a later high temperature fluid such as the one which is represented by the type III inclusions. The type I inclusions contain CO<sub>2</sub>, which was observed in raman and in microthermometry. Given that these are the only inclusions to show microthermometric evidence of CO<sub>2</sub> they probably contain more CO<sub>2</sub> than the type IV inclusions (Hedenquist & Henley 1985, discussed further below), which suggests that they are part of an early CO<sub>2</sub>-rich fluid stage.

The type II inclusions successfully analysed were all from the M-4 veinset, and it is here that they are most common, only appearing in very small amounts in M-5. They show moderate salinities, relatively low temperatures and are pseudo-secondary. The vapour phase in type II inclusions is CO<sub>2</sub> and they are quite rare. They could be a transitional fluid between the CO<sub>2</sub> vapour of type IV and the brine of type III, or they could represent boiling of type III, and this would be supported by the fact that they are only found in mineralising veinsets and boiling has been suggested as a means of precipitation of sulphides (Bodnar & Beane 1980). However, it is not possible for vapour rich inclusions to be in equilibrium with halite-dissolution inclusions, as vapour rich inclusions must be trapped on a vapour saturation boundary and halite dissolution inclusions cannot be in equilibrium with a vapour phase (figure 35). This means that the type II inclusions would have to undergo either post-entrapment volume reduction, selective H<sub>2</sub>O loss, or result from heterogeneous trapping (Audétat & Günther 1999; Bodnar 2003b; Becker et al. 2008). The inclusions analysed showed a wide range of salinities for this population and that, coupled with the morphological and textural evidence outlined above, suggests that these are the result of post-entrapment modification of type IIIA inclusions rather than being a separate inclusion type.

#### 4.5.2.1 Halite-dissolution inclusions

The type III inclusions in Skouries are high temperature, high salinity brines, probably of magmatic origin. Type IIIA inclusions have marginally higher homogenisation temperatures and salinities than type IIIB inclusions, and are interpreted to be primary, while secondary trails of type IIIB



inclusions have been observed suggesting they are a later fluid phase. This means that type IIIA is more likely to be representative of the conditions of quartz vein formation in the main stage veins. Type III inclusions homogenise to liquid via halite dissolution, which means they homogenise along the halite liquidus and traverse the liquid + halite field after vapour homogenisation (figure 35). Figure 35 shows the three possible paths a high salinity inclusion can take to homogenise: A, where  $T_{H-L} > T_{m_{HAL}}$ ; B where  $T_{H-L} = T_{m_{HAL}}$  and C, halite-dissolution, where  $T_{H-L} < T_{m_{HAL}}$  (Becker et al. 2008). Halite-dissolution inclusions are trapped within field 'C' of figure 35, bounded by the halite liquidus and the isochore which meets the L+V+H curve at the same point as the liquidus (Bodnar 1994; Becker et al. 2008). Often all three modes of homogenisation are reported in the same deposit (e.g. Bodnar & Beane 1980), and this could be caused by a change of temperature or pressure of the system, or re-equilibration of the inclusions after entrapment (Becker et al. 2008). Halite-dissolution inclusions commonly occur in ore deposits and have been observed in many porphyry deposits worldwide, including the Questa deposit, New Mexico (Cline & Bodnar 1994); Bingham Canyon deposit, Utah (Becker et al. 2008) and Red Mountain, Arizona (Bodnar & Beane 1980). There are many theories for their origin, including post-entrapment inclusion modification, such as necking (Erwood et al. 1979; Audétat & Günther 1999), high pressure brine exsolution from a silicate melt (Cline & Bodnar 1994; Student & Bodnar 1999; Student & Bodnar 2004) or heterogeneous trapping under halite saturated conditions (Eastoe 1982; Becker et al. 2008; Lecumberri-Sanchez et al. 2012; Lecumberri-Sanchez et al. 2015).

PVTX data is available for high salinity NaCl-H<sub>2</sub>O and NaCl-KCl-H<sub>2</sub>O systems in the liquid field (Sternner et al. 1988; Sternner et al. 1992; Chou et al. 1992; Anderko & Pitzer 1993; Bodnar 1994; Bakker 2014), however these systems are all vapour saturated. Until recently PVTX data was only available for the two phase liquid + halite field for 40 wt% NaCl (Bodnar 1994), meaning the isochore from the point of vapour homogenisation to the halite liquidus could not be calculated, however densities have now been calculated for NaCl-H<sub>2</sub>O solutions in the solid-liquid two phase field (Chen et al. 2015), although this does not take into account the presence of KCl or other solutes. An empirical equation is available to estimate pressure in the inclusion at the time of formation using  $T_{H-L}$  and  $T_{m_{HAL}}$  for a  $T_{m_{HAL}}$  range of 150°C to 500°C, and a  $T_{H-L}$  range of 275°C to 550°C, which provides a minimum pressure of formation (Becker et al. 2008). While valid for the ranges it was calculated for, this equation has been found to yield large discrepancies outside of those fields, so a new model was developed by Lecumberri-Sanchez et al (2012), which is based on a numerical model describing the isochoric P-T trajectory followed by halite-saturated fluids during heating, and is valid at temperatures from 100°C to 600°C, and up to 300 MPa. As the majority of the inclusions in Skouries lie outside the ranges of the equation presented in Becker et

al (2008) the model presented in Lecumberri-Sanchez et al (2012) was used (figure 36), however it is worth noting that any pressures yielded will only be approximate as the model is for an NaCl-H<sub>2</sub>O system, while the type III brines in Skouries are a NaCl-KCl-H<sub>2</sub>O-FeCl<sub>2</sub>+MnCl<sub>2</sub>+/-CO<sub>2</sub> system.

In order to ascertain whether inclusions have followed Roedder's rules (were trapped at the same time in a single, homogenous phase; and have remained isochoric following trapping, so have not gained or lost anything) careful petrographic observations are needed to define potential assemblages before plotting  $T_{m_{HAL}}$  vs  $Th_{V-L}$  (Roedder 1992; Bodnar 2003b; Chi & Lu 2008). If the inclusions obey Roedder's rules they should show similar  $T_{m_{HAL}}$  and  $Th_{V-L}$ , however it is also possible to distinguish whether the inclusions have undergone post-entrapment modification or heterogenous trapping by identifying patterns in  $T_{m_{HAL}}$  vs  $Th_{V-L}$  of assemblages (Becker et al. 2008, figure 35, figure 36). Heterogenous trapping can occur when the fluid becomes saturated in halite, resulting in the precipitation of halite crystals on crystal growth surfaces. This can result in contemporaneous inclusions trapping different proportions of the liquid and solid phase, or just the liquid phase. This results in a wide range of  $T_{m_{HAL}}$  for a constant  $Th_{V-L}$  value - the density of the inclusions would still be the same, with any halite crystals trapped acting as an incompressible phase, meaning they will follow the same isochore through the halite + liquid field (Bodnar 1994; Becker et al. 2008). The inclusions which trapped the liquid phase only will have the lowest  $T_{m_{hal}}$ , and these represent the correct trapping pressure, with the other inclusions over-estimating pressure (Becker et al. 2008, figure 35, figure 36). A range of  $T_{m_{HAL}}$  temperatures for a single  $Th_{V-L}$  value can also indicate that necking has occurred. If necking occurs during cooling and reaches a temperature lower than the liquidus of the original fluid then some of the inclusions will contain liquid + halite, and some just liquid, resulting in a range of  $T_{m_{hal}}$  for a constant  $Th_{L-V}$  the same as that seen for heterogenous trapping. However in this case the lowest  $T_{m_{HAL}}$  represents the modified fluid after necking, and so using this value would result in an under-estimation of trapping pressure (Becker et al. 2008, figure 35). Distinguishing between assemblages which have been necked and those that result from heterogenous trapping is not possible from micro-thermometric or petrological data, although if heterogenous trapping has occurred there should be halite crystals present in the host quartz matrix, as well as in the inclusions, as the quartz would be precipitated above the halite saturation point. Inclusions can also undergo stretching post-entrapment, which results in a reduction of density as volume increases, without changing the bulk composition (Bodnar 2003b). Stretched inclusions therefore follow a lower density isochore, resulting in a higher  $Th_{L-V}$ , so giving a range of  $Th_{V-L}$  for a constant (correct)  $T_{m_{HAL}}$ . This means that the lowest  $Th_{V-L}$  value approximately represents the minimum trapping pressure (Becker et al. 2008).

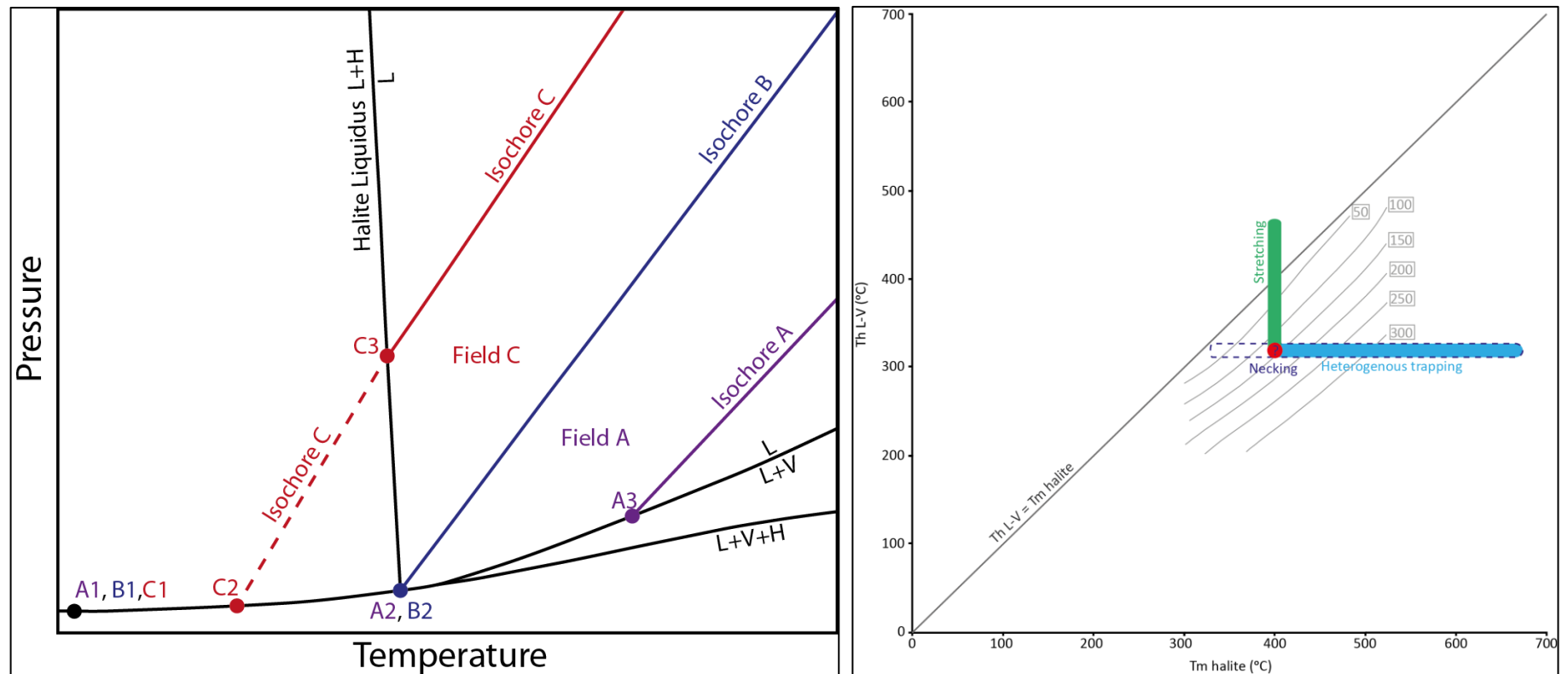


Figure 35: a.) Schematic P-T projection of the high-salinity (>27 wt%, daughter mineral present at room temperature) H<sub>2</sub>O-NaCl system (after Bodnar, 1984 and Becker, 2002). It shows the pathway of three fictitious fluid inclusions – fluid inclusion A was trapped in field A, and on heating from room temperature (A1) it follows the liquid (L) + vapour (V) + halite (H) curve until the halite crystal disappears, at A2 where the halite liquidus intersects the L+V+H curve. With further heating inclusion A follows the L+V curve until it homogenises by vapour homogenisation at point A3. If heating continues the inclusion will follow isochore A. Inclusion B was trapped along isochore B, which is the isochore which intersects the halite liquidus and L+V+H curve at the same place. Inclusion B when heated from room temperature (B1) will homogenise at B2, where the vapour bubble and halite crystal will disappear at the same time, before following isochore B. Inclusion C homogenises by halite-dissolution and was trapped in field C, which is bounded by the halite liquidus and isochore B. When heated from room temperature (C1) the vapour bubble disappears at C2, at which point the inclusion follows isochore C until meeting the liquidus at C3, where the halite crystal disappears and the inclusion continues along isochore C. It is worth noting that halite-dissolution inclusions must be trapped in field C and so cannot be formed in equilibrium with a vapour phase. Isochores between L+V+H and the liquidus are still relatively unknown, only having recently been modelled (Lecumbbarri). b.) Illustration of patterns of data when plotted as  $T_{m\text{halite}}$  vs  $T_{h\text{L-V}}$  which indicate different styles of post-entrapment modification. The red dot indicates the true values for that dataset, except in the case of necking where the true value cannot be estimated (Becker, 2002).

The large number of type III inclusions in Skouries with  $T_{m_{HAL}}$  of 580°C - 600°C is a function of the stage limits - the LINKAM 600 micro thermometry stage used for this study had a limit of between 580°C and 600°C, and unfortunately a large proportion of the type III inclusions did not fully homogenise within the stage limits. Due to the large proportion of inclusions with  $T_{HOM} > \sim 580^\circ\text{C}$  those inclusions which did not homogenise were plotted as having a minimum  $T_{m_{HAL}}$  of 600°C. This makes it difficult to interpret these data points as there is no way of knowing what their final homogenisation temperature would be. The high temperatures of the fluids at Skouries also has implications for the preservation of fluid inclusions, as quartz changes polymorph from trigonal  $\alpha$ -quartz to hexagonal  $\beta$ -quartz at 573°C (at surface pressure - could be up to 600°C at porphyry depths) (Tuttle 1940; Shen et al. 1993). This phase transition is instantaneous, displacive and reversible meaning that although  $\beta$ -quartz is metastable it will slowly alter to the  $\alpha$ -quartz polymorph. This will affect any inclusions which were trapped above the phase transition, causing post-entrapment modification. Post-entrapment modification is common in the type III inclusions in Skouries as there is a very large range of  $T_{m_{HAL}}$  and  $T_{h_{V-L}}$  within the same samples, and even within observed assemblages, as illustrated in figure 36.

The type III inclusions in the first main mineralising veinset, M-3, contain a wide range of vapour homogenisation temperatures ( $T_{h_{V-L}}$ ) and halite dissolution temperatures ( $T_{m_{HAL}}$ ) (figure 36). When discriminated by observed assemblage (inclusions which are petrographically identical and spatially associated) assemblages of both type IIIA and type IIIB show evidence of either heterogenous trapping or necking (figure 35, 36). It is difficult to tell which it is, but given that no halite crystals are observed in quartz in Skouries and that the minimum trapping pressure if it was heterogenous trapping is very low for a porphyry it is probable that the inclusions have undergone necking. Two assemblages were observed which complied with Roedder's rules - a type IIIA assemblage with a  $T_{m_{HAL}}$  of 580°C and a  $T_{h_{V-L}}$  of 512°C, and a type IIIB assemblage with a  $T_{m_{HAL}}$  of 585°C and a  $T_{h_{V-L}}$  of 515°C. The type IIIA assemblage has salinities of 45 wt% NaCl and 45 wt% KCl, while the type IIIB inclusions have salinities of 39 wt% NaCl and 54 wt% KCl. These two assemblages are both high temperature, high salinity brines showing that the physical conditions of the fluids which formed the two inclusion populations in this veinset were very similar. Both inclusion assemblages yield minimum trapping pressures of 40 - 45 MPa when estimated graphically using the method described in Lecumberri-Sanchez et al (2012, fig. 35), which equates to a depth of approximately 1.8 km at lithostatic pressure. This is lower than the estimate produced using the equations from Becker et al. (2008), which yielded a minimum trapping pressure of 100 MPa, and is at the shallow end of the depth of formation range of porphyries globally (Hedenquist & Richards 1998; Sillitoe 2010). However, it appears to be a geologically

reasonable value, especially given that previous methods of finding pressure from halite-dissolution inclusions tend to over-estimate pressure (Lecumberri-Sanchez et al. 2012).

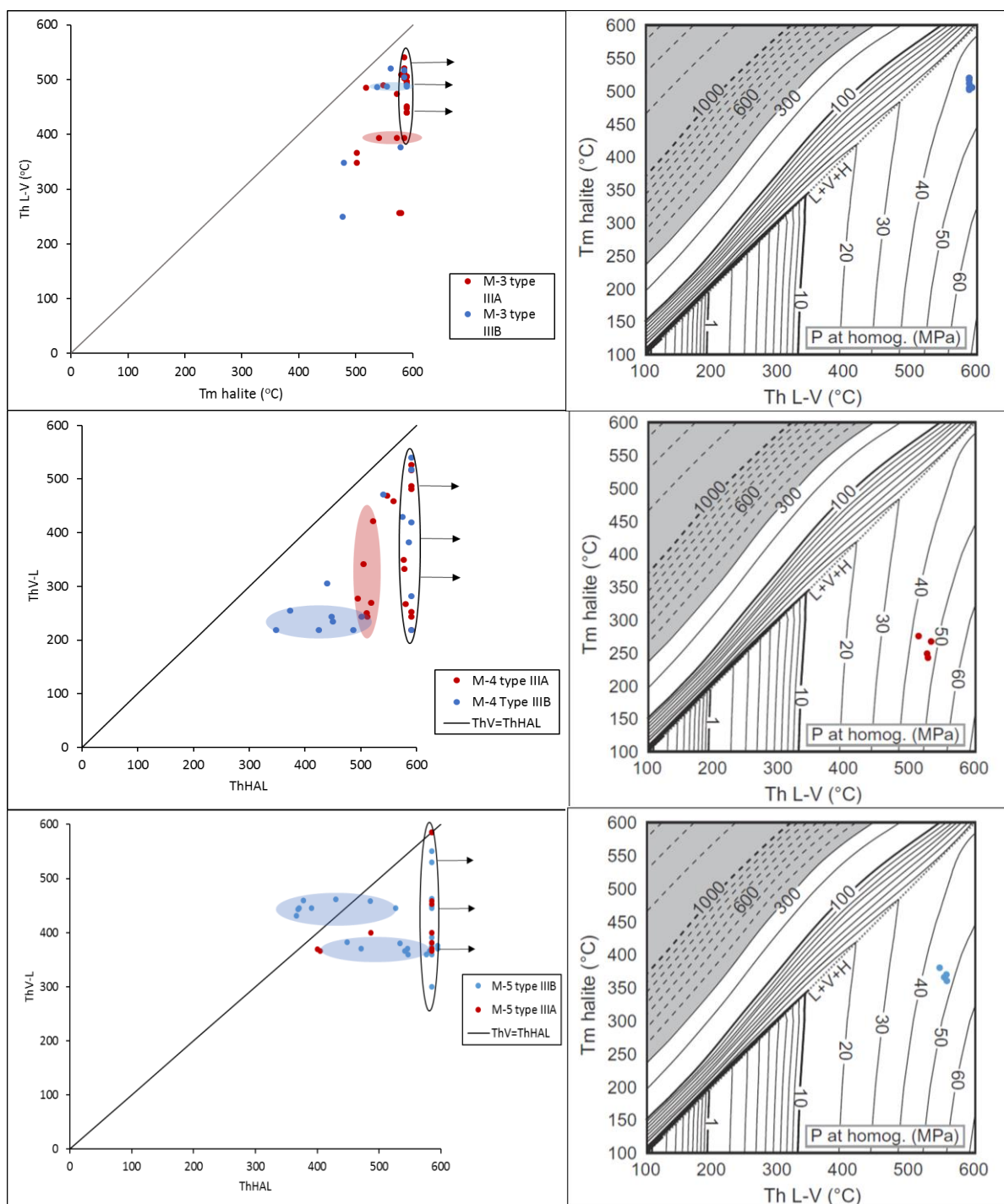


Figure 36: Graphs on the left show vapour homogenisation temperature plotted against halite dissolution temperature for type III inclusions for the main 3 mineralising veinsets. Shaded backgrounds highlight assemblages which show evidence of post-entrapment modification: stretching (vertical pattern) or necking (horizontal pattern). Horizontal trends in assemblages may also indicate heterogenous trapping (Becker et al. 2008). Inclusions with halite dissolution temperatures between 580-600°C did not fully homogenise within the limits of the stage, so this should be interpreted as a minimum dissolution temperature. This has been indicated by circling the inclusions which still had not undergone halite dissolution by the stage limit. Graphs on the right show data for unmodified assemblages (as defined by Roedder's rules) plotted against isobars from Lecumberri-Sanchez et al (2012), showing minimum trapping pressures of 45 – 50 MPa. These pressures are consistent between veinsets and seem geologically reasonable.

The next mineralising veinset, M-4, contains a much wider range of  $T_{H-L}$  and  $T_{HAL}$  values than M-3, with more low temperature inclusions. Both type IIIA and IIIB show evidence of post-entrapment modification, with a large proportion of both populations not homogenising below 600°C. The type IIIA inclusions show evidence of stretching, both as a population with a  $T_{HAL}$  of ~500°C, and the inclusions which did not homogenise above 600°C have a  $T_{H-L}$  range of 200°C to 530°C, suggesting that at least some of them have undergone stretching. The type IIIB inclusions also show a large  $T_{H-L}$  range in those which did not homogenise under 600°C, but also show evidence of necking at a  $T_{H-L}$  of 230°C. This shows that the type IIIB inclusions in this veinset are lower temperature than the type IIIA, suggesting they are from a later fluid, which tallies with their petrology. A seemingly unmodified assemblage of type IIIA inclusions with 42 wt% NaCl and 37 wt% KCl have  $T_{HAL}$  of 508°C, and  $T_{H-L}$  of 240°C. This gives an approximate minimum trapping pressure of 43 to 48 MPa (Lecumberri-Sanchez et al. 2012, figure 36), which is very similar to those seen in veinset M-3, and gives an approximate minimum depth of formation of 1.9 km, assuming lithostatic pressure.

The final mineralising veinset from the main stage, M-5, has also undergone the most post-entrapment deformation. The type IIIA inclusions mainly have  $T_{HAL}$  of >600°C, with  $T_{H-L}$  of 350°C to 600°C, again suggesting stretching has occurred. The type IIIB inclusions form two main populations, both of which have undergone necking. One, at  $T_{H-L}$  of 380°C, is still all within the halite dissolution field, but the other population, at 448°C, crosses into the  $T_{H-L} > T_{HAL}$  field. These inclusions are all one assemblage, formed along a secondary fracture in a quartz crystal, and so have definitely undergone necking. An observed assemblage which complies with Roedder's rules consists of inclusions with  $T_{HAL}$  of 542°C, and  $T_{H-L}$  of 369°C, with salinities of 18 wt% NaCl and 71 wt% KCl. These give an approximate minimum trapping pressure of 44 - 48 MPa (Lecumberri-Sanchez et al. 2012), which matches those estimated for veinset M-4.

In general terms the slightly higher temperature, more saline type IIIA inclusions are interpreted to be the primary brine phase, with type IIIB interpreted to be a secondary fluid phase formed from a micro-thermometrically similar brine, lacking in CO<sub>2</sub> and less Fe rich. Both of these populations have undergone significant post-entrapment modification, resulting in large ranges of  $T_{HAL}$  and  $T_{H-L}$ . Type IIIA contains more KCl (figure 33) than type IIIB, which contains more NaCl in the later stages M-4 and M-5. Type IIIB inclusions also show lower total salinities in the later vein stages, away from the ~95 wt% total salt saturation curve which the other inclusions fall on (figure 33). The majority of the inclusions in both type IIIA and type IIIB have ~58 wt% KCl and ~ 38 wt% NaCl. This shows that the inclusions are salt saturated as the remaining 5-10% is probably made up by the other daughter minerals, including FeCl<sub>2</sub>. This suggests that the fluid was salt saturated

at the time of trapping, although no halite crystals were observed in the quartz, and so heterogenous trapping cannot be ruled out as an explanation for the range of data seen.

#### **4.5.2.2 Carbon dioxide rich inclusions**

Type IV inclusions are the dominant inclusion type in early stage veins, and make up 75% of the inclusions in the earliest veinset, M-3, but only 35% of M-4 inclusions and 10% of M-5 inclusions. This suggests the CO<sub>2</sub> bearing fluid was an early fluid, which waned during the main stage, and this is supported by the fact that the type IV inclusions are thought to be primary. Raman spectroscopy has shown these inclusions to be pure CO<sub>2</sub>, however no evidence for CO<sub>2</sub> was observed during micro-thermometry, with the inclusions not freezing and showing no change when heated, until they burst at temperatures >500°C. The only inclusions that showed any change homogenised to vapour at 537°C, showing these to be high temperature inclusions. It is not uncommon for CO<sub>2</sub> inclusions in ore deposits to not display the formation of liquid CO<sub>2</sub> or CO<sub>2</sub> hydrate (clathrate) (Hedenquist & Henley 1985), and this constrains the CO<sub>2</sub> contents of the fluids to below 0.85 molal. This value is greater than most crush leach extracts from fluid inclusions and so is not unrealistic (Hedenquist & Henley 1985). Another possibility is that the type IV inclusions have undergone post-trapping modification, and as such have undergone stretching or leaked. As discussed above post-trapping modification has been observed in type III inclusions, and as type IV inclusions are interpreted to predate the type III inclusions they will also have undergone stretching, and this could have caused leakage of the liquid phase.

#### **4.5.3 Fluid chemistry**

The type III inclusions are divided into populations based on whether they contain hematite or not. Hematite is only present in fluid inclusions, not as inclusions in quartz crystals, which indicates it is a daughter mineral. However, the hematite daughter minerals in type IIIA inclusions do not dissolve on heating, thus it may not be a true daughter mineral, but could instead be the result of post trapping Fe-oxidation (Naden, personal communication). This provides evidence for the high  $fO_2$  of the type IIIA fluid, and the fact that the fluid is very iron rich. Type IIIB inclusions come from a less iron rich fluid which nevertheless is still highly oxidised, as shown by the presence of anhydrite and barite, showing sulphur is present as SO<sub>4</sub>. Type III inclusions in the main stage mineralising veins also contain sulphides, showing H<sub>2</sub>S and SO<sub>4</sub> to both be present. This means the fluid is at a redox boundary, and indeed the reduction of sulphur in an oxidised fluid has been suggested as a precipitation mechanism for ore minerals in porphyries (Gustafson 1978; Sillitoe 2010; Wilkinson 2013; Blundy et al. 2015).

Manganese is also present in the system, shown by the jacobsonite daughter minerals present in type III inclusions, as is calcite and apatite in the M-4 and M-5 veinsets. This shows that the fluids in Skouries have a complex cation chemistry, as has been reported for porphyries globally -  $\text{Mn}^{2+}$  was found to be the most common cation in fluid inclusions after  $\text{Na}^+$ ,  $\text{K}^+$  and  $\text{Fe}^{2+}$  (Fornadel et al. 2012). The fluids which were trapped in type III inclusions also contain Pb, Cu and As, as shown by the identification of galena, chalcopyrite, bornite and tennantite as daughter minerals in fluid inclusions.

Skouries has been reported as having relatively high levels of thorium (Kroll et al. 2002), and this is observed as hydrothermal thorites and monazites associated with potassic alteration, suggesting the fluids have high levels of Th. Skouries also has high levels of large-ion lithophile elements - K, Cs, Sr, Ba and Rb (Kroll et al. 2002) and these are seen in the fluid inclusions when laser ablated. This suggests that there has been some crustal input (Kroll et al. 2002; Siron et al. 2016).

#### 4.5.3.1 Fluid inclusion LA-ICP-MS

LA-ICP-MS of fluid inclusions has shown that K, Mn, Fe, Mg and Ca are major components of all the brine inclusions, supporting the observed daughter minerals and showing the fluids at Skouries to have a complex cation chemistry. The differences seen in the major, minor and ore forming elements between the inclusion types in the veinsets supports the conclusion that they represent different magmatic source fluids rather than the development of the same fluid.

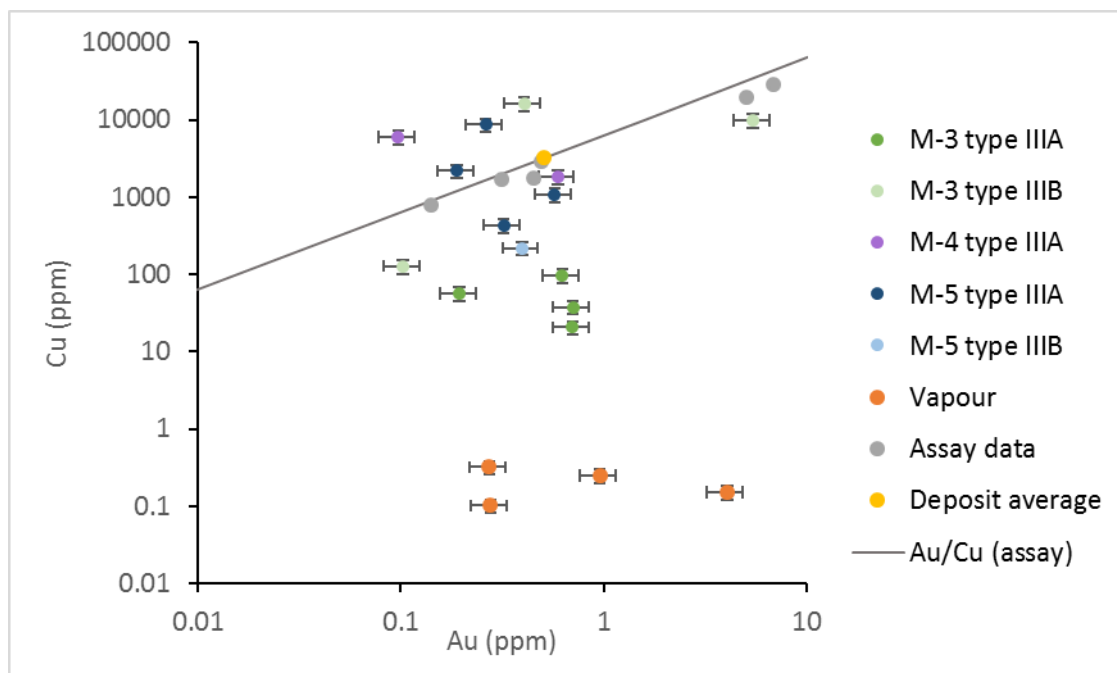


Figure 37: Cu and Au concentrations in fluid inclusions plotted with bulk rock Cu and Au concentrations from the assay intervals these samples were taken from, the Cu/Au from assay data, and the deposit average.



Both the brine inclusions and vapour inclusions contain Cu and Au, with both staying at similar levels throughout the main vein stages, with no evidence of an order of magnitude 'drop off' seen in some mineralising systems, which has been interpreted to show deposition (Audétat et al. 1998). Figure 37 shows all Au analyses of individual inclusions plotted against their Cu concentration in comparison to the bulk ore ratio of the deposit (gold circle) and assay data from the sections of the core the fluid inclusion samples are taken from (grey circles). The Au/Cu ratio from the brine inclusions is 0.0045, the Au/Cu ratio of the vapour inclusions is 0.00034 and the Au/Cu ratio of the deposit (from assay data) is 0.00016 (figure 37). The majority of the brine inclusions show Cu-Au ratios similar to that seen in the bulk ore, however the earliest and highest temperature fluid inclusion generation - M-3 type IIIA - has lower Cu concentrations than the rest of the brines. Without these inclusions the rest of the brines have an Au/Cu ratio of 0.00045, which is much closer to the ratio seen in the bulk ore. Type IIIA inclusions from veinset M-4 have Au/Cu ratios of 0.00017, and type IIIA inclusions in veinset M-5 have an average Au/Cu ratio of 0.00028. As these ratios most closely approximate that of the bulk ore these are interpreted to be the closest approximation to the main input ore fluid (Ulrich et al. 1999; Ulrich et al. 2002). The early type IIIA M-3 inclusions have undergone Cu loss compared to the bulk ore values. This could be due to fractionation of Cu into the vapour, or it could be due to fractionation of Cu into already formed Cu-sulphides (Ulrich et al. 1999; Ulrich et al. 2002). The vapour inclusions in M-3 have the highest Cu concentrations of all the vapour inclusions. However, there is no evidence that they were trapped at the same time as the type IIIA inclusions in M-3 as they are often seen as pseudo-secondary trails, while the brine inclusions are primary. The type IIIA inclusions in veinset M-3 are observed forming trails with sulphide blebs in places, which suggests that the Cu loss may be due to fractionation into sulphides.

The last mineralising veinset, M-5, contains secondary type IIIB inclusions, and these have lower ore metal concentrations and higher Ca contents than the rest of the inclusions, as well as having the lowest  $T_{\text{HOM}}$  and salinities. This suggests that this fluid is post-depositional and represents the waning of the ore forming fluids.

#### 4.5.4 Synthesis and fluid history

Mineralisation at the Skouries deposit is spatially and temporally associated with multiple intrusive phases of quartz monzonite to syenite composition. These are all highly oxidised, with primary magnetite present in all phases, and are interpreted to represent dykes from the top of a larger magma body at depth, with their changing compositions representing the evolution of this larger igneous melt. The majority of the mineralisation in the core of the deposit is hosted in a quartz vein stockwork, which is made up of several vein generations: the early stage veins; the

main stage mineralising veins; and the late veins. The late stage veins are interpreted to represent a later, low temperature fluid, based on their association with phyllic and argillic alteration and their use of late stage fractures as structural control. This study has focussed on the early and main stage veins in order to gain an insight into the hypogene mineralisation.

There are two main fluid types in this deposit - a CO<sub>2</sub> rich fluid which is represented by the pure CO<sub>2</sub> type IV inclusions (and to a lesser extent type I inclusions); and a highly saline brine, represented by type III inclusions (classification from Nash 1976). The deposit shows an overall evolution from a CO<sub>2</sub>-rich fluid to a brine dominated fluid, which is shown by the change in proportions of inclusion populations through the paragenesis of the deposit. In the early stage veins examined, E-2 and E-3, the dominant fluid inclusion population is primary type IV, CO<sub>2</sub> inclusions which make up >90% of the inclusions observed and are found in crystal growth zones. In the main stage veinsets type IV CO<sub>2</sub> inclusions make up 75% of the inclusions in the earliest mineralising veinset, M-3, but only 10% of the inclusions in the latest main stage veinset, M-5, showing that the CO<sub>2</sub> input waned over time. In contrast the brines go from being very rare in the early veinsets, to making up 25% of the inclusions in M-3 to comprising 80% of the inclusions in veinset M-5. This notable increase in the proportion of brine inclusions suggests that the brine was a later fluid, and indeed the type IIIB inclusions form secondary trails in M-4 and M-5, showing it is a later fluid than the type IV and IIIA inclusions.

### 4.5.4.1 CO<sub>2</sub> sources in Skouries

There are two possibilities for the source of the CO<sub>2</sub> in the Skouries deposit 1) the CO<sub>2</sub> is magmatic; 2) the source melt has interacted with limestones at depth and the CO<sub>2</sub> has been driven off these country rocks. There are limestones present within the Vertiskos formation, and there are many skarns in the region such as Madem Lakos (Kalogeropoulos et al. 1989), and carbonate replacement deposits such as Olympias (Kalogeropoulos et al. 1989; Eldorado Gold Corp 2015), suggesting the CO<sub>2</sub> may derive from the limestones. However, there is also evidence for CO<sub>2</sub> degassing from arc magmas (Blundy et al. 2010), and the CO<sub>2</sub> rich fluid may represent a different stage of volatile exsolution from the underlying magmas of the deposit (Edmonds 2008; Christopher et al. 2010; Lesne et al. 2011; Blundy et al. 2015).

Sulphur isotope analysis shows that there is no change in sulphur source during the paragenesis of the deposit, with all the sulphides analysed grouping tightly around the deposit mean  $\delta^{34}\text{S}_{\text{CDT}}$  of -1.4‰. This is within the range of values for 'magmatic' sulphur (Hattori & Keith, 2001), and also well within the range of values seen for porphyries globally (Hattori & Keith 2001). It is however a bit lower than the surrounding deposits, which have a mean  $\delta^{34}\text{S}_{\text{CDT}}$  of +1.5‰ (Hahn 2015), perhaps suggesting some sedimentary input may have occurred. This magmatic signature is

echoed by the oxygen and hydrogen isotopes (oxygen isotopes measured from vein quartz), which also do not show any variation between veinsets. This shows the system to be orthomagmatic, with no changes in sulphur or fluid source meaning any changes in mineralisation seen between veinsets are the result of changing fluid conditions, not a new external source of metals or fluid. The only way to distinguish whether the CO<sub>2</sub> is magmatic in source or from the surrounding limestone is to perform crush-leach stable isotope analysis on the CO<sub>2</sub> inclusions, however that was outside the scope of this study.

#### **4.5.4.2 Metal enrichment and transport in Skouries**

The input of mafic melt into felsic source melts is an important metal and sulphur enrichment mechanism in porphyry deposits (Hattori & Keith 2001; Wilkinson 2013; Blundy et al. 2015). In the Skouries deposit the main stage mineralising veins only occur after the intrusion of the 'mafic' porphyritic syenite, which is interpreted to represent a fresh input of mafic melt into the underlying magma body. This could trigger the formation of an immiscible sulphide melt, which would scavenge chalcophile metals from the surrounding melt, including Cu, Au and PGEs (Nadeau et al. 2010). The input of a mafic magma could also trigger volatile exsolution, and these volatiles could dissolve the sulphide melt to produce anomalously metal rich hydrothermal fluids (Halter et al. 2002; Harris et al. 2003; Nadeau et al. 2010; Wilkinson 2013).

The igneous bodies at Skouries are all highly oxidised, containing primary magnetite. Gold solubility in a melt has been shown to increase with  $fO_2$  (Bell et al. 2011; Wilkinson 2013) and copper enrichment and transport is favoured by oxidised, chlorine rich fluids (Lee et al. 2012), however hypogene ore mineralisation is dominated by reduced sulphides so a reduction mechanism is needed. Magnetite crystallisation in melts can reduce magmas by sequestering oxidised iron, causing the formation of reduced sulphide species and extracting Au and Cu. If the melt is saturated in volatiles this mechanism could also lead to the formation of metal enriched fluids, or to the formation of an immiscible sulphide melt (Shinohara 1994; Halter et al. 2002; Sun et al. 2004; Jenner et al. 2010; Wilkinson 2013; Sun et al. 2015). An alternative reduction mechanism is that of gas-brine reaction (Blundy et al. 2015). Here copper enrichment is proposed to occur through the differentiation of oxidised, volatile-rich mafic parent arc magmas to form chlorine and copper rich, sulphur poor silicic magmas. These exsolve magmatic brines during protracted, low pressure degassing, which become trapped, driving potassic alteration (Cline et al. 1991; Hedenquist & Lowenstern 1994; Shinohara 1994). Periodic destabilisation of cogenetic volatile-rich mafic magmas in deeper reservoirs releases sulphur-rich gases (Hattori & Keith 2001; Burgisser & Scaillet 2007; Christopher et al. 2010) which react with the shallow stored brines, reducing them. These magmatic gases would also contain CO<sub>2</sub> (Edmonds 2008; Christopher et al.

2010; Blundy et al. 2010), which could provide an explanation for the presence of type IV inclusions with halite-dissolution type III inclusions in the main stage veins, and this reduction mechanism could also provide a precipitation mechanism for sulphides.

### 4.5.4.3 Precipitation mechanisms

An effective precipitation trigger is needed to concentrate ore minerals into an economic deposit and to form mineralised veinsets from metal-rich fluids (Wilkinson 2013). The expansion and cooling of fluids has been suggested, as chalcopyrite undergoes a dramatic drop in solubility between 400 - 250°C (Crerar & Barnes 1976; Landtwing et al. 2005), however the fluids in Skouries are all very high temperature, with minimum homogenisation temperatures of type III inclusions of >550°C. Salt precipitation has also been proposed as a mechanism for the precipitation of ore minerals in porphyry deposits (Lecumberri-Sanchez et al. 2015) - as metal bearing brines traverse the phase boundary from liquid-vapour stability to vapour-halite stability the mass fraction of liquid decreases rapidly, meaning the capacity of the aqueous phase to carry copper is reduced. This may act as a direct precipitation mechanism, or metal may be temporarily stored as solid base-metal chlorides (Gruen et al. 2014). If the type III halite-dissolution inclusions in Skouries formed by heterogenous trapping it could provide evidence that salt precipitation has occurred, however as discussed above the fluid inclusion data is inconclusive as the micro-thermometric signature of salt precipitation could also be formed by post-trapping modification and no independent evidence of salt precipitation is seen.

Another potential precipitation mechanism is that of sulphur-rich, magmatic gases reacting with the metal bearing brines (Blundy et al. 2015). This would elevate sulphur activity, triggering the precipitation of sulphides through sulphidation reactions (Crerar & Barnes 1976; Landtwing et al. 2005). Water rich magmatic gases contain both H<sub>2</sub>S and SO<sub>2</sub> (Burgisser & Scaillet 2007) - and while reduced sulphur drives the sulphide precipitation, the oxidised sulphur may react with calcium bearing phases in the wall rocks to create anhydrite (Newton & Manning 2005). The co-existence of anhydrite and sulphides is observed in type III inclusions in Skouries, and is present in all the main stage veinsets. The combination of oxidised, fractionated parent magmas at Skouries (quartz monzonite and syenites), evidence for cogenetic mafic magmas ('mafic' syenites), and the presence of both highly saline, high temperature brine inclusions and vapour rich CO<sub>2</sub> inclusions suggest that the gas-brine reaction model may have occurred, however in Skouries the CO<sub>2</sub> inclusions are interpreted to be an earlier phase than the brine inclusions. There is some evidence of co-existence of brines and CO<sub>2</sub> vapour as the type IIIA and type IV inclusions are both primary in the main mineralising veinsets, and type IIIA brine inclusions contain a small amount of CO<sub>2</sub>. This

suggests that while the CO<sub>2</sub> gas phase waned over time it may have still co-existed with the ore forming fluids represented by the type IIIA inclusions, however their relative timing is not certain.

Another potential precipitation mechanism is a change in the redox conditions of the deposit, as reduction of sulphur in an oxidised fluid can trigger the precipitation of ore minerals (Gustafson 1978; Sillitoe 2010; Wilkinson 2013; Blundy et al. 2015). The earlier type IIIA inclusions contain both hematite and sulphide daughter minerals, while some of the type IIIB brine inclusions contain both sulphides and sulphate daughter minerals showing the fluid to have been on a redox boundary.

## 4.6 Conclusions and genetic model

The Skouries deposit is hosted in a pipe shaped system consisting of several generations of porphyritic intrusions of a monzonitic to syenitic composition. These intrusions are similar petrologically, close temporally, and are interpreted to be small intrusions originating in a large magma chamber at depth, meaning that their changing composition represents the evolution of this magma chamber. These intrusions can be grouped into igneous phases: an early quartz monzonite, an intermineral 'mafic' syenite and a late 'pink' syenite. All of these are strongly potassically altered, with only patchy propylitic alteration present, and all contain primary magnetite, showing that the magma was oxidised. The main Cu-Au mineralisation is associated with the main stage veins, and is hosted in bornite, chalcopyrite and electrum. The deposit is orthomagmatic, with the sulphur, oxygen and hydrogen isotopes from the mineralising veinsets showing magmatic values.

The fluid inclusions show an evolution from an early CO<sub>2</sub> rich fluid to later highly saline brines, all of which are very high temperature (>450°C). The brines homogenise by halite dissolution with a wide range of  $T_{m_{hal}}$  temperatures, which are thought to either be the result of heterogeneous trapping, or post-entrapment modification. The brines contain diverse daughter minerals including hematite, anhydrite, barite, sulphides and Mn minerals. LA-ICP-MS of fluid inclusions has shown the brines to contain high Mn, Fe, Ca, Mg, Pb and Zn contents, with an average Cu content of 0.34 wt% and an average Au content of 0.71 ppm, which is similar to the values observed at large Cu-Au porphyry deposits such as Grasberg (Ulrich et al. 1999). The vapour inclusions also show high levels of the major elements, with an average Cu content of 0.89 wt% and an average Au content of 1.39 ppm. The co-existing metal-rich CO<sub>2</sub> and brine inclusions are suggested to indicate that magmatic CO<sub>2</sub> rich vapours from mafic recharge of the magma chamber reacted with shallow brines to trigger sulphide precipitation. The first generation of brine inclusions in the M-4 and M-5 veinsets are interpreted to be the main mineralising fluid

phases from Au/Cu values. The fluids contain high levels of LILE such as Sr, Ba, Th and U. This is also seen in whole rock analyses by Kroll et al and Siron et al and is indicative of crustal contamination of the source magmas (Kroll et al. 2002; Siron et al. 2016).

Based on the observations and analyses presented in this paper and the discussions above, it is possible to generate a speculative genetic model for the main stage of mineralisation in the Skouries deposit:

1. An initial oxidised, volatile-rich shoshonitic magma chamber is formed at depth by emplacement of volatile-rich, oxidised magmas derived from post-subduction magmatism associated with the exhumation of the Rhodope core.
2. As these melts fractionate magnetite precipitation triggers a reduction of the melt and immiscible sulphide melt formation, concentrating Au, Cu and PGEs.
3. Quartz monzonite intrusions ascend through a zone of structural weakness to form pipe-like bodies (early porphyritic quartz monzonite). The reduction in pressure causes volatile exsolution, leading to the formation of the largely barren, magnetite rich early veinset.
4. An injection of mafic magma into the underlying magma chamber further enriches the melt in Cu, Au, PGEs and S. This periodic mafic input leads to the intrusion of the 'mafic' syenite dykes into the overlying system, representing the change in underlying magma chemistry, and also triggers volatile exsolution from the underlying melt.
5. Multiple intrusions of the 'pink' syenite phase are intruded into the overlying system and undergo degassing, forming brines.
6. Sulphide precipitation is triggered either by gas-brine interaction or by a change in redox conditions causing a reduction of sulphur in the fluid. This precipitation mechanism forms the main ore minerals and veinsets. The amount of magmatic gas present in the system wanes over time, leading to the changes seen in inclusion populations between the high temperature, high salinity, CO<sub>2</sub> dominated inclusions of M-3 to the lower temperature, lower salinity, CO<sub>2</sub> poor inclusions in M-5, and the decrease in ore metal concentrations seen in the final inclusion stage of M-5.

## Chapter 5: Platinum group minerals in the Skouries Cu-Au (Pd, Pt, Te) porphyry deposit

### 5.1 Introduction

#### 5.1.1 Platinum group elements in Porphyries

Porphyry deposits often contain PGEs as by-products (Tarkian & Stribrny 1999; Economou-Eliopoulos 2005; Economou-Eliopoulos 2010), and the economic extraction of these valuable co-products is of increasing interest. With recent advances in extraction technology such as the use of ionic liquids (Jenkin et al. 2016), understanding the distribution and mineralogy of platinum group minerals in porphyry deposits is increasingly important. Elevated PGE levels have been described for several porphyries worldwide at an average Pt + Pd content of 5 ppm – the level which is required to be economic (Economou-Eliopoulos 2010). The most well-studied is the Elatsite deposit, Bulgaria, which has an average whole rock Pt content of 16 ppb, and Pd content of 40 ppb, with Pt contents in flotation concentrates of 0.15 g/T and Pd contents of 0.72 g/T (Tarkian et al. 2003; Auge et al. 2005). Other PGE enriched porphyries are summarised in table 13, with the ones which have been studied in more detail include Santo Tomas II, Philippines (Tarkian & Koopmann 1995); Galore Creek, Lorraine, Mt. Milligan, Mt. Polley & Island Copper, British Columbia (Thompson et al. 2001). Although these deposits are in different geodynamic settings, with different ore and alteration mineralogies, they do have some common features: they are all Cu-Au porphyries with alkaline to calc-alkaline host rocks and they usually contain primary magnetite (with the exception of Ok Tedi), indicating an oxidised source magma (Kehayov & Bogdanov 1987; Tarkian & Koopmann 1995; Tarkian & Stribrny 1999; Sotnikov et al. 2001; Thompson et al. 2001; Tarkian, Hünken, et al. 2003; Auge et al. 2005; Bogdanov et al. 2005; Pašava et al. 2010).

It was originally suggested that PGE enrichment in porphyries was associated with the later, shallower and cooler mineralisation phases (Eliopoulos & Economou-Eliopoulos 1991), however PGEs have been located within the paragenesis of the Elatsite, Santo Tomas II, Kalmakyr, Mamut and Majdanpek deposits. In all of these they are found associated with the main, potassic, ore forming stage of the deposit genesis. The Elatsite and Santo Tomas II deposits also show high fluid inclusion homogenisation temperatures (>350°C) and high salinities (>50%) in the veins associated with PGE enrichment (Kehayov & Bogdanov 1987; Tarkian & Koopmann 1995; Tarkian & Stribrny 1999). This means it is likely that PGE enrichment in porphyries is associated with hypogene, early

phase ore forming processes (Economou-Eliopoulos & Eliopoulos 2000). The high  $fO_2$  (as shown by the presence of magnetite), temperature and salinity of the PGE bearing veins favours the hydrothermal transport of PGEs as chloride complexes, and this is currently the accepted mechanism of transport in porphyry deposits (Xiong & Wood 2000).

Only the Elatsite and Santo Tomas II deposits have undergone thorough petrological surveys in order to identify the platinum group minerals present. Elatsite hosts its PGEs in merenskyite, and in solid solution of merenskyite-moncheite. These are found as rounded, 5 – 20  $\mu\text{m}$  inclusions in chalcopyrite in the main magnetite-chalcopyrite-bornite stage of the deposit, with rare cylindrical merenskyite crystals up to 120  $\mu\text{m}$  in diameter. The deposit also contains a range of other tellurides, including Ag tellurides hessite, empressite, bohdanowiczite and stützite as well as the Ag selenide naumannite. It also contains a range of Ni-Co sulphides, including linnaeite-siegenite-carrollite complexes. Other semi-metal minerals present include tetrahedrite, tennantite, clausthalite and wittichenite (Tarkian et al. 2003; Bogdanov et al. 2005; Aue et al. 2005). Santo Tomas II hosts its PGEs in merenskyite, moncheite and kotulskite. These are present as intergrown, rounded, 1-12  $\mu\text{m}$  inclusions in chalcopyrite and bornite in the main magnetite-bornite-chalcopyrite bearing veins of the potassic core of the deposit. Other semi-metal bearing minerals present include tetrahedrite, tennantite, hessite and petzite (Tarkian & Koopmann 1995). Additionally stibiopalladinite and vysotskite have been identified in sulphide concentrates from Santo Tomas II (Pięstrzynski 1994), while merenskyite has been identified in sulphide concentrates from Biga and Majdanpek (Tarkian & Stribny 1999).



*Table 13: A summary of PGE enriched porphyries globally showing their common features, Pd and Pt concentrations, PGMs present and any other features which may be associated with the PGE enrichment. The Skouries data is a summary of data from past work, not including that from this study. Blank cells indicate that these features have not yet been classified for that deposit (Kehayov & Bogdanov 1987; Tarkian & Koopmann 1995; Tarkian & Stribrny 1999; Thompson et al. 2001; Sotnikov et al. 2001; Tarkian, Hünken, et al. 2003; Auge et al. 2005; Bogdanov et al. 2005; Pašava et al. 2010). BC = British Columbia, bn = bornite, cpy = chalcopyrite, FI = fluid inclusions, hem = hematite, mag = magnetite, PNG = Papua New Guinea, TMB = Tethyan Metallogenic Belt*

Deposit	Type	Area	Host rock	Country rock	Pt (whole rock, ppb)	Pt (concentrate)	Pd (whole rock, ppb)	Pd (concentrate)	Other metals	Where are PGEs?	PGMs present	Other semi-metal bearing minerals present	Other features
Elastsite	Alkaline	Bulgaria, TMB	Multiphase monzonite	Phyllites	16 av, 72-170	0.15 g/T	40 av, 760-1900	0.72 g/T	Au, Ag, Cu	Mag-bn-cpy veins, in cpy and bn	Merenskyite, moncheite	Linnaeite-siegenite-carrollite, tetrahedrite-tennantite, electrum, hessite, naumannite, clausthalite, sylvanite, empressite, stutzite, wittichenite, bohdanowiczite	High salinity and temperature FIs; fO2 conditions near mag-hem buffer
Medet	Calc-alkaline	Bulgaria, TMB	Granodiorite	Gneisses, granites		8 ppb	160						High salinity and temperature FIs
Majdanpek	Calc-alkaline	Serbia, TMB	Diorite	Andesites, gneisses, phyllites		16-24 ppb		130-240 ppb		In cpy	Merenskyite	Hessite	
<i>Skouries</i>	<i>Shoshonite</i>	<i>Greece, TMB</i>	<i>Syenite</i>			<i>8 ppb</i>	<i>160</i>			<i>In cpy</i>	<i>Merenskyite</i>		
Erdenetuin-Obo	Calc-alkaline	Mongolia	Diorite-granodiorite-granite		21	33 ppb	14	20					Sr isotopes indicate mantle source
Santo Tomas II (Philex)	Calc-alkaline	Phillipines	Quartz diorite (tonalite)	Volcanic rocks	13940	0.4 g/T	15-160	1.5 g/T	Au, Ag, Cu	Mag-bn-cpy veins, potassic alteration	Merenskyite, moncheite, kotulskite	Tertahedrite tennantite, electrum, hessite, petzite	High salinity and temperature FIs
Bozshakol	Calc-alkaline	Kazakhstan	Tonalite			<dt		245 ppb					
Kalmakyr	K-calc-alkaline	Uzbekistan	Multiphase Monzonite		6		55		Cu, Mo, Au, Ag	Mag-cpy-py-bn veins	Tetrahedrite		
Sora	K-calc-alkaline	Russia	Monzodiorite-diorite-syenite		<10	60-110 ppb	13	46-52 ppb					Sr isotopes indicate rift magmatism
Aksug	Calc-alkaline	Russia	Diorite-tonalite		22	25-96 ppb	17	17-924 ppb					Sr isotopes indicate mantle source
Zhireken	K-calc-alkaline	Russia	Diorite-granodiorite		28	299 ppb	84	684 ppb					
Mamut	Calc-alkaline	Malaysia	Adamellite	Siltstones and pyroclastics		450-490 ppb		1180-1600 ppb	Cu Au	In cpy	Merenskyite		High salinity and temperature FIs
Ok Tedi	Calc-alkaline	PNG	Latite	Sediments		24 ppb		650-980 ppb		No PGM, in lattice of cpy			No magnetite present, PGMs in skarns
Galore Creek	Alkaline	BC			15-107		103-407						Oxidised magma
Lorraine	Alkaline	BC			11		19						Oxidised magma
Mt Milligan	Alkaline	BC			17-111		51-6312						Oxidised magma
Mt Polley	Alkaline	BC			12236		23-320						Oxidised magma
Island Copper	Alkaline	BC			31-38		63-320						Oxidised magma

### 5.1.2 Previous work on PGEs in Skouries

Skouries has long been known for having elevated concentrations of PGEs (Eliopoulos & Economou-Eliopoulos 1991; Tarkian & Stribrny 1999) - in 1991 several core samples were analysed for PGEs, along with flotation concentrate samples. These showed Pd contents of between 52 – 480 ppb and Pt contents of 1 – 10 ppb in whole rock samples, while the ore concentrate samples contained 70 – 110 ppb Pd and 10 ppb Pt (Economou-Eliopoulos, 1991). It was suggested that the Au, Ag, Pd and Te have a common genesis and were associated with silica enrichment, and may have formed due to leaching and oxidation of primary mineralisation (Eliopoulos & Economou-Eliopoulos 1991). In 2000 several more samples from different alteration zones of Skouries were analysed for PGEs along with a chalcopyrite concentrate sample. The potassic zone was shown to have Pd contents of 60 – 200 ppb and Pt contents of 5 – 10 ppb, while samples from the oxidised zone have Pd contents of 65 – 490 ppb and Pt contents of 10 ppb. The chalcopyrite concentrate sample was found to contain 2400 ppb Pd and 40 ppb Pt (Economou-Eliopoulos & Eliopoulos 2000). Further precious metal analysis has been performed on 27 flotation concentrate samples, with Pd values ranging from 1 – 396 ppb, and Pt values of <10 – 81 ppb (Eliopoulos et al. 2014). It is thought that the PGEs in Skouries originate from either crustal rock contribution from the surrounding amphibolites or from the mixing of felsic and mafic alkaline magmas (Eliopoulos et al. 2014). It has been suggested that this PGE enrichment is promoted by high oxygen fugacity of the magma allowing the hydrothermal transport of Pd and Pt (Eliopoulos & Economou-Eliopoulos 1991; Economou-Eliopoulos & Eliopoulos 2000).

Although bulk rock precious metal analysis has identified the primary PGE enrichment to be in the potassic zone of the deposit (Economou-Eliopoulos & Eliopoulos 2000), there has been little work done on the mineralogy of the PGEs. Merenskyite has been identified as an inclusion in a chalcopyrite grain from Skouries along with hessite and sylvanite (Tarkian & Stribrny 1999), and other occurrences of merenskyite, hessite, electrum and an unnamed Pd-Bi-Te mineral have been reported (Eliopoulos et al. 2014). To date, however, no one has satisfactorily placed the PGEs within the paragenesis of the deposit, or done a thorough in situ survey to identify their host minerals, their abundance and distribution.

## 5.2 Mineral chemistry and platinum group mineral classification

### 5.2.1 Samples analysed

Samples were selected for analysis based on the assay data Pd and Pt values - intervals with the highest values were sampled. The samples were then made into polished thin sections and examined under optical microscope for visible PGMs in reflective light. As the PGMs are mainly <20 µm in diameter they were difficult to identify through optical microscopy, so the 7 samples with the highest assay values were chosen to analyse further on the SEM and EPMA (table 14).

Table 14: Samples analysed for PGMs

Sample	Drill hole	Depth (m)	Lithology	Alteration	Veins present	Ore mineralogy	Pd assay value (ppm)	Pt assay value (ppm)
3	134	261	PPO	Potassic, chlorite & sericite present	M5	Pyrite, chalcopyrite, bornite	0.139	0.002
8	137	133.9	PPO	Potassic	M5	Chalcopyrite, magnetite	0.189	0.006
9	139	655	BPO	Clay	M4	Chalcopyrite, magnetite	0.393	0.006
26	134	266.1	PPO	Potassic	M3	Pyrite, chalcopyrite, bornite, magnetite	0.036	0.001
31	139	514	BPO	Potassic & clay	M4	Chalcopyrite, bornite, magnetite, Au	1.051	0.011
34	139	497.6	BPO	Clay	M3	Chalcopyrite, bornite, magnetite	0.33	0.007
36	137	128.1	PPO	Potassic & clay	M3	Chalcopyrite	0.728	0.012

### 5.2.2 Platinum group minerals

The samples with the highest Pd and Pt values from assay were systematically scanned at 500x magnification on the SEM with the BSE calibrated to highlight 'heavy' elements, with any element with a high atomic number (>82) being examined with EDS in order to identify it. If the mineral contained Pd, Pt, Au, Ag, Te or Se it was analysed more thoroughly using EDS in order for a probable mineral identification to be acquired. EPMA was then used to confirm the minerals present and to gain trace element data for three of these samples (those with the most PGMs), using the method outlined in chapter 2.

*Table 15: Semi-quantitative results from EDS and EPMA analysis of platinum group minerals (PGMs), including location (cpy=chalcopyrite, bn=bornite, mag=magnetite, chl=chlorite, hem=hematite, pot alt=potassic alteration), elements present and probable mineral classification.*

Sample	PGM no	Size (µm <sup>2</sup> )	Host mineral and vein	Elements present (from EDS)	Elements present (from EPMA)	Probable mineral	Mineral formula
3	1	12	Edge of bn in A vein	Pd Bi (Pb)	Pd Bi (Pt Se)	Sobolevskite	PdBi
3	2	16	In bn in A vein	Pd Bi	Pd Bi (Pt Se Ag Os)	Sobolevskite	PdBi
3	3	8	Edge of mag in pot alt	Pd Bi (Pb)		Sobolevskite	PdBi
3	4	24	In bn in pot alt	Pd Bi	Pd Bi (Pt Se Au)	Sobolevskite	PdBi
3	5	15	Edge of cpy on edge of A vein, intergrown with chl	Pd Ag Te Bi Se (Pb)	Pd Ag Te Sb (Bi Se As Rh)	Sopcheite	Ag <sub>4</sub> Pd <sub>3</sub> Te <sub>4</sub>
3	6	4	Edge of cpy in centre of altered feldspar crystal	Pd Au Ag Te (Pt)	Ag Pd Te Se Au (Sb As)	Sopcheite	Ag <sub>4</sub> Pd <sub>3</sub> Te <sub>5</sub>
9	2	10	In cpy in pot alt	Pd Pt Au Ag (Pb)		Merenskyite?	(Pd,Pt)(Te,Bi) <sub>2</sub>
31	1	5	In hem in Q-m-s vein	Pd Au Ag Te (Pt)		Kotulskite?	Pd(Te,Bi)
31	2	10	Edge of bn in Q-m-s vein	Pd Au Ag Te Bi (Pb)		Sopcheite	Ag <sub>4</sub> Pd <sub>3</sub> Te <sub>5</sub>
31	3	10	In cpy in Q-m-s vein	Pd Au Ag Te Bi (Pb)		Sopcheite	Ag <sub>4</sub> Pd <sub>3</sub> Te <sub>5</sub>
31	4	100	In cpy in Q-m-s vein	Pd Ag Bi (Pb)		Sopcheite	Ag <sub>4</sub> Pd <sub>3</sub> Te <sub>5</sub>
31	5	8	In cpy in Q-m-s vein	Pd Ag Te Bi		Sopcheite	Ag <sub>4</sub> Pd <sub>3</sub> Te <sub>5</sub>

Sample	PGM no	Size (μm <sup>2</sup> )	Host mineral and vein	Elements present (from EDS)	Elements present (from EPMA)	Probable mineral	Mineral formula
34	3	30	Edge of cpy in A vein	Pt Ag Bi	Pd Te Bi Ag	Merenskyite	(Pd,Pt)(Te,Bi) <sub>2</sub>
34	4	50	Edge of bn in pot alt	Pd Te (Pt) (Pb)	Pd Te (Sb Rh Os)	Testibiopalladite	PdTe(Sb,Te)
34	6	12	Between cpy and mag in pot alt at edge of A vein	Pd Ag Te Bi	Pd Te Bi Ag (Rh)	Kotulskite with Ag?	Pd(Te,Bi)
34	9	16	In cpy in A vein	Pd Ag Te Bi (Pt)	Pd Te Bi (Ag Se Rh Os)	Merenskyite	(Pd,Pt)(Te,Bi) <sub>2</sub>
34	10a	70	Edge of bn in pot alt	Pd Ag Te Bi	Pd Te Bi (Ag Se Rh)	Kotulskite	Pd(Te,Bi)
34	10b	15	Edge of bn in pot alt	Ag Bi Pt	Pd Te Ag Bi (Se)	Sopcheite-Merenskyite	Ag <sub>4</sub> Pd <sub>3</sub> Te <sub>5</sub> -(Pt,Pd)(Te,Bi) <sub>2</sub>
36	1	100	Edge of hole in cpy in vein	Ag Se Bi	(Pd Te Se Ag)	Sopcheite	Ag <sub>4</sub> Pd <sub>3</sub> Te <sub>5</sub>
36	4	10	Edge of hole in cpy in vein	Se Ag Te Bi	Pd Bi (Pt)	Sobolevskite	PdBi
36	5	10	Edge of hole in cpy in vein	Se Ag Te	Pd Ag Te Bi (Se Rh)	Sopcheite	Ag <sub>4</sub> Pd <sub>3</sub> Te <sub>5</sub>
36	12	10	In cpy in vein	Pd Pt Ag Te Bi	Pd Te Bi (Pt Sb Rh Os)	Merenskyite	(Pd,Pt)(Te,Bi) <sub>2</sub>
36	18	10	In cpy in vein	Pd Pt Te Bi	Pd Pt Te Bi (Ag Sb Rh Os)	Merenskyite	(Pd,Pt)(Te,Bi) <sub>2</sub>

Sample	PGM no	Size (μm <sup>2</sup> )	Host mineral and vein	Elements present (from EDS)	Elements present (from EPMA)	Probable mineral	Mineral formula
8	1	5	Free in pot alt	Ag Te		Empressite	AgTe
34	1	40	In bn in A vein	Pt Ag Bi	Ag Au (Te)	Electrum	AuAg
34	2a	10	Edge of cpy in A vein	Pt Au Ag	Ag Au	Electrum	AuAg
34	2b	100	Edge of cpy in A vein	Pt Au Ag	Ag Au	Electrum	AuAg
34	5	15	Between cpy and mag in pot alt	Pt Te Bi/Pd Ag Te Bi	Ag Te (Se)	Stützite	Ag <sub>5-x</sub> Te <sub>3</sub> (x=0.24-0.36)
36	10	25	In cpy in vein	Pt Ag Te Bi	Ag Te Bi (Se Rh)	Empressite	AgTe
36	18	10	In cpy in vein	Ag Te	Ag Te (Bi Se Rh Os)	Hessite	Ag <sub>2</sub> Te

Table 15 shows a summary of the platinum group minerals (PGMs) present in the samples analysed, with their size, mineral associations and semi-quantitative data from EDS and EPMA showing which elements are present, along with a probable mineral classification. The PGMs are small, with an average size of  $24 \mu\text{m}^2$ , and a range of  $4 \mu\text{m}^2$  -  $100 \mu\text{m}^2$ . They are usually found associated with bornite or chalcopyrite and are found both as inclusions within these ore minerals and as crystals on the edge of them. The PGMs are also found solo, or associated with magnetite, and are often observed on the edge of holes in the sample - perhaps where another mineral has been plucked out by polishing. They are irregular in morphology, often occurring as blebs, as cubic crystals or as infill of a fracture. The PGMs are found within all the main stage mineralising veinsets - M-3, M-4 and M-5 veins and also associated with disseminated ore minerals in potassic alteration around the veins (figure 38). The PGMs visible in optical microscopy are often a composite of several crystals of slightly differing composition rather than one species only - however as they are so small it is difficult to resolve the individual species with EPMA.

The PGMs analysed in this study were predominately Pd PGMs, with rare Pt. Using the semi-quantitative data, the PGMs in Skouries can be split into three broad 'families', defined by their semi-metal content. The most common is the Pd-Ag-Te family, which often also contains smaller concentrations of Bi, Au and Se. These are predominately found associated with chalcopyrite, and are the only type of PGM found in the early M-3 and M-4 veins. They were also observed in alteration around M-5, and were present in all samples analysed. Next is the Pd-Bi family, which often contains minor amounts of Pt, Se and rare Ag and Au. These are usually associated with bornite, and are found in M-5 veins and in potassic alteration, and are only found in samples 3 and 36. Finally, there is the Pd-Te-Bi family, which often also contain Pt, and minor amounts of Ag, Se and Sb. These are found associated with both bornite and chalcopyrite in M-5 veins and potassic alteration, and are only found in two samples - 34 and 36.

EPMA results, which are shown in table 16, have confirmed the presence of Sobolevskite ( $\text{PdBi}$ ), Sopcheite ( $\text{Ag}_4\text{Pd}_3\text{Te}_4$ ), Testibiopalladite ( $\text{PdTe}(\text{Sb},\text{Te})$ ) and Merenskyite ( $(\text{Pd},\text{Pt})(\text{Te},\text{Bi})_2$ ). Taking into account the EPMA data with totals outside the 95-102 range and EDS data, Kotulskite ( $\text{Pd}(\text{Te},\text{Bi})$ ) also appears to be present. Of the 23 PGMs analysed nine are Sopcheite, five are Sobolevskite, three are Merenskyite, two are Kotulskite and one is Testibiopalladite, with three minerals with unclear compositions from the semi-quantitative data.

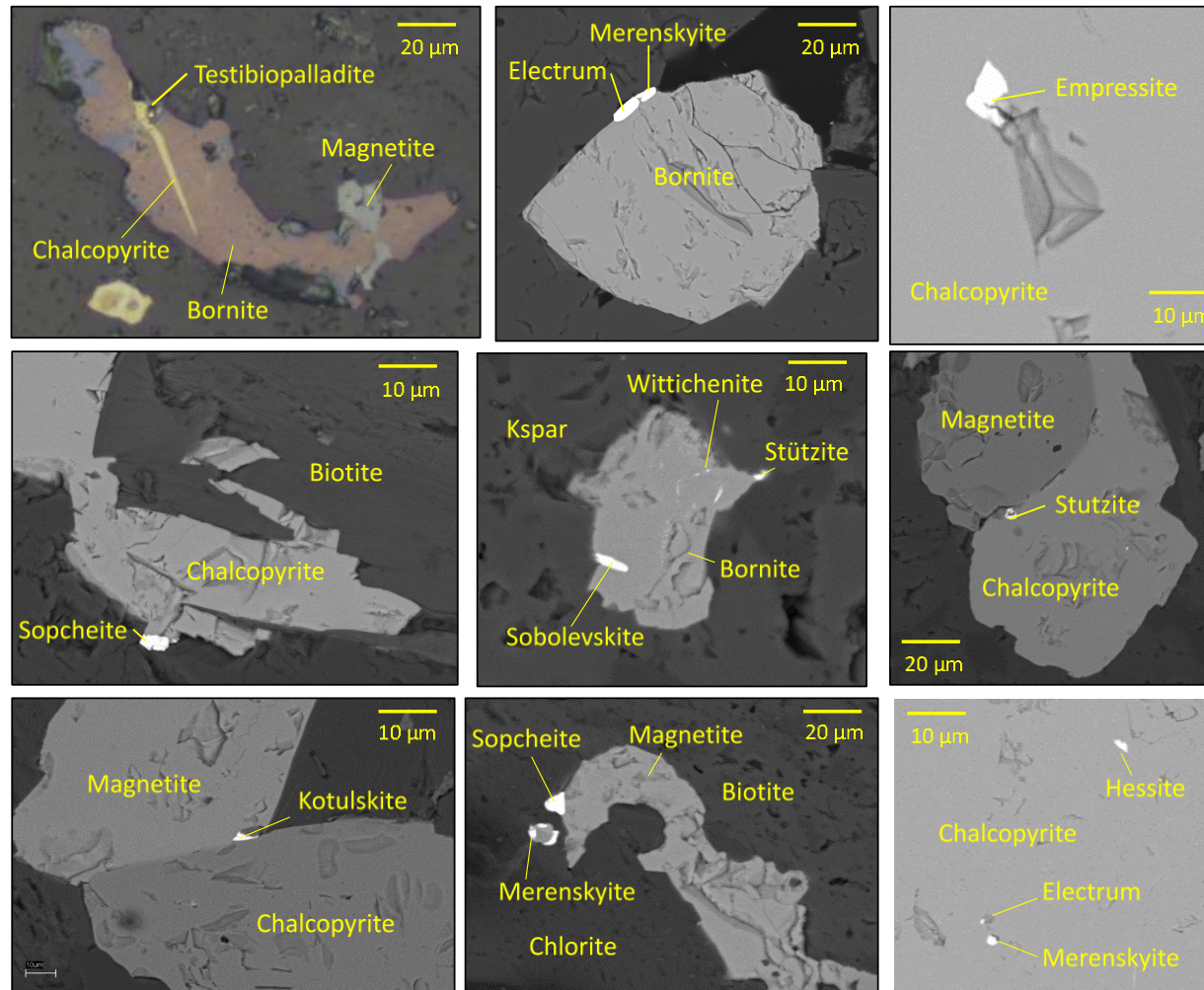


Figure 38: Photomicrographs and SEM BSE images showing platinum group minerals and precious metal tellurides in situ.



Table 16: Results from quantitative EPMA analysis in wt%. \* = has undergone empirical correction to eliminate peak overlap. Shaded results are precious metal tellurides, non-shaded are PGMs.

Sample	3	3	34	34	36	36	34	34	34	34	36	36	Error (2σ)	Detection limit
PGE #	PGE 4	PGE 5	PGE 4	PGM 3	PGE 12	PGE 18a	PGE 1	PGM 2a	PGM 2b	PGM 5	PGE 10	PGE 18b		
<b>S*</b>	19.5	5.3	0.4	1.28	3.0	0.9	<dt	<dt	<dt	0.54	16.6	0.9	0.57	0.07
<b>Pt*</b>	0.59	<dt	<dt	<dt	0.96	<dt	<dt	<dt	<dt	<dt	<dt	2.33	0.24	0.14
<b>Mn</b>	<dt	<dt	<dt	<dt	<dt	<dt	<dt	<dt	<dt	<dt	<dt	<dt	0.05	0.03
<b>Fe</b>	2.78	0.87	0.33	1.26	4.47	2.40	0.72	0.48	0.33	0.20	18.17	1.66	0.15	0.03
<b>Co</b>	<dt	<dt	<dt	<dt	<dt	<dt	<dt	<dt	<dt	0.23	<dt	<dt	0.06	0.03
<b>Ni*</b>	<dt	<dt	<dt	<dt	<dt	<dt	<dt	<dt	<dt	0.21	<dt	<dt	0.06	0.03
<b>Cu*</b>	14.37	2.48	1.11	1.72	2.98	2.54	0.92	0.53	0.29	2.76	20.24	2.22	0.32	0.05
<b>Zn</b>	<dt	<dt	<dt	<dt	<dt	<dt	<dt	<dt	<dt	<dt	<dt	<dt	0.03	0.02
<b>As</b>	<dt	0.40	<dt	<dt	<dt	<dt	<dt	<dt	<dt	<dt	<dt	<dt	0.05	0.03
<b>Se</b>	2.17	2.47	<dt	<dt	<dt	0.11	<dt	<dt	<dt	0.86	0.09	<dt	0.06	0.03
<b>Pd*</b>	20.64	15.95	28.41	32.74	25.18	<dt	<dt	<dt	<dt	<dt	<dt	25.29	0.27	0.08
<b>Ag*</b>	<dt	25.22	<dt	2.36	<dt	58.74	19.20	17.17	16.13	54.77	22.74	0.52	0.31	0.05
<b>Sb*</b>	<dt	2.89	0.11	0.15	0.14	<dt	<dt	<dt	<dt	0.11	<dt	0.13	0.13	0.08
<b>Te*</b>	<dt	22.03	67.12	54.10	61.78	37.51	0.63	<dt	<dt	37.19	18.03	63.07	0.42	0.10
<b>Pb*</b>	<dt	20.95	1.19	<dt	<dt	<dt	<dt	<dt	<dt	3.02	0.15	<dt	0.33	0.14
<b>Bi*</b>	39.7	0.8	<dt	8.75	1.7	0.6	<dt	<dt	<dt	<dt	6.5	3.2	0.50	0.17
<b>Cr</b>	<dt	<dt	<dt	<dt	<dt	<dt	<dt	<dt	<dt	<dt	<dt	<dt	0.06	0.04
<b>Ru</b>	<dt	<dt	<dt	<dt	<dt	<dt	<dt	<dt	<dt	<dt	<dt	<dt	0.18	0.11
<b>Rh*</b>	<dt	0.29	0.77	0.54	0.70	0.43	<dt	<dt	<dt	0.47	0.14	0.78	0.23	0.14
<b>Os*</b>	<dt	<dt	0.25	0.19	0.17	0.09	<dt	<dt	<dt	0.11	<dt	0.19	0.08	0.05
<b>Ir*</b>	<dt	<dt	<dt	<dt	<dt	<dt	<dt	<dt	<dt	<dt	<dt	<dt	0.21	0.12
<b>Au*</b>	0.22	<dt	<dt	<dt	<dt	<dt	80.89	84.08	85.40	<dt	<dt	<dt	0.45	0.19
<b>Si</b>	0.17	0.66	0.03	0.06	0.02	<dt	0.06	<dt	0.06	<dt	<dt	<dt	0.04	0.01
<b>Total</b>	99.30	100.54	98.08	101.61	100.30	102.51	101.77	102.27	102.21	98.83	102.05	99.52		
<b>Mineral</b>	Sobolevskite	Sopcheite	Testibiopalladite	Merenskyite	Merenskyite	Merenskyite	Electrum	Electrum	Electrum	Stutzite	Empressite	Hessite		

### 5.2.3 Other precious-metal bearing minerals

The samples analysed also contained other precious metal bearing minerals, often as blebs within chalcopyrite and bornite, or free within M-5 veins. These fall into two categories: Ag-Au minerals, and Ag-Te minerals, which sometimes contain Bi and Se. These are usually rounded in morphology, with an average size of  $29\text{ }\mu\text{m}^2$  and a range of  $5\text{ }\mu\text{m}^2$  –  $100\text{ }\mu\text{m}^2$  and are much more common than PGMs, being found as an accessory mineral in all thin sections analysed. EPMA has confirmed that the mineral species present are Electrum (AgAu), Empressite (AgTe), Hesseite (Ag<sub>2</sub>Te) and rare Stützite (Ag<sub>5-x</sub>Te<sub>3</sub>, (x=0.24-0.36)) (figure 38).

### 5.2.4 Bornite and galena chemistry

EDS analysis identified common Bi-Cu minerals on the edges of bornite, with the majority of bornites analysed also containing some Bi. EDS also showed the galena in the system to contain significant levels of Ag and Se. In order to confirm that these findings were not due to peak overlap EPMA was used to analyse galena on the edge of bornite, some of the Bi-Cu minerals seen on the edge of bornite and to map a Bi enriched, zoned bornite crystal (table 17, figure 39).

The galena analysed showed an Se content of 3.99 wt%, which is consistent with that seen in EDS analysis of galena. It also contains Cu and Fe, but this is likely to be signal contamination from the surrounding bornite. The galena analysed with EPMA has Ag below detection limit, suggesting that the Ag seen in EDS is an artefact resulting from peak overlap, and that the majority of the Ag in the Skouries deposit is hosted in precious metal bearing minerals.

The Cu-Bi minerals analysed are confirmed to be Wittichenite (Cu<sub>3</sub>BiS<sub>3</sub>), and contain 43 wt% Bi, 38 wt% Cu and 18 wt% S, also containing trace amounts of Pt (average 0.58 wt%), Fe (average 0.74 wt%) and Se (average 0.13 wt%) (table 17). The zoned bornite analysed with EPMA (figure 39) does not contain any Bi in either of the outer zones, only in the innermost region where Wittichenite forms an exsolution texture. The outer zone is pure bornite, with trace Se content (0.07 wt%). The inner zone contains higher concentrations of Cu, and less Fe, still with trace amounts of Se (0.06 wt%). The wittichenite area is also zoned, with the outermost part containing less Bi and more Cu than the inner part, and the wittichenite also contains trace amounts of Se (0.05 wt%) and Pt (0.51 wt%).

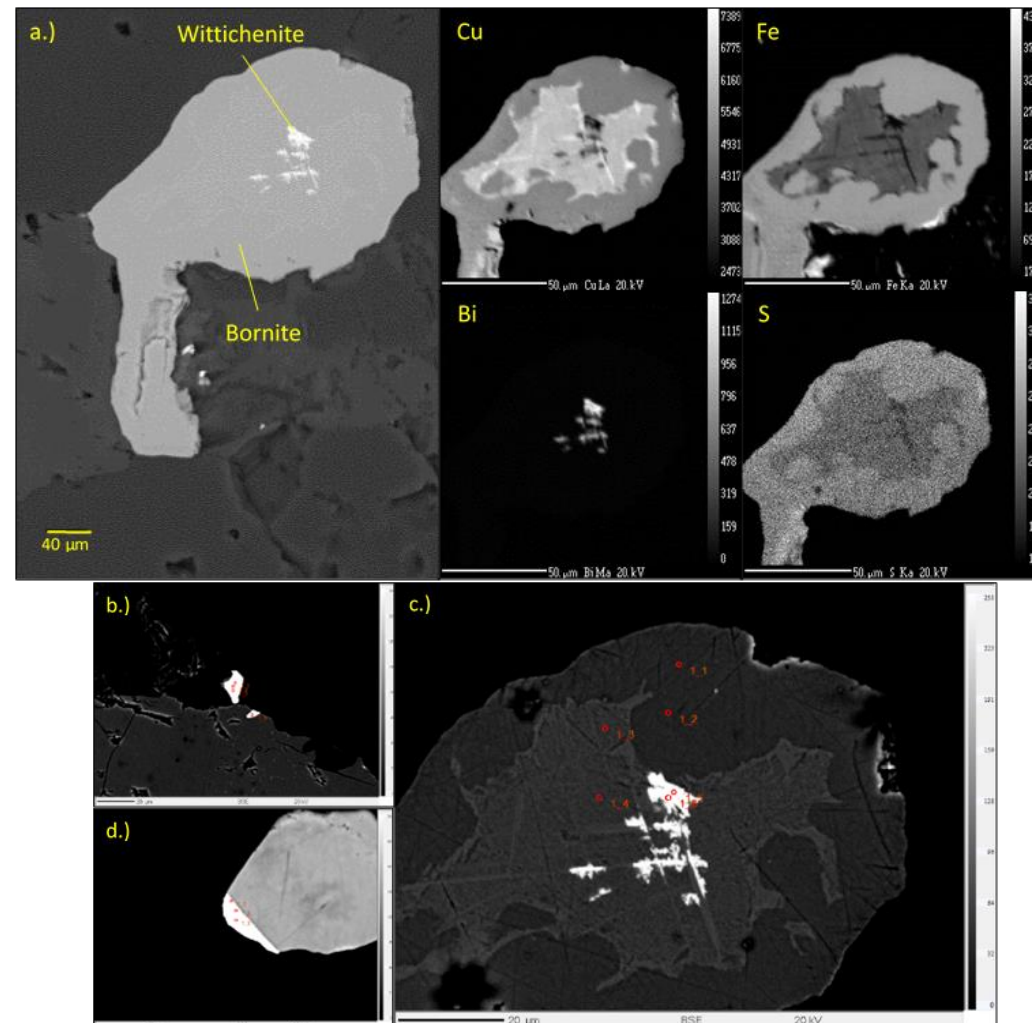


Figure 39: a.) EPMA element map of a zoned bornite crystal showing the distribution of Cu, Bi, Fe and S. b.) Sample 34a showing the points analysed with EPMA on wittichenite crystal. c.) Sample 34c showing points analysed by EPMA. d.) Sample 34b showing points analysed on galena with EPMA.

Table 17: EPMA results in wt% for CuBi minerals on the edge of bornite (sample 34a), galena (sample 34b) and across the zoned bornite (sample 34c, figure 39)

Sample	34a	34a	34a	34b	34c	34c	34c	34c	34c	34c	Error (2 $\sigma$ )	Detection limit
<b>S*</b>	16.46	16.47	17.97	14.84	25.71	25.33	23.31	22.30	19.65	18.65		
<b>Pt*</b>	0.54	0.57	0.64	<dt	<dt	<dt	<dt	<dt	0.47	0.56	0.57	0.07
<b>Mn</b>	<dt	<dt	<dt	<dt	<dt	<dt	<dt	<dt	<dt	<dt	0.24	0.14
<b>Fe</b>	0.71	0.72	0.80	7.10	10.75	10.89	5.45	5.33	3.50	1.42	0.05	0.03
<b>Co</b>	<dt	<dt	<dt	<dt	<dt	<dt	<dt	<dt	<dt	<dt	0.15	0.03
<b>Ni*</b>	<dt	<dt	<dt	0.21	<dt	<dt	<dt	<dt	<dt	<dt	0.06	0.03
<b>Cu*</b>	36.71	36.72	37.58	7.46	61.47	61.75	69.02	69.07	46.00	40.48	0.06	0.03
<b>Zn</b>	<dt	<dt	<dt	<dt	<dt	<dt	<dt	<dt	<dt	<dt	0.32	0.05
<b>As</b>	<dt	<dt	<dt	<dt	<dt	0.03	<dt	<dt	<dt	<dt	0.03	0.02
<b>Se</b>	0.14	0.12	0.13	3.99	0.07	0.05	0.06	0.06	0.05	<dt	0.05	0.03
<b>Pd*</b>	<dt	<dt	<dt	<dt	<dt	<dt	<dt	<dt	<dt	<dt	0.06	0.03
<b>Ag*</b>	<dt	<dt	<dt	<dt	<dt	<dt	<dt	<dt	<dt	<dt	0.27	0.08
<b>Sb*</b>	<dt	<dt	<dt	<dt	<dt	<dt	<dt	<dt	<dt	<dt	0.31	0.05
<b>Te*</b>	<dt	<dt	<dt	<dt	<dt	<dt	<dt	<dt	<dt	<dt	0.13	0.08
<b>Pb*</b>	<dt	<dt	<dt	61.13	<dt	<dt	<dt	<dt	<dt	<dt	0.42	0.10
<b>Bi*</b>	43.14	43.27	42.88	0.91	<dt	<dt	<dt	<dt	28.66	38.06	0.33	0.14
<b>Rh*</b>	<dt	<dt	<dt	<dt	<dt	<dt	<dt	<dt	<dt	<dt	0.18	0.11
<b>Os*</b>	<dt	<dt	<dt	0.52	<dt	<dt	<dt	<dt	<dt	<dt	0.23	0.14
<b>Ir*</b>	<dt	<dt	<dt	0.18	<dt	<dt	<dt	<dt	<dt	<dt	0.08	0.05
<b>Au*</b>	<dt	<dt	<dt	<dt	<dt	<dt	<dt	<dt	<dt	<dt	0.21	0.12
<b>Si</b>	0.05	0.10	0.05	0.17	0.04	0.03	0.03	<dt	<dt	0.08	0.45	0.19
<b>Total</b>	97.75	97.97	100.05	96.52	98.04	98.08	97.87	96.76	98.33	99.25	0.04	0.01
<b>Mineral</b>	Wittichenite	Wittichenite	Wittichenite	Galena	Bornite	Bornite	Yarrowite	Betekhtinite	Wittichenite	Wittichenite		
	Cu <sub>3</sub> BiS <sub>3</sub>	Cu <sub>3</sub> BiS <sub>3</sub>	Cu <sub>3</sub> BiS <sub>3</sub>	PbS	Cu <sub>5</sub> FeS <sub>4</sub>	Cu <sub>5</sub> FeS <sub>4</sub>	Cu <sub>9</sub> S <sub>8</sub>	Cu <sub>10</sub> (Fe,Pb)S <sub>6</sub>	Cu <sub>3</sub> BiS <sub>3</sub>	Cu <sub>3</sub> BiS <sub>3</sub>		

### 5.3 Discussion

This study has confirmed that the PGEs in Skouries are associated with the main vein stage of Cu deposition in this deposit. This agrees with work by Economou-Eliopoulos and Eliopoulos (2000), who analysed samples for PGE content and found that samples from the potassic zone of the deposit showed elevated Pd and Pt contents. Early work postulated the theory that the precious metal tellurides were formed in relatively shallow, cool environments, and that the PGEs may have been redistributed in a late hydrothermal event (Mutschler et al. 1985; Eliopoulos & Economou-Eliopoulos 1991). This study has shown evidence that this is not the case as no PGEs were observed in the late stage veins, or associated with argillic alteration. Some PGMs were observed in chlorite-altered secondary biotite, however it is likely that the propylitic alteration post-dates the PGM deposition as the biotite has grown around the PGM (figure 38). This is similar to the distribution of PGMs in other porphyry deposits – PGEs in Elatsite, Santo Tomas II, Mamut and Majdanpek deposits are all associated with the main, hypogene mineralisation and with potassic alteration (Tarkian & Koopmann 1995; Tarkian & Stribrny 1999; Tarkian et al. 2003).

The PGMs in Skouries are associated with M-3 and M-4 veins, as inclusions in bornite-chalcopyrite-magnetite assemblages, and in M-5 veins as inclusions in bornite-chalcopyrite-pyrite assemblages. The PGMs in Elatsite and Santo Tomas II (Tarkian & Koopmann 1995; Tarkian, et al. 2003) are also found in chalcopyrite-bornite-magnetite assemblages as inclusions in chalcopyrite. Unlike in these deposits, the PGMs in Skouries are also found as discrete crystals on the edge of sulphides and magnetite in potassic alteration selvages surrounding the M-5 veins, suggesting that they were carried by the altering fluid (Xiong & Wood 2000). The earlier M-3 and M-4 veins only contain sopcheite, with no other, non Ag bearing, PGMs present. Rare sopcheite is also seen in the M-5 veins, as is electrum and the silver telluride minerals, however the M-5 veins also host sobolevskite, kotulskite, merenskyite and testibiopalladite. Pt is present in trace amounts in wittichenite in Skouries and the texture of the wittichenite suggests it may have exsolved from the surrounding bornite. This could mean that the Cu ore minerals may also host trace amounts of Pt.

Skouries contains a more varied suite of PGMs than Elatsite and Santo Tomas II, the only other two porphyries to have undergone a thorough in situ PGM survey (Tarkian & Koopmann 1995; Auge et al. 2005). Skouries is the only porphyry to have reported presence of sopcheite, sobolevskite and testibiopalladite to date. Elatsite contains merenskyite and merenskyite-moncheite solid solutions (Tarkian et al. 2003; Bogdanov et al. 2005), while Santo Tomas II contains merenskyite, kotulskite and moncheite (Tarkian & Koopmann 1995). Although both of

these deposits also contain a range of silver tellurides, neither of them contain sopcheite, suggesting the Ag and PGEs in those deposits are either being transported by different mechanisms or are temporally or spatially separate. The precious metal and semi-metal accessory minerals at Skouries (stützite, empressite, hessite and tetrahedrite) have also been observed in Elatsite and Santo Tomas II, giving further evidence that PGE enriched porphyry deposits contain an abundance of semi-metals. Elatsite however also contains a range of Ni and Co-bearing accessory minerals which are not seen in Skouries, and which have been suggested to show mafic input as Ni and Co minerals are not normally found in porphyry copper deposits (Kehayov & Bogdanov 1987; Tarkian et al. 2003; Bogdanov et al. 2005; Eliopoulos et al. 2014). Santo Tomas II has been found to contain more selenides than Skouries (Tarkian & Koopmann 1995), suggesting that the semi-metal budget in these systems varies between deposits.

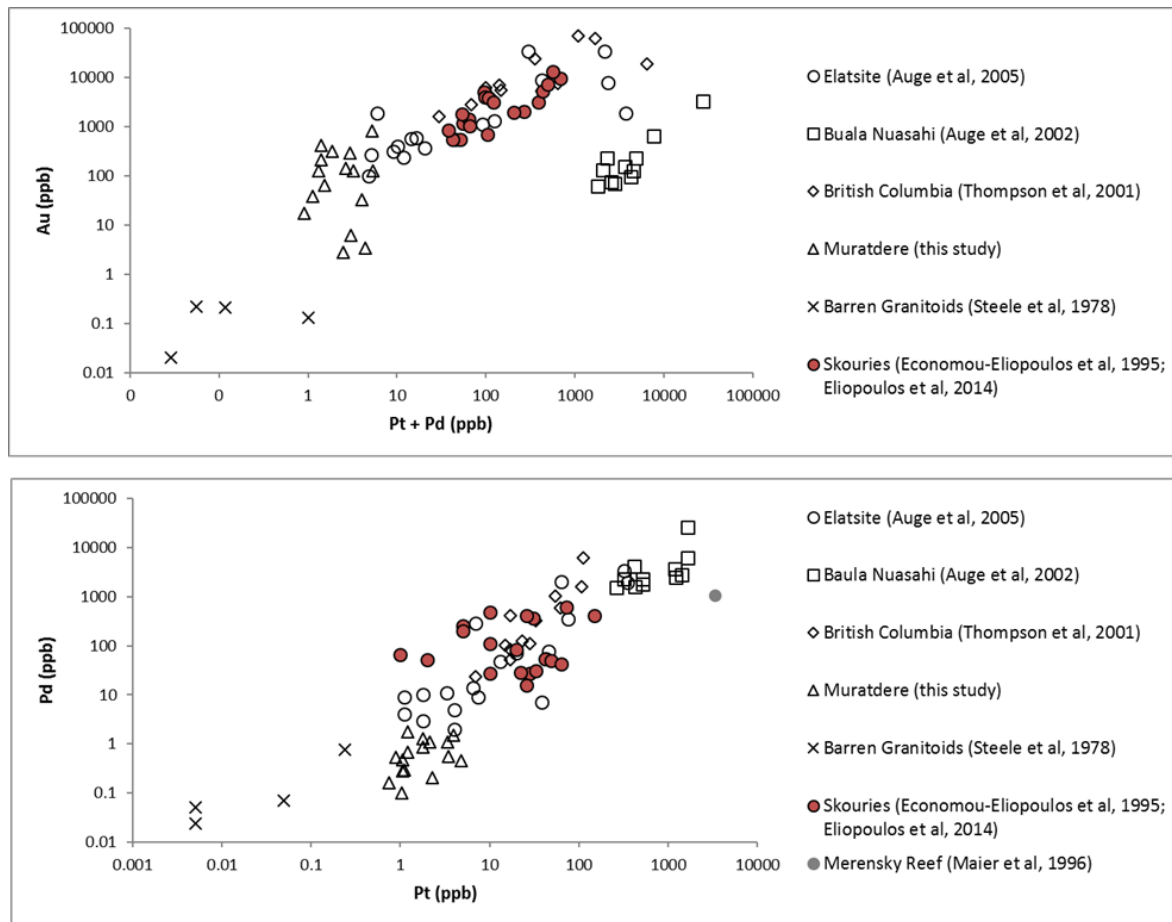


Figure 40: Comparison of whole rock Au, Pt and Pd results from Skouries (from earlier studies) with other ore deposit results: PGE enriched porphyries Elatsite and the British Columbia region, the non-PGE enriched Muratdere porphyry deposit, barren granitoids, a layered ultra-mafic intrusion Buala Nuasahi, and the Merensky Reef deposit.

Skouries has a large Pd/Pt ratio, with the Merenskyites analysed either falling on the Pd end member, or containing approximately 10:1 Pd:Pt. Assay data from the 'PGE enriched' sections at Skouries usually show Pd:Pt ratios of approximately 100:1, while previous studies have reported Pd:Pt ratios of approximately 10:1 from whole rock analyses (Eliopoulos & Economou-Eliopoulos

1991; Economou-Eliopoulos & Eliopoulos 2000), suggesting that significantly more Pd than Pt was mobilised in this deposit. This relative Pd enrichment is seen in whole rock data from all other PGE enriched porphyries (figure 40), except for the Aksug deposit in Russia (Sotnikov et al. 2001), and it is thought this reflects the relative PGE contents in the source magma (Economou-Eliopoulos & Eliopoulos 2000), or the fractionation of the mineralising fluid (Eliopoulos et al. 2014). Porphyry deposits globally, whether PGE-enriched or not, have very similar Au/(Pd+Pt) and Pd/Pt, plotting on the same gradient as barren granitoids and the PGE mineralised layered ultramafic intrusion Buala Nuasahi (figure 40). This suggests Pd/Pt is likely to represent source magma PGE concentrations.

The zoned bornites in M-5 give an idea of the evolution of the mineralising fluid, with the zoned bornite analysed in this study (figure 39) showing the fluid to have become more Cu poor and Fe rich over time as the crystal was formed. A later fluid event in the M-3, M-4 and M-5 veins deposited Se-rich galena. This has been reported in other PGE enriched porphyries, such as Elatsite and Santo Tomas II where galena was reported to be in a solid solution with clausthalite - indeed that may be the case in this deposit. The galena-clausthalite solid solution postdates the PGMs, Bi-rich bornite and other precious metal tellurides showing the system to have become progressively less Te and Bi rich and more Se rich over time.

## 5.4 Conclusions

The Skouries Cu-Au deposit is PGE enriched, with a large Pd/Pt ratio. This Pd and Pt enrichment is associated with the main Cu ore forming mineralising event with platinum group minerals (PGMs) identified in the main mineralising veinsets and associated with potassic alteration minerals. The PGMs in Muratdere have been identified as Sobolevskite (PdBi), Sopcheite ( $\text{Ag}_4\text{Pd}_3\text{Te}_4$ ), Testibiopalladite ( $\text{PdTe}(\text{Sb},\text{Te})$ ), Pd rich Merenskyite ( $(\text{Pd},\text{Pt})(\text{Te},\text{Bi})_2$ ) and Kotulskite ( $\text{Pd}(\text{Te},\text{Bi})$ ). The most common PGM is sopcheite, reported here for the first time in a porphyry deposit, with only rare merenskyite crystals observed. This is different from other PGE enriched porphyries where merenskyite is the dominant PGM (Tarkian & Koopmann 1995; Tarkian & Stribrny 1999; Tarkian et al. 2003). The PGMs in Skouries are small, <10  $\mu\text{m}$  in diameter on average, and are hosted both as inclusions within bornite and chalcopyrite but also free within the vein and within potassic alteration minerals. This evidence shows the Pd and Pt in this deposit to be part of the same mineralising event as the Cu and Au, and confirms findings that PGE mineralisation in porphyries is a hypogene event associated with potassic alteration.

Skouries contains a large proportion of semi metals, with Electrum (AgAu), Empressite (AgTe), Hessite ( $\text{Ag}_2\text{Te}$ ) and Stützite ( $\text{Ag}_{5-x}\text{Te}_3$ , ( $x=0.24-0.36$ )) having been identified as accessory

## Chapter 5

minerals. These are found in all the main stage mineralising veinsets, and are observed as inclusions in ore minerals, free within veins and are often associated with PGMs. The Skouries semi-metal system evolves from a Bi-Te dominated system, as evidenced by Bi rich bornites and the fact that wittichenite is a common accessory mineral, to a more Se rich system, as shown by the late stage galena-clausthalite solid solution. These semi-metal accessory minerals are also seen in other PGE enriched porphyries Elatsite and Santo Tomas II (Tarkian & Koopmann 1995; Tarkian et al. 2003) and appear to be a feature of these systems. The importance of semi-metals for PGE transport in poprhyries is discussed further in chapter 6.



## Chapter 6: Platinum group element transport in the Skouries Cu-Au (Pd, Pt, Te) porphyry deposit

### 6.1 Introduction

Although porphyries are a potential economic source of PGEs, Te and Bi, the transport mechanisms and source of these critical metals in porphyry deposits are still uncertain. Theoretical studies have shown PGEs to be hydrothermally mobile (e.g. Xiong & Wood 2000), however PGEs have yet to be observed in natural fluid inclusions, and PGE compatibility into magmatic volatile phases is poorly constrained (Park et al. 2016). Moreover in order to generate the economic concentrations of Pd and Pt observed in porphyry systems a mechanism is needed to enrich the normally PGE poor felsic source magma chamber (Wilkinson 2013), and to concentrate dispersed PGEs into the fluid in levels at which platinum group minerals can be precipitated. This chapter presents preliminary results from LA-ICP-MS of fluid inclusions focussing on precious and semi-metals, including the potential detection of palladium for the first time in natural fluid inclusions, and discusses implications of the fluid chemistry and PGM mineralogy in Skouries for critical metal transport and ore formation mechanisms.

As discussed in chapter 5 Skouries is Pd, Pt, Te, Se and Bi enriched porphyry. These critical metals are hosted in platinum group minerals (PGMs) in the main hypogene stages of ore formation, associated with potassic alteration. This close association between potassic alteration minerals and PGMs suggests that the Pd, Pt and semi-metals were carried by the altering fluid. Experimental work has shown that Pd is hydrothermally mobile in saline, high temperature, oxidising fluids (Xiong & Wood 2000), and it has been shown that Pt and Au can be dissolved from a peraluminous melt by high temperature hydrothermal fluids at pressures of 1.5 kbar and temperatures of 600 to 800°C (Hanley et al. 2005), which are similar to the temperatures and pressures calculated for the main mineralising vein stages of Skouries (chapter 4). Both Pt and Pd are transported as bisulphide complexes in reduced conditions, with Pd forming  $\text{Pd}(\text{HS})_4^{2-}$  in low temperature, fluid buffered conditions (Barnes & Liu 2012; Mei et al. 2015). Palladium has been shown to have limited solubility as a bisulphide complex in rock buffered conditions (Mei et al. 2015), and in high temperature, high salinity, oxidised fluids, such as those seen in porphyry deposits, Pd and Pt are transported as chloride complexes, with Pd preferentially forming  $\text{PdCl}_4^{2-}$  complexes (Fleet & Wu 1993; Fleet & Wu 1995; Xiong & Wood 2000; Hanley et al. 2005; Tagirov et al. 2013; Mei et al. 2015). The stability of these chloride complexes increases with increasing temperature, and decreases with increased  $f\text{S}^{2-}$ , meaning that a drop in temperature or the

introduction of reduced sulphur to the system could trigger Pd precipitation (Xiong & Wood 2000; Tagirov et al. 2013; Bazarkina et al. 2014).

Tellurium is transported as hydrated tellurite species in oxidised fluids, with aqueous  $\text{H}_2\text{TeO}_3$  the most common species in oxidised, acidic, high temperature fluids (P. V. Grundler et al. 2013). Tellurium has been identified in vesicles in pumice and in volcanic sublimate (Fulignati & Sbrana 1998; Larocque et al. 2008), showing that Te can be present in the vapour phase of a magmatic system, although in oxidising conditions such as those seen in Skouries Te preferentially partitions into the aqueous phase (Grundler et al. 2013). Bismuth is transported primarily as hydroxide complexes, with temperatures  $>400^\circ\text{C}$  needed for significant Bi transport in aqueous fluids (Tooth et al. 2013).

Porphyry Cu-Au deposits commonly show high Pd/Pt in ore samples, and this is seen in Skouries where the Pd/Pt is 10:1 in assay. This has been suggested to be due to secondary hydrothermal fluids preferentially remobilising Pd to the other PGEs (Thompson et al. 2001; Auge et al. 2005), or to Pd being more compatible in magmatic volatile phases than Pt or the other PGEs. Experimental work suggests that Pd is the most hydrothermally mobile PGE (Xiong & Wood 2000; Barnes & Liu 2012), however there are still a lot of variables which are unknown – for example the majority of experimental studies have focussed on S-free, saline fluids, whereas the initial volatile phase in porphyry deposits is thought to be a low density,  $\text{CO}_2$  rich, S-bearing, low salinity fluid (Williams-Jones & Heinrich 2005; Landtwing et al. 2010; Park et al. 2016). Direct measurement of PGEs in airborne particles, volcanic gas and condensates from modern arc volcanoes Kudryavy and Tolbachik have shown Re and Os to be significantly enriched in gases, while Pd is only present in very minor amounts (Tessalina et al. 2008; Zelenski et al. 2014). Analysis of condensates on the Niuatahi-Motutahi volcano in the Tonga arc gave concentrations of 0.379-0.71 ppb Pd, 0.414-0.780 ppb Pt, and showed PGE compatibilities in magmatic volatiles to be significantly less than those of Au, Re and Cu. Pd had the lowest compatibility of the PGEs in that system (Park et al. 2016), and did not show any secondary hydrothermal mobilisation (Park et al. 2016). It is therefore argued that the Pd/Pt of porphyry ore bodies is a direct indicator of the Pd/Pt of the source magma (Park et al. 2016).

## 6.2 Methods

Fluid inclusions from the main mineralising veinsets were analysed for major and trace elements by LA-ICP-MS (chapter 2, chapter 4). Although Te, Se and Pd are not commonly analysed for in fluid inclusions (Pettke et al. 2012)  $^{206}\text{Pd}$ ,  $^{78}\text{Se}$ ,  $^{130}\text{Te}$  and  $^{209}\text{Bi}$  were added to the element list of 'method 1' in order to attempt to identify their carrier fluids, as Skouries is known to be enriched

in these elements. Further analyses were carried out using ‘method 2’, which has longer dwell times for the precious metals, including  $^{106}\text{Pd}$ , as well as adding  $^{110}\text{Pd}$  in order to confirm that Pd is present. Several assemblages of petrologically-identical fluid inclusions were analysed in order to allow estimation of the uncertainties associated with the measurements (chapter 2 - Heinrich et al. 2003; Pettke 2008; Pettke et al. 2012).

## 6.3 Results

This chapter presents the preliminary results of the ‘method 2’ ablation element menu, focussing on precious and semi-metals, including data which show the detection of palladium in the fluid.

### 6.3.1 Interferences on palladium

The potential interferences on  $^{106}\text{Pd}$  are  $^{106}\text{Cd}$ ,  $^{90}\text{Zr}^{16}\text{O}$ , and potentially  $^{40}\text{Ar}^{66}\text{Zn}$ . Covariance and correlation coefficients were used to determine whether these potential interferences were responsible for the Pd values seen. Covariance can be expressed by equation (1). It measures the number of ‘matches’ amongst pairs of data elements between two populations, so a positive covariance means the number of matches outweigh the mismatches and a positive number means the opposite. Covariance is influenced by the scale of the data elements, so large differences in concentration between elements will create large covariance values. Therefore, correlation coefficient, or  $R^2$  value, was used as a scale free measure of the linear association between two variables (equation 2).  $R^2$  function produces a number between 0 and 1, with 1 being a strong correlation and 0 being no correlation.

$$\text{cov}(x, y) = \sum_{i=1}^n (x_i - \bar{x})(y_i - \bar{y}) / (n - 1) \quad (1)$$

$$\frac{\sum_{i=1}^n x_i y_i - n \bar{x} \bar{y}}{\sqrt{(\sum_{i=1}^n x_i^2 - n \bar{x}^2)(\sum_{i=1}^n y_i^2 - n \bar{y}^2)}} \quad (2)$$

$x_i$  = variable 1;  $y_i$  = variable 2;  $n$  = number of variables;  $\bar{x}$  and  $\bar{y}$  = mean of variables.

$^{106}\text{Pd}$  does not show any correlation with  $^{66}\text{Zn}$ , with an  $R^2$  value of 0.02, meaning that the  $^{40}\text{Ar}^{66}\text{Zn}$  interference on  $^{106}\text{Pd}$  is probably not responsible for the Pd values seen. However given that the inclusions contain wt% levels of  $^{66}\text{Zn}$  and ppm levels of  $^{106}\text{Pd}$  it is difficult to rule this interference out completely.  $^{106}\text{Pd}$  also does not show any correlation with  $^{90}\text{Zr}$ , with the majority of Pd bearing inclusions showing Zr values of below detection, despite having very similar LODs.  $^{90}\text{Zr}$  and  $^{106}\text{Pd}$

have a covariance of -0.03 (dataset too small to calculate  $R^2$ ,  $n=5$ ), and the laser signals for  $^{90}\text{Zr}$  and  $^{106}\text{Pd}$  do not match, showing that  $^{90}\text{Zr}^{16}\text{O}$  is not a major interference.

In order to measure for potential isobaric  $^{106}\text{Cd}$  interference both  $^{106}\text{Cd}$  and  $^{111}\text{Cd}$  were measured, in order to do background interference corrections, as detailed below:

The total counts, or intensity ( $I$ ) at mass 106 =  $I^{106}\text{Pd}$  +  $I^{106}\text{Cd}$ , therefore  $I^{106}\text{Pd} = I(106) - I^{106}\text{Cd}$ . The contribution of  $^{106}\text{Cd}$  can be calculated by measuring another isotope of Cd, in this case  $^{111}\text{Cd}$ , and correcting it according to the natural abundance ( $A$ ) ratio of  $^{106}\text{Cd}/^{111}\text{Cd}$ , which is 1.25%/12.8%. So  $I(106\text{Cd}) = (1.25\%/12.8\%) \times I(111\text{Cd})$ . Therefore  $I^{106}\text{Pd} = I(106) - [0.0977 \times I(111\text{Cd})]$ . This correction was applied to the total counts measured prior to data processing using ExLAM in order to give the true  $^{106}\text{Pd}$  concentrations.

This interference correction is complicated by the fact that  $^{111}\text{Cd}$  has several polyatomic interferences, including  $^{95}\text{Mo}^{16}\text{O}^+$  and  $^{39}\text{K}_2^{16}\text{O}_2^1\text{H}^+$  (May et al. 1998), both of which are likely to be present in significant amounts in the analyte. However this means that  $I(111) = I(^{111}\text{Cd}) + (^{95}\text{Mo}^{16}\text{O}^+) + (^{39}\text{K}_2^{16}\text{O}_2^1\text{H}^+)$  and so  $I(^{111}\text{Cd}) = I(111) - [(^{95}\text{Mo}^{16}\text{O}^+) + (^{39}\text{K}_2^{16}\text{O}_2^1\text{H}^+)]$ . If these polyatomic interferences are large it will reduce the intensity of  $^{111}\text{Cd}$ , meaning that it will reduce the intensity of  $^{106}\text{Cd}$ , thus increasing  $^{106}\text{Pd}$  intensity. This means that the corrected  $^{106}\text{Pd}$  values should be viewed as minimum estimates, but also that Pd is definitely present.

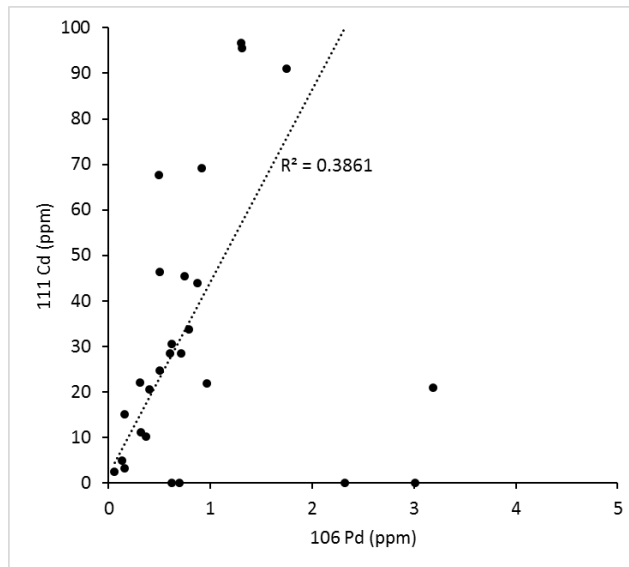


Figure 41: Measured concentrations of  $^{111}\text{Cd}$  and  $^{106}\text{Pd}$  in fluid inclusions.

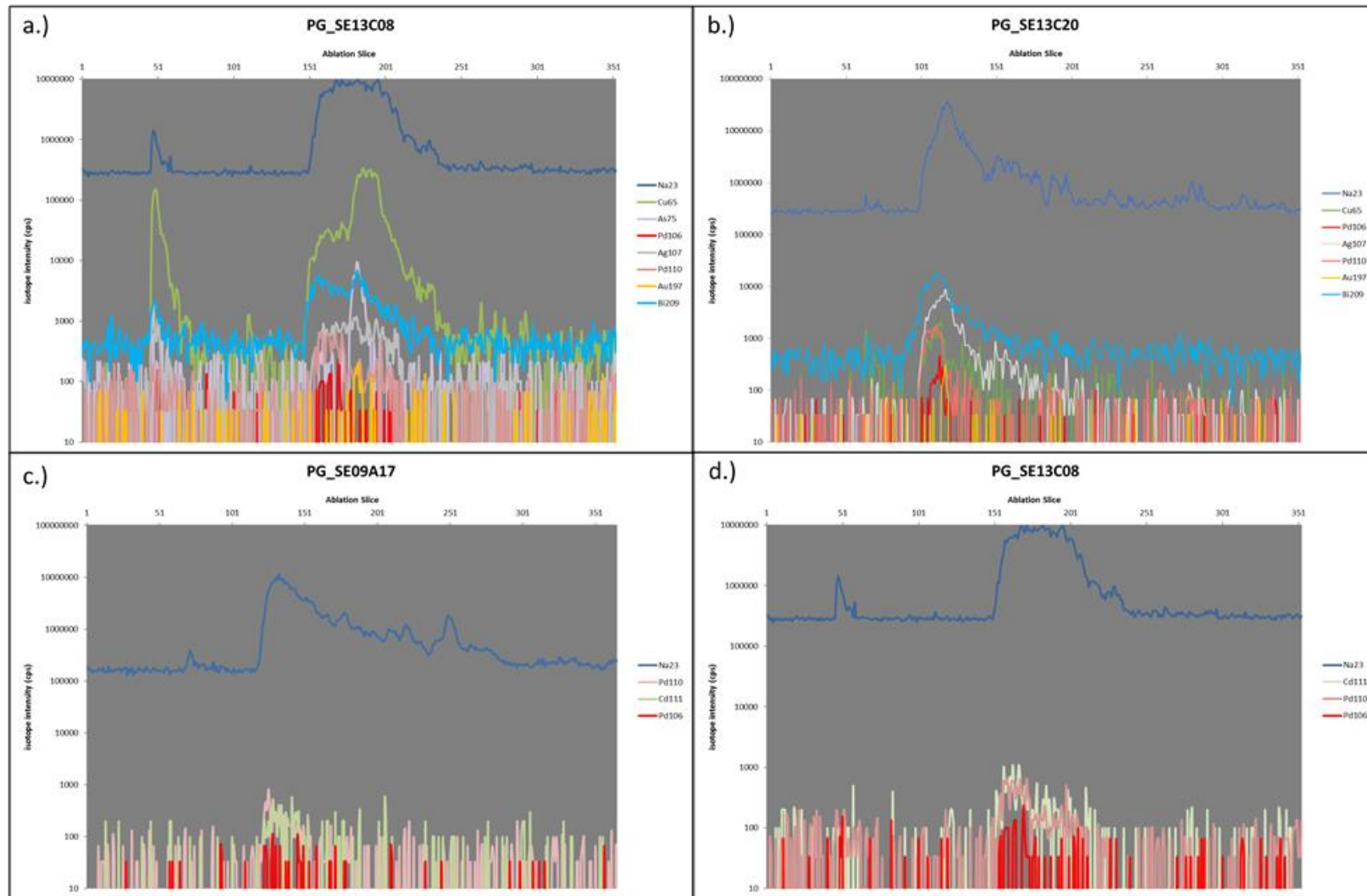


Figure 42: Laser signals for Pd bearing fluid inclusions showing counts intensity against time slice. a.) Brine inclusion containing an Au bearing bornite daughter mineral (indicated by increase in Cu, As and Bi at ~180) – Pd is detected in the fluid, not the daughter mineral. b.) Brine inclusion with halite daughter mineral (indicated by increase in Na at ~115) showing Pd, Bi and Au in the fluid – Pd and Bi co-vary. c.) Brine inclusion showing decoupling of  $^{110}\text{Pd}$  signal and  $^{111}\text{Cd}$  signals. d.) Brine inclusion showing the decoupling of  $^{106}\text{Pd}$  and  $^{111}\text{Cd}$  signals.

### 6.3.2 Platinum group element and semi-metal concentrations in fluid inclusions

This study presents the first reported detection of  $^{106}\text{Pd}$  in natural fluid inclusions, with Pd signals were recorded in 13 out of the 47 inclusions analysed using 'method 1', and in 12 out of 19 of the inclusions analysed using 'method 2' (appendix A3.5, electronic appendix C), with both  $^{106}\text{Pd}$  and  $^{110}\text{Pd}$  are visible as clear peaks in the laser signal (figure 42).

Palladium was only detected in the type III brine inclusions, with  $^{106}\text{Pd}$  concentrations in the brines ranging between 0.12 ppm and 4.36 ppm, with an average of 0.94 ppm (1 SD = 0.97). Limits of detection for  $^{106}\text{Pd}$  using 'method 1' range between 0 ppm and 4.1 ppm, with an average of 0.7 ppm. Limits of detection for  $^{106}\text{Pd}$  using 'method 2' range between 0.1 ppm to 2.5 ppm, with an average of 0.5 ppm.  $^{110}\text{Pd}$  concentrations in the brine range from 0.28 ppm to 3.61 ppm, with an average of 1.2 ppm ( $\sigma = 0.85$ ), with limits of detection between 0.1 ppm and 1.3 ppm, with an average of 0.4 ppm (appendix A3.5). However, the  $^{110}\text{Pd}$  results have not been interference corrected and so may not be entirely the result of Pd, instead reflecting Cd interference, and so should be treated as maximum estimates.

When plotted by assemblage (figure 43)  $^{106}\text{Pd}$  does not show much difference across veinsets and inclusion types, although it is not observed in any of the secondary type IIIB inclusions in veinset M-4 or M-5.  $^{106}\text{Pd}$  does not show a significant correlation with Cu or Au, with  $R^2$  values of 0.1 and 0.03 respectively. When plotted against whole rock assay data (figure 44) the fluid has higher Pd values, but lower Cu, and does not reflect the same Pd/Cu or Pd/Au as the bulk ore (from assay).

Te and Se were not detected in the fluid inclusions, however they both had very high LODs (100s ppm) so it is likely this is an analytical effect. Bi was detected in the majority of the fluid inclusions analysed, with concentrations ranging between 1 ppm and 475 ppm, with an average of 100 ppm in the brines ( $\sigma = 75$ ) and 167 ppm in the vapour ( $\sigma = 85$ ). This is a significant enrichment when compared to the whole rock assay data, where Bi has an average of 4 ppm. Bi is fairly constant across all the vein generations and inclusion types measured, showing a drop in concentration in the secondary inclusions of the final mineralising veinset, M-5. Bi and Pd show limited covariance in the inclusion assemblages analysed using method 2 (figure 43), and Bi and As show similar concentrations in the inclusions measured using method 1. Sb is present in lower amounts than Bi, but appears to co-vary with Bi. Au was detected in 10 of the inclusion assemblages analysed using 'method 2', with concentrations ranging between 0.2 ppm and 1.4 ppm, and Au has a positive covariance with Bi.

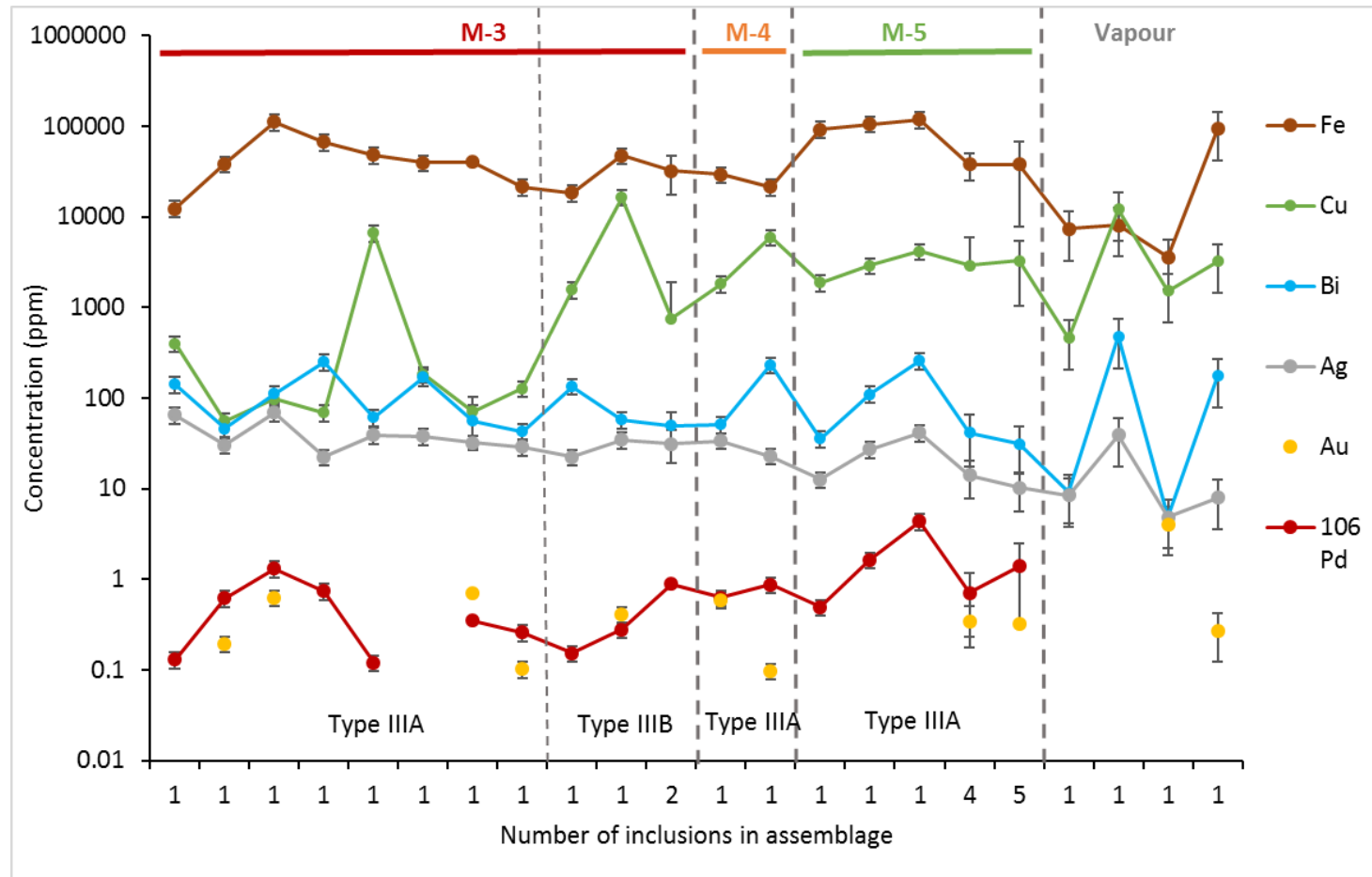


Figure 43: Concentrations of precious metals and semi-metals from laser ablation of fluid inclusions using 'method 2'. Each data point represents the average value of a fluid inclusion assemblage, with the number of inclusions in the assemblage along the bottom. The error bars represent the standard deviation of the measured inclusions, with error bars on assemblages with only one inclusion representing the potential error from Na% estimation (see chapter 2). Inclusions are divided by veinset and inclusion type, with the earliest brine phases on the left, and the latest on the right. The vapour phases are shown separately as they are interpreted to represent a separate fluid phase (chapter 4).

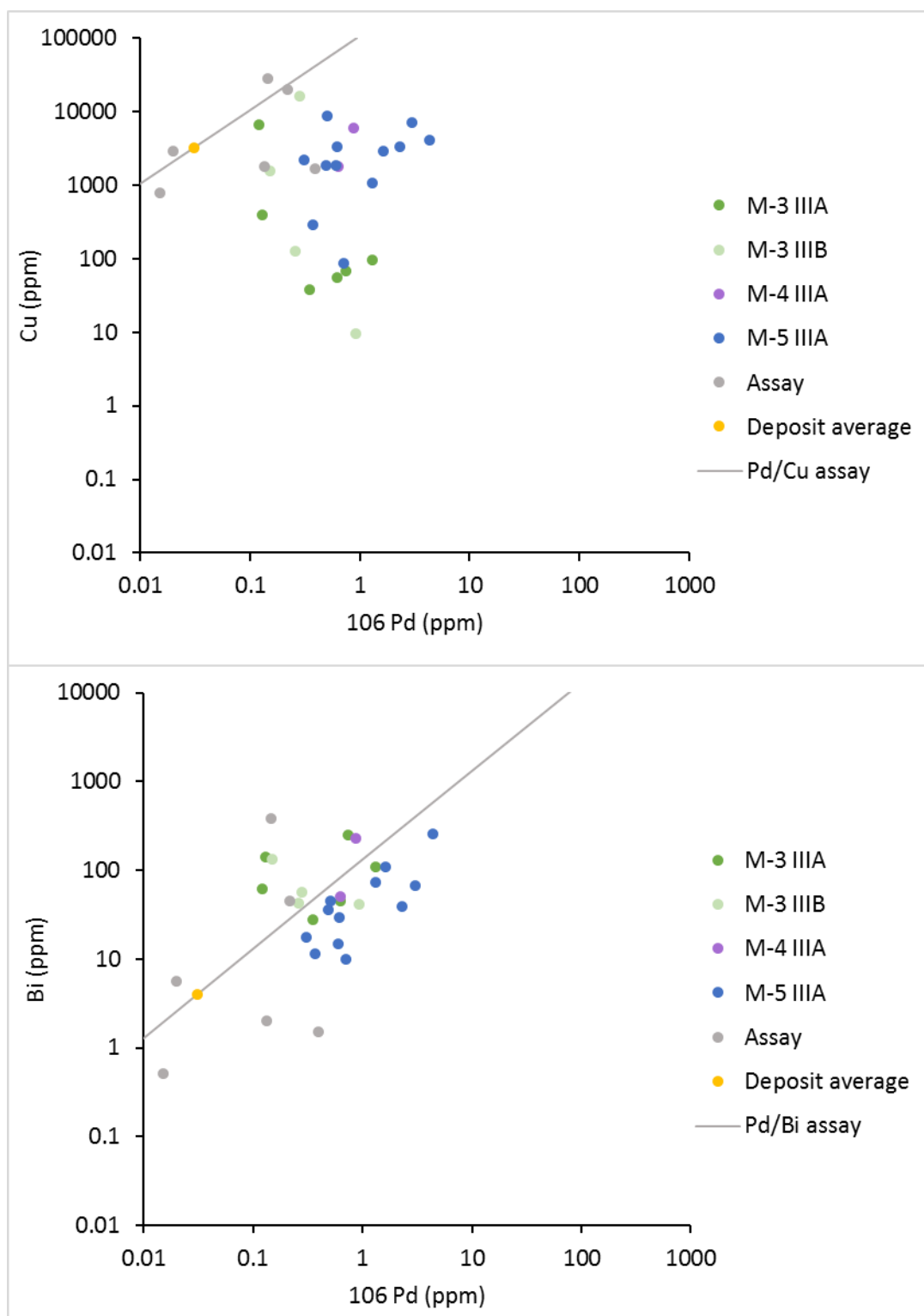


Figure 44: Graphs showing preliminary concentrations of elements in fluid inclusions from LA-ICP-MS (coloured circles) plotted with bulk rock assay data from the core intervals the samples were taken from (grey circles), the assay data element ratios (black line), and the deposit average (gold circle) for a.) Cu vs  $^{106}\text{Pd}$ , and b.) Bi vs  $^{106}\text{Pd}$ .



## 6.4 Discussion

### 6.4.1 Hydrothermal transport of PGEs

The presence of Pd in fluid inclusions shows Pd to be transported hydrothermally, which supports the evidence seen from several deposits of PGMs being present in hydrothermal veinsets and alteration minerals (chapter 5, Tarkian & Koopmann 1995; Auge et al. 2005). Pd is present in a significant proportion of the brine inclusions analysed, which represent high temperature (minimum temperatures of 503°C to >600°C), high salinity (60 to 85 wt% NaCl+KCl), oxidised fluids (chapter 4). This is consistent with experimental work which shows Pd to form chloride complexes in hydrothermal fluids of these conditions (Xiong et al. 2006; Bazarkina et al. 2014; Mei et al. 2015). However, the inclusions also contain anhydrite and sulphides, showing a high sulphur content which is thought to depress the solubility of Pd (Tagirov et al. 2013). These high salinity, high temperature polyphase brine inclusions are very similar to those observed in the PGE enriched porphyry deposits in the Urals (Sotnikov et al. 2001), Elatsite (Tarkian et al. 2003), and Santo Tomas II (Tarkian & Koopmann 1995). The brine inclusions at Santo Tomas II however do not homogenise by halite dissolution, and show evidence of boiling assemblages, which is not present at Skouries (Tarkian & Koopmann 1995). Of the other PGE enriched porphyries globally LA-ICP-MS has only been performed on fluid inclusions from Elatsite (Kehayov et al. 2003), and no Pd is reported. However, that may be due to the fact that Pd is not included in most analysis menus due to the standard and interference issues discussed in this chapter and in chapter 2. Skouries fluid inclusions show Ag and Bi concentrations approximately an order of magnitude higher than those seen in Elatsite inclusions (Kehayov et al. 2003).

The type IV vapour inclusions in Skouries are interpreted to represent magmatic vapour, potentially exsolving from the mafic dyke phase (chapter 4). Pd is rarely observed in modern arc volcano sublimates, and then only at ppb levels (Svetlana G Tessalina et al. 2008; Park et al. 2016; Zelenski et al. 2014), and this is also the case here as no Pd was analysed in vapour inclusions.

### 6.4.2 The role of semi-metals in PGE enrichment

One of the problems associated with the formation of PGE enriched porphyries is that it is very unlikely that hydrothermal fluids will contain enough Pd to reach saturation (Bazarkina et al. 2014). This means a mechanism is needed to collect the PGEs into high enough concentrations to precipitate platinum group minerals.

Co-existing polymetallic melts in hydrothermal systems can partition metals from the fluid and concentrate them as melt components (Douglas 2000). Semi-metals act as fluxes, lowering the

melting point of these poly-metallic melts - for example Au-Bi melt has a eutectic at 241°C. This has led to bismuth being suggested as a 'collector' for Au in hydrothermal fluids (e.g. Douglas 2000; Tooth et al. 2008; Cockerton & Tomkins 2012), acting as an enrichment mechanism and allowing the formation of hydrothermal ore deposits from fluids under-saturated in Au. Experimental studies have shown that in Au-Bi-Na-Cl-S-H-O systems Au preferentially partitions into an Au-Bi melt rather than the fluid (Tooth et al. 2008; Tooth et al. 2011), and natural examples of liquid bismuth co-existing with hydrothermal fluid have been seen (Cockerton & Tomkins 2012). Au-Bi melts are only present in a limited range of  $fO_2$  conditions, however it is thought that Bi-Te melts may act as Au scavengers in high  $fO_2$  conditions, as native tellurium stability is coincident with hematite (Ciobanu et al. 2005; Grundler et al. 2013). Bi-Te melts have eutectics of 266°C (Bi-rich), and 413°C (Te-rich) (Ciobanu et al. 2005), both within the range of temperatures seen in porphyry hydrothermal fluids, and Bi-Te-(+/-Au) droplets are often seen in hydrothermal quartz crystals, implying they were precipitated in a molten state (Ciobanu et al. 2005; Mavrogenes et al. 2010). Similarly the Au-Ag-Te ternary system has been shown to be molten at above 435°C (Cabri 1965), again within the range of temperatures for main stage ore forming veins in porphyries.

This semi-metal collector mechanism could also scavenge PGEs from fluids, concentrating them into a co-existing semi-metal melt. Palladium partitions strongly into semi-metal melts in the magmatic environment (Holwell & McDonald 2010), and is found primarily in semi-metal assemblages (PGMs) in porphyry deposits, rather than hosted in the sulphides (Tarkian & Koopmann 1995; Tarkian & Stribny 1999; Thompson et al. 2001; Tarkian et al. 2003; Eliopoulos et al. 2014). The Pd-Bi-Te system is molten above 489°C (Cabri & Harris 1973; Cabri 1981), which is within the temperature range of porphyry system hydrothermal fluids. A model is therefore proposed whereby Pd is scavenged from high temperature (>490°C) hydrothermal fluids by a co-existing Bi-Te melt. This creates a Pd-Bi-Te melt which precipitates palladium bismuthides, tellurides and tellurobismuthides according to the phase diagrams of Cabri (1981).

This semi-metal collector model requires both Bi and Te to be present as the Pd-Te binary system is only molten above 720 – 740°C (Hoffman & Maclean 1976; Cabri 1981), and the Pd-Bi binary system is only molten above 620°C (Cabri 1981). Binary systems of palladium with other semi-metals also only produce melts above the temperatures seen in porphyry fluids – the Pd-Sb binary system is only molten above 800°C, the Pd-As system is only molten above 835°C and the Pd-Se system is only molten above 678°C (Cabri 1981). However, phase diagrams have yet to be defined for the full range of ternary and quaternary PGE - semi-metal systems and so it is possible that there may be other complexes which have a low enough melting point to act as a PGE collector.

The main stage ore forming fluids in Skouries have minimum temperatures of 503°C to >600°C (chapter 4), at which point the Pd-Bi-Te, Bi-Te-Au, and Au-Ag-Te systems are all thought to be molten (Markham 1960; Cabri 1965; Cabri & Harris 1973; Hoffman & Maclean 1976; Ciobanu et al. 2005). Platinum group minerals and semi-metal assemblages in Skouries have bleb shaped morphologies, and precious metal tellurides and tellurobismuthides such as hessite are commonly found as droplets in the centre of quartz crystals, as are rare PGMs. This implies that they precipitated as molten droplets (Ciobanu & Cook 2002; Ciobanu et al. 2005; Mavrogenes et al. 2010) as the temperature of the fluids fell below 489°C. Bi and Au show a positive correlation in assay data, with an  $R^2$  value of 0.43. Pd and Bi show less of a correlation in assay, with an  $R^2$  value of 0.13, and Pd and Te have an  $R^2$  value of 0.12. These low  $R^2$  values may however be due to analytical limitations as the precision and accuracy of the assay data is not known. Significant concentrations of Bi are present in fluid inclusions in Skouries, and Pd is also present in the fluid inclusions. Pd and Bi concentrations in the inclusions show a positive correlation, with an  $R^2$  value of 0.29, and are consistent with the Pd/Bi of the assay data (figure 44), albeit at an order of magnitude higher concentration, suggesting the fluids may have been responsible for the enrichment seen in assay.

Although PGEs in porphyries globally have been reported to be hosted in semi-metal PGMs (Tarkian & Stribrny 1999), there is a paucity of data on the Te and Bi content of PGE enriched porphyry systems, or indeed the semi-metal content of porphyry systems generally. Elatsite has Bi concentrations in ore samples of between 0.2 and 291 ppm, and Te concentrations between 0.2 ppm and 3.8 ppm, with a positive correlation reported between Pd, Au, Te and Bi (Tarkian et al. 2003). These concentrations are similar to those seen in Skouries, and Elatsite has similar Bi concentrations in fluid inclusions to Skouries (Kehayov et al. 2003), suggesting that similar semi-metal collector mechanisms may have been operating. However, more data is needed on semi-metal and PGE concentrations in porphyry deposits and in porphyry fluid inclusions in order to test this hypothesis.

#### **6.4.3 The source of PGE enrichment in Skouries**

Platinum group elements in porphyries have been suggested to be sourced from the remelting of previously subduction-modified upper plate lithosphere (Tarkian & Stribrny 1999; Economou-Eliopoulos & Eliopoulos 2000; Thompson et al. 2001; Auge et al. 2005). Skouries is a post-collisional porphyry deposit, situated in a post-subduction extensional tectonic setting, and shows evidence of crustal contamination of the melt at depth such as high levels of LILE (chapter 4, Kroll et al. 2002; Siron et al. 2016), which supports this hypothesis. Whole rock analyses by Siron et al (2016) show trace element signatures indicating amphibole fractionation has occurred, suggesting

that the source of the metals in Skouries is likely to be re-melted amphibolitic cumulate roots of previous arc magmatic complexes (Richards 2011), which may contain residual sulphides from previous fractionation of arc magmas (McInnes & Cameron 1994; Richards 2011). This is the suggested source for PGE enrichment seen in alkaline porphyries in British Columbia. However, not all PGE enriched porphyries are in post-collisional environments or alkaline magmas. Santo Tomas II, for example, is a calc-alkaline porphyry deposit associated with arc subduction, and yet still shows a significant PGE enrichment (Tarkian & Koopmann 1995). Similarly, regional intrusions and ore prospects in Stratonis such as Aspro Lakkos and Piavitsa, which are compositionally similar to Skouries and interpreted to stem from the same source, do not show any evidence of PGE mineralisation (Siron et al. 2016, Russell, personal communication). All PGE enriched porphyry deposits do however show evidence of oxidised source magmas (Kehayov & Bogdanov 1987; Tarkian & Koopmann 1995; Tarkian & Stribny 1999; Sotnikov et al. 2001; Thompson et al. 2001; Tarkian et al. 2003; Auge et al. 2005; Bogdanov et al. 2005; Pašava et al. 2010), and this high  $fO_2$  is important as it would inhibit sulphide precipitation during ascent through the crust, meaning that PGEs stay in the melt and are therefore introduced into the porphyry source magma chamber (Thompson et al. 2001; Richards 2011).

Mafic magma contribution has been suggested as a source of precious metal and sulphur enrichment in porphyry deposits (Hattori & Keith 2001). It is likely that the late mafic dyking stage of the Skouries intrusions added PGEs to the source magma chamber, especially if these dykes represent deeper sourced lower crustal melts enriched in residual sulphide. This is the mechanism suggested for the addition of PGEs and other precious metals to the Bingham porphyry deposit (Maughan et al. 2002), and Elatsite also has mafic igneous phases which are proposed to be responsible for the 'mafic' (Ni-Co-PGE) metal assemblage found in that deposit (Auge et al. 2005; Eliopoulos et al. 2014). The Santo Tomas II deposit also contains a late dioritic dyking phase, although it is unclear how they fit with the mineralisation (Tarkian & Koopmann 1995). Mafic input in Skouries is further supported by the presence of mafic enclaves within the 'pink' syenitic porphyry phase (figure 45), which are 3 – 10 cm in diameter.

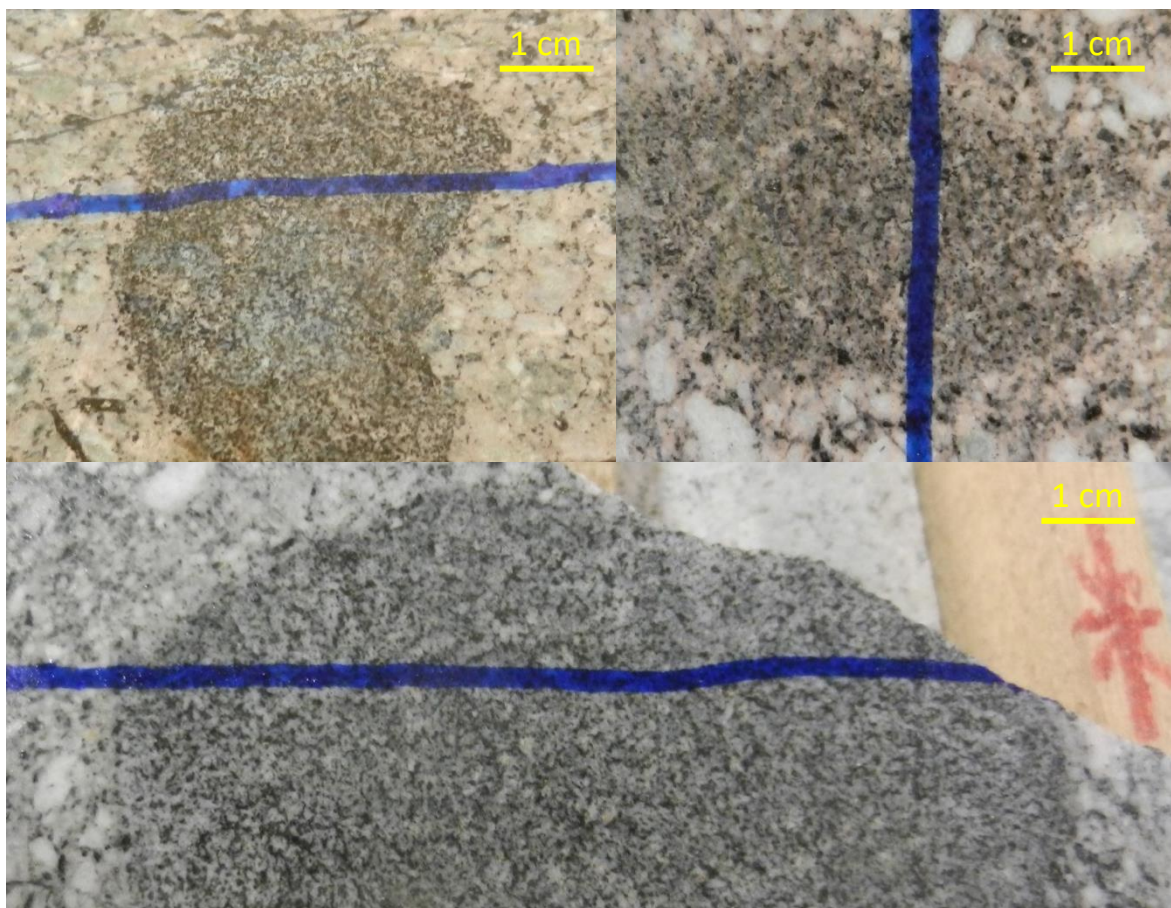


Figure 45: Mafic enclaves in drill core from the Skouries deposit

Another potential PGE enrichment process in Skouries could be the formation of an immiscible sulphide melt in the source magma chamber, possibly triggered by the addition of a mafic melt (Wilkinson 2013). The resulting immiscible sulphide melt would concentrate any PGEs in the magma, as well as other chalcophile elements such as Au, Cu, Ag, Bi and Te. In ultra-mafic environments it has been shown that in the presence of semi-metals Pt and Pd preferentially partition into semi-metal rich melts which act as highly potent PGE collectors, rather than partitioning into Cu-rich sulphide melts (Helmy et al. 2007; Holwell & McDonald 2010; Patten et al. 2013). Although the felsic source magma chambers of porphyry deposits are lower temperature systems it is likely that any semi-metals present would act in a similar fashion, concentrating Pd and Pt. This sulphide-semi-metal immiscible melt could then be destabilised by the release of volatiles, making PGEs, Cu, Au and S<sub>2</sub> available to the volatile phase for hydrothermal transport (Halter et al. 2002; Holwell & McDonald 2010; Wilkinson 2013).

The PGEs are associated with the main Cu and Au mineralisation, however they are in distinct minerals suggesting that although they were transported together they have separate precipitation mechanisms. The precipitation method for the copper sulphides in the mineralising veinsets have been discussed in chapter 4, and it is suggested that a drop in temperature (below

489°C) of these fluids causes the solidification of the Bi-Te-PGE melt droplets into PGMs. This drop in temperature is suggested to occur soon after the precipitation of the sulphides, explaining the presence of PGMs on the edges of sulphide minerals.

## 6.5 Conclusions

PGE enriched porphyries are commonly alkaline systems in post-subduction settings with oxidised magmas. Although these conditions provide potentially fertile systems, not all porphyry deposits in these systems are PGE enriched, and some PGE enriched porphyries have different magma chemistry and tectonic settings. This means that as well as an enriched source, the presence of further enrichment mechanisms is important for the development of a PGE enriched porphyry. By looking at the geological and geochemical features, the PGM mineralogy, fluid conditions and fluid chemistry of the Skouries deposit and comparing it to other PGE enriched porphyries this study has proposed five potential PGE enrichment mechanisms:

1. *Oxidised source magmas allow PGE transport in the melt to higher crustal levels.* All PGE enriched porphyries have oxidised source magmas, as shown in Skouries by the presence of primary magnetite in the intrusions.
2. *The introduction of additional S, Au, Cu and PGEs by late stage mafic input into the source magma chamber of the deposit.* In Skouries this is seen as the late mafic dyking event, which occurs before the main mineralisation stage and then throughout the rest of the paragenesis (chapter 4), and as mafic enclaves in the 'pink' syenite phase.
3. *The formation of an immiscible sulphide melt in the source magma chamber, allowing the concentration of dispersed PGEs, Bi, Te and Au.* The formation of this immiscible sulphide melt may be triggered by the precipitation of magnetite, or the input of a mafic melt. The intrusions at Skouries all contain primary magnetite, and the input of mafic melt is interpreted from the presence of the mafic igneous phase.
4. *Fluid conditions which allow effective hydrothermal transport of PGEs and semi-metals.* The highly oxidised, high temperature, highly saline fluid conditions at Skouries favour the hydrothermal transport of these critical metals, as is shown by the the detection of Pd in the fluid inclusions, high concentrations of Bi analysed in fluid inclusions, and the association of Pd, Bi and Te bearing PGMs with hydrothermal alteration.
5. *The presence of relatively high concentrations of semi-metals, which can act as PGE collectors.* Au-Ag-Te, Au-Bi-Te and Pd-Bi-Te systems are all molten at the fluid temperatures seen in the Skouries deposit and this, coupled with the presence of Pd-Bi-Te (+/-Ag) PGMs and Ag-Te (+/-Au) minerals in droplet-like morphologies in vein quartz, suggests semi-metal melts may be present in hydrothermal fluids. These co-melts are

proposed to act as PGE and precious metal collectors, scavenging Pd, Pt, Au and Ag from the fluid and allowing PGM precipitation from Pd and Pt under-saturated fluids. It is important to note that both Te and Bi are needed to scavenge Pd at porphyry temperatures.

These mechanisms suggest some exploration indicators for potential PGE enrichment in porphyry deposits: oxidised host rocks, as indicated by the presence of primary magnetite; the association of more mafic phases with the felsic host porphyry; high temperature, oxidised, high salinity fluids, indicated by polyphase brine inclusions incorporating hematite or anhydrite; and high Bi and Te contents in assay. PGMs in porphyry deposits are very small (<10 – 50 µm) and usually require an SEM to identify - as PGEs are not part of the traditional element suite assayed for by most companies it is likely that 'PGE enriched' porphyries may be more common than previously thought, and that the PGMs in the ore are not being identified. As PGEs and their co-precipitated semi-metals are all critical elements it is important to evaluate their potential in porphyry deposits, and to ensure that the PGEs are being recovered at smelter. As well as aiding exploration, these features could provide a first order indicator of whether PGEs are likely to be present in the ore of a porphyry deposit.





## Chapter 7: Conclusions

### 7.1 Comparing the Muratdere and Skouries deposits

The two deposits examined in this thesis are both porphyry copper deposits in the Tethyan metallogenic belt which are enriched in critical metals. Both deposits are interpreted to be situated in extensional post-collisional settings, with the initial source of their metal enrichment interpreted to be due to the melting of previously subduction-modified upper plate lithosphere by upwelling asthenospheric mantle. However, they both have very different metal budgets - Skouries is a Cu-Au porphyry deposit, enriched in Pd, Pt, Te and Bi, but not in Re. Muratdere is a Cu-Mo porphyry deposit enriched in Re and Te, but not in Pd, Pt or Bi. Given that Cu, Au, Re, PGEs, Te and Bi are all chalcophile and behave in very similar manners in magmatic systems, this raises the question - why do these deposits have such different metal endowments?

Although Skouries is an alkaline system and Muratdere appears to be a calc-alkaline system, it has been shown that not all PGE-enriched porphyries are alkaline (Tarkian & Koopmann 1995), and some alkaline systems can be Re enriched (Fornadel et al. 2012). Instead it is likely that the  $fO_2$  of the magma played an important role. The Skouries magmatic system is highly oxidised, with primary magnetite observed in all igneous phases, whereas this high magmatic  $fO_2$  is not seen at Muratdere, where only hydrothermal magnetite is present. Oxidised magmas prevent the precipitation of sulphides during ascent through the crust, allowing highly chalcophile elements such as Pd and Pt to remain in the melt (Thompson et al. 2001). It is possible that the source melt at Muratdere formed sulphides at depth, which partitioned the highly chalcophile Pd and Pt, plus a large proportion of the Au. Both Cu and Re have lower melt-sulphide partition co-efficients than Au and PGEs (Naldrett 2010; Patten et al. 2013), so if only a small amount of sulphide was precipitated then these more incompatible elements would stay in the melt, forming a Cu-Mo, Re-enriched deposit rather than a Cu-Au (PGE-enriched) deposit. If this is the case then Skouries may be expected to show Re-enrichment, as well as Au and PGE. The occurrence of a high-Re molybdenite in the Skouries deposit has been reported (Berzina et al. 2005), however no significant molybdenite occurrences were observed during this study, and average whole rock assay Mo and Re values for Skouries are low (11 ppm and 0.09 ppm respectively). This suggests that the absence of molybdenum, and therefore molybdenite, is the controlling factor on potential Re enrichment in Skouries.

Muratdere and Skouries also have different hydrothermal fluid evolution histories, and these differences in fluid conditions may also explain the difference in metal endowment. The primary

mineralising fluids in Skouries were very high temperature ( $>550^{\circ}\text{C}$ ), highly saline ( $>65$  wt% KCl + NaCl) and highly oxidised. The primary mineralising veins in the Muratdere deposit have undergone a late, low temperature ( $\sim 280^{\circ}\text{C}$ ) fluid overprint, but remnant primary fluid inclusions are less saline ( $\sim 14$  wt% NaCl), and less oxidised, with no hematite or sulphate daughter minerals present. Hydrothermal PGE transport is favoured by high salinity, high temperature and high  $f\text{O}_2$  fluids, so the primary fluids at Muratdere may not have had the correct conditions to transport Pd and Pt. However, hydrothermal transport of Re requires very similar fluid conditions to those needed for PGE transport (Xiong & Wood 2000; Xiong & Wood 2002), and the remnant inclusions are unlikely to be representative.

Another difference between the two deposits is semi-metal content – Skouries has high concentrations of both Bi and Te, whereas Muratdere only has high concentrations of Te, and low concentrations of Bi. This study has proposed a semi-metal collector model to allow the precipitation of platinum group minerals from PGE-undersaturated hydrothermal fluids. This mechanism requires the presence of both Bi and Te, as the ternary Pd-Bi-Te system is molten above  $489^{\circ}\text{C}$ , whereas the binary Pd-Te system is only molten above hydrothermal temperatures ( $>700^{\circ}\text{C}$ ). As Muratdere only contains Te, and not Bi, this semi-metal enrichment mechanism cannot occur in this deposit.

Hydrothermal fluid interaction with surrounding Re-enriched country rocks is proposed as an upgrading mechanism for Re content in the Muratdere deposit. This is unlikely to have occurred at the Skouries deposit as it is orthomagmatic, with stable isotope results consistent with a magmatic origin ( $\delta^{34}\text{S}$  between  $-3.8\text{‰}$  and  $+1\text{‰}$ ). Skouries does not show the isotopic evidence for fluid mixing or sulphur assimilation seen in Muratdere. Like at Muratdere the host porphyries at Skouries also intrude a metamorphic complex associated with limestones and ultramafic intrusions. There are, however, no peridotites or other Re-enriched country rocks within the alteration footprint of the deposit.

## 7.2 Source and distribution of critical metals in porphyry deposits

The primary objective of this thesis was to investigate the source and distribution of critical metals in the Muratdere and Skouries deposits, with the goal of understanding the processes responsible for their critical metal enrichment and how that may apply to porphyry systems generally. Other aims were to aid research into the economic extraction of Pd, Pt, Bi and Te as co-products, and to generate exploration indicators for other critical metal enriched porphyries. Four main research questions were outlined in the introduction, and the answers to these provided by the work carried out in this thesis are outlined below.

### 7.2.1 Where are critical metals hosted in porphyry deposits?

- Rhenium has been found hosted in molybdenite in the hypogene mineralisation of the Muratdere deposit, with Re concentration found to be independent of polytype. Deposits with multiple generations of molybdenite may show marked differences in rhenium concentration between these generations, as is observed in Muratdere, where the later generation of molybdenite has higher rhenium content than the early phase.
- Semi-metals bismuth and tellurium are hosted in precious metal tellurides and bismuthides, commonly associated with primary ore minerals in mineralising veinsets. Bismuth is also hosted in primary bornite, which is associated with wittichenite in the Skouries deposit. Tellurium is enriched in late intermediate sulphidation veins in the Muratdere deposit, and this remobilisation and enrichment in low temperature veins has been reported in many other deposits.
- Platinum group elements (PGEs) have been located in the primary ore bearing veinsets of the Skouries deposit, associated with potassic alteration. They are hosted in a wide variety of small (<10  $\mu\text{m}$ ) platinum group minerals (PGMs). These PGMs are found as inclusions in primary ore minerals, free in quartz veins and also in association with potassic alteration minerals. In Skouries, and in other PGE rich porphyries, PGMs are all bismuthides or tellurides, showing a strong link between PGEs and semi-metals in porphyry deposits.

### 7.2.2 What is the source of critical metal enrichment in porphyry copper deposits?

- There is evidence that the initial metal endowment of porphyry deposits is from fertile source melts. In post-collisional porphyries, such as Skouries and Muratdere, the metal endowment is thought to be due to upwelling asthenospheric mantle melting previously subduction-modified crust.
- Oxidised source melts play an important role in the enrichment of highly chalcophile elements such as PGEs - where sulphides are present the PGEs will partition into them rather than remain in the melt, depleting the source melt of PGEs. However, if the melt is oxidised then the sulphur will be present as  $\text{SO}_4$  and the PGEs will remain in the porphyry source melt. The host porphyry stocks in the Skouries deposit are highly oxidised, as are igneous units in other PGE-enriched porphyry deposits.
- Input from mafic melts is an important critical metal source in porphyry deposits. The source of platinum group elements in the Skouries deposit is hypothesised to be from periodic recharge of the deposit's source magma chamber with fertile mafic melts, which are seen as primitive mafic dykes both within the deposit and in the surrounding area.

- Although initial metal concentrations in porphyries are likely to be mantle derived, hydrothermal fluid-country rock interaction may 'upgrade' the deposits' metal content. In Muratdere there are two generations of molybdenite, and the later generation is more Re enriched than the early one. This is suggested to be due to interaction between hot, saline hydrothermal fluids and the surrounding rhenium enriched country rocks, scavenging Re, S and other metals.

### **7.2.3 How are these metals transported and enriched within the system?**

- Rhenium is hydrothermally transported as chlorine complexes in high temperature, moderately saline fluids. Secondary rhenium enrichment in Muratdere is proposed to be due to interaction between the ore forming fluids and the surrounding ophiolitic country rock.
- The presence of PGMs in hydrothermal alteration selvages, and the detection of palladium in brine fluid inclusions from the main ore forming veins at Skouries shows PGEs to be hydrothermally transported by high temperature (>550°C), high salinity (>65 wt% NaCl + KCl), oxidised fluids, which agrees with experimental work.
- Bismuth – tellurium melts are proposed to act as PGE collectors in porphyry systems. Co-existing Bi-Te melts could scavenge Pd and Pt from the hydrothermal fluid, allowing the precipitation of platinum group minerals from an under-saturated fluid.

### **7.2.4 What features can be used as an exploration aid to discover more critical metal enriched porphyries?**

- Prospective regions for PGE-enriched porphyries include areas with oxidised intrusions (identified by the presence of primary magnetite) in post-subduction settings. The association of more mafic phases with the felsic host porphyry may indicate further enrichment.
- High semi-metal contents in assay, particularly bismuth and tellurium, may indicate the presence of PGEs. This is particularly important as while bismuth is routinely assayed for as an indicator mineral, PGEs are not part of the standard assay element suite. Platinum group minerals in porphyry deposits are also very small (<10 – 50 µm) and usually require an SEM to identify. This could therefore provide an indicator for projects which are currently being mined that the ore may have un-identified PGMs, which could be claimed as smelter credits.
- Rhenium enriched porphyries may be associated with ophiolites or other rhenium enriched country rocks, and are usually Cu-Mo deposits. Tellurium enrichment is

commonly found with PGE enrichment, but can also be found in intermediate sulphide veins associated with Re-enriched porphyry deposits.

### 7.3 Further work

#### 7.3.1 Platinum group element enrichment in porphyry deposits and the Skouries deposit

- Although there are some exceptions, our understanding of PGE enrichment in porphyry deposits is hampered by a lack of data on the location of PGEs within deposits, their host mineralogy, and the fluid conditions and chemistry of PGE bearing veins. Detailed platinum group mineral (PGM) surveys of deposits which have high measured whole rock PGE values, coupled with fluid inclusion studies and micro-analysis would allow comparison between deposits in order to build a global understanding of these systems.
- The semi-metal PGE collector model proposed in this study could be tested further by:
  - Measuring semi-metal content in other PGE enriched deposits, including in fluid inclusions, and surveying hydrothermal veins for PGM textures which may indicate a molten origin.
  - Experimental work to determine fluid-melt partitioning co-efficients for semi-metal melts, and to define a larger range of PGE – semi-metal phase diagrams in order to better understand the Pd-Pt-Bi-Te+/-As-Se-Sb-Au-Ag system observed in nature.
  - Thermodynamic modelling to determine the speciation of the various components using the hydrothermal conditions observed in the Skouries deposit
- The potential of semi-metal content as an indicator for PGE enrichment could be tested by analysing samples for PGEs from deposits with high Bi and Te contents which have not been previously analysed for PGEs.
- The role of late mafic recharge of the source magma chamber as a PGE source in porphyries could be tested at the Skouries deposit by performing whole rock PGE analysis on the mafic dykes within the deposit, and the related mafic dykes from the surrounding area. If these dykes are responsible for the PGE enrichment in the deposit they should be Pd and Pt depleted in comparison to normal arc magmas. Similarly, most arc magmas are Pd and Pt depleted, so if the igneous intrusions at Skouries are not it could indicate a different magma generation process at depth. Trace element analysis of melt inclusions could also allow examination of these processes, as well as providing further constraints on the fluid-melt system.

### 7.3.2 Rhenium enrichment in porphyries and the Muratdere deposit

- The hypothesis that the late Re concentration upgrading in Muratdere is due to hydrothermal fluid – country rock interaction could be tested further by:
  - Performing whole rock analysis of country rock samples in order to assess their rhenium content. Samples could be analysed within the deposit alteration halo and outside it – if the rhenium enrichment in V3 was sourced from hydrothermal interaction with the surrounding country rock the rocks showing hydrothermal alteration should be Re depleted.
  - Performing whole rock sulphur isotope analysis of the surrounding country rock to allow comparison with  $\delta^{34}\text{S}_{\text{CDT}}$  values in V3.
  - Modelling Re scavenging from peridotites in order to understand the mechanisms and the fluid conditions needed.
  - Undertaking stable isotope and molybdenite chemistry surveys on other rhenium enriched porphyries, both with and without Re bearing country rocks for comparison purposes.
- The mechanism of Re hosting in molybdenite is still not clear – Pagoni Rachi molybdenites show evidence for isovalent substitution, while Muratdere molybdenites may show evidence for the formation of nanophases within the lattice. Analysis of individual molybdenite crystals from Muratdere, and other deposits, with a single-crystal diffractometer for bond-distances, atom coordinates and displacement parameters would allow full comparison with molybdenites from Pagoni Rachi.

## Appendices



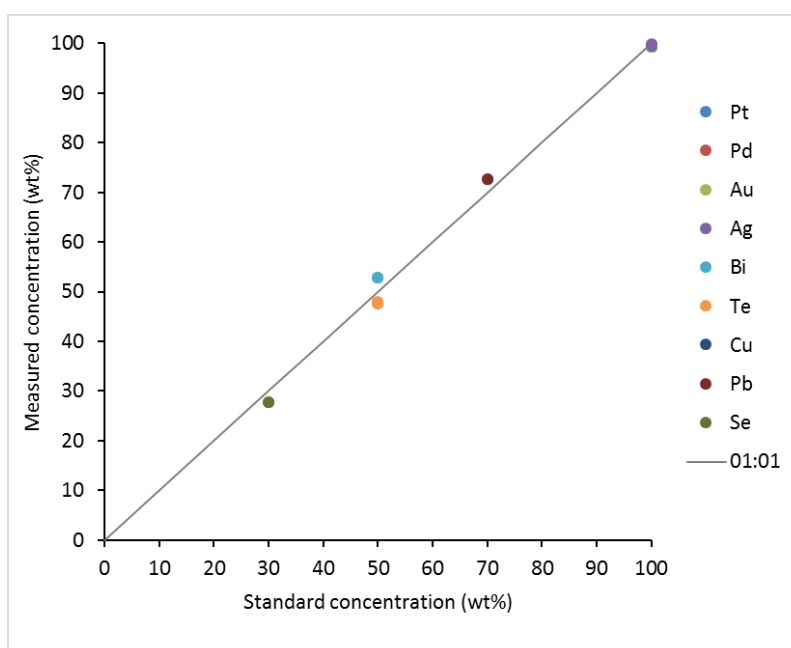


## Appendix A

### A.1 Methodology

#### A.1.1 EPMA calibration data

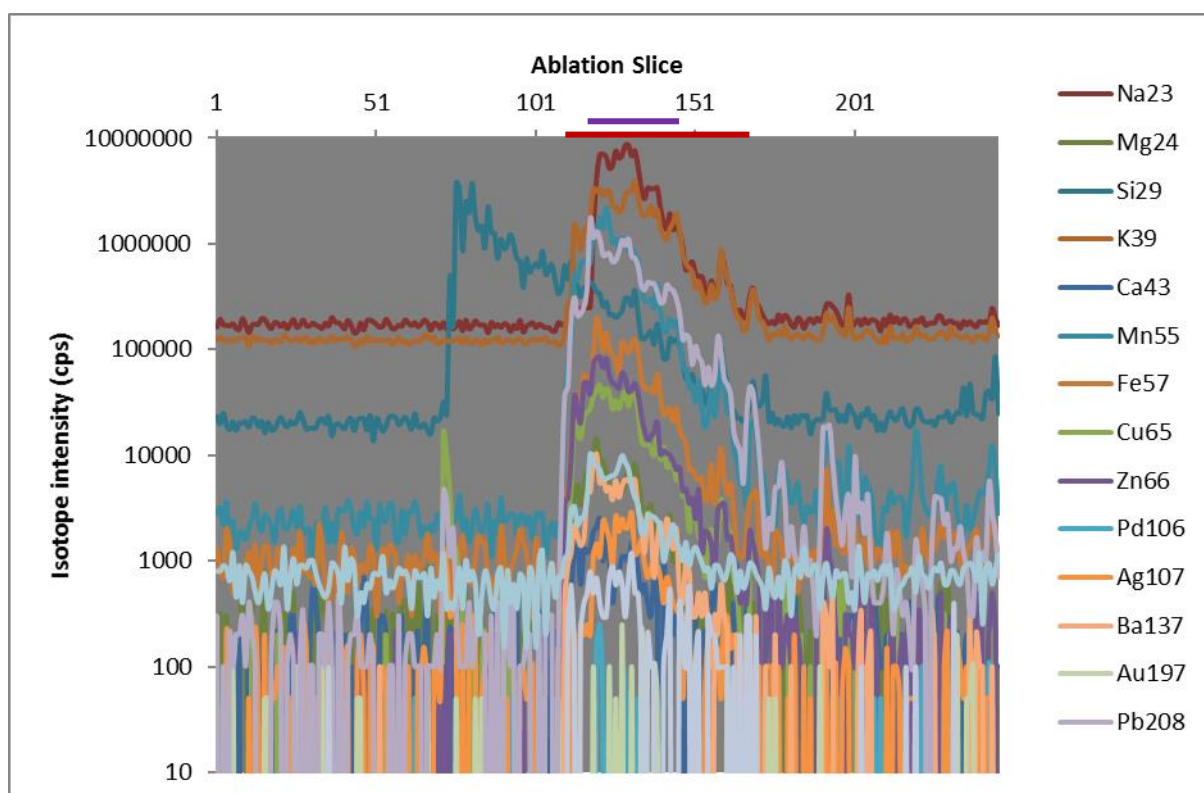
The table and graph below show the results of EPMA analysis of in-house standards at the NHM in order to check calibration and instrumental precision. The graph shows the results of the analysis plotted against the known standard values, showing the instrumental accuracy.



<b>S</b>	<b>Pt</b>	<b>Cu</b>	<b>Se</b>	<b>Pd</b>	<b>Ag</b>	<b>Te</b>	<b>Pb</b>	<b>Bi</b>	<b>Ir</b>	<b>Au</b>	<b>Total</b>
<dt	99.31	<dt	<dt	<dt	<dt	<dt	<dt	<dt	<dt	<dt	99.74
<dt	99.41	<dt	<dt	<dt	<dt	<dt	<dt	<dt	<dt	<dt	99.69
<dt	99.59	<dt	<dt	<dt	<dt	<dt	<dt	<dt	<dt	<dt	99.85
<dt	99.32	<dt	<dt	<dt	<dt	<dt	<dt	<dt	<dt	<dt	99.32
<dt	<dt	<dt	<dt	99.76	1.22	<dt	<dt	<dt	<dt	<dt	100.75
<dt	<dt	<dt	<dt	99.76	<dt	<dt	<dt	<dt	<dt	<dt	99.76
<dt	<dt	<dt	<dt	<dt	<dt	<dt	<dt	<dt	<dt	99.76	98.94
<dt	<dt	<dt	<dt	<dt	<dt	<dt	<dt	<dt	<dt	99.39	98.65
<dt	<dt	<dt	<dt	<dt	99.97	<dt	<dt	<dt	<dt	<dt	99.81
<dt	<dt	<dt	<dt	<dt	99.57	<dt	<dt	<dt	<dt	<dt	99.30
<dt	<dt	<dt	<dt	<dt	<dt	47.74	<dt	52.87	<dt	<dt	100.99
<dt	<dt	<dt	<dt	<dt	<dt	47.9	<dt	52.82	<dt	<dt	101.36
<dt	<dt	<dt	<dt	<dt	<dt	47.62	<dt	52.76	<dt	<dt	101.39
<dt	<dt	<dt	27.73	<dt	<dt	<dt	72.73	<dt	1.48	<dt	100.49
<dt	<dt	<dt	27.7	<dt	<dt	<dt	72.76	<dt	1.5	<dt	100.77
<dt	<dt	100.85	<dt	<dt	<dt	<dt	<dt	<dt	<dt	<dt	100.49
<dt	<dt	100.86	<dt	<dt	<dt	<dt	<dt	<dt	<dt	<dt	100.21

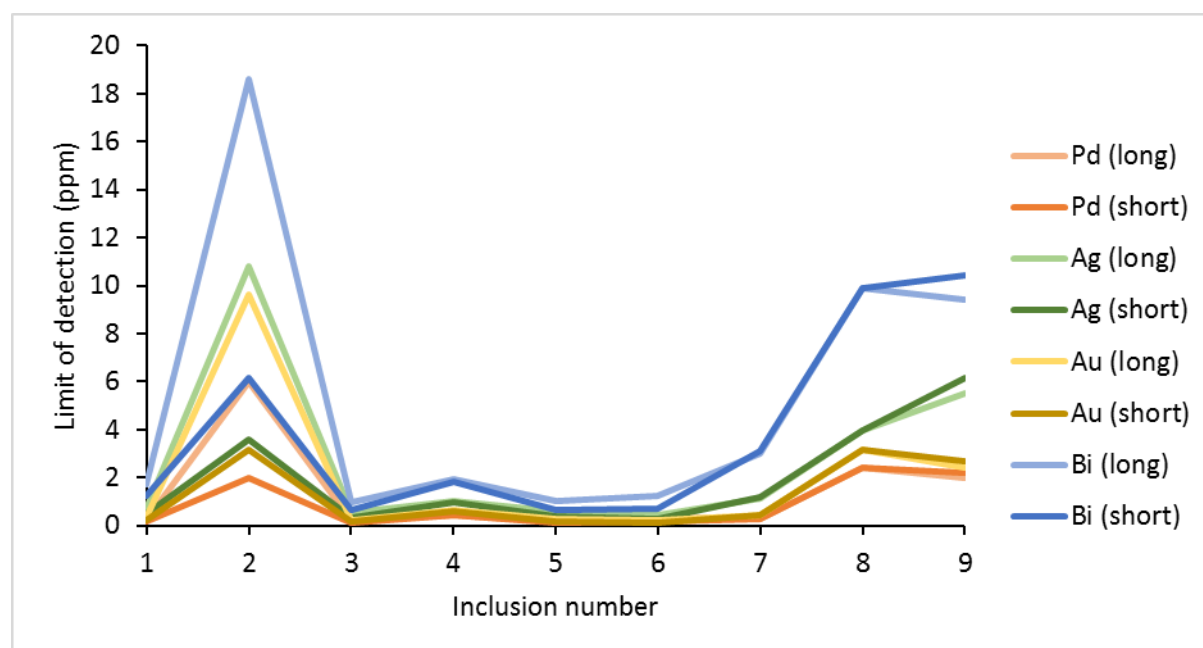
### A.1.2 Transient signal fluid inclusion LA-ICP-MS signal and integration intervals

The figure below shows transient signal responses for LA-ICP-MS analysis of a type IIIA fluid inclusion from veinset M-4 (run SE08A07). The laser was turned on at around ablation slice 70, as indicated by the rise in Si. The inclusion was breached at around ablation slice 115, as indicated by the rise in intensity of elements found in the fluid such as Na and K. Note the peak in Pd, quantified as 0.9 ppm, and the peak for Au, quantified as 0.6 ppm. The red line on the x axis represents the number of ablation slices integrated during the 'long' signal interval used in processing, while the purple line represents the 'short' signal interval used in processing.



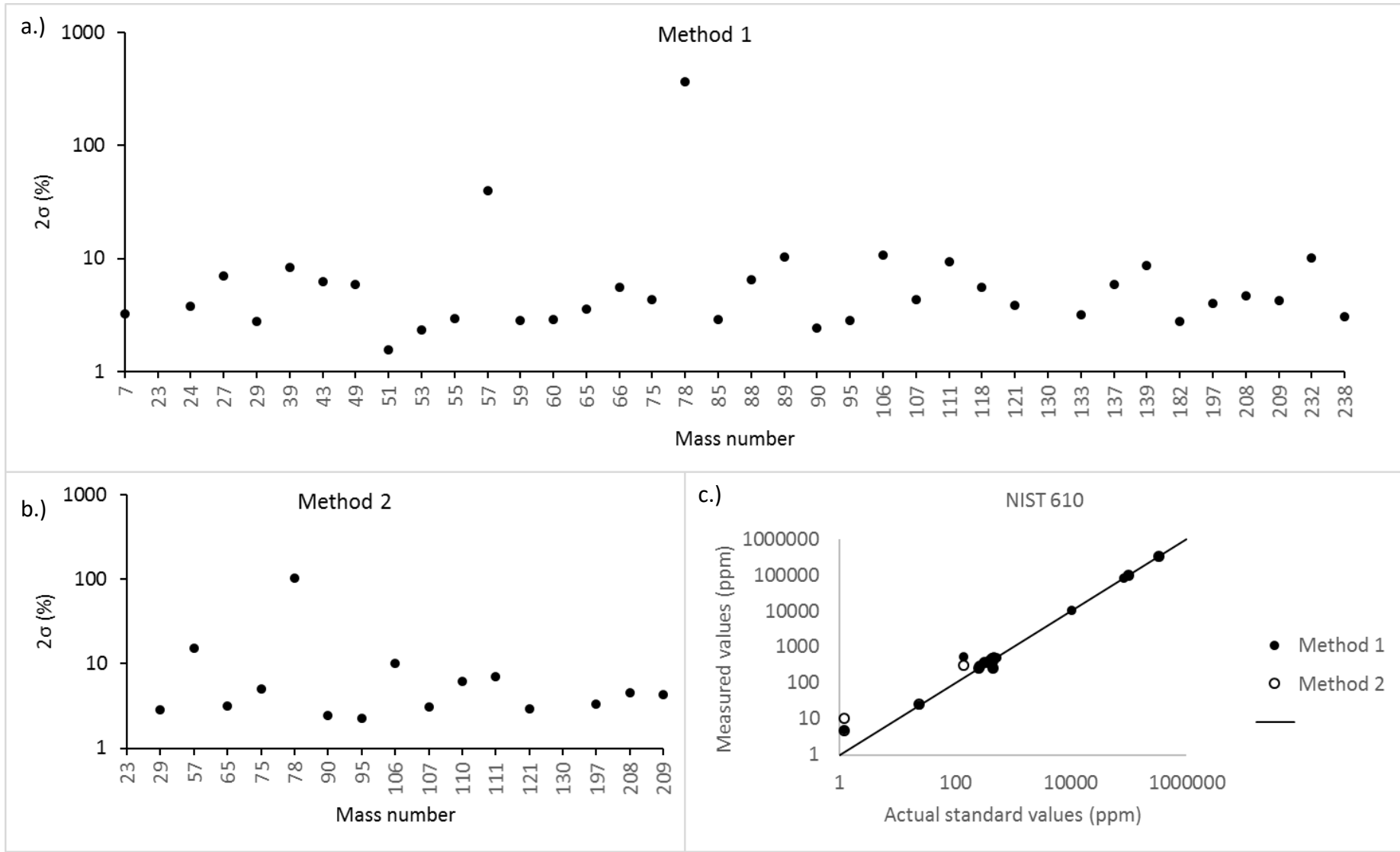
### A.1.3 Changes in LA-ICP-MS limits of detection in fluid inclusions with change in signal integration length

The figure below shows limits of detection for a selected group of elements from an assemblage of type IIA fluid inclusions all trapped in the same healed quartz fracture in an M-5 vein sample. The inclusions have been processed by integrating a long signal interval (long), and a short signal interval (short). This figure shows the affect these different interval lengths have on the LODs for the precious metals and bismuth – the short intervals give lower detection limits.



### A.1.4 Accuracy and precision of LA-ICP-MS of fluid inclusions

The figure below shows a graphical representation of the accuracy and precision of the LA-ICP-MS of fluid inclusions. Graph a.) shows two standard deviations as a percentage of the mean for elements in NIST 610 measured at the beginning and end of each run in method 1 (full element suite, reduced dwell time on precious metals), with mass number of the isotopes measured along the x-axis. Graph b.) shows the same for method 2 (which has a reduced element suite and longer dwell time on precious metals), showing the instrumental error. Selenium has very poor precision ( $2\sigma > 100\%$ ) in both methods, and as such should be discounted from results. Fe also shows poor precision in method 1, with a  $2\sigma$  of 40%, and a  $2\sigma$  of 15% in method 2, and so care should be taken when interpreting Fe results. Graph c.) shows instrumental accuracy by plotting actual NIST 610 values against measured NIST 610 values.



## A.2 Muratdere deposit

### A.2.1 LA-ICP-MS summary table

The tables below show the LA-ICP-MS results for molybdenite crystals from Muratdere. The element concentrations are the average of the readings for that crystal, and the standard deviation is shown, along with the number of readings (n). The molybdenites are classified by morphology – the ‘bladed’ molybdenites are the late vein hosted generation, and the ‘bleb’ molybdenites are the early micro-fracture hosted generation.

Sample	Grain	Type	n	97Mo (wt%)	107Ag (ppm)	182W (ppm)	185Re (ppm)	187Re (ppm)	195Pt (ppm)	197Au (ppm)	Total Re (ppm)	SD
MDD 03 12.45	Moly 12	Bleb	1	36.19	3.4	2.3	200	197	1.1	0.1	198	
MDD 03 12.45	Moly 2	Bleb	3	39.79	1.2	4.9	459	461	0.7	0.1	460	194
MDD 03 12.45	Moly 3	Bleb	1	43.35	0.9	2.2	249	251	0.3	0.1	251	
MDD 03 12.45	Moly 9	Bleb	2	45.67	2.5	7.4	703	705	0.8	0.1	704	7
MDD 33 155	Moly 10	Bleb	5	68.61	4.2	1.7	556	558	0.8	0.5	557	289
MDD 33 155	Moly 14	Bleb	3	67.61	4.5	1.5	242	244	0.8	2.5	243	98
MDD 33 155	Moly 15	Bleb	1	67.28	1.2	1.1	183	185	0.8	0.3	184	
MDD 33 155	Moly 16	Bleb	1	68.23	2.3	1.6	231	229	1.0	0.2	230	
MDD 33 155	Moly 17	Bleb	1	66.42	1.2	0.4	73	72	0.7	0.1	72	
MDD 33 155	Moly 27	Bleb	3	70.11	13.7	1.5	236	236	0.8	0.8	236	59
MDD 33 155	Moly 28	Bleb	2	50.46	12.0	1.0	213	213	1.1	0.5	213	61
MDD 33 155	Moly 29	Bleb	4	48.19	2.9	1.0	233	233	0.7	0.2	233	72
MDD 33 155	Moly 30	Bleb	2	60.39	2.2	1.0	257	257	0.8	1.0	257	56
MDD 33 155	Moly 4	Bleb	1	60.24	12.5	2.2	601	609	0.6	1.8	606	
MDD 33 155	Moly 5	Bleb	1	62.41	13.8	2.1	316	320	0.9	4.2	319	
MDD 33 155	Moly 6	Bleb	1	64.90	2.0	2.4	722	713	0.7	0.2	716	
MDD 33 155	Moly 7	Bleb	1	62.84	1.7	1.4	141	140	0.7	0.1	140	
MDD 33 155	Moly 8	Bleb	1	63.28	2.3	3.8	179	180	0.4	0.2	179	
MDD 33 155	Moly 9	Bleb	4	64.77	3.1	2.9	707	713	0.8	0.4	711	7
		<b>Average</b>		<b>58.46</b>	<b>4.61</b>	<b>2.23</b>	<b>342</b>	<b>343</b>	<b>0.75</b>	<b>0.71</b>	<b>343</b>	
		<b>SD</b>		<b>10.54</b>	<b>4.44</b>	<b>1.60</b>	<b>205</b>	<b>206</b>	<b>0.19</b>	<b>1.04</b>	<b>205</b>	

Sample	Grain	Type	n	97Mo (wt%)	107Ag (ppm)	182W (ppm)	185Re (ppm)	187Re (ppm)	195Pt (ppm)	197Au (ppm)	Total Re (ppm)	SD
MDD 03 12.45	Moly 10	Dendritic	2	41.60	75.9	4.53	406	404	0.64	0.30	404	26
MDD 03 12.45	Moly 11	Dendritic	5	36.73	7.9	2.68	232	233	0.82	0.16	232	188
MDD 03 12.45	Moly 4	Dendritic	7	41.99	16.1	3.07	614	617	0.60	0.20	616	243
MDD 22 84	Moly 1	Dendritic	3	48.79	5.2	6.25	536	538	1.17	0.22	537	114
MDD 22 84	Moly 10	Dendritic	1	58.06	2.6	7.46	667	667	1.10	0.16	667	
MDD 22 84	Moly 11	Dendritic	2	61.10	18.4	8.36	1340	1339	0.95	1.87	1339	166
MDD 22 84	Moly 12	Dendritic	3	58.69	4.1	13.24	783	792	0.88	0.32	789	79
MDD 22 84	Moly 13	Dendritic	2	59.66	8.5	8.97	994	991	0.82	0.51	992	322
MDD 22 84	Moly 14	Dendritic	2	56.22	12.0	7.14	712	717	1.01	0.29	715	178
MDD 22 84	Moly 15	Dendritic	1	58.69	2.5	8.13	771	769	0.95	0.07	769	
MDD 22 84	Moly 16	Dendritic	1	59.57	2.3	21.09	726	727	0.79	0.20	727	
MDD 22 84	Moly 17	Dendritic	2	56.78	7.1	8.24	1000	995	0.89	0.52	997	173
MDD 22 84	Moly 18	Dendritic	2	57.84	13.8	8.68	840	841	0.85	0.38	840	232
MDD 22 84	Moly 19	Dendritic	5	50.37	2.2	13.32	656	655	0.89	0.10	656	246
MDD 22 84	Moly 2	Dendritic	3	48.29	9.7	3.53	815	822	0.91	0.46	819	53
MDD 22 84	Moly 20	Dendritic	2	51.94	5.4	5.30	721	721	0.85	0.20	721	202
MDD 22 84	Moly 21	Dendritic	4	60.90	9.2	6.63	1018	1021	0.89	0.59	1020	393
MDD 22 84	Moly 22	Dendritic	1	62.33	7.3	6.09	694	690	0.74	0.79	692	
MDD 22 84	Moly 23	Dendritic	1	59.80	1.8	7.33	691	684	1.30	0.07	687	
MDD 22 84	Moly 24	Dendritic	1	59.60	2.1	4.84	1027	1020	0.94	0.13	1023	
MDD 22 84	Moly 3	Dendritic	3	49.05	12.7	5.68	403	406	0.85	0.40	405	36
MDD 22 84	Moly 4	Dendritic	5	49.42	2.0	10.46	697	698	1.03	0.44	697	99
MDD 22 84	Moly 5	Dendritic	5	54.52	26.6	10.48	816	823	0.98	3.08	821	260
MDD 22 84	Moly 6	Dendritic	8	57.03	26.2	9.61	932	936	0.92	1.50	935	210
MDD 22 84	Moly 7	Dendritic	1	48.04	2.9	4.73	1330	1336	1.17	0.07	1334	
MDD 22 84	Moly 8	Dendritic	1	60.72	2.2	9.08	517	517	0.82	0.11	517	
MDD 22 84	Moly 9	Dendritic	1	45.85	4.7	6.39	887	889	0.92	0.23	888	
MDD 33 155	Moly 1	Dendritic	27	67.18	20.9	3.54	910	917	0.78	1.82	914	147
MDD 33 155	Moly 11	Dendritic	4	60.27	4.3	1.54	1194	1201	0.74	0.77	1198	142
MDD 33 155	Moly 12	Dendritic	4	63.38	5.9	2.19	297	299	0.74	0.93	298	135
MDD 33 155	Moly 13	Dendritic	2	66.70	1.4	1.60	430	434	0.70	0.05	432	74
MDD 33 155	Moly 18	Dendritic	3	64.16	1.8	0.79	364	365	0.74	0.16	365	
MDD 33 155	Moly 19	Dendritic	3	58.99	1.9	0.70	420	423	0.77	0.09	422	
MDD 33 155	Moly 2	Dendritic	3	67.49	14.5	3.05	781	783	0.82	1.50	783	
MDD 33 155	Moly 20	Dendritic	2	55.32	2.2	0.91	431	430	0.70	0.09	430	40
MDD 33 155	Moly 21	Dendritic	3	48.05	3.6	1.21	200	199	0.84	0.16	199	205
MDD 33 155	Moly 22	Dendritic	1	47.47	1.6	2.08	376	381	0.81	0.04	379	
MDD 33 155	Moly 23	Dendritic	3	44.61	2.3	1.14	401	406	0.72	0.17	404	184
MDD 33 155	Moly 24	Dendritic	4	51.92	2.4	1.49	263	265	0.86	0.31	264	79
MDD 33 155	Moly 25	Dendritic	8	71.24	2.7	1.73	580	582	0.78	0.61	581	53
MDD 33 155	Moly 26	Dendritic	2	76.62	3.3	1.79	316	316	0.85	0.55	316	37
MDD 33 155	Moly 3	Dendritic	4	65.52	6.0	1.96	924	932	0.73	0.39	929	188
MDD 33 155	Moly 31	Dendritic	2	59.36	1.8	1.35	295	299	0.60	0.15	297	56
MDD 33 155	Moly 32	Dendritic	1	59.20	1.0	1.30	389	389	0.88	0.15	389	
MDD 33 155	Moly 33	Dendritic	2	66.11	2.0	1.34	527	527	0.84	0.30	527	77
MDD 33 155	Moly 34	Dendritic	3	61.78	2.8	2.61	843	850	1.00	0.16	847	114
MDD 33 155	Moly 35	Dendritic	5	72.41	4.7	4.03	1002	1005	0.81	0.47	1004	140
MDD 33 155	Moly 36	Dendritic	2	69.11	10.6	2.17	850	860	0.80	2.80	856	188
MDD 33 155	Moly 37	Dendritic	2	69.47	1.8	1.76	429	430	0.81	0.18	430	78
		<b>Average</b>		<b>57.55</b>	<b>7.98</b>	<b>5.13</b>	<b>674</b>	<b>676</b>	<b>0.86</b>	<b>0.51</b>	<b>675.59</b>	
		<b>SD</b>		<b>8.57</b>	<b>11.64</b>	<b>4.10</b>	<b>283</b>	<b>283</b>	<b>0.14</b>	<b>0.66</b>	<b>283</b>	

**A.2.2 PGE analysis data table**

The table below shows the results of Ni-S fire assay analysis for PGEs carried out at Cardiff University.

	Veinset present	189Os (ppb)	193Ir (ppb)	99Ru (ppb)	103Rh (ppb)	195Pt (ppb)	106Pd (ppb)	197Au (ppb)	185Re (ppb)
Blank-1		<0.03	<0.03	<0.09	<0.08	0.23	0.11	1.18	0.19
Blank-2		<0.03	<0.03	<0.09	<0.08	0.41	0.09	1.48	0.25
Blank-3		<0.03	<0.03	<0.09	<0.08	0.58	0.11	1.05	0.24
MDD 01 127.7	V2	<0.03	0.03	0.10	<0.08	2.28	0.20	2.74	0.73
MDD 03 10.0	V3	<0.03	<0.03	<0.09	0.13	1.06	0.47	63.93	38.00
MDD 03 245.3a	V3	<0.03	0.04	0.59	0.22	1.21	1.77	282.59	85.64
MDD 03 245.3b	V3	<0.03	<0.03	0.49	0.18	1.87	1.68	316.23	94.67
MDD 03 265.0a	V2	<0.03	<0.03	<0.09	0.09	1.03	0.10	38.47	60.78
MDD 03 265.0b	V2	<0.03	<0.03	<0.09	0.10	0.78	0.12	40.49	69.70
MDD 03 291.6	Peridotite	1.15	1.78	2.72	0.58	3.35	1.07	3.33	0.25
MDD 15 55.1	V2	<0.03	0.08	0.13	0.17	1.77	0.87	141.00	27.21
MDD 15 68.2	V3	<0.03	0.03	0.10	0.15	1.20	0.68	310.08	101.40
MDD 15 95.0	V2	<0.03	<0.03	<0.09	0.09	1.78	1.28	6.14	0.55
MDD 22 119.7	V2	<0.03	<0.03	0.19	0.12	2.11	1.09	126.62	2.51
MDD 22 133.9	V5	<0.03	0.04	<0.09	0.28	4.84	0.45	803.82	0.14
MDD 22 84.7	V3	<0.03	<0.03	0.25	0.28	3.44	0.56	31.72	2917.52
MDD 24 109.1	V5	0.06	0.03	<0.09	<0.08	1.05	0.28	127.07	0.31
MDD 33 118.0	V3	<0.03	<0.03	<0.09	0.13	3.92	1.48	124.32	30.72
MDD 33 155.7	V3	<0.03	0.04	0.20	0.09	0.88	0.52	416.10	32.71
MDD 33 177.6	MF	<0.03	<0.03	<0.09	0.09	0.75	0.16	16.88	1.39
MDD 33 55.5a	MF	0.03	0.04	0.15	0.11	1.11	0.29	210.57	34.83
MDD 33 55.5b	MF	0.03	0.04	0.13	<0.08	1.26	0.31	4.66	0.35
Sand 15		<0.03	<0.03	<0.09	<0.08	0.28	0.11	0.43	4.25
Sand 16		<0.03	<0.03	<0.09	0.09	0.66	0.13	0.21	0.23
WITS1		1.11	1.48	4.08	1.12	6.24	5.42	6.55	0.02
WMG1		22.56	48.01	31.47	26.77	727.20	393.16	108.81	0.31



### A.2.3 Stable isotope summary data table

The table below shows a summary of the results from stable isotope analysis on the Muratdere deposit. The results shown here are an average of multiple repeats on each sample – full results are given in appendix B.

Drill hole	Depth	Main Veinset	$\delta^{18}\text{O}_{\text{SMOW}}$ Quartz	Approximate temperature	$\delta^{18}\text{O}_{\text{SMOW}}$ Fluid	$\delta\text{D}$	$\delta^{34}\text{S}_{\text{CDT}}$ sulphide (av)	$\delta^{34}\text{S}_{\text{CDT}}$ sulphide (min)	$\delta^{34}\text{S}_{\text{CDT}}$ sulphide (max)	$\delta^{34}\text{S}_{\text{CDT}}$ sulphate
MDD01	42.9	Microfracturing	8.8	~350	3.51		1.1			
MDD01	127.7	Microfracturing					3.1			
MDD03	112.05	Microfracturing					4			19.4
MDD03	142.05	Microfracturing	7.5	~350	1.61		4.2			
MDD15	68.2	Microfracturing					2.3	1.9	2.6	
MDD19	85.7	Microfracturing					3			
MDD24	49.5	Microfracturing					3.5	2.7	3.9	
MDD33	177.6	Microfracturing					-2.2			
MDD24	86.1	V1	9.6	316	3.25					
MDD22	119.7	V1/V4	9.6	314	3.25					
MDD24	86.1	V4	9.6	313	3.09	-74				
MDD03	12.45	V2					4.7			
MDD03	230.3	V2					4.6			
MDD15	29.8	V2				-72	6.3			
MDD33	55.5	V2					1.87			
MDD33	74.6	V2				-74				
MDD33	125	V2	8.5	~320	2.32					
MDD33	118	V3	8.6	~320	2.42		6.9	5.6	8.2	
MDD33	155.7	V3	7.6	~320	1.42		7.9	6.3	8.9	
MDD10	70.25	V5					1.8	0.4	2.7	
MDD15	39.2	V5	10.4	~250	1.51	-70	-1.5	-5.5	3.1	17
MDD22	133.9	V5					-0.6	-4	2.1	
MDD24	109.1	V5	12.3	~250	3.31	-75	1.3			18.3
MDD33	185	V6								18.2
MDD33	165.1	V7								19.4
MDD33	194.2	V7								12.8

### A.3 Skouries deposit

#### A.3.1 Stable isotope summary data table

The table below shows the results of the stable isotope analyses carried out on samples from the Skouries deposit

Drill hole	Depth	Main Veinset	del18O measured	Temp hom	del18O fluid	delD	del34S sulphide av	del34S sulphide min	del34S sulphide max
SOP 102A	273.9	L-4		~350			-2.2		
SOP 134	86.2	M-5		505			-2.3		
SOP 134	135.1	M-4	10.3	550	7.22	-60	-2.2	-3.8	-0.6
SOP 134	261.1	M-5		505			-2.4	-2.2	-0.4
SOP 134	266.1	M-3		580			-1.4	-1.7	-1.1
SOP 134	323	L-4	9.8	~350	6.72	-66	-1		
SOP 134	500.9	M-3	10.0	580	6.92				
SOP 134	634.6	L-4		~350			0.8		
SOP 137	133.9	M-4		550			-2.3	-2.7	-2.1
SOP 137	307	M-4	10.3	550	7.22	-76	-1.3	-1.3	-1.2
SOP 137	419.5	M-5		505			-1.4	-1.5	-1.3
SOP 137	587.3	M-4		550			-2.6	-3.3	-1.8
SOP 137	702.4	M-3	9.5	580	6.42	-53	-0.8		
SOP 137	710.3	M-3		580			-0.04		
SOP 137	720	M-3		580			0.61	0.22	1
SOP 137	733	M-3		580			-1.4		
SOP 137	745.3	M-4		550			-1.6		
SOP 139	497.6	M-4		550			-1.7		
SOP 139	505.4	L-4		~350			0.77		
SOP 139	514	M-4	10	550	6.92		-0.1		
SOP 139	521.7	M-4		550			-1		
SOP 139	655	E-4	9.7	~550	6.62	-79	-3.2		
SOP 139	687.6	L-4		~350			-1.9	-3	-1.2
SOP 139	695.9	M-5	9.8	505	6.72				
SOP 142	78.9	M-4	10.5	550	7.42	-54	-2.1		

#### A.3.2 Samples chosen for fluid inclusion analysis

The table below shows the samples chosen for fluid inclusion analysis and their features

Sample	Drill hole	Depth	Veinset	Vein description	Quartz description	Alteration associated	Lithology	Fluid inclusion distribution
1	SOP 134	500.9	M-4	5 cm thick area of quartz-magnetite-chalcopyrite-bornite veins - several ~1cm thick veins overprinting each other so chip made from most recent. Magnetite disseminated throughout veins, and concentrated with secondary biotite crystals at edges of veins. Some secondary biotite crystals caught within quartz of crosscutting veins. Sulphides irregularly distributed within the veins.	Irregular quartz crystals containing small magnetite crystals and sulphide blebs. Quartz crystals larger at centre of vein, and smaller, cloudy and annealed at the edge and when in contact with another vein.	Potassic alteration, magnetite and biotite at edges of individual veins. Composite vein area has clay selvage.	BPO	Fluid inclusions more isolated, with some trails ending at edges of crystals. A lot of decrepitated inclusions in overprinted veins.
2	SOP 137	702.4	M-3	>5cm wide pegmatitic vein with interlocking euhedral potassium feldspar and quartz crystals with rare interstitial chalcopyrite	Large, clear, equigranular, euhedral quartz crystals	Potassic alteration with silicification and some propylitic overprint.	BPO	Multiple stages of isolated inclusions, some trails of inclusions which stop at crystal boundaries, many large inclusions decrepitated.

Sample	Drill hole	Depth	Veinset	Vein description	Quartz description	Alteration associated	Lithology	Fluid inclusion distribution
3	SOP 134	135.1	M-3	2 cm wide quartz-chalcopyrite-(bornite) vein with large euhedral potassium feldspar crystals along the edges and interstitial sulphides in the centre.	Smaller (1 mm) subhedral cloudy quartz crystals intergrown with feldspar crystals at the edge of the vein, large (2 mm) clear euhedral quartz crystals in the centre of the vein	Potassium feldspar selvage, secondary biotite crystals, clay.	PPO	Secondary trails of inclusions across multiple quartz crystals, some trails stop at crystal boundaries, some isolated inclusions
4	SOP 139	695.9	E-2	Irregular quartz vein 5mm thick.	Microcrystalline interlocking cloudy quartz crystals, some of which contain opaques.	Calcite, chlorite, biotite + pyrophyllite	BPO	Rare isolated inclusions seen, most inclusions decrepitated.
5	SOP 134	323	M-5	1 cm wide quartz-chalcopyrite-bornite vein, straight edged with sulphides in a central suture. Assay shows elevated Pd levels.	Equant, clear, euhedral quartz crystals 0.5 - 1 mm growing perpendicular to vein edges.	Pervasive potassium alteration, argillic overprint - feldspars altered to sericite and clay in places	PPO	Trails of inclusions, both crossing and stopped at crystal boundaries, isolated crystals in centre of quartz crystals
6	SOP 139	655	E-3	4cm thick area of overprinting quartz-magnetite veins, with irregular edges. Magnetite selvages and magnetite disseminated through the veins.	Quartz crystals 10-20 $\mu$ m in diameter, cloudy and annealed. Crystals contain blebs of sulphides.	Secondary biotite, magnetite, diaspore	BPO	Rare isolated fluid inclusions seen.
7	SOP 142	78.9	M-4	3cm wide quartz-magnetite-pyrite-chalcopyrite vein with irregular edges. Interstitial sulphides in irregular 2.4 mm thick trails through vein, often intergrown with magnetite. Magnetite also disseminated through vein.	Outer 5mm of vein made up of irregular, small (<1mm) annealed quartz, centre of vein made up of large (2mm), euhedral, clear quartz crystals.	Pervasive silicification surrounded by magnetite and secondary biotite	Biotite schist country rock	Trails of fluid inclusions trapped in quartz growth zones, isolated fluid inclusions within large crystals and trails across the crystals

### A.3.3 Laser Raman results table

The table below shows the qualitative results of laser raman analysis of fluid inclusions.

Sample	Inclusion number	Inclusion type	Phase analysed	Result
5	1	Type III	Daughter mineral	Hematite
5	1	Type III	Vapour	CO <sub>2</sub> ?
5	2	Type III	Vapour	H <sub>2</sub> O
5	2	Type III	Liquid	H <sub>2</sub> O and unknown
5	2	Type III	Daughter mineral	Anhydrite
5	2	Type III	Daughter mineral	Hematite
5	3	Type I	Vapour	CO <sub>2</sub> + H <sub>2</sub> O
5	4	Type I	Vapour	CO <sub>2</sub> + H <sub>2</sub> O
5	5	Type III	Vapour	H <sub>2</sub> O
5	5	Type III	Liquid	H <sub>2</sub> O
5	7	Type III	Vapour	H <sub>2</sub> O
5	7	Type III	Liquid	H <sub>2</sub> O
5	8	Type IV	Vapour	CO <sub>2</sub>
5	9	Type IV	Vapour	CO <sub>2</sub> + CH <sub>4</sub>
5	10	Type III	Vapour	H <sub>2</sub> O
5	10	Type III	Daughter mineral	Bismuth
5	11	Type III	Vapour	H <sub>2</sub> O
5	11	Type III	Liquid	H <sub>2</sub> O
5	11	Type III	Daughter mineral	Halite
5	12	Type IV	Vapour	CO <sub>2</sub>
5	13	Type IV	Vapour	CO <sub>2</sub>
5	14	Type IV	Vapour	CO <sub>2</sub>
5	15	Type IV	Vapour	CO <sub>2</sub>
5	16	Type I	Vapour	CO <sub>2</sub>
5	16	Type I	Liquid	H <sub>2</sub> O
5	17	Type I	Liquid	H <sub>2</sub> O
5	18	Type I	Liquid	H <sub>2</sub> O
5	19	Type I	Liquid	H <sub>2</sub> O
5	20	Type III	Vapour	H <sub>2</sub> O
3	1	Type III	Vapour	CO <sub>2</sub> + H <sub>2</sub> O
3	1	Type III	Daughter mineral	Barite
3	1	Type III	Daughter mineral	Hematite
3	2	Type III	Vapour	CO <sub>2</sub> + H <sub>2</sub> O
3	2	Type III	Liquid	H <sub>2</sub> O

## Appendix A

Sample	Inclusion number	Inclusion type	Phase analysed	Result
3	2	Type III	Daughter mineral	Hematite
3	3	Type I	Vapour	CO <sub>2</sub> + H <sub>2</sub> O
3	4	Type III	Vapour	H <sub>2</sub> O (CO <sub>2</sub> ?)
3	4	Type III	Liquid	H <sub>2</sub> O
3	4	Type III	Daughter mineral	Hematite
3	5	Type III	Vapour	H <sub>2</sub> O
3	5	Type III	Daughter mineral	Anhydrite
3	5	Type III	Daughter mineral	Anhydrite
3	6	Type III	Vapour	H <sub>2</sub> O
3	6	Type III	Liquid	H <sub>2</sub> O
3	6	Type III	Daughter mineral	Sylvite
3	6	Type III	Daughter mineral	Aragonite
3	6	Type III	Daughter mineral	Anhydrite
3	7	Type IV	Vapour	CO <sub>2</sub>
3	8	Type III	Vapour	H <sub>2</sub> O
3	8	Type III	Daughter mineral	Anhydrite
3	8	Type III	Daughter mineral	Hematite
3	9	Type III	Vapour	CO <sub>2</sub> + H <sub>2</sub> O
3	9	Type III	Liquid	H <sub>2</sub> O
3	9	Type III	Daughter mineral	Barite
3	9	Type III	Daughter mineral	Hematite
3	10	Type III	Vapour	CO <sub>2</sub> + H <sub>2</sub> O
3	10	Type III	Liquid	H <sub>2</sub> O
3	11	Type III	Vapour	CO <sub>2</sub> + H <sub>2</sub> O
3	11	Type III	Liquid	H <sub>2</sub> O
3	12	Type I	Liquid	H <sub>2</sub> O
2	1	Type I	Liquid	H <sub>2</sub> O
2	2	Type I	Vapour	CO <sub>2</sub>
2	2	Type I	Liquid	H <sub>2</sub> O
2	3	Type III	Vapour	H <sub>2</sub> O
2	3	Type III	Daughter mineral	Anhydrite
2	4	Type III	Vapour	H <sub>2</sub> O + CO <sub>2</sub>
2	4	Type III	Daughter mineral	Hematite
2	5	Type III	Vapour	CO <sub>2</sub>

**A.3.4 Summary data table of LA-ICP-MS of fluid inclusions using 'method 1'**

The tables below shows results from 'method 1' LA-ICP-MS of fluid inclusions. The average element concentrations for the main fluid inclusion types in each vein are given, along with the calculated NaCl concentration used in data processing and their homogenisation temperature. The standard deviation of the measurements averaged is also given. Full results can be found in electronic appendix C.

Appendix A

Veinset	Inclusion type	Average salinity (NaCl wt%)	Average THOM	K (wt%)	1SD	Ca (wt%)	1SD	Mn (wt%)	1SD	Fe (wt%)	1SD	Cu (wt%)	1SD	Zn (wt%)	1SD	Pb (wt%)	1SD
M-3	Type IIIA	38	577	14.47	0.01	1.28	0.00	1.52	0.01	5.63	0.01	0.09	0.01	1.25	0.01	2.52	0.01
M-3	Type IIIB	39	554	6.86	0.01	0.23	0.01	1.12	0.01	4.25	0.01	0.45	0.01	0.69	0.01	2.50	0.01
M-3	Vapour	10	~481	4.36	0.00	1.22	0.00	0.41	0.00	1.12	0.00	1.23	0.00	0.53	0.00	1.02	0.00
M-4	Type IIIA	44	558	9.75	8.91	0.94	0.90	1.57	1.08	2.53	3.36	0.39	0.21	0.84	0.75	2.88	1.45
M-4	Type IIIB	39	508	12.62	3.41		0.08	2.79	0.52	7.63	1.80	2.06	0.58	1.21	0.44	4.28	1.94
M-4	Vapour	10	481	3.88	3.18	0.92	0.00	0.65	0.31	1.53	0.67	0.83	2.59	0.38	0.39	1.25	0.78
M-5	Type IIIA	36	503	19.64	3.98	1.95	0.20	3.71	0.59	10.54	2.42	0.30	0.80	2.00	0.25	3.22	1.43
M-5	Type IIIB	37	490	8.94	0.00	1.42	0.00	1.43	0.00	1.42	0.00	0.16	0.00	0.59	0.00	0.76	0.00
M-5	Vapour	10	~481	14.06	1.70	2.44	1.93	5.62	0.08	5.96	0.16	0.93	0.95	3.54	0.16	2.63	0.82

Veinset	Inclusion type	Li (ppm)	1SD	Mg (ppm)	1SD	Rb (ppm)	1SD	Sr (ppm)	1SD	Y (ppm)	1SD	Cs (ppm)	1SD	Ba (ppm)	1SD	La (ppm)	1SD	Th (ppm)	1SD	U (ppm)	1SD
M-3	Type IIIA	29	18	506	455	1291	684	263	242	2.0	1.1	275	160	283	348	8	7			9.1	10.5
M-3	Type IIIB	18	4	202	142	938	374	171	156	5.6	5.6	182	91	370	287	17	17	5.8	7.6	9.5	14.2
M-3	Vapour	406	405	234	110	410	283	47	53	2.3	2.2	100	59	85	71	6	7	2.7	2.1	0.9	0.9
M-4	Type IIIA	18	0	242	168	1148	406	269	87	1.5	1.1	237	92	462	188	3	22	0.1	0.0	4.0	5.0
M-4	Type IIIB			596		1935		365				431		170		49				14.6	
M-4	Vapour	34	122	804	2774	509	186	118	30	10.1	9.5	105	33	212	180	79	100	0.8	2.0	13.6	6.9
M-5	Type IIIA	30	12	720	415	2145	1286	557	189	1.1	0.1	449	295	243	104	52	33	1242	1241.6	8.4	1.5
M-5	Type IIIB	244	173	601	647	771	750	493	455	8.7	7.6	211	89	75	82	35	35	0.4	0.0	2.5	2.3
M-5	Vapour	554	533	3264	3990	3131	2209	528	338	3.4	4.3	666	405	242	331	6	7	1.6	2.5	25.4	20.3

Veinset	Inclusion type	Pd (ppm)	1SD	Ag (ppm)	1SD	Au (ppm)	1SD	Co (ppm)	1SD	Ni (ppm)	1SD	Mo (ppm)	1SD	W (ppm)	1SD	Sn (ppm)	1SD	As (ppm)	1SD	Bi (ppm)	1SD	Sb (ppm)	1SD
M-3	Type IIIA	0.84	0.54	42	15	0.51	0.22	46	45	14	9	193	178	84	129	14	0	110	57	99	72	8	4.9
M-3	Type IIIB	0.55	0.28	40	27	1.98	2.45	36	33	301	501	144	100	77	132	20	0	41	22	90	36	5	2.8
M-3	Vapour	0.06	0.00	17	8			15	14	59	0	50	29	20	19			229	269	77	82	5	3.8
M-4	Type IIIA	0.92	0.05	28	5	0.35	0.25	38	6	14	2	153	59	46	7	8	0	94	32	142	673	8	0.8
M-4	Type IIIB																			1561			
M-4	Vapour	0.98	1.10	16	12	0.62	1.41	19	14	64	198	100	93	277	1132	4923	18882	46	40	287	161	6	9.6
M-5	Type IIIA	2.16	1.62	27	12	0.00	0.00	53	34	5	0	970	654	526	261	22	22	291	259	135	92	7	1.9
M-5	Type IIIB	0.00	0.00	12	2	0.40	0.00	25	28		0	58	44	16	0	48	48	111	61	52	25	3	0.0
M-5	Vapour	2.06	3.47	7	5	0.31	0.39	32	53	30	52	395	504	113	89	208	358	256	287	137	91	43	68.9



### A.3.5 LA-ICP-MS data from 'method 2'

The table below shows the results from 'method 2' analysis of fluid inclusions for precious metals and semi-metals. The first table shows the limits of detection (LOD) in ppm. The second table shows the results. Full results for fluid inclusion LA-ICP-MS are given in electronic appendix C.

23 Na LOD	57 Fe LOD	208 Pb LOD	65 Cu LOD	75 As LOD	90 Zr LOD	95 Mo LOD	106 Pd LOD	107 Ag LOD	110 Pd LOD	111 Cd LOD	121 Sb LOD	197 Au LOD	209 Bi LOD
262	88	1.5	1.5	7.0		0.55	0.08	0.49	0.14	5.54	0.97	0.19	1.27
2750	907	14.6	13.5	76.4		12.64	3.55	3.92	1.39	57.30	13.15	1.96	13.81
179	42	0.7	0.7	5.6	0.09	0.31	0.12	0.21	0.08	3.35	0.61	0.09	0.51
1141	372	4.1	10.6	50.3	0.82	8.78	0.65	2.52	0.77	31.72	5.79	0.96	4.69
1907	469	7.2	11.5	41.3	2.27	3.53	0.59	3.42	0.82	66.10	6.78	1.31	6.27
2245	519	8.1	7.8	57.2	3.52	4.33	0.72	3.63	1.05	62.27	7.60	2.86	9.14
110	47	0.8	1.4	5.7		0.20	0.14	0.45	0.11	4.41	0.98	0.12	0.72
544	150	4.1	3.2	15.3		1.18	0.67	1.05	0.25	18.42	3.23	0.50	2.20
437	211	3.4	4.1	23.3		1.33	0.60	1.20	0.29	8.02	3.17	0.64	2.53
239	107	1.1	1.6	7.9		0.47	0.17	0.46	0.13	7.87	1.32	0.29	1.32
132	66	1.0	0.6	4.5		0.35	0.13	0.32	0.09	3.43	0.67	0.16	0.64
195	55	1.0	1.3	5.5	0.14	0.50	0.18	0.50	0.20	7.57	1.37	0.24	1.26
154	43	0.8	0.7	5.1	0.11	0.39	0.14	0.35	0.07	4.85	0.58	0.15	0.62
510	109	1.2	2.6	13.1	0.28	0.96	0.44	0.98	0.18	15.54	2.38	0.60	1.82
173	57	1.0	1.6	7.4	0.13	0.45	0.12	0.38	0.13	4.90	1.41	0.18	0.67
152	53	0.6	1.2	7.3	0.11	0.36	0.17	0.26	0.07	4.76	0.74	0.12	0.71
794	234	3.4	3.9	26.9	0.47	3.27	0.27	1.17	0.54	27.26	3.88	0.42	3.09
1559	547	8.1	14.8	55.8	1.25	8.59	2.44	3.98	1.27	42.97	10.23	3.15	9.90
2505	490	13.5	11.7	67.3	1.52	10.41	2.18	6.14	0.95	61.74	15.34	2.71	10.45

## Appendix A

Interval	Salinity	Sample Label	Sample	Inclusion number	Veinset	Inclusion type	23Na wt%	57Fe ppm	208 Pb ppm	65 Cu ppm	75 As ppm	90 Zr ppm	95 Mo ppm	106 Pd ppm	107 Ag ppm	110 Pd ppm	111 Cd ppm	121 Sb ppm	197 Au ppm	209 Bi ppm
Short	Average	SE09A17	3	T2	M-3	Type IIIA	15	4.01	1.0	38	32		364	0.40	27	0.79	21	< 1	0.71	28
Short	Average	SE09A18	3	T2	M-3	Type IIIA	15	4.07	2.3	104	< 76.4		67	< 3.6	38	< 1.4	< 57.3	< 13.1	< 2	84
Short	Average	SE13C20	3	Isolated	M-3	Type IIIB	15	4.58	1.4	10	42	< 0.1	184	0.92	40	1.91	69	1.21	< 0.1	42
Short	Average	SE13C17	3	T3	M-3	Type IIIB	15	3.86	1.4	238	63	< 0.8	55	< 0.6	13	< 0.8	37	< 5.8	< 1	77
Short	Average	SE13C18	3	T3	M-3	Type IIIB	15	3.63	1.2	34	< 41.3	< 2.3	559	< 0.6	27	1.06	< 66.1	< 6.8	< 1.3	23
Short	Average	SE13C19	3	T3	M-3	Type IIIB	15	0.75	0.9	2709	448	< 3.5	288	0.86	46	< 1.1	< 62.3	< 7.6	< 2.9	56
Short	Average	SE09A07	5	T1	M-5	Type IIIA	14	5.61	1.5	8655	125		399	0.51	12	1.70	46	7.33	0.26	46
Short	Average	SE09A09	5	T1	M-5	Type IIIA	14	4.51	2.3	1089	118		419	1.31	26	3.61	97	5.48	0.57	73
Short	Average	SE09A10	5	T1	M-5	Type IIIA	14	3.95	0.7	2603	58		733	< 0.6	13	0.50	40	4.71	< 0.6	60
Short	Average	SE09A11	5	T1	M-5	Type IIIA	14	2.48	0.5	86	15		39	0.32	7	0.64	11	< 1.3	< 0.3	10
Short	Average	SE09A12	5	T1	M-5	Type IIIA	14	2.35	0.7	2196	32		135	0.31	11	0.89	22	1.95	0.19	18
Short	Average	SE13C08	5	T5	M-5	Type IIIA	14	1.56	0.7	5106	183	0.644	155	< 0.2	12	0.53	19	3.35	< 0.2	23
Short	Average	SE13C10	5	T5	M-5	Type IIIA	14	2.50	1.0	433	67	< 0.1	222	< 0.1	10	0.28	< 4.9	< 0.6	0.32	26
Short	Average	SE13C11	5	T5	M-5	Type IIIA	14	2.74	0.8	4609	106	< 0.3	332	< 0.4	10	0.86	< 15.5	3.50	< 0.6	40
Short	Average	SE13C12	5	T5	M-5	Type IIIA	14	1.57	0.6	292	< 7.4	< 0.1	115	0.37	4	0.84	10	< 1.4	< 0.2	11
Short	Average	SE13C13	5	T5	M-5	Type IIIA	14	1.76	0.4	1866	34	< 0.1	151	0.60	5	0.79	28	1.77	< 0.1	15

Interval	Salinity	Sample Label	Sample	Inclusion number	Veinset	Inclusion type	23Na wt%	57Fe ppm	208Pb ppm	65Cu ppm	75As ppm	90Zr ppm	95Mo ppm	106Pd ppm	107Ag ppm	110Pd ppm	111Cd ppm	121Sb ppm	197Au ppm	209Bi ppm
Short	Average	SE13C14	5	T5	M-5	Type IIIA	14	2.30	0.8	3352	136	< 0.5	257	0.62	12	0.73	< 27.3	5.05	< 0.4	29
Short	Average	SE13C15	5	T5	M-5	Type IIIA	14	9.49	2.9	7186	57	< 1.3	1102	3.01	19	2.54	< 43	13.05	< 3.2	68
Short	Average	SE13C16	5	T5	M-5	Type IIIA	14	8.33	1.2	3292	69	< 1.5	317	2.32	< 6.1	1.59	< 61.7	< 15.3	< 2.7	39

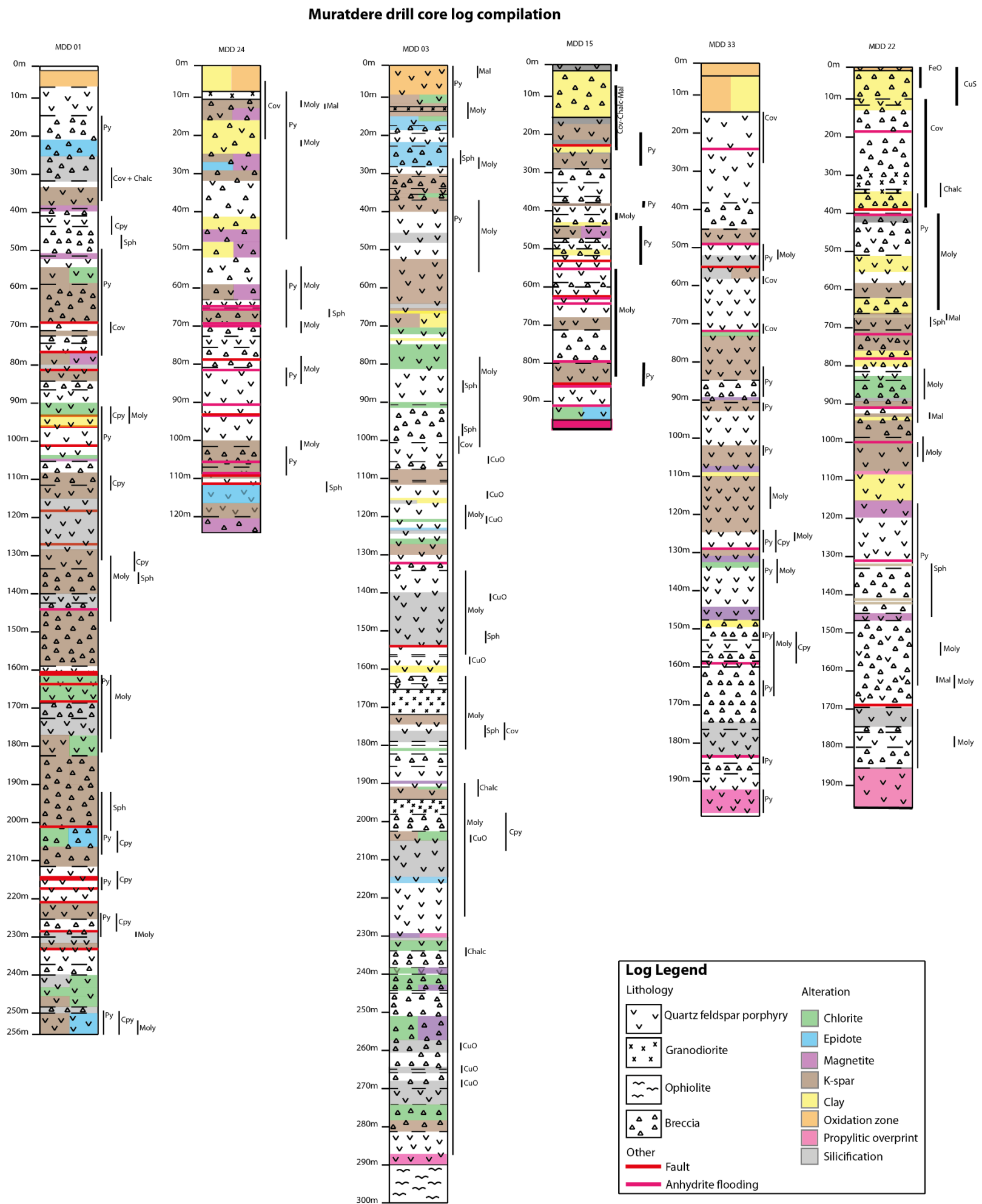


## **A.4 Drill core log compilations**

### **A.4.1 Compilation of Muratdere drill core logs**

The logs below are graphical representations of the 6 diamond drill cores logged at Muratdere. The core was logged at a 5 - 10 m scale, with a total of 1160 m of core logged over 10 days. The graphical logs show a summary of lithology and alteration observed.





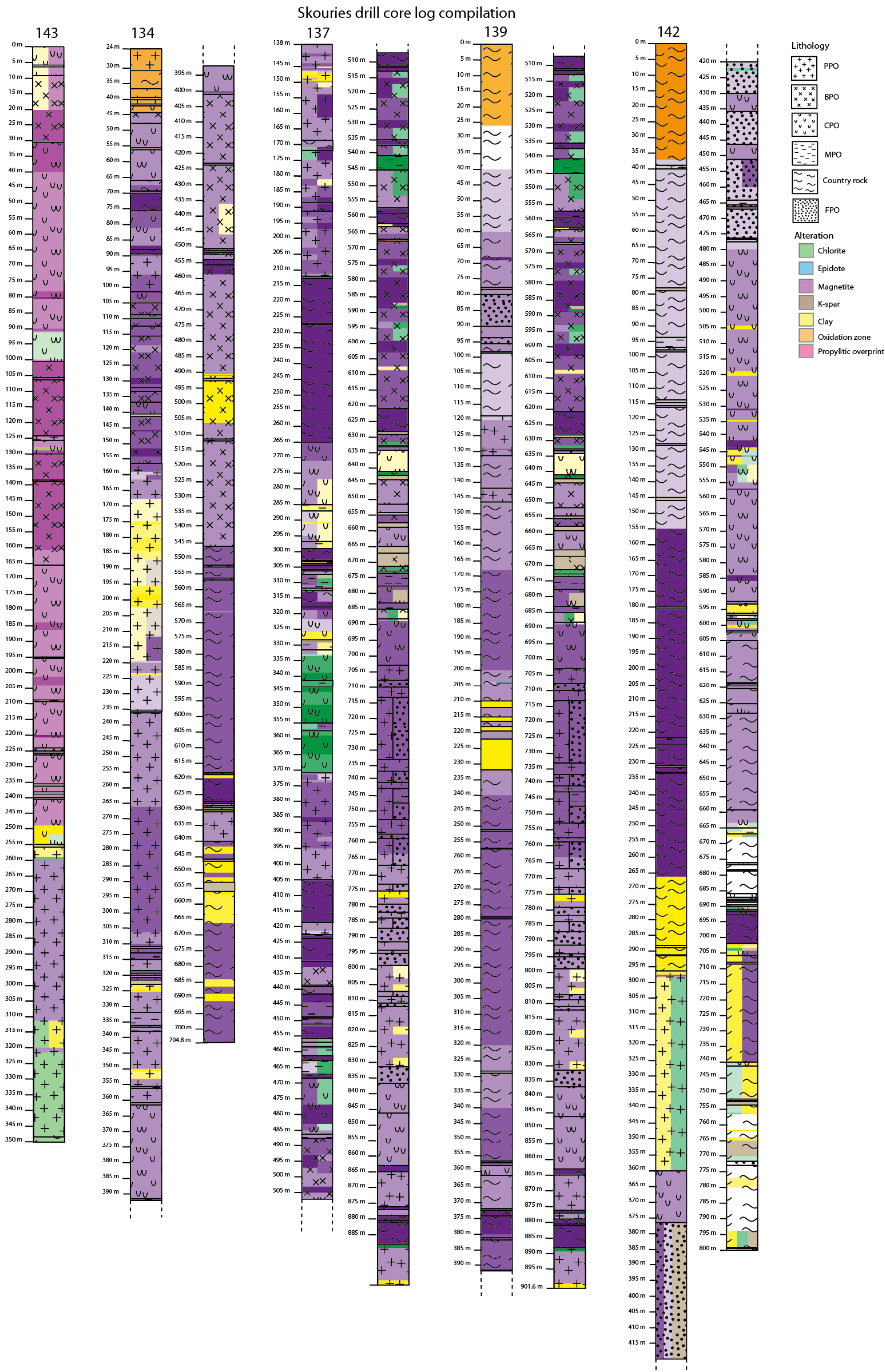




#### **A.4.2      Compilation of Skouries drill core logs**

The logs below are graphical representations of the 5 drill holes were logged at Skouries. The core was logged at a 2m scale, with a total of 3464 m of core logged over 6 weeks. The graphical logs show a summary of the main lithologies and alteration types observed.







## **Appendix B**

Appendix B consists of data tables for the Muratdere deposit, which are included in the attached CD-rom. The CD contains a full list of samples taken and analyses run, XRD results table, full stable isotope results, full results from the LA-ICP-MS of molybdenites and full fluid inclusion microthermometry data tables.

## **Appendix C**

Appendix C consists of data tables for the Skouries deposit, which are included in the attached CD-rom. The CD contains a full list of samples taken and analysis run, full fluid inclusion microthermometry data, full EPMA data tables and full results from the LA-ICP-MS of fluid inclusions.



## List of References

- Aghazadeh, M., Hou, Z., Badrzadeh, Z. & Zhou, L., 2015. Temporal–spatial distribution and tectonic setting of porphyry copper deposits in Iran: Constraints from zircon U–Pb and molybdenite Re–Os geochronology. *Ore Geology Reviews*, 70, pp.385–406.
- Akay, E., 2009. Geology and petrology of the Simav Magmatic Complex (NW Anatolia) and its comparison with the Oligo-Miocene granitoids in NW Anatolia: implications on Tertiary tectonic evolution of the region. *International Journal of Earth Sciences*, 98(7), pp.1655–1675.
- Alt, J.C., 1994. A sulfur isotopic profile through the Troodos ophiolite, Cyprus: primary composition and the effects of seawater hydrothermal alteration. *Geochimica et cosmochimica acta*, 58(7), pp.1825–1840.
- Alt, J.C., Shanks, W.C. & Jackson, M.C., 1993. Cycling of sulfur in subduction zones: The geochemistry of sulfur in the Mariana Island Arc and back-arc trough. *Earth and Planetary Science Letters*, 119(4), pp.477–494.
- Altunkaynak, Ş., 2007. Collision-driven slab breakoff magmatism in northwestern Anatolia, Turkey. *The Journal of geology*, 115(1), pp.63–82.
- Altunkaynak, Ş. & Dilek, Y., 2006. Timing and nature of postcollisional volcanism in western Anatolia and geodynamic implications. *Geological Society of America Special Papers*, 409, pp.321–351.
- Anderko, a & Pitzer, K.S., 1993. Phase-Equilibria and Volumetric Properties of the Systems KCl–H<sub>2</sub>O and NaCl–KCl–H<sub>2</sub>O above 573-K - Equation of State Representation. *Geochimica et Cosmochimica Acta*, 57(20), pp.4885–4897.
- Anderson, C.S., 2014. Bismuth. *USGS Minerals Yearbook*.
- Anderson, C.S., 2016a. Bismuth. *USGS Mineral Commodity Summaries*.
- Anderson, C.S., 2016b. Tellurium. *USGS Mineral Commodity Summaries*.
- Annen, C., Blundy, J.D. & Sparks, R.S.J., 2006. The genesis of intermediate and silicic magmas in deep crustal hot zones. *Journal of Petrology*, 47(3), pp.505–539.
- Arslan, M., Temizel, I., Abdioğlu, E., Kolaylı, H., Yücel, C., Boztuğ, D. & Şen, C., 2013. <sup>40</sup>Ar–<sup>39</sup>Ar dating, whole-rock and Sr–Nd–Pb isotope geochemistry of post-collisional Eocene volcanic

## List of References

- rocks in the southern part of the Eastern Pontides (NE Turkey): implications for magma evolution in extension-induced origin. *Contributions to Mineralogy and Petrology*, 166(1), pp.113–142.
- Ataman, G., 1972. L'âge radiométrique du massif granodioritique d'Orhaneli. *Bulletin of the Geological Society of Turkey*, 15, pp.125–130.
- Audétat, A. & Günther, D., 1999. Mobility and H<sub>2</sub>O loss from fluid inclusions in natural quartz crystals. *Contributions to Mineralogy and Petrology*, 137(1–2), pp.1–14.
- Audétat, A., Günther, D., Heinrich, C. & Audétat, a., 1998. Formation of a Magmatic-Hydrothermal Ore Deposit: Insights with LA-ICP-MS Analysis of Fluid Inclusions. *Science*, 279(5359), pp.2091–2094.
- Audétat, A., Pettke, T., Heinrich, C.A. & Bodnar, R.J., 2008. Special paper: the composition of magmatic-hydrothermal fluids in barren and mineralized intrusions. *Economic Geology*, 103(5), pp.877–908.
- Augé, T., Bailly, L., Cocherie, A., Genna, A., Guerrot, C., Lerouge, C., Mukherjee, M.M. & Patra, R.N., 2002. Magmatic and hydrothermal Platinum-group element mineralization in the Baula area, Orissa, India. In *Proceedings of the 9th International Platinum Symposium, Billings, Montana, USA*. pp. 21–24.
- Auge, T., Petrunov, R. & Bailly, L., 2005. On the origin of the PGE mineralization in the elatsite porphyry Cu-Au deposit, Bulgaria: Comparison with the baula-nuasahi complex, India, and other alkaline PGE-rich porphyries. *Canadian Mineralogist*, 43(4), pp.1355–1372.
- Bakker, R.J., 2014. Comment on “Effect of the vapor phase on the salinity of halite-bearing aqueous fluid inclusions estimated from the halite dissolution temperature”, by M. Steele-MacInnis and R.J. Bodnar. *Geochimica et Cosmochimica Acta*, 135, pp.350–353.
- Bakker, R.J., 2012. Package FLUIDS. part 4: Thermodynamic modelling and purely empirical equations for H<sub>2</sub>O-NaCl-KCl solutions. *Mineralogy and Petrology*, 105, pp.1–29.
- Bakker, R.J., 2003. Package FLUIDS 1. Computer programs for analysis of fluid inclusion data and for modelling bulk fluid properties. *Chemical Geology*, 194(1–3), pp.3–23.
- Barnes, S.J. & Liu, W., 2012. Pt and Pd mobility in hydrothermal fluids: evidence from komatiites and from thermodynamic modelling. *Ore Geology Reviews*, 44, pp.49–58.
- Barrie, C.T., 1993. Petrochemistry of shoshonitic rocks associated with porphyry copper-gold



- deposits of central Quesnellia , British Columbia , Canada. , 48, pp.225–258.
- Bauer, D., Diamond, D., Li, J., Sandalow, D., Telleen, P. & Wanneret, B., 2010. Critical Materials Strategy, US Department of Energy.
- Bazarkina, E.F., Pokrovski, G.S. & Hazemann, J.-L., 2014. Structure, stability and geochemical role of palladium chloride complexes in hydrothermal fluids. *Geochimica et Cosmochimica Acta*, 146, pp.107–131.
- Becker, H. & Dale, C.W., 2016. Re–Pt–Os Isotopic and Highly Siderophile Element Behavior in Oceanic and Continental Mantle Tectonites. *Reviews in Mineralogy and Geochemistry*, 81(1), pp.369–440.
- Becker, S.P., Fall, A. & Bodnar, R.J., 2008. Synthetic fluid inclusions. XVII. PVTX properties of high salinity H<sub>2</sub>O–NaCl solutions (>30 wt % NaCl): Application to fluid inclusions that homogenize by halite disappearance from porphyry copper and other hydrothermal ore deposits. *Economic Geology*, 103(3), pp.539–554.
- Bell, A.S., Simon, A. & Guillong, M., 2011. Gold solubility in oxidized and reduced, water-saturated mafic melt. *Geochimica et Cosmochimica Acta*, 75(7), pp.1718–1732.
- Bernard, A., Symonds, R.B. & Rose, W.I., 1990. Volatile transport and deposition of Mo, W and Re in high temperature magmatic fluids. *Applied Geochemistry*, 5(3), pp.317–326.
- Berzina, A.N., Sotnikov, V.I., Economou-Eliopoulos, M. & Eliopoulos, D.G., 2005. Distribution of rhenium in molybdenite from porphyry Cu–Mo and Mo–Cu deposits of Russia (Siberia) and Mongolia. *Ore Geology Reviews*, 26(1–2), pp.91–113.
- Bingöl, E., Delaloye, M. & Ataman, G., 1982. Granitic intrusions in western Anatolia: a contribution to the geodynamic study of this area. *Eclogae Geologicae Helveticae*, 75(2), pp.437–446.
- Bissig, T. & Cooke, D., 2014. Introduction to the Special Issue Devoted to Alkalic Porphyry Cu–Au and Epithermal Au Deposits. *Economic Geology*, 109(3), pp.819–825.
- Blundy, J., Cashman, K. V., Rust, A. & Witham, F., 2010. A case for CO<sub>2</sub>-rich arc magmas. *Earth and Planetary Science Letters*, 290(3–4), pp.289–301.
- Blundy, J., Mavrogenes, J., Tattitch, B., Sparks, S. & Gilmer, A., 2015. Generation of porphyry copper deposits by gas-brine reaction in volcanic arcs. *Nature Geoscience*, 8(3), pp.235–240.
- Bodnar, R.J., 2003a. Introduction to aqueous-electrolyte fluid inclusions. *Fluid Inclusions: Analysis and Interpretation*, 32, pp.81–100.

## List of References

- Bodnar, R.J., 2003b. Introduction to fluid inclusions. *Fluid inclusions: analysis and interpretation*, pp.1–8.
- Bodnar, R.J., 1994. Synthetic fluid inclusions: XII. The system H<sub>2</sub>O-NaCl. Experimental determination of the halite liquidus and isochores for a 40 wt% NaCl solution. *Geochimica et Cosmochimica Acta*, 58(3), pp.1053–1063.
- Bodnar, R.J. & Beane, R.E., 1980. Temporal and spatial variations in hydrothermal fluid characteristics during vein filling in preore cover overlying deeply buried porphyry copper-type mineralization at Red Mountain, Arizona. *Economic Geology*, 75(6), p.876 LP-893.
- Bogdanov, K., Filipov, A. & Kehayov, R., 2005. Au-Ag-Te-Se minerals in the Elatsite porphyry-copper deposit, Bulgaria. *Geochemistry, mineralogy and petrology*, (September), pp.14–19.
- Bowman, J.R., Parry, W.T., Kropp, W.P. & Kruer, S.A., 1987. Chemical and isotopic evolution of hydrothermal solutions at Bingham, Utah. *Economic Geology*, 82(2), pp.395–428.
- Boztug, D. & Arehart, G.B., 2007. Oxygen and sulfur isotope geochemistry revealing a significant crustal signature in the genesis of the post-collisional granitoids in central Anatolia, Turkey. *Journal of Asian Earth Sciences*, 30(2), pp.403–416.
- Boztuğ, D., Erçin, A.İ., Kuruçelik, M.K., Göç, D., Kömür, İ. & İskenderoğlu, A., 2006. Geochemical characteristics of the composite Kaçkar batholith generated in a Neo-Tethyan convergence system, Eastern Pontides, Turkey. *Journal of Asian Earth Sciences*, 27(3), pp.286–302.
- Boztuğ, D. & Harlavan, Y., 2008. K–Ar ages of granitoids unravel the stages of Neo-Tethyan convergence in the eastern Pontides and central Anatolia, Turkey. *International Journal of Earth Sciences*, 97(3), pp.585–599.
- British Geological Survey, 2014. Minerals profile: Platinum. *Minerals profiles*, pp.1–32.
- Brun, J.P. & Sokoutis, D., 2010. 45 m.y. of Aegean crust and mantle flow driven by trench retreat. *Geology*, 38(9), pp.815–818.
- Brun, J.P. & Sokoutis, D., 2007. Kinematics of the Southern Rhodope Core Complex (North Greece). *International Journal of Earth Sciences*, 96(6), pp.1079–1099.
- Buchert, M., Schüler, D. & Bleher, D., 2009. Critical Metals for Future Sustainable Technologies and their Recycling Potential. *United Nations Environmental Program*, p.107.
- Buijs, B. & Sievers, H., 2011. Resource Security Risks in Perspective Complexity and Nuance. *Polinares working paper*, 33(November), pp.1–42.

- Buijs, B., Sievers, H. & Tercero Espinoza, L., 2012. Limits to critical raw materials approach. *Waste and Resource Management*, 165, pp.201–208.
- Burgisser, A. & Scaillet, B., 2007. Redox evolution of a degassing magma rising to the surface. *Nature*, 445(January), pp.194–197.
- Burke, E.A.J., 2001. Raman microspectrometry of fluid inclusions. *Lithos*, 55(1), pp.139–158.
- Cabri, L.J., 1965. Phase relations in the Au-Ag-Te system and their mineralogical significance. *Economic Geology*, 60, pp.1569–1606.
- Cabri, L.J., 1981. *Platinum-group elements: mineralogy, geology, recovery*, Published for the Geology division of CIM by the Canadian Institute of Mining and Metallurgy.
- Cabri, L.J., 2002. The platinum-group minerals. *The geology, geochemistry, mineralogy and mineral beneficiation of platinum-group elements*, 54, pp.13–129.
- Cabri, L.J. & Harris, D.C., 1973. Michenerite (PdBiTe) redefined and froodite (PdBi<sub>2</sub>) confirmed from the Sudbury area. *The Canadian Mineralogist*, 11(5), pp.903–912.
- Campbell, I.H. & Naldrett, A.J., 1979. The influence of silicate: sulfide ratios on the geochemistry of magmatic sulfides. *Economic Geology*, 74(6), pp.1503–1506.
- Candela, P.A. & Holland, H.D., 1986. A mass transfer model for copper and molybdenum in magmatic hydrothermal systems: the origin of porphyry-type ore deposits. *Economic Geology*, 81(1), pp.1–19.
- Carrette, L., Friedrich, K.A. & Stimming, U., 2001. Fuel cells—fundamentals and applications. *Fuel cells*, 1(1), pp.5–39.
- Chakhmouradian, A.R., Smith, M.P. & Kynicky, J., 2015. From “strategic” tungsten to “green” neodymium: A century of critical metals at a glance. *Ore Geology Reviews*, 64(1), pp.455–458.
- Chaussidon, M., Albarède, F. & Sheppard, S.M.F., 1989. Sulphur isotope variations in the mantle from ion microprobe analyses of micro-sulphide inclusions. *Earth and Planetary Science Letters*, 92(2), pp.144–156.
- Chen, J., Xu, J., Wang, B., Yang, Z., Ren, J., Yu, H., Liu, H. & Feng, Y., 2015. Geochemical differences between subduction-and collision-related copper-bearing porphyries and implications for metallogenesis. *Ore Geology Reviews*, 70, pp.424–437.

## List of References

- Chen, W., Wang, Y. & Weishi, C., 2015. Density calculation for NaCl-H<sub>2</sub>O solutions in the liquid-solid two-phase field in NaCl-H<sub>2</sub>O three-phase inclusions. *Acta Geologica Sinica*, 89, pp.911–917.
- Chi, G.X. & Lu, H.Z., 2008. Validation and representation of fluid inclusion microthermometric data using the fluid inclusion assemblage (FIA) concept. *Acta Petrologica Sinica*, 25, pp.1945–1953.
- Chou, I.M., Sterner, S.M. & Pitzer, K.S., 1992. Phase relations in the system NaCl-KCl-H<sub>2</sub>O: IV. Differential thermal analysis of the sylvite liquidus in the KCl-H<sub>2</sub>O binary, the liquidus in the NaCl-KCl-H<sub>2</sub>O ternary, and the solidus in the NaCl-KCl binary to 2 kb pressure, and a summary of experimental d. *Geochimica et Cosmochimica Acta*, 56(6), pp.2281–2293.
- Christopher, T., Edmonds, M., Humphreys, M.C.S. & Herd, R.A., 2010. Volcanic gas emissions from Soufrière Hills Volcano, Montserrat 1995-2009, with implications for mafic magma supply and degassing. *Geophysical Research Letters*, 37(3), pp.1–5.
- Ciobanu, C.L. & Cook, N.J., 2002. Tellurides, selenides (and Bi-sulphosalts) in gold deposits. In *11th Quadrennial IAGOD symposium—Geocongress 2002, Windhoek, Namibia, July 2002. CD Volume of extended abstracts*.
- Ciobanu, C.L., Cook, N.J., Kelson, C.R., Guerin, R., Kalleske, N. & Danyushevsky, L., 2013. Trace element heterogeneity in molybdenite fingerprints stages of mineralization. *Chemical Geology*, 347, pp.175–189.
- Ciobanu, C.L., Cook, N.J. & Pring, A., 2005. Bismuth tellurides as gold scavengers. In *Mineral Deposit Research: Meeting the Global Challenge*. Springer, pp. 1383–1386.
- Clark, A.H. & Ullrich, T.D., 2004. <sup>40</sup>Ar-<sup>39</sup>Ar age data for andesitic magmatism and hydrothermal activity in the Timok Massif, eastern Serbia: implications for metallogenetic relationships in the Bor copper-gold subprovince. *Mineralium Deposita*, 39(2), pp.256–262.
- Claypool, G.E., Holser, W.T., Kaplan, I.R., Sakai, H. & Zak, I., 1980. The age curves of sulfur and oxygen isotopes in marine sulfate and their mutual interpretation. *Chemical Geology*, 28, pp.199–260.
- Clayton, R.N., O'Neil, J.R. & Mayeda, T.K., 1972. Oxygen isotope exchange between quartz and water. *Journal of Geophysical Research*, 77(17), pp.3057–3067.
- Cline, J.S. & Bodnar, R.J., 1994. Direct evolution of brine from a crystallizing silicic melt at the Questa, New Mexico, molybdenum deposit. *Economic Geology*, 89(8), pp.1780–1802.

- Cline, J.S., Bodnar, R.J., Schroeder, J. & Bodnar, R.J., 1991. Can Economic Porphyry Copper Mineralization be Generated by a Typical Calc-Alkaline Melt? *Journal of Geophysical Research*, 96(91), pp.8113–8126.
- Cloos, M., 2001. Bubbling Magma Chambers, Cupolas, and Porphyry Copper Deposits Bubbling Magma Chambers , Cupolas ,. *International Geology Review*, 43(4), pp.37–41.
- Cockerton, A.B.D. & Tomkins, A.G., 2012. Insights into the liquid bismuth collector model through analysis of the Bi-Au Stormont skarn prospect, Northwest Tasmania. *Economic Geology*, 107(4), pp.667–682.
- Cooke, D.R., Hollings, P. & Walshe, J.L., 2005. Giant porphyry deposits: Characteristics, distribution, and tectonic controls. *Economic Geology*, 100(5), pp.801–818.
- Core, D.P., Kesler, S.E. & Essene, E.J., 2006. Unusually Cu-rich magmas associated with giant porphyry copper deposits: Evidence from Bingham, Utah. *Geology*, 34(1), pp.41–44.
- Crerar, D.A. & Barnes, H.L., 1976. Ore solution chemistry; V, Solubilities of chalcopyrite and chalcocite assemblages in hydrothermal solution at 200 degrees to 350 degrees C. *Economic Geology*, 71(4), pp.772–794.
- Danyushevsky, L., Robinson, P., Gilbert, S., Norman, M., Large, R., McGoldrick, P. & Shelley, M., 2011. Routine quantitative multi-element analysis of sulphide minerals by laser ablation ICP-MS: Standard development and consideration of matrix effects. *Geochemistry: Exploration, Environment, Analysis*, 11(1), pp.51–60.
- Davidson, J.P., 1996. Deciphering mantle and crustal signatures in subduction zone magmatism. *Subduction top to bottom*, pp.251–262.
- Davies, J.H. & von Blanckenburg, F., 1995. Slab breakoff: a model of lithosphere detachment and its test in the magmatism and deformation of collisional orogens. *Earth and Planetary Science Letters*, 129(1), pp.85–102.
- Delaloye, M. & Bingol, E., 2000. Granitoids from western and northwestern Anatolia: geochemistry and modeling of geodynamic evolution. *International Geology Review*, 42(3), pp.241–268.
- Delibaş, O., Moritz, R., Ulianov, A., Chiaradia, M., Saraç, C., Revan, K.M. & Göç, D., 2016. Cretaceous subduction-related magmatism and associated porphyry-type Cu-Mo prospects in the Eastern Pontides, Turkey: New constraints from geochronology and geochemistry. *Lithos*, 248–251, pp.119–137.

## List of References

- Dixon, J.E. & Dimitriadis, S., 1984. Metamorphosed ophiolitic rocks from the Serbo-Macedonian Massif, near Lake Volvi, North-east Greece. *Geological Society, London, Special Publications*, 17(1), pp.603–618.
- DoD, U.S., 2013. Strategic and critical materials 2013 report on stockpile requirements. *Office of the Under Secretary of Defense, US Department of Defense* (189 pp.).
- Dokuz, A., Karsli, O., Chen, B. & Uysal, İ., 2010. Sources and petrogenesis of Jurassic granitoids in the Yusufeli area, Northeastern Turkey: Implications for pre-and post-collisional lithospheric thinning of the eastern Pontides. *Tectonophysics*, 480(1), pp.259–279.
- Douglas, N., 2000. The liquid bismuth collector model: an alternative gold deposition mechanism. In *Geological Society of Australia Abstracts*. Geological Society of Australia; 1999, p. p-135.
- Dreyer, B.M., Morris, J.D. & Gill, J.B., 2010. Incorporation of subducted slab-derived sediment and fluid in arc magmas: B–Be–10Be– $\epsilon$ Nd systematics of the Kurile convergent margin, Russia. *Journal of Petrology*, 51(8), pp.1761–1782.
- Eastoe, C.J., 1982. Physics and chemistry of the hydrothermal system at the Panguna porphyry copper deposit, Bougainville, Papua New Guinea. *Economic Geology*, 77(1), pp.127–153.
- Eastoe, C.J., 1983. Sulfur isotope data and the nature of the hydrothermal systems at the Panguna and Frieda porphyry copper deposits, Papua New Guinea. *Economic Geology*, 78(2), pp.201–213.
- Economou-Eliopoulos, M., 2005. Exploration for Deposits of Platinum-Group Elements. *Mineralogical Association of Canada Short Course 35*, 35(August), pp.203–246.
- Economou-Eliopoulos, M., 2010. Platinum-group elements(PGE)in various geotectonic settings: Opportunities and risks. *Hellenic Journal of Geosciences*, vol. 45, 45, pp.65–82.
- Economou-Eliopoulos, M. & Eliopoulos, D.G., 2000. Palladium, platinum and gold concentration in porphyry copper systems of Greece and their genetic significance. *Ore Geology Reviews*, 16(1–2), pp.59–70.
- Edmonds, M., 2008. New geochemical insights into volcanic degassing. *Philosophical Transactions of the Royal Society A: Mathematical, Physical and Engineering Sciences*, 366(1885), pp.4559–4579.
- Einaudi, M.T., Hedenquist, J.W. & Inan, E.E., 2003. Porphyry to Epithermal Environments. In S. F. Simmons, ed. *Society of Economic Geologists and Geochemical Society Special Publication*

10. pp. 1–50.

- Eldorado Gold Corp, 2015. Eldorado Gold Corporation - Assets - Resources and Reserves. Available at: <http://www.eldoradogold.com/assets/resources-and-reserves/default.aspx> [Accessed August 31, 2016].
- Eliopoulos, D., Economou-Eliopoulos, M. & Zelyaskova-Panayiotova, M., 2014. Critical Factors Controlling Pd and Pt Potential in Porphyry Cu–Au Deposits: Evidence from the Balkan Peninsula. *Geosciences*, 4(1), pp.31–49.
- Eliopoulos, D.G. & Economou-Eliopoulos, M., 1991. Platinum-group element and gold contents in the Skouries porphyry copper deposit, Chalkidiki Peninsula, northern Greece. *Economic Geology*, 86(4), pp.740–749.
- Erwood, R.J., Kesler, S.E. & Cloke, P.L., 1979. Compositionally distinct, saline hydrothermal solutions, Naica mine, Chihuahua, Mexico. *Economic Geology*, 74(1), pp.95–108.
- Espurt, N., Hippolyte, J.-C., Kaymakci, N. & Sangu, E., 2014. Lithospheric structural control on inversion of the southern margin of the Black Sea Basin, Central Pontides, Turkey. *Lithosphere*, 6(1), pp.26–34.
- European Commission, 2014. Communication from the Commission: On the review of the list of critical raw materials for the EU and the implementation of the Raw Materials Initiative. , p.COM(2014) 297 final.
- European Commission, 2010. Critical raw materials for the EU, Report of the Ad-hoc Working Group on defining critical raw materials. *Eucom*, 39(July), pp.1–84.
- Eyuboglu, Y., Chung, S.-L., Santosh, M., Dudas, F.O. & Akaryalı, E., 2011. Transition from shoshonitic to adakitic magmatism in the eastern Pontides, NE Turkey: Implications for slab window melting. *Gondwana Research*, 19(2), pp.413–429.
- Fallick, A.E., McConville, P., Boyce, A.J., Burgess, R. & Kelley, S.P., 1992. Laser microprobe stable isotope measurements on geological materials: Some experimental considerations (with special reference to  $\delta^{34}\text{S}$  in sulphides). *Chemical Geology: Isotope Geoscience Section*, 101(1–2), pp.53–61.
- Farmer, G.L. & Depaolo, D.J., 1984. Origin of Mesozoic and Tertiary granite in the western United States and implications for Pre-Mesozoic crustal structure: 2. Nd and Sr isotopic studies of unmineralized and Cu-and Mo-mineralized granite in the Precambrian Craton. *Journal of Geophysical Research: Solid Earth*, 89(B12), pp.10141–10160.

## List of References

- Fleet, M.E. & Wu, T.-W., 1993. Volatile transport of platinum-group elements in sulfide-chloride assemblages at 1000 C. *Geochimica et Cosmochimica Acta*, 57(15), pp.3519–3531.
- Fleet, M.E. & Wu, T.-W., 1995. Volatile transport of precious metals at 1000 C: Speciation, fractionation, and effect of base-metal sulfide. *Geochimica et Cosmochimica Acta*, 59(3), pp.487–495.
- Fleischer, M., 1959. The geochemistry of rhenium, with special reference to its occurrence in molybdenite. *Economic geology*, 54(8), pp.1406–1413.
- Fonseca, R., Mallmann, G., St.C.O'Neill, H. & Campbell, I.H., 2007. How chalcophile is rhenium? An experimental study of the solubility of Re in sulphide mattes. *Earth and Planetary Science Letters*, 260(3–4), pp.537–548.
- Ford, J.H. & Green, D.C., 1977. An oxygen-and hydrogen-isotope study of the Panguna porphyry-copper deposit, Bougainville. *Journal of the Geological Society of Australia*, 24(1–2), pp.63–80.
- Fornadel, A.P., Voudouris, P.C., Spry, P.G. & Melfos, V., 2012. Mineralogical, stable isotope, and fluid inclusion studies of spatially related porphyry Cu and epithermal Au-Te mineralization, Fakos Peninsula, Limnos Island, Greece. *Mineralogy and Petrology*, 105(1–2), pp.85–111.
- Forward, P., Smith, D.J.F., Eng, C. & Francis, A., 2011. *Skouries Cu / Au Project , Greece NI 43-101 Technical Report*,
- Fournier, R.O., 1999. Hydrothermal processes related to movement of fluid from plastic into brittle rock in the magmatic-epithermal environment. *Economic Geology*, 94(8), pp.1193–1211.
- Frei, R., 1995. Evolution of Mineralizing Fluid in the Porphyry Copper System of the Skouries Deposit, Northeast Chalkidiki (Greece): Evidence from Combined Pb-Sr and Stable Isotope Data. *Economic Geology*, 90, pp.746–762.
- Frei, R., 1992. *Isotope (Pb, Rb-Sr, S, O, C, U-Pb) geochemical investigations on Tertiary intrusives and related mineralizations in the Serbomacedonian Pb-Zn, Sb+Cu-Mo metallogenic province in Northern Greece*. Swiss Federal Institute of Technology (ETH), Zurich.
- Friedman, I., 1953. Deuterium content of natural waters and other substances. *Geochimica et Cosmochimica Acta*, 4(1), pp.89–103.
- Fron del, J.W. & Wickman, F.E., 1970. Molybdenite polytypes in theory and occurrence. II. Some



- naturally-occurring polytypes of molybdenite. *American Mineralogist*, 55, pp.1857–1875.
- Fuentevilla, D.A., Sengers, J. V & Anisimov, M.A., 2012. Critical locus of aqueous solutions of sodium chloride revisited. *International Journal of Thermophysics*, pp.1–16.
- Fulginiti, P. & Sbrana, A., 1998. Presence of native gold and tellurium in the active high-sulfidation hydrothermal system of the La Fossa volcano (Vulcano, Italy). *Journal of Volcanology and Geothermal Research*, 86(1), pp.187–198.
- Fyfe, W.S., 1992. Magma underplating of continental crust. *Journal of Volcanology and Geothermal Research*, 50(1–2), pp.33–40.
- Gerhardt, N.I., Palant, A.A., Petrova, V.A. & Tagirov, R.K., 2001. Solvent extraction of molybdenum (VI), tungsten (VI) and rhenium (VII) by diisododecylamine from leach liquors. *Hydrometallurgy*, 60(1), pp.1–5.
- Glazner, A.F., Bartley, J.M., Coleman, D.S., Gray, W. & Taylor, R.Z., 2004. Are plutons assembled over millions of years by amalgamation from small magma chambers? *GSA today*, 14(4/5), pp.4–12.
- Gloeckler, M., Sankin, I. & Zhao, Z., 2013. CdTe solar cells at the threshold to 20% efficiency. *IEEE Journal of Photovoltaics*, 3(4), pp.1389–1393.
- Golden, J., McMillan, M., Downs, R.T., Hystad, G., Goldstein, I., Stein, H.J., Zimmerman, A., Sverjensky, D.A., Armstrong, J.T. & Hazen, R.M., 2013. Rhenium variations in molybdenite (MoS<sub>2</sub>): Evidence for progressive subsurface oxidation. *Earth and Planetary Science Letters*, 366, pp.1–5.
- Goldfarb, R., 2015. Tellurium —The Bright Future of Solar Energy. *USGS Science for a changing world 2014-3077*, pp.1–2.
- Grabezhev, A.I. & Voudouris, P.C., 2014. Rhenium distribution in molybdenite from the Vosnesensk porphyry Cu ± (Mo,Au) deposit (Southern Urals, Russia). *Canadian Mineralogist*, 52(4), pp.671–686.
- Grabezhev, a. I., 2007. Rhenium in ores of porphyry copper deposits in the Urals. *Doklady Earth Sciences*, 413(1), pp.265–268.
- Graedel, T.E., Barr, R., Chandler, C., Chase, T., Choi, J., Christoffersen, L., Friedlander, E., Henly, C., Jun, C. & Nassar, N.T., 2012. Methodology of metal criticality determination. *Environmental science & technology*, 46(2), pp.1063–1070.

## List of References

- Graedel, T.E., Gunn, G. & Tercero Espinoza, L., 2014. Metal resources, use and criticality. *Critical metals handbook*, pp.1–19.
- Green, M.A., Emery, K., Hishikawa, Y., Warta, W. & Dunlop, E.D., 2015. Solar cell efficiency tables (Version 45). *Progress in photovoltaics: research and applications*, 23(1), pp.1–9.
- Gruen, G., Weis, P., Driesner, T., Heinrich, C.A. & de Ronde, C.E.J., 2014. Hydrodynamic modeling of magmatic-hydrothermal activity at submarine arc volcanoes, with implications for ore formation. *Earth and Planetary Science Letters*, 404, pp.307–318.
- Grundler, P. V., Brugger, J., Etschmann, B.E., Helm, L., Liu, W., Spry, P.G., Tian, Y., Testemale, D. & Pring, A., 2013. Speciation of aqueous tellurium(IV) in hydrothermal solutions and vapors, and the role of oxidized tellurium species in Te transport and gold deposition. *Geochimica et Cosmochimica Acta*, 120, pp.298–325.
- Grundler, P. V, Brugger, J., Etschmann, B.E., Helm, L., Liu, W., Spry, P.G., Tian, Y., Testemale, D. & Pring, A., 2013. Speciation of aqueous tellurium (IV) in hydrothermal solutions and vapors, and the role of oxidized tellurium species in Te transport and gold deposition. *Geochimica et Cosmochimica Acta*, 120, pp.298–325.
- Gundlach, H., Kockel, F., Mollat, H., Walther, H.W., Antoniadis, P., Ioannidis, K. & Mitsaki, T., 1971. Prospektion auf Kupfer in Porphyritstocken der ostlichen Chalkidiki. *Bundesanstalt für Bodenforschung und IREY Hannover*, pp.1–46.
- Gunn, G., 2014a. *Critical metals handbook*, John Wiley & Sons.
- Gunn, G., 2014b. Platinum-group metals. *Critical Metals Handbook*, pp.284–311.
- Gustafson, L.B., 1978. Some major factors of porphyry copper genesis. *Economic Geology*, 73(5), pp.600–607.
- Hagelüken, C., 2014. Recycling of (critical) metals. *Critical metals handbook*, pp.41–69.
- Hahn, A., 2015. *Nature , timing and geodynamic context of polymetallic mineralisation in the Kassandra mining district , North Greece*. Kingston University.
- Hahn, A., Naden, J., Treloar, P.J., Kilias, S.P., Rankin, A.H. & Forward, P., 2012. A new time framefor the mineralisation in the Kassandra mine district , N Greece: deposit formation during metamorphic core complex exhumation. In *European Mineralogical Conference 2012*.
- Halter, W.E., Pettke, T. & Heinrich, C.A., 2002. The Origin of Cu / Au Ratios in Porphyry-Type Ore

- Deposits. *Science*, 296(1844), pp.2–5.
- Halter, W.E., Pettke, T. & Heinrich, C. a, 2002. The origin of Cu/Au ratios in porphyry-type ore deposits. *Science (New York, N.Y.)*, 296(5574), pp.1844–1846.
- Hamlyn, P.R., Keays, R.R., Cameron, W.E., Crawford, A.J. & Waldron, H.M., 1985. Precious metals in magnesian low-Ti lavas: implications for metallogenesis and sulfur saturation in primary magmas. *Geochimica et Cosmochimica Acta*, 49(8), pp.1797–1811.
- Hanley, J.J., Pettke, T., Mungall, J.E. & Spooner, E.T.C., 2005. The solubility of platinum and gold in NaCl brines at 1.5 kbar, 600 to 800°C: A laser ablation ICP-MS pilot study of synthetic fluid inclusions. *Geochimica et Cosmochimica Acta*, 69(10), pp.2593–2611.
- Harangi, S., Downes, H., Thirlwall, M. & Gm??ling, K., 2007. Geochemistry, petrogenesis and geodynamic relationships of miocene calc-alkaline volcanic rocks in the western Carpathian arc, Eastern Central Europe. *Journal of Petrology*, 48(12), pp.2261–2287.
- Harris, A.C., Cooke, D.R., Blackwell, J.L., Fox, N. & Orovan, E.A., 2013. Volcanotectonic setting of world-class alkalic porphyry and epithermal Au±Cu deposits of the southwest Pacific. In M. Colpron, T. Bissig, B. Rusk, & J. Thompson, eds. *Special publication no. 17: Tectonics, Metallogeny, and Discovery: The North American Cordillera and Similar Accretionary Settings*. Society of Economic Geologists, pp. 337–359.
- Harris, A.C., Kamenetsky, V.S., White, N.C., van Achterbergh, E. & Ryan, C.G., 2003. Melt inclusions in veins: linking magmas and porphyry Cu deposits. *Science*, 302(5653), pp.2109–2111.
- Harris, C.R., Pettke, T., Heinrich, C.A., Rosu, E., Woodland, S. & Fry, B., 2013. Tethyan mantle metasomatism creates subduction geochemical signatures in non-arc Cu–Au–Te mineralizing magmas, Apuseni Mountains (Romania). *Earth and Planetary Science Letters*, 366, pp.122–136.
- Harris, N.B.W., Pearce, J.A. & Tindle, A.G., 1986. Geochemical characteristics of collision-zone magmatism. *Geological Society, London, Special Publications*, 19(1), pp.67–81.
- Hattori, K.H. & Keith, J.D., 2001. Contribution of mafic melt to porphyry copper mineralization: Evidence from Mount Pinatubo, Philippines, and Bingham Canyon, Utah, USA. *Mineralium Deposita*, 36(8), pp.799–806.
- Hayes, S., Spry, P., Spaleta, K., Skidmore, A., Witte, R., Knight, N., Knight, D. & Milke, K., 2013. Mineralogy and chemistry of tellurium in the hypogene and supergene environments. , pp.1–39.

## List of References

- Hedenquist, J.W. & Henley, R.W., 1985. The Importance of CO<sub>2</sub> on Freezing Point Measurements of Fluid Inclusions: Evidence from Active Geothermal Systems and Implications for Epithermal Ore Deposition. *Economic Geology*, 80, pp.1379–1406.
- Hedenquist, J.W. & Lowenstern, J.B., 1994. The role of magmas in the formation of hydrothermal ore deposits. *Nature*, 370(6490), pp.519–527.
- Hedenquist, J.W. & Richards, J.P., 1998. The influence of geochemical techniques on the development of genetic models for porphyry copper deposits. *Reviews in Economic Geology*, 10(10), pp.235–256.
- Heinrich, C.A., Pettke, T., Halter, W.E., Aigner-Torres, M., Audétat, A., Günther, D., Hattendorf, B., Bleiner, D., Guillong, M. & Horn, I., 2003. Quantitative multi-element analysis of minerals, fluid and melt inclusions by laser-ablation inductively-coupled-plasma mass-spectrometry. *Geochimica et Cosmochimica Acta*, 67(18), pp.3473–3496.
- Heithersay, P.S. & Walshe, J.L., 1995. Endeavour 26 North; a porphyry copper-gold deposit in the Late Ordovician, shoshonitic Goonumbla volcanic complex, New South Wales, Australia. *Economic Geology*, 90(6), pp.1506–1532.
- Helmy, H.M., Ballhaus, C., Berndt, J., Bockrath, C. & Wohlgemuth-Ueberwasser, C., 2007. Formation of Pt, Pd and Ni tellurides: Experiments in sulfide-telluride systems. *Contributions to Mineralogy and Petrology*, 153(5), pp.577–591.
- Henley, R.W. & Berger, B.R., 2013. Nature's refineries - Metals and metalloids in arc volcanoes. *Earth-Science Reviews*, 125, pp.146–170.
- Henley, R.W. & McNabb, A., 1978. Magmatic vapor plumes and ground-water interaction in porphyry copper emplacement. *Economic Geology*, 73(1), pp.1–18.
- Herzberg, C.T., Fyfe, W.S. & Carr, M.J., 1983. Density constraints on the formation of the continental Moho and crust. *Contributions to Mineralogy and Petrology*, 84(1), pp.1–5.
- Hezarkhani, A. & Williams-Jones, A.E., 1998. Controls of alteration and mineralization in the Sungun porphyry copper deposit, Iran; evidence from fluid inclusions and stable isotopes. *Economic Geology*, 93(5), pp.651–670.
- Hildreth, W. & Moorbath, S., 1988. Crustal contributions to arc magmatism in the Andes of central Chile. *Contributions to mineralogy and petrology*, 98(4), pp.455–489.
- Hoffman, E. & Maclean, W.H., 1976. Phase relations of Michenerite and Merenskyite in the Pd-Bi-

- Te system. *Economic Geology*, 71, pp.1461–1468.
- Holliday, J.R., Wilson, A.J., Blevin, P.L., Tedder, I.J., Dunham, P.D. & Pfitzner, M., 2002. Porphyry gold-copper mineralisation in the Cadia district, Eastern Lachlan Fold Belt, New South Wales, and its relationship to shoshonitic magmatism. *Mineralium Deposita*, 37(1), pp.100–116.
- Holliday, J.R., Wilson, A.J., Blevin, P.L., Tedder, I.J., Dunham, P.D. & Pfitzner, M., 2002. Porphyry gold–copper mineralisation in the Cadia district, eastern Lachlan Fold Belt, New South Wales, and its relationship to shoshonitic magmatism. *Mineralium Deposita*, 37(1), pp.100–116.
- Holwell, D.A. & McDonald, I., 2010. A review of the behaviour of platinum group elements within natural magmatic sulfide ore systems. *Platinum Metals Review*, 54(1), pp.26–36.
- De Hoog, J.C.M., Mason, P.R.D. & van Bergen, M.J. m, 2001. Sulfur and chalcophile elements in subduction zones: constraints from a laser ablation ICP-MS study of melt inclusions from Galunggung Volcano, Indonesia. *Geochimica et Cosmochimica Acta*, 65(18), pp.3147–3164.
- Hou, Z.-Q., Gao, Y.-F., Qu, X.-M., Rui, Z.-Y. & Mo, X.-X., 2004. Origin of adakitic intrusives generated during mid-Miocene east–west extension in southern Tibet. *Earth and Planetary Science Letters*, 220(1), pp.139–155.
- Hou, Z., Zhang, H., Pan, X. & Yang, Z., 2011. Porphyry Cu (–Mo–Au) deposits related to melting of thickened mafic lower crust: Examples from the eastern Tethyan metallogenic domain. *Ore Geology Reviews*, 39(1–2), pp.21–45.
- Huppert, H.E. & Sparks, R.S.J., 1988. The generation of granitic magmas by intrusion of basalt into continental crust. *Journal of Petrology*, 29(3), pp.599–624.
- Imai, N., Terashima, S., Itoh, S. & And, A., 1995. 1994 Compilation of Analytical Data for Minor and Trace Elements in Seventeen Reference “ Igneous Series .” *Geostandards Newsletter*, 19(2), pp.135–213.
- Ishihara, S., 2008. On bismuth resources of Japan and world. *Shigen-Chishitsu*, 58(2), pp.131–138.
- Ishihara, S., 1981. The granitoid series and mineralization. *Econ. Geol. 75th Anniv. Vol.*, pp.458–484.
- Ito, K. & Kennedy, G.C., 1967. Melting and phase relations in a natural peridotite to 40 kilobars. *American Journal of Science*, 265(6), pp.519–538.
- Jaffe, R., Price, J., Ceder, G., Eggert, R., Graedel, T., Gschneidner, K., Hitzman, M., Houle, F., Hurd,

## List of References

- A., Kelley, R., King, A., Milliron, D., Skinner, B. & Slakey, F., 2011. Energy Critical Elements. *Materials Research Society*, 103(103), pp.1–28.
- Jankovic, S., 1977. *Metallogeny and Plate Tectonics in the North-eastern Mediterranean.*
- Jankovic, S., 1997. The Carpatho-Balkanides and adjacent area: a sector of the Tethyan Eurasian metallogenic belt. *Mineralium Deposita*, 32(5), pp.426–433.
- Jeffries, T.E., Jackson, S.E. & Longerich, H.P., 1998. Application of a frequency quintupled Nd: YAG source ( $\lambda = 213$  nm) for laser ablation inductively coupled plasma mass spectrometric analysis of minerals. *Journal of Analytical Atomic Spectrometry*, 13(9), pp.935–940.
- Jenkin, G.R.T., Al-Bassam, A.Z.M., Harris, R.C., Abbott, A.P., Smith, D.J., Holwell, D.A., Chapman, R.J. & Stanley, C.J., 2016. The application of deep eutectic solvent ionic liquids for environmentally-friendly dissolution and recovery of precious metals. *Minerals Engineering*, 87, pp.18–24.
- Jenner, F.E., O'Neill, H.S.C., Arculus, R.J. & Mavrogenes, J.A., 2010. The magnetite crisis in the evolution of arc-related magmas and the initial concentration of Au, Ag and Cu. *Journal of Petrology*, 51(12), pp.2445–2464.
- Jochum, K.P., Weis, U., Stoll, B., Kuzmin, D., Yang, Q., Raczek, I., Jacob, D.E., Stracke, A., Birbaum, K. & Frick, D.A., 2011. Determination of reference values for NIST SRM 610–617 glasses following ISO guidelines. *Geostandards and Geoanalytical Research*, 35(4), pp.397–429.
- John, D., 2015. Rhenium — A Rare Metal Critical to Modern Transportation. *USGS Mineral Resources Program*, pp.6–7.
- Kalogeropoulos, S.I., Kilias, S.P., Bitzios, D.C., Nicolaou, M. & Both, R.A., 1989. Genesis of the Olympias carbonate-hosted Pb-Zn(Au,Ag) sulfide ore deposit, eastern Chalkidiki Peninsula, northern Greece. *Economic Geology*, 84(5), pp.1210–1234.
- Kaygusuz, A., Siebel, W., Şen, C. & Satir, M., 2008. Petrochemistry and petrology of I-type granitoids in an arc setting: the composite Torul pluton, Eastern Pontides, NE Turkey. *International Journal of Earth Sciences*, 97(4), pp.739–764.
- Kaymakci, N., Özçelik, Y., White, S.H. & Van Dijk, P.M., 2009. Tectono-stratigraphy of the Çankırı Basin: late Cretaceous to early Miocene evolution of the Neotethyan suture zone in Turkey. *Geological Society, London, Special Publications*, 311(1), pp.67–106.
- Kehayov, R. & Bogdanov, K., 1987. The fluid chemical evolution of the Elatsite porphyry Cu-Au-

- PGE deposit , Bulgaria. *Petrology*, (August 2016), pp.1173–1176.
- Kehayov, R., Bogdanov, K., Fanger, L., Von Quadt, A., Pettke, T. & Heinrich, C.A., 2003. The fluid chemical evolution of the Elatsite porphyry Cu-Au-PGE deposit , Bulgaria. In D. Eliopoulos, ed. *Mineral Exploration and Sustainable Development: Proceedings of the Seventh Biennial SGA Meeting, Athens, Greece, 24-28 August 2003, Volume 2*. Rotterdam: Millpress, pp. 1173–1176.
- Kelly, W.C. & Rye, R.O., 1979. Geologic, fluid inclusion, and stable isotope studies of the tungsten deposits of Panasqueira, Portugal. *Economic Geology*, 74(8), pp.1721–1822.
- Khaligh, A. & Li, Z., 2010. Battery, ultracapacitor, fuel cell, and hybrid energy storage systems for electric, hybrid electric, fuel cell, and plug-in hybrid electric vehicles: State of the art. *IEEE transactions on Vehicular Technology*, 59(6), pp.2806–2814.
- Kopp, C., Fruehn, J., Flueh, E.R., Reichert, C., Kukowski, N., Bialas, J. & Klaeschen, D., 2000. Structure of the Makran subduction zone from wide-angle and reflection seismic data. *Tectonophysics*, 329(1), pp.171–191.
- Koptagel, O., Efe, A., Ulusoy, U. & Fallick, A.E., 1998. Sulfur-isotope study of the Ana Yatak massive sulfide deposit, southeastern Turkey. *International geology review*, 40(4), pp.363–374.
- Koptagel, O., Efe, A., Ulusoy, U. & Fallick, A.E., 1998. Sulfur-isotope study of the Ana Yatak massive sulfide deposit, southeastern Turkey. *International Geology Review*, 40(4), pp.363–374.
- Korzhinsky, M.A., Tkachenko, S.I., Shmulovich, K.I., Taran, Y.A. & Steinberg, G.S., 1994. Discovery of a pure rhenium mineral at Kudriav volcano.
- Kroll, T., Muller, D., Seifert, T., Herzig, P.M. & Schneider, A., 2002. Petrology and geochemistry of the shoshonite-hosted Skouries porphyry Cu-Au deposit, Chalkidiki, Greece. *Mineralium Deposita*, 37(1), pp.137–144.
- Kuscu, I., 2016. Magmatic evolution and metallogeny of Turkey. In *SEG conference 2016:Tethyan tectonics and metallogeny*.
- Landtwing, M.R., Furrer, C., Redmond, P.B., Pettke, T., Guillong, M. & Heinrich, C.A., 2010. The Bingham Canyon porphyry Cu-Mo-Au deposit. III. Zoned copper-gold ore deposition by magmatic vapor expansion. *Economic Geology*, 105(1), pp.91–118.
- Landtwing, M.R., Pettke, T., Halter, W.E., Heinrich, C.A., Redmond, P.B., Einaudi, M.T. & Kunze, K., 2005. Copper deposition during quartz dissolution by cooling magmatic-hydrothermal fluids:

## List of References

- The Bingham porphyry. *Earth and Planetary Science Letters*, 235(1–2), pp.229–243.
- Larocque, A.C.L., Stimac, J.A., Siebe, C., Greengrass, K., Chapman, R. & Mejia, S.R., 2008. Deposition of a high-sulfidation Au assemblage from a magmatic volatile phase, Volcán Popocatepetl, Mexico. *Journal of Volcanology and Geothermal Research*, 170(1), pp.51–60.
- Lecumberri-Sanchez, P., Steele-MacInnis, M. & Bodnar, R.J., 2012. A numerical model to estimate trapping conditions of fluid inclusions that homogenize by halite disappearance. *Geochimica et Cosmochimica Acta*, 92, pp.14–22.
- Lecumberri-Sanchez, P., Steele-MacInnis, M., Weis, P., Driesner, T. & Bodnar, R.J., 2015. Salt precipitation in magmatic-hydrothermal systems associated with upper crustal plutons. *Geology*, 43(12), pp.1063–1066.
- Lee, C.-T.A., Luffi, P., Chin, E.J., Bouchet, R., Dasgupta, R., Morton, D.M., Le Roux, V., Yin, Q.Q. & Jin, D., 2012. Copper systematics in arc magmas and implications for crust-mantle differentiation. *Science*, 336(6077), pp.64–68.
- Lee, C.-T., Luffi, P., Chin, E., Bouchet, R., Dasgupta, R., Morton, D., Le Roux, V., Yin, Q. & Jin, D., 2012. Copper systematics in arc magmas and implications for crust–mantle differentiation. *Science*, 336(April), pp.64–68.
- Lefebvre, C., Meijers, M.J.M., Kaymakci, N., Peynircioğlu, A., Langereis, C.G. & Van Hinsbergen, D.J.J., 2013. Reconstructing the geometry of central Anatolia during the late Cretaceous: Large-scale Cenozoic rotations and deformation between the Pontides and Taurides. *Earth and Planetary Science Letters*, 366, pp.83–98.
- Lesne, P., Kohn, S.C., Blundy, J., Witham, F., Botcharnikov, R.E. & Behrens, H., 2011. Experimental simulation of closed-system degassing in the system basalt-H<sub>2</sub>O-CO<sub>2</sub>-S-Cl. *Journal of Petrology*, 52(9), pp.1737–1762.
- Li, C., Van der Hilst, R.D., Meltzer, A.S. & Engdahl, E.R., 2008. Subduction of the Indian lithosphere beneath the Tibetan Plateau and Burma. *Earth and Planetary Science Letters*, 274(1), pp.157–168.
- Lickfold, V., Cooke, D.R., Crawford, a. J. & Fanning, C.M., 2007. Shoshonitic magmatism and the formation of the Northparkes porphyry Cu – Au deposits, New South Wales. *Australian Journal of Earth Sciences*, 54, pp.417–444.
- Loferski, P.J., 2016. Platinum-Group Metals. *USGS Mineral Commodity Summaries*.



- Lukac, M., 2010. Strike at Chile's largest copper mine to hit prices. *IBT Commodities Online*. Available at: <http://www.ibtimes.com/strike-chiles-largest-copper-mine-hit-prices-358019> [Accessed September 30, 2016].
- Maier, W.D., 1999. THE FRACTIONATION OF NI, CU AND THE NOBLE METALS IN SILICATE AND SULFIDE LIQUIDS. *Geological Association of Canada Short Course Notes*, 13, pp.69–106.
- Mao, J., Du, A., Seltmann, R. & Yu, J., 2003. Re–Os ages for the Shameika porphyry Mo deposit and the Lipovy Log rare metal pegmatite, central Urals, Russia. *Mineralium Deposita*, 38(2), pp.251–257.
- Mao, J., Wang, Y., Ding, T., Chen, Y., Wei, J. & Yin, J., 2002. Dashuigou tellurium deposit in Sichuan Province, China: S, C, O, and H isotope data and their implications on hydrothermal mineralization. *Resource Geology*, 52(1), pp.15–23.
- Markham, N.L., 1960. Synthetic and natural phases in the system Au-Ag-Te. *Economic Geology*, 55(6), pp.1148–1178.
- Matsuhisa, Y., Goldsmith, J.R. & Clayton, R.N., 1979. Oxygen isotopic fractionation in the system quartz-albite-anorthite-water. *Geochimica et Cosmochimica Acta*, 43(7), pp.1131–1140.
- Matzel, J.E.P., Bowring, S.A. & Miller, R.B., 2006. Time scales of pluton construction at differing crustal levels: Examples from the Mount Stuart and Tenpeak intrusions, North Cascades, Washington. *Geological Society of America Bulletin*, 118(11–12), pp.1412–1430.
- Maughan, D.T., Keith, J.D., Christiansen, E.H., Pulsipher, T., Hattori, K. & Evans, N.J., 2002. Contributions from mafic alkaline magmas to the Bingham porphyry Cu-Au-Mo deposit, Utah, USA. *Mineralium Deposita*, 37(1), pp.14–37.
- Mavrogenes, J., Henley, R.W., Reyes, A.G. & Berger, B., 2010. Sulfosalt melts: Evidence of high-temperature vapor transport of metals in the formation of high-sulfidation lode gold deposits. *Economic Geology*, 105(2), pp.257–262.
- May, T.W., Wiedmeyer, R.H., Chaudhary-webb, M., Paschal, D.C., Elliott, W.C., Hopkins, H.P., Ghazi, a M., Ting, B.C., Romieu, I., Vicente, O., Pelfort, E., Martinez, L., Olsina, R., Marchevsky, E., Chen, H.P., Miller, D.T. & Morrow, J.C., 1998. A table of polyatomic interferences in ICP-MS. *Atomic Spectroscopy*, 19(5), pp.150–155.
- McDonald, I., 1998. The Need for a Common Framework for Collection and Interpretation of Data in Platinum-Group Element Geochemistry. *Geostandards Newsletter*, 22(1), pp.85–91.

## List of References

- McInnes, B.I.A. & Cameron, E.M., 1994. Carbonated, alkaline hybridizing melts from a sub-arc environment: Mantle wedge samples from the Tabar-Lihir-Tanga-Feni arc, Papua New Guinea. *Earth and Planetary Science Letters*, 122(1–2), pp.125–141.
- McInnes, B.I.A., McBride, J.S., Evans, N.J., Lambert, D.D. & Andrew, A.S., 1999. Osmium isotope constraints on ore metal recycling in subduction zones. *Science*, 286(5439), pp.512–516.
- Mei, Y., Etschmann, B., Liu, W., Sherman, D.M., Barnes, S.J., Fiorentini, M.L., Seward, T.M., Testemale, D. & Brugger, J., 2015. Palladium complexation in chloride-and bisulfide-rich fluids: Insights from ab initio molecular dynamics simulations and X-ray absorption spectroscopy. *Geochimica et Cosmochimica Acta*, 161, pp.128–145.
- Michael, L., Loferski, Z. & Loferski, P., 2014. Platinum-Group elements: So many excellent properties. *USGS Mineral Resources Program*.
- Micko, J.M., Tosdal, R.M.T., Bissig, T.B., Chamberlain, C.M.C. & Simpson, K.A.S., 2014. Hydrothermal Alteration and Mineralization of the Galore Creek Alkaline Cu-Au Porphyry Deposit, Northwestern British Columbia, Canada. *Economic Geology*, pp.891–914.
- Millensifer, T., Sinclair, D., Jonasson, I. & Lipmann, A., 2014. Rhenium. *Critical Metals Handbook*, pp.340–360.
- Moretti, R., Arienzo, I., Civetta, L., Orsi, G. & Papale, P., 2013. Multiple magma degassing sources at an explosive volcano. *Earth and Planetary Science Letters*, 367, pp.95–104.
- Moritz, R., Rezeau, H., Ovtcharova, M., Tayan, R., Melkonyan, R., Hovakimyan, S., Ramazanov, V., Selby, D., Ulianov, A., Chiaradia, M. & Putlitz, B., 2016. Long-lived, stationary magmatism and pulsed porphyry systems during Tethyan subduction to post-collision evolution in the southernmost Lesser Caucasus, Armenia and Nakhichevan. *Gondwana Research*, 37, pp.465–503.
- Morris, D.F.C. & Short, E.L., 1969. Rhenium. *Handbook of Geochemistry*, 11(1).
- Moss, R.L., Tzimas, E., Kara, H., Willis, P. & Kooroshy, J., 2011. *Critical Metals in Strategic Energy Technologies*,
- Motelica-Heino, M., Rauch, S., Morrison, G.M. & Donard, O.F.X., 2001. Determination of palladium, platinum and rhodium concentrations in urban road sediments by laser ablation-ICP-MS. *Analytica Chimica Acta*, 436(2), pp.233–244.
- Mountain, B.W. & Wood, S.A., 1988. Chemical controls on the solubility, transport and deposition

- of platinum and palladium in hydrothermal solutions; a thermodynamic approach. *Economic Geology*, 83(3), pp.492–510.
- Mudd, G.M., Jowitt, S.M. & Werner, T.T., 2016. The world's by-product and critical metal resources part I: Uncertainties, current reporting practices, implications and grounds for optimism. *Ore Geology Reviews*.
- Müller, D. & Forrestal, P., 1998. The shoshonite porphyry Cu-Au association at Bajo de la Alumbrera, Catamarca Province, Argentina. *Mineralogy and Petrology*, 64(1), pp.47–64.
- Müller, D. & Groves, D.I., 1993. Direct and indirect associations between potassic igneous rocks, shoshonites and gold-copper deposits. *Ore Geology Reviews*, 8(5), pp.383–406.
- Mungall, J.E., 2002. Roasting the mantle: Slab melting and the genesis of major Au and Au-rich Cu deposits. *Geology*, 30(10), pp.915–918.
- Mutschler, F.E., Griffen, M.E., Stevens, D.S. & Shannon, S.S., 1985. Precious metal deposits related to alkaline rocks in the North American Cordillera; an interpretive review. *South African Journal of Geology*, 88(2), p.355 LP-377.
- Nadeau, O., Williams-Jones, A.E. & Stix, J., 2010. Sulphide magma as a source of metals in arc-related magmatic hydrothermal ore fluids. *Nature Geoscience*, 3(7), pp.501–505.
- Naldrett, A.J., 2010. Secular variation of magmatic sulfide deposits and their source magmas. *Economic Geology*, 105(3), pp.669–688.
- Nash, J.T., 1976. *Fluid-inclusion petrology-data from porphyry copper deposits and applications to exploration: a summary of new and published descriptions of fluid inclusions from 36 porphyry copper deposits and discussion of possible applications to exploration for copper*, US Govt. Print. Off.
- Naumov, A., 2007. Rhythms of rhenium. *Russian Journal of Non-Ferrous Metals*, 48(6), pp.418–423.
- Neubauer, W.H., 1957. Geologie der blei-zinkreichen Kieslagerstätten von Kassandra (Chalkidike, Griechenland). *Berg und Huttenmannische Monatshefte*, 102, pp.1–16.
- Newberry, R., 1979a. Polytypism in molybdenite (I): a non-equilibrium impurity-induced phenomenon. *American mineralogist*, 64(I), pp.758–767.
- Newberry, R., 1979b. Polytypism in molybdenite (II); Relationships between polytypism, ore deposition/alteration stages and rhenium contents. *American Mineralogist*, 64(II), pp.768–

## List of References

775.

Newton, R.C. & Manning, C.E., 2005. Solubility of anhydrite, CaSO<sub>4</sub>, in NaCl-H<sub>2</sub>O solutions at high pressures and temperatures: Applications to fluid-rock interaction. *Journal of Petrology*, 46(4), pp.701–716.

NRC Minerals, 2008. Critical minerals, and the US Economy.

Oeser, M., Strauss, H., Wolff, P.E., Koepke, J., Peters, M., Garbe-Schönberg, D. & Dietrich, M., 2012. A profile of multiple sulfur isotopes through the Oman ophiolite. *Chemical Geology*, 312–313, pp.27–46.

Oeser, M., Strauss, H., Wolff, P.E., Koepke, J., Peters, M., Garbe-Schönberg, D. & Dietrich, M., 2012. A profile of multiple sulfur isotopes through the Oman ophiolite. *Chemical Geology*, 312, pp.27–46.

Ohmoto, H., 1972. Systematics of sulfur and carbon isotopes in hydrothermal ore deposits. *Economic Geology*, 67(5), pp.551–578.

Okay, A.I., 2008. Geology of Turkey : A synopsis. *Anschnitt*, 21, pp.19–42.

Okay, A.I. & Tüysüz, O., 1999. Tethyan sutures of northern Turkey. *Geological Society, London, Special Publications*, 156(1), pp.475–515.

Ortoleva, P., Merino, E., Moore, C. & Chadam, J., 1987. Geochemical self-organization I: reaction-transport feedbacks and modeling approach. *American Journal of science*, 287(10), pp.979–1007.

Papadakis, A. & Michailidis, K., 1976. Hydrothermal Alteration and Porphyry copper type mineralization in the subvolcanic rocks of Eastern Chalkidiki (Greece). *Scientific Annals, Faculty of Physics and Mathematics, University of Thessaloniki*, 16, pp.451–473.

Paquette, J.-L., Ménot, R.-P., Pin, C. & Orsini, J.-B., 2003. Episodic and short-lived granitic pulses in a post-collisional setting: evidence from precise U–Pb zircon dating through a crustal cross-section in Corsica. *Chemical Geology*, 198(1), pp.1–20.

Park, J.-W., Campbell, I.H. & Kim, J., 2016. Abundances of platinum group elements in native sulfur condensates from the Niuatahi-Motutahi submarine volcano, Tonga rear arc: Implications for PGE mineralization in porphyry deposits. *Geochimica et Cosmochimica Acta*, 174, pp.236–246.

Pašava, J., Vymazalová, A., Košler, J., Koneev, R.I., Jukov, A. V. & Khalmatov, R.A., 2010. Platinum-

- group elements in ores from the Kalmakyr porphyry Cu-Au-Mo deposit, Uzbekistan: Bulk geochemical and laser ablation ICP-MS data. *Mineralium Deposita*, 45(5), pp.411–418.
- Pass, H.E., Cooke, D.R., Davidson, G., Maas, R., Dipple, G., Rees, C., Ferreira, L., Taylor, C. & Deyell, C.L., 2014. Isotope geochemistry of the Northeast zone, Mount Polley alkalic Cu-Au-Ag porphyry deposit, British Columbia: A case for carbonate assimilation. *Economic Geology*, 109(4), pp.859–890.
- Pasteris, J.D., Wopenka, B. & Seitz, J.C., 1988. Practical aspects of quantitative laser Raman microprobe spectroscopy for the study of fluid inclusions. *Geochimica et Cosmochimica Acta*, 52(5), pp.979–988.
- Patten, C., Barnes, S.J., Mathez, E.A. & Jenner, F.E., 2013. Partition coefficients of chalcophile elements between sulfide and silicate melts and the early crystallization history of sulfide liquid: LA-ICP-MS analysis of MORB sulfide droplets. *Chemical Geology*, 358, pp.170–188.
- Patrick, R.A.D., 1986. *A Practical Guide to Fluid Inclusion Studies*,
- Peacock, S.M., Rushmer, T. & Thompson, A.B., 1994. Partial melting of subducting oceanic crust. *Earth and planetary science letters*, 121(1), pp.227–244.
- Pearce, J.A., Lippard, S.J. & Roberts, S., 1984. Characteristics and tectonic significance of supra-subduction zone ophiolites. *Geological Society, London, Special Publications*, 16(1), pp.77–94.
- Perelló, J., Cox, D., Garamjav, D., Sanjdorj, S., Diakov, S., Schissel, D., Munkhbat, T.-O. & Oyun, G., 2001. Oyu Tolgoi, Mongolia: Siluro-Devonian porphyry Cu-Au-(Mo) and high-sulfidation Cu mineralization with a cretaceous chalcocite blanket. *Economic Geology*, 96(6), pp.1407–1428.
- Pettke, T., 2008. Analytical protocols for element concentration and isotope ratio measurements in fluid inclusions by LA-(MC)-ICP-MS. *Laser Ablation ICP-MS in the Earth Sciences: Current ...*, (October), pp.189–217.
- Pettke, T., Audétat, A., Schaltegger, U. & Heinrich, C.A., 2005. Magmatic-to-hydrothermal crystallization in the W-Sn mineralized Mole Granite (NSW, Australia). Part II: Evolving zircon and thorite trace element chemistry. *Chemical Geology*, 220(3–4), pp.191–213.
- Pettke, T., Oberli, F., Audétat, A., Guillong, M., Simon, A.C., Hanley, J.J. & Klemm, L.M., 2012. Recent developments in element concentration and isotope ratio analysis of individual fluid inclusions by laser ablation single and multiple collector ICP-MS. *Ore Geology Reviews*, 44,

## List of References

pp.10–38.

- Pettke, T., Oberli, F. & Heinrich, C.A., 2010. The magma and metal source of giant porphyry-type ore deposits, based on lead isotope microanalysis of individual fluid inclusions. *Earth and Planetary Science Letters*, 296(3), pp.267–277.
- Peucker-Ehrenbrink, B., Hanghoj, K., Atwood, T. & Kelemen, P.B., 2012. Rhenium-osmium isotope systematics and platinum group element concentrations in oceanic crust. *Geology*, 40(3), pp.199–202.
- Piercey, S.J., 2014. Modern Analytical Facilities 2. A review of quality assurance and quality control (QA/QC) procedures for lithogeochemical data. *Geoscience Canada*, 41(1), pp.75–88.
- Piestrzynski, A., 1994. Pd-minerals in the Santo Tomas II porphyry copper deposit, Tuba, Benguet, Philippines. *Mineral. Polonica*, 25, pp.21–31.
- Polyak, D.E., 2016. Rhenium. *USGS Mineral Commodity Summaries*.
- Polyak, D.E., 2015. Rhenium. *USGS Mineral Commodity Summaries*.
- Popov, P., Strashimirov, S. & Popov, K., 2003. Geology and metallogeny of the Srednogorie zone and Panagyurishte ore region. *Cretaceous porphyry–epithermal systems of the Srednogorie Zone, Bulgaria. SEG Guidebook Series*, 36, pp.7–27.
- Popov, V.S., 1988. The magmatic sources of the ore material of porphyry molybdenum and porphyry copper deposits. *International Geology Review*, 30(7), pp.772–781.
- Von Quadt, A., Peytcheva, I., Kamenov, B., Fanger, L., Heinrich, C.A. & Frank, M., 2002. The Elatsite porphyry copper deposit in the Panagyurishte ore district, Srednogorie zone, Bulgaria: U-Pb zircon geochronology and isotope-geochemical investigations of magmatism and ore genesis. *Geological Society, London, Special Publications*, 204(1), pp.119–135.
- Ravizza, G., Blusztajn, J. & Prichard, H.M., 2001. Re–Os systematics and platinum-group element distribution in metalliferous sediments from the Troodos ophiolite. *Earth and Planetary Science Letters*, 188(3), pp.369–381.
- Razique, A., Tosdal, R.M. & Creaser, R.A., 2014. Temporal evolution of the western porphyry Cu–Au systems at Reko Diq, Balochistan, western Pakistan. *Economic Geology*, 109(7), pp.2003–2021.
- Rezeau, H., Moritz, R., Wotzlaw, J., Tayan, R., Melkonyan, R., Ulianov, A., Selby, D., Abzac, F. & Stern, R.A., 2016. Temporal and genetic link between incremental pluton assembly and

- pulsed porphyry Cu-Mo formation in accretionary orogens. , 44(8), pp.627–630.
- Richards, J., 2016a. Tectonics and Metallogeny of the Tethyan Orogenic Belt: Preface. *SEG special publication*, (19), pp.v–vii.
- Richards, J., 2016b. Tethyan Tectonomagmatic Processes and Metallogeny. In *SEG-MJD 2016 Conference*.
- Richards, J.P., 2013. Giant ore deposits formed by optimal alignments and combinations of geological processes. *Nature Geoscience*, 6(11), pp.911–916.
- Richards, J.P., 2011. Magmatic to hydrothermal metal fluxes in convergent and collided margins. *Ore Geology Reviews*, 40(1), pp.1–26.
- Richards, J.P., 2014. Porphyry and Related Deposits in Subduction and Post-Subduction Settings. , 88, pp.535–537.
- Richards, J.P., 2009. Postsubduction porphyry Cu-Au and epithermal Au deposits: Products of remelting of subduction-modified lithosphere. *Geology*, 37(3), pp.247–250.
- Richards, J.P., 2015. Tectonic, magmatic, and metallogenic evolution of the Tethyan orogen: From subduction to collision. *Ore Geology Reviews*, 70, pp.323–345.
- Richards, J.P., 2003. Tectono-magmatic precursors for porphyry Cu-(Mo-Au) deposit formation. *Economic Geology*, 98(8), pp.1515–1533.
- Richards, J.P., Chappell, B.W. & McCulloch, M.T., 1990. Intraplate-type magmatism in a continent-island-arc collision zone: Porgera intrusive complex, Papua New Guinea. *Geology*, 18(10), pp.958–961.
- Richards, J.P., McCulloch, M.T., Chappell, B.W. & Kerrich, R., 1991. Sources of metals in the Porgera gold deposit, Papua New Guinea: evidence from alteration, isotope, and noble metal geochemistry. *Geochimica et Cosmochimica Acta*, 55(2), pp.565–580.
- Robertson, A.H.F., 2002. Overview of the genesis and emplacement of Mesozoic ophiolites in the Eastern Mediterranean Tethyan region. *Lithos*, 65(1), pp.1–67.
- Robertson, A.H.F., Parlak, O. & Ustaömer, T., 2009. Melange genesis and ophiolite emplacement related to subduction of the northern margin of the Tauride–Anatolide continent, central and western Turkey. *Geological Society, London, Special Publications*, 311(1), pp.9–66.
- Robinson, B.W. & Kusakabe, M., 1975. Quantitative preparation of sulfur dioxide, for sulfur-

## List of References

- 34/sulfur-32 analyses, from sulfides by combustion with cuprous oxide. *Analytical Chemistry*, 47(7), pp.1179–1181.
- Roedder, E., 1992. Optical microscopy identification of the phases in fluid inclusions in minerals. *Microscope*, 40, pp.59–79.
- Roedder, E. & Ribbe, P.H., 1984. *Fluid inclusions*, Mineralogical Society of America Washington, DC.
- Ronacher, E., Richards, J.P., Reed, M.H., Bray, C.J., Spooner, E.T.C. & Adams, P.D., 2004. Characteristics and evolution of the hydrothermal fluid in the North zone high-grade area, Porgera gold deposit, Papua New Guinea. *Economic Geology*, 99(5), pp.843–867.
- Rosu, E., Seghedi, I., Downes, H., Alderton, D., Szakacs, A., Pecskey, Z., Panaiotu, C., Panaiotu, C. & Nedelcu, L., 2005. Extension-related Miocene calc-alkaline magmatism in the Apuseni Mountains, Romania: Origin of magmas. *Schweizerische Mineralogische and Petrographische Mitteilungen*, 83, pp.153–172.
- Rusk, B.G., Reed, M.H., Dilles, J.H., Klemm, L.M. & Heinrich, C.A., 2004. Compositions of magmatic hydrothermal fluids determined by LA-ICP-MS of fluid inclusions from the porphyry copper-molybdenum deposit at Butte, MT. *Chemical Geology*, 210(1–4), pp.173–199.
- Sakıncı, M., Yaltırak, C. & Oktay, F.Y., 1999. Palaeogeographical evolution of the Thrace Neogene Basin and the Tethys–Paratethys relations at northwestern Turkey (Thrace). *Palaeogeography, Palaeoclimatology, Palaeoecology*, 153(1), pp.17–40.
- Sanematsu, K. & Ishihara, S., 2011.  $^{40}\text{Ar}/^{39}\text{Ar}$  ages of the Da Lien granite related to the Nui Phao W mineralization in Northern Vietnam. *Resource Geology*, 61(3), pp.304–310.
- Sarıfakioğlu, E., Dilek, Y. & Winchester, J.A., 2013. Late Cretaceous subduction initiation and Palaeocene–Eocene slab breakoff magmatism in South-Central Anatolia, Turkey. *International Geology Review*, 55(1), pp.66–87.
- Sarıfakioğlu, E., Özen, H., Çolakoğlu, A. & Sayak, H., 2010. Petrology, mineral chemistry, and tectonomagmatic evolution of Late Cretaceous suprasubduction-zone ophiolites in the İzmir–Ankara–Erzincan suture zone, Turkey. *International Geology Review*, 52(2–3), pp.187–222.
- Scailliet, B., 2010. Economic geology: Volatile destruction. *Nature Geoscience*, 3(7), pp.456–457.
- Schaltegger, U., Brack, P., Ovtcharova, M., Peytcheva, I., Schoene, B., Stracke, A., Marocchi, M. &



- Bargossi, G.M., 2009. Zircon and titanite recording 1.5 million years of magma accretion, crystallization and initial cooling in a composite pluton (southern Adamello batholith, northern Italy). *Earth and Planetary Science Letters*, 286(1), pp.208–218.
- Schönfeld, B., Huang, J.J. & Moss, S.C., 1983. Anisotropic mean-square displacements (MSD) in single-crystals of 2H-and 3R-MoS<sub>2</sub>. *Acta Crystallographica Section B: Structural Science*, 39(4), pp.404–407.
- Scrosati, B. & Garche, J., 2010. Lithium batteries: Status, prospects and future. *Journal of Power Sources*, 195(9), pp.2419–2430.
- Seedorff, E., Dilles, J.H., Proffett, J.M., Einaudi, M.T., Zurcher, L., Stavast, W.J.A., Johnson, D.A. & Barton, M.D., 2005. Porphyry deposits: Characteristics and origin of hypogene features. *Economic Geology 100th anniversary volume*, 29, pp.251–298.
- Şengör, A.M.C. & Atayman, S., 2009. The Permian Extinction and the Tethys: An Exercise in Global Geology. *Geological Society of America Special Papers*, 448, pp.1–85.
- Shafiei, B., 2010. Lead isotope signatures of the igneous rocks and porphyry copper deposits from the Kerman Cenozoic magmatic arc (SE Iran), and their magmatic-metallogenetic implications. *Ore Geology Reviews*, 38(1–2), pp.27–36.
- Shannon, R.D., 1981. Bond distances in sulfides and a preliminary table of sulfide crystal radii. *Structure and bonding in crystals*, 2, pp.53–70.
- Shen, A.H., Bassett, W.A. & I-Ming Chou, 1993. The ??-?? quartz transition at high temperatures and pressures in a diamond-anvil cell by laser interferometry. *American Mineralogist*, 78(7–8), pp.694–698.
- Shepherd, T.J., Rankin, A.H. & Alderton, D.H.M., 1985. *A practical guide to fluid inclusion studies*, Blackie.
- Sheppard, S.M.F., 1981. Stable isotope geochemistry of fluids. *Physics and Chemistry of the Earth*, 13(1), pp.419–445.
- Sheppard, S.M.F. & Gustafson, L.B., 1976. Oxygen and hydrogen isotopes in the porphyry copper deposit at El Salvador, Chile. *Economic Geology*, 71(8), pp.1549–1559.
- Sheppard, S.M.F., Nielsen, R.L. & Taylor, H.P., 1971. Hydrogen and oxygen isotope ratios in minerals from porphyry copper deposits. *Economic Geology*, 66(4), pp.515–542.
- Shinohara, H., 1994. Exsolution of immiscible vapor and liquid phases from a crystallizing silicate

## List of References

- melt: Implications for chlorine and metal transport. *Geochimica et Cosmochimica Acta*, 58(23), pp.5215–5221.
- Sillitoe, R.H., 2010. Porphyry copper systems. *Economic Geology*, 105(1), pp.3–41.
- Sillitoe, R.H., 1979. Some thoughts on gold-rich porphyry copper deposits. *Mineralium Deposita*, 14(2), pp.161–174.
- Sillitoe, R.H., 1973. The tops and bottoms of porphyry copper deposits. *Economic Geology*, 68(6), pp.799–815.
- Sillitoe, R.H. & Bonham, H.F., 1984. Volcanic landforms and ore deposits. *Economic Geology*, 79(6), pp.1286–1298.
- da Silva, T.P., Figueiredo, M.-O., de Oliveira, D., Veiga, J.P. & Batista, M.J., 2013. Molybdenite as a Rhenium Carrier: First Results of a Spectroscopic Approach Using Synchrotron Radiation. *Journal of Minerals and Materials Characterization and Engineering*, 1, pp.207–211.
- Sinclair, W. & Jonasson, I., 2014. Highly Siderophile Elements (Re, Au and PGE) in Porphyry Deposits and Their Mantle Origins. *Acta Geologica Sinica (English Edition)*, 88(s2), pp.616–618.
- Sinclair, W.D., 2007. Porphyry Deposits. *Special Publication*, (5), pp.223–243.
- Sinclair, W.D. & Jonasson, I.R., 2014. Highly Siderophile Elements (Re, Au and PGE) in Porphyry Deposits and Their Mantle Origins. *Acta Geologica Sinica*, 88(2), pp.616–618.
- Singer, D.A., Berger, V.I., Menzie, W.D. & Berger, B.R., 2005. Porphyry copper deposit density. *Economic Geology*, 100(3), pp.491–514.
- Siron, C.R., Thompson, J.F.H., Baker, T., Friedman, R., Tsitsanis, P., Russell, S., Randall, S. & Mortensen, J., 2016. Chapter 2 Magmatic and Metallogenic Framework of Au-Cu Porphyry and Polymetallic Carbonate- Hosted Replacement Deposits of the Kassandra Mining District , Northern Greece. *Economic Geology Special Publication*, 19, pp.29–55.
- Skirrow, R.G., Huston, D.L., Mernagh, T.P., Thorne, J.P., Dulfer, H. & Senior, A., 2013. Critical commodities for a high-tech world: Australia's potential to supply global demand. *Austral. Govern. Geosci. Australia*, (118 pp.).
- Solano, J.M.S., Jackson, M.D., Sparks, R.S.J., Blundy, J.D. & Annen, C., 2012a. Melt Segregation in Deep Crustal Hot Zones: a Mechanism for Chemical Differentiation, Crustal Assimilation and the Formation of Evolved Magmas. *Journal of Petrology*, 53(10), pp.1999–2026.

- Solano, J.M.S., Jackson, M.D., Sparks, R.S.J., Blundy, J.D. & Annen, C., 2012b. Melt Segregation in Deep Crustal Hot Zones: a Mechanism for Chemical Differentiation, Crustal Assimilation and the Formation of Evolved Magmas. *Journal of Petrology*, 53(10), pp.1999–2026.
- Solomon, M., 1990. Subduction, arc reversal, and the origin of porphyry copper-gold deposits in island arcs. *Geology*, 18(7), pp.630–633.
- Sotnikov, V.I., Berzina, A.N., Economou-Eliopoulos, M. & Eliopoulos, D.G., 2001. Palladium, platinum and gold distribution in porphyry Cu - Mo deposits of Russia and Mongolia. *Ore Geology Reviews*, 18(1–2), pp.95–111.
- Spencer, E.T., Wilkinson, J.J., Creaser, R.A. & Seguel, J., 2015. The distribution and timing of molybdenite mineralization at the El Teniente cu-mo porphyry deposit, Chile. *Economic Geology*, 110(2), pp.387–421.
- Spooner, E.T.C., 1993. Magmatic sulphide/volatile interaction as a mechanism for producing chalcophile element enriched, Archean Au-quartz, epithermal Au-Ag and Au skarn hydrothermal ore fluids. *Ore Geology Reviews*, 7(5), pp.359–379.
- Stampfli, G.M. & Borel, G.D., 2004. The TRANSMED transects in space and time: constraints on the paleotectonic evolution of the Mediterranean domain. In *The TRANSMED Atlas. The Mediterranean region from crust to mantle*. Springer, pp. 53–80.
- Steele-MacInnis, M., Ridley, J., Lecumberri-Sanchez, P., Schlegel, T.U. & Heinrich, C.A., 2016. Application of low-temperature microthermometric data for interpreting multicomponent fluid inclusion compositions. *Earth-Science Reviews*, 159, pp.14–35.
- Stein, H., Scherst n, A., Hannah, J. & Markey, R., 2003. Subgrain-scale decoupling of Re and 187Os and assessment of laser ablation ICP-MS spot dating in molybdenite. *Geochimica et Cosmochimica Acta*, 67(19), pp.3673–3686.
- Stein, H.J., Markey, R.J., Morgan, J.W., Hannah, J.L. & Scherst n, A., 2001. The remarkable Re-Os chronometer in molybdenite: How and why it works. *Terra Nova*, 13(6), pp.479–486.
- Steinberger, I., Hinks, D., Driesner, T. & Heinrich, C.A., 2013. Source plutons driving porphyry copper ore formation: Combining geomagnetic data, thermal constraints, and chemical mass balance to quantify the magma chamber beneath the bingham canyon deposit. *Economic Geology*, 108(4), pp.605–624.
- Sterner, S., Chou, I., Downs, R. & Pitzer, K., 1992. Phase relations in the system NaCl-KCl-H<sub>2</sub>O: V. Thermodynamic- PTX analysis of solid-liquid equilibria at high temperatures and pressures.

## List of References

- Geochimica et cosmochimica ...*, 56(6), pp.2295–2309.
- Sterner, S.M., Hall, D.L. & Bodnar, R.J., 1988. Synthetic fluid inclusions. V. Solubility relations in the system NaCl-KCl-H<sub>2</sub>O under vapor-saturated conditions. *Geochimica et Cosmochimica Acta*, 52(5), pp.989–1005.
- Stoffell, B., Wilkinson, J.J. & Jeffries, T.E., 2004. Metal transport and deposition in hydrothermal veins revealed by 213nm UV laser ablation microanalysis of single fluid inclusions. *American Journal of Science*, 304(6), pp.533–557.
- Stratex International, 2016. Muratdere JORC compliant resource. Available at: <http://www.stratexinternational.com/project/muratdere> [Accessed July 20, 2016].
- Student, J.J. & Bodnar, R.J., 2004. Silicate Melt Inclusions in Porphyry Copper Deposits: Identification and Homogenization Behavior. *The Canadian Mineralogist*, 42(5), pp.1583–1599.
- Student, J.J. & Bodnar, R.J., 1999. Synthetic Fluid Inclusions XIV: Coexisting Silicate Melt and Aqueous Fluid Inclusions in the Haplogranite-H<sub>2</sub>O-NaCl-KCl System. *Journal of Petrology*, 40(10), pp.1509–1525.
- Sun, W., Arculus, R.J., Bennett, V.C., Eggins, S.M. & Binns, R.A., 2003. Evidence for rhenium enrichment in the mantle wedge from submarine arc-like volcanic glasses (Papua New Guinea). *Geology*, 31(10), pp.845–848.
- Sun, W., Arculus, R.J., Kamenetsky, V.S. & Binns, R. a, 2004. Release of gold-bearing fluids in convergent margin magmas prompted by magnetite crystallization. *Nature*, 431(7011), pp.975–978.
- Sun, W., Huang, R. fang, Li, H., Hu, Y. bin, Zhang, C. chan, Sun, S. jun, Zhang, L. peng, Ding, X., Li, C. ying, Zartman, R.E. & Ling, M. xing, 2015. Porphyry deposits and oxidized magmas. *Ore Geology Reviews*, 65(P1), pp.97–131.
- Sykes, J., Wright, J. & Trench, A., 2016. Discovery, supply and demand: from Metals of Antiquity to critical metals. *Applied Earth Sciences*, 125(1), pp.3–20.
- Sylvester, P.J. & Eggins, S.M., 1997. Analysis of Re, Au, Pd, Pt and Rh in NIST Glass Certified Reference Materials and Natural Basalt Glasses by Laser Ablation ICP-MS. *Geostandards Newsletter*, 21(2), pp.215–229.
- Tagirov, B.R., Baranova, N.N., Zotov, A. V, Akinfiev, N.N., Polotnyanko, N.A., Shikina, N.D.,

- Koroleva, L.A., Shvarov, Y. V & Bastrakov, E.N., 2013. The speciation and transport of palladium in hydrothermal fluids: experimental modeling and thermodynamic constraints. *Geochimica et Cosmochimica Acta*, 117, pp.348–373.
- Tapster, S., Condon, D.J., Naden, J., Noble, S.R., Petterson, M.G., Roberts, N.M.W., Saunders, A.D. & Smith, D.J., 2016. Rapid thermal rejuvenation of high-crystallinity magma linked to porphyry copper deposit formation; evidence from the Koloula Porphyry Prospect, Solomon Islands. *Earth and Planetary Science Letters*, 442, pp.206–217.
- Tarkian, M., Hunken, U., Tokmakchieva, M. & Bogdanov, K., 2003. Precious-metal distribution and fluid-inclusion petrography of the Elatsite porphyry copper deposit , Bulgaria. *Mineralium Deposita*, 38(10), pp.261–281.
- Tarkian, M., Hünken, U., Tokmakchieva, M. & Bogdanov, K., 2003. Precious-metal distribution and fluid-inclusion petrography of the Elatsite porphyry copper deposit, Bulgaria. *Mineralium Deposita*, 38(3), pp.261–281.
- Tarkian, M. & Koopmann, G., 1995. Platinum-group minerals in the Santo Tomas II (Philex) porphyry copper-gold deposit, Luzon Island, Philippines. *Mineralium Deposita*, 30(1), pp.39–47.
- Tarkian, M. & Stribrny, B., 1999. Platinum-group elements in porphyry copper deposits: a reconnaissance study. *Mineralogy and Petrology*, 65(3–4), pp.161–183.
- Tatsumi, Y., 1989. Migration of fluid phases and genesis of basalt magmas in subduction zones. *Journal of Geophysical Research: Solid Earth*, 94(B4), pp.4697–4707.
- Taylor, H.P. & Sheppard, S.M.F., 1986. Igneous rocks; I, Processes of isotopic fractionation and isotope systematics. *Reviews in Mineralogy and Geochemistry*, 16(1), pp.227–271.
- Tekeli, O., 1981. Subduction complex of pre-Jurassic age, northern Anatolia, Turkey. *Geology*, 9(2), pp.68–72.
- Tessalina, S.G., Yudovskaya, M.A., Chaplygin, I. V., Birck, J.L. & Capmas, F., 2008. Sources of unique rhenium enrichment in fumaroles and sulphides at Kudryavy volcano. *Geochimica et Cosmochimica Acta*, 72(3), pp.889–909.
- Tessalina, S.G., Yudovskaya, M.A., Chaplygin, I. V, Birck, J.-L. & Capmas, F., 2008. Sources of unique rhenium enrichment in fumaroles and sulphides at Kudryavy volcano. *Geochimica et Cosmochimica Acta*, 72(3), pp.889–909.

## List of References

- Thode, H.G. & Monster, J., 1965. Sulfur-isotope geochemistry of petroleum, evaporites, and ancient seas.
- Thomas, R., 2002. A Beginner's Guide to ICP-MS Part 4: A Review of Interferences. *Spectroscopy*, 16(April), p.4.
- Thompson, J.F.H., 2016. Changing World-Changing Exploration. In *Proceedings of SEG 2016: Tethyan Tectonics and Metallogeny*.
- Thompson, J.F.H., Lang, J.R. & Stanley, C.R., 2001. Platinum group elements in alkaline porphyry deposits, British Columbia. *Exploration and Mining in British Columbia, Mines Branch*, Part B(January 2001), pp.57–64.
- Tiepolo, M. & Tribuzio, R., 2008. Petrology and U–Pb zircon geochronology of amphibole-rich cumulates with sanukitic affinity from Husky Ridge (Northern Victoria Land, Antarctica): insights into the role of amphibole in the petrogenesis of subduction-related magmas. *Journal of Petrology*, 49(5), pp.937–970.
- Tooth, B., Brugger, J., Ciobanu, C. & Liu, W., 2008. Modeling of gold scavenging by bismuth melts coexisting with hydrothermal fluids. *Geology*, 36(10), pp.815–818.
- Tooth, B., Ciobanu, C.L., Green, L., O'Neill, B. & Brugger, J., 2011. Bi-melt formation and gold scavenging from hydrothermal fluids: An experimental study. *Geochimica et Cosmochimica Acta*, 75(19), pp.5423–5443.
- Tooth, B., Etschmann, B., Pokrovski, G.S., Testemale, D., Hazemann, J.-L., Grundler, P. V & Brugger, J., 2013. Bismuth speciation in hydrothermal fluids: An X-ray absorption spectroscopy and solubility study. *Geochimica et Cosmochimica Acta*, 101, pp.156–172.
- Tuttle, O.F., 1940. *The variable inversion temperature of quartz as a possible geologic thermometer*, Carnegie Institution.
- UK House of Commons, 2010. *Strategically important metals*,
- Ulrich, T., Günther, D. & Heinrich, C.A., 2002. The evolution of a porphyry Cu-Au deposit, based on LA-ICP-MS analysis of fluid inclusions: Bajo de la Alumbrera, Argentina. *Economic Geology*, 97(8), pp.1889–1920.
- Ulrich, T., Günther, D. & Heinrich, C. a., 1999. Gold concentrations of magmatic brines and the metal budget of porphyry copper deposits. *Nature*, 399(6737), pp.676–679.
- Ulrich, T. & Heinrich, C.A., 2002. Geology and Alteration Geochemistry of the Porphyry Cu-Au

- Deposit at Bajo de la Alumbrera, Argentina. *Economic Geology*, 97(8), pp.1865–1888.
- Uysal, I., Zaccarini, F., Sadiklar, M.B., Tarkian, M., Thalhahmer, O.A.R. & Garuti, G., 2009. The podiform chromitites in the Dagküplü and Kavad mines, Eskisehir ophiolite (NW-Turkey): Genetic implications of mineralogical and geochemical data. *Geologica Acta*, 7(3), pp.351–362.
- Voudouris, P., 2006. A comparative mineralogical study of Te-rich magmatic-hydrothermal systems in northeastern Greece. *Mineralogy and Petrology*, 87(3–4), pp.241–275.
- Voudouris, P., Tarkian, M. & Arikas, K., 2006. Mineralogy of telluride-bearing epithermal ores in the Kassiteres-Sappes area, western Thrace, Greece. *Mineralogy and Petrology*, 87(1–2), pp.31–52.
- Voudouris, P.C., Melfos, V., Spry, P.G., Bindi, L., Kartal, T., Arikas, K., Moritz, R. & Ortelli, M., 2009. Rhenium-rich molybdenite and rheniite in the Pagoni Rachi Mo-Cu-Te-Ag-Au prospect, northern Greece: Implications for the re geochemistry of porphyry-style Cu-Mo and Mo mineralization. *Canadian Mineralogist*, 47(5), pp.1013–1036.
- Voudouris, P.C., Melfos, V., Spry, P.G., Kartal, T., Schleicher, H., Moritz, R. & Ortelli, M., 2013. The Pagoni Rachi/Kirki Cu-Mo±Re±Au deposit, northern Greece: Mineralogical and fluid inclusion constraints on the evolution of a telescoped porphyry-epithermal system. *Canadian Mineralogist*, 51(2), pp.253–284.
- Waite, K.A., Keith, J.D., CHRISTIANSEN, E.H., Whitney, J.A., Hattori, K., Tingey, D.G. & Hook, C.J., 1997. Petrogenesis of the volcanic and intrusive rocks associated with the Bingham Canyon porphyry Cu–Au–Mo deposit, Utah. *Soc Econ Geol Guidebook Ser*, 29, pp.91–128.
- Wang, R., Richards, J., Hou, Z., Yang, Z. & DuFrane, S.A., 2014. Increased magmatic water content-the key to oligo-miocene porphyry Cu-Mo +/- Au formation in the Eastern Gangdese Belt, Tibet. *Economic Geology*, 109(5), pp.1315–1339.
- Wang, R., Richards, J.P., Hou, Z.Q., Yang, Z.M., Gou, Z. Bin & DuFrane, S.A., 2014. Increasing magmatic oxidation state from paleocene to miocene in the eastern gangdese belt, tibet: Implication for collision-related porphyry Cu-Mo ±Au mineralization. *Economic Geology*, 109(7), pp.1943–1965.
- Watterson, J.R., Gott, G.B., Neuerburg, G.J., Lakin, H.W. & Cathrall, J.B., 1977. Tellurium, a guide to mineral deposits. *Journal of Geochemical Exploration*, 8(1–2), pp.31–48.
- Webber, J. & Farchy, J., 2010. Chile miners' strike turns cost of copper red hot. *Financial Times*.

## List of References

- Available at: <https://www.ft.com/content/ccf75f58-ec33-11df-9e11-00144feab49a>  
[Accessed September 30, 2016].
- Weis, P., Driesner, T. & Heinrich, C. a, 2012. Porphyry-copper ore shells form at stable pressure-temperature fronts within dynamic fluid plumes. *Science (New York, N.Y.)*, 338(6114), pp.1613–6.
- Wilkinson, J.J., 2001. Fluid inclusions in hydrothermal ore deposits. *Lithos*, 55(1), pp.229–272.
- Wilkinson, J.J., 2013. Triggers for the formation of porphyry ore deposits in magmatic arcs. *Nature Geoscience*, 6(11), pp.917–925.
- Williams-Jones, A.E. & Heinrich, C.A., 2005. 100th Anniversary special paper: vapor transport of metals and the formation of magmatic-hydrothermal ore deposits. *Economic Geology*, 100(7), pp.1287–1312.
- Wilson, A.J., Cooke, D.R. & Harper, B.L., 2003. The Ridgeway gold-copper deposit: A high-grade alkalic porphyry deposit in the Lachlan fold belt, New South Wales, Australia. *Economic Geology*, 98(8), pp.1637–1666.
- Wyllie, P.J. & Huang, W.L., 1976. High CO<sub>2</sub> solubilities in mantle magmas. *Geology*, 4(1), pp.21–24.
- Xiong, Y. & Wood, S.A., 2002. Experimental determination of the hydrothermal solubility of ReS<sub>2</sub> and the Re–ReO<sub>2</sub> buffer assemblage and transport of rhenium under supercritical conditions. *Geochemical Transactions*, 3(1), p.1.
- Xiong, Y. & Wood, S.A., 2000. Experimental quantification of hydrothermal solubility of platinum-group elements with special reference to porphyry copper environments. *Mineralogy and Petrology*, 68(1–3), pp.1–28.
- Xiong, Y., Wood, S. & Kruszewski, J., 2006. Hydrothermal transport and deposition of rhenium under subcritical conditions revisited. *Economic Geology*, 101(2), pp.471–478.
- Yang, Z., Goldfarb, R. & Chang, Z., 2016. Chapter 11 Generation of Postcollisional Porphyry Copper Deposits in Southern Tibet Triggered by Subduction of the Indian Continental Plate \*. *Economic Geology Special Publication*, 19, pp.279–300.
- Yigit, O., 2012. A prospective sector in the Tethyan Metallogenic Belt: Geology and geochronology of mineral deposits in the Biga Peninsula, NW Turkey. *Ore Geology Reviews*, 46, pp.118–148.
- Yigit, O., 2006. Gold in Turkey—a missing link in Tethyan metallogeny. *Ore Geology Reviews*, 28(2), pp.147–179.



- Yigit, O., 2009. Mineral deposits of Turkey in relation to Tethyan metallogeny: implications for future mineral exploration. *Economic Geology*, 104(1), pp.19–51.
- Zacharias, J. & Wilkinson, J., 2007. ExLAM 2000: Excel VBA application for processing of transient signals from laser ablation (LA-ICP-MS) of fluid inclusions and solid phases [abs.]. *Bern, Switzerland, Abstracts*.
- Zachos, K., 1963. Discovery of a copper deposit in Chalkidiki peninsula, N-Greece. *Geology and Geophysics Research*, 8(1), p.26.
- Zaluski, G., Nesbitt, B. & Muehlenbachs, K., 1994. Hydrothermal alteration and stable isotope systematics of the Babine porphyry Cu deposits, British Columbia; implications for fluid evolution of porphyry systems. *Economic Geology*, 89(7), pp.1518–1541.
- Zelenski, M., Malik, N. & Taran, Y., 2014. Emissions of trace elements during the 2012–2013 effusive eruption of Tolbachik volcano, Kamchatka: enrichment factors, partition coefficients and aerosol contribution. *Journal of Volcanology and Geothermal Research*, 285, pp.136–149.
- Zhan-Fang, C., Hong, Z. & Zhao-hui, Q., 2009. Solvent extraction of rhenium from molybdenum in alkaline solution. *Hydrometallurgy*, 97(3), pp.153–157.
- Zimmerman, A., Stein, H., Markey, R., Fanger, L., Heinrich, C., Von Quadt, A. & Peytcheva, I., 2003. Re–Os ages for the elatsite Cu–Au deposit, Srednogorie zone, Bulgaria. *Mineral exploration and sustainable development, Millpress, Rotterdam*, pp.1253–1256.